Development of Heterogeneous Electrocatalysts for Conversion of Small Molecules Toward Sustainable Energy Transition

Dissertation

in kumulativer Form

zur Erlangung des akademischen Grades

Doktor rerum naturalium (Dr. rer. nat.)

der Mathematisch-Naturwissenschaftlichen Fakultät

der Universität Rostock

vorgelegt von Trang Minh Pham

geboren am 27.09.1995 in Hai Phong, Vietnam

Rostock, 05.08.2025

https://doi.org/10.18453/rosdok_id00005657

Die vorliegende Dissertation und die zugrunde liegenden Arbeiten wurden im Zeitraum von September 2021 bis August 2025 am Leibniz-Institut für Katalyse e.V. in Rostock unter der Betreuung von Prof. Dr. Robert Francke in der Themengruppe „Heterogene Elektrokatalysatoren“ von Dr. Annette-Enrica Surkus durchgeführt und abgeschlossen.

Gutachter:

Prof. Dr. Robert Francke, Leibniz-Institut für Katalyse, Rostock, Deutschland

Prof. Dr. Adam Holewinski, University of Colorado Boulder, USA

Datum der Einreichung: 08.08.2025

Datum der Verteidigung: 11.11.2025

Statement of Authorship

I hereby affirm that I have written the present work by myself without outside assistance. No other resources were utilized than stated. All references as well as verbatim extracts were quoted, and all sources of information were specifically acknowledged.

Ich versichere hiermit an Eides statt, dass ich die vorliegende Arbeit selbständig angefertigt und ohne fremde Hilfe verfasst habe. Dazu habe ich keine außer den von mir angegebenen Hilfsmitteln und Quellen verwendet. Die den benutzten Werken inhaltlich und wörtlich entnommenen Stellen habe ich als solche kenntlich gemacht.

Rostock, 05.08.2025

Trang Minh Pham

Acknowledgments

I would like to take this opportunity to thank those who have always supported me and made this work possible. First, I would like to thank my first supervisor, Prof. Dr. Robert Francke. Thank you for allowing me to be a join your group and work under your supervision. I am grateful for the knowledge and experience you shared with me, which helped me improve my scientific approach and work skills over the past four years.

I would also like to thank my second supervisor, Dr. Annette-Enrica Surkus, for her dedicated supervision. I am grateful to have worked in her laboratory daily, which was very well organized, and to have had her support on this journey. Despite being far away from family in a country significantly distant from my homeland, I have received full support and kindness.

I would like to acknowledge the RoHan DAAD Project for providing me with a scholarship that allowed me to come to Rostock and conduct this study. The RoHan Project funded my Ph. D studies for the past three years and gave me the opportunity to study abroad for six months while I was a Master student in 2020. I would also like to thank the IREKA project (part of the German H2Giga project) for their financial support.

Then, I would like to thank my colleagues in the Department of Electrochemistry & Catalysis. I am especially thankful to Na Liu, Dr. Wen Ju, and an amazing lab assistant Tuyen Thanh Do, who contributed to this work and supported me in my research. Furthermore, I would like to express my pride in being part of Prof. Francke's group. I would like to express my sincere gratitude to Prof. Robert Francke and Dr. Annette-Enrica Surkus for reviewing, commenting on, improving, and polishing my Ph.D. thesis.

I am grateful to the analytical department of LIKAT. In particular, I would like to thank Dr. Stephan Bartling and Dr. Nils Rockstroh for their XPS and STEM measurements and discussions. Thanks also to Dr. Annette-Enrica Surkus and Dr. Carsten Robert Kreyenschulte for SEM/EDX measurements and discussions, and to Dr. Henrik Lund and Kathleen Schubert for numerous XRD measurements. I thank also Anja Simmula and Sandra Leiminger for the EA and ICP-OES measurements. I would also like to thank the technician teams, especially Mr. Andreas Hutter, for his enthusiasm and kindness.

Thanks also to the other LIKAT colleagues: Dr. Yong Peng, Evaristo Salaya, Dr. Guangxin Xue, and Dr. Tobias Täufer. I am particularly grateful to Nicolette Surkus, Richard Surkus, Dr. Shital Kale, and Mrs. Christine Streu for being my wonderful friends in Rostock.

Finally, my heart goes out to my family in Vietnam who have always waited patiently and encouraged me. Most especially, I would like to thank my husband, Tuyen Thanh Do, who has been my greatest companion and has silently encouraged and takes good care of me on this journey.

Abstract

The goal of this work is to develop highly active and stable electrocatalysts that convert small molecules to facilitate a sustainable energy transition and a cleaner environment. The primary focus is on producing green hydrogen through water electrolysis using electricity from renewable energy sources, as green hydrogen can replace fossil fuels, thereby reducing their carbon footprint. The oxygen evolution reaction (OER) is significantly slower than the hydrogen evolution reaction (HER) at the cathode. Thus, developing high-active, stable, and affordable OER materials is essential for improving overall efficiency. Furthermore, mixed oxides of transition metals have emerged as promising OER catalysts in alkaline water electrolysis (AWE). In this context, a promising method for preparing $CoNiFeO_x$ electrocatalysts through one-pot sol-gel synthesis followed by thermal treatment is presented. An optimal ratio between Co : Ni : Fe, as well as the thermal treatment in an oxygen-deficient atmosphere, contributes to the superior electrocatalytic properties, such as high performance and excellent stability of the electrocatalyst, in both rotating disc electrode (RDE) and anion exchange membrane (AEM) electrolyzer studies.

Although Co and Ni are much cheaper than precious metal catalysts used for proton exchange membrane water electrolysis (PEMWE), the limited supply of Co and the poor environmental footprint of Co and Ni mining remain challenges for scaling up AWE capacities. Therefore, the approach is to reduce the metal content while maintaining catalytic performance by adding conductive carbon to the optimal CoNiFeOx catalyst. Reducing the metal oxide content by 40 wt% results in an optimized metal oxide-carbon composite material that exhibits attractive OER performance and outstanding stability in both RDE and flow AEM studies. In addition to electrochemical analysis, material characterization methods including XRD, XPS, SEM, EDX, STEM, EELS, BET, and XAS were applied to investigate the chemical and physical properties of the electrocatalysts.

Converting CO_2 into valuable carbon products, particularly C_{2+} products, is an appealing approach for industrial applications. Molecular copper catalysts with well-defined active sites have emerged as promising candidates for the electrochemical reduction of CO_2 to C_{2+} products. Based on the promising performance data obtained in an H-cell and a membrane electrode assembly (MEA) electrolyzer, a heterogenized molecular copper phenanthroline catalyst was studied using electrochemical impedance spectroscopy (EIS) in order to obtain mechanistic insights with special focus on the role of the supporting electrolyte cation.

Zusammenfassung

Das Ziel dieser Arbeit ist die Entwicklung hochaktiver und stabiler Elektrokatalysatoren, die kleine Moleküle umwandeln, um eine nachhaltige Energiewende im Hinblick auf eine sauberere Umwelt zu ermöglichen. Das Hauptaugenmerk liegt auf der Herstellung von grünem Wasserstoff durch Wasserelektrolyse unter Verwendung von Strom aus erneuerbaren Energiequellen, da grüner Wasserstoff fossile Brennstoffe ersetzen und damit deren CO_2-Bilanz verbessern kann. Die anodische Sauerstoffentwicklungsreaktion (OER) ist wesentlich langsamer als die Wasserstoffentwicklungsreduktion (HER) an der Kathode. Daher ist die Entwicklung hochaktiver, stabiler und erschwinglicher OER-Materialien der Schlüssel zur Verbesserung der Gesamteffizienz. Unter der Vielzahl an untersuchten Systemen haben sich Mischoxide von Übergangsmetallen als vielversprechende OER-Katalysatoren für die alkalische Wasserelektrolyse (AWE) erwiesen. In diesem Zusammenhang wird eine vielversprechende Methode zur Herstellung von CoNiFeOx-Elektrokatalysatoren durch eine Sol-Gel-Synthese mit anschließender thermischer Behandlung vorgestellt. Ein optimales Verhältnis zwischen Co : Ni : Fe sowie die thermische Behandlung in einer sauerstoffarmen Atmosphäre tragen zu den überlegenen elektrokatalytischen Eigenschaften bei, wie z. B. durch hohe Leistung und ausgezeichnete Stabilität, sowohl in Studien mit der rotierenden Scheibenelektrode (RDE) als auch im Elektrolyseur mit Anionenaustauschermembran (AEM).

Obwohl Co und Ni viel billiger sind als Edelmetallkatalysatoren, die für die Protonenaustauschmembran-Wasserelektrolyse (PEMWE) verwendet werden, stellen das begrenzte Co-Angebot und der schlechte ökologische Fußabdruck de Co- und Ni-Abbaus nach wie vor eine Herausforderung für die Erhöhung der AWE-Kapazitäten dar. Daher wurde ein Ansatz zur Verringerung des Metallgehalts bei gleichzeitiger Aufrechterhaltung der katalytischen Leistung durch Zugabe von leitfähigem Kohlenstoff zum optimalen $CoNiFeO_x$-Katalysator entwickelt. Die Reduzierung des Metalloxidgehalts um 40 Gew.-% führt zu einem optimierten Metalloxid-Kohlenstoff-Verbundmaterial, das sowohl in RDE- als auch in AEM-Flusszell-Studien eine attraktive OER-Leistung und hervorragende Stabilität aufweist. Neben der elektrochemischen Analyse wurden Materialcharakterisierungsmethoden wie XRD, XPS, SEM, EDX, STEM, EELS, BET und XAS zur Untersuchung der chemischen und physikalischen Eigenschaften der Elektrokatalysatoren eingesetzt.

Schließlich ist die Umwandlung von CO_2 in wertvolle Produkte, insbesondere C_{2+}-Verbindungen, eine attraktive Strategie für industrielle Anwendungen. Molekulare Kupferkatalysatoren mit gut definierten aktiven Zentren haben sich als vielversprechende Kandidaten für die elektrochemische Reduktion von CO_2 in C_{2+}-Produkte erwiesen. Auf der Grundlage vielversprechender Leistungsdaten, gewonnen in H-Zellen- und im MEA-Elektrolyseur, wurde ein heterogenisierter molekularer Kupfer-Phenanthrolin-Katalysator mit Hilfe der elektrochemischen Impedanzspektroskopie (EIS) untersucht, um mechanistische Erkenntnisse zu gewinnen, wobei dabei der Schwerpunkt auf der Rolle des Leitsalzkations lag.

List of Abbreviations

Abbreviation	Full description
AC	alternating current
AEM	anion exchange membrane
AWE	alkaline water electrolysis
BET	Brunauer–Emmett–Teller
C_1 product	product containing one carbon atom
C_{2+} product	product containing two or more carbon atoms
CB	carbon black
C-C coupling	carbon-carbon coupling
C_{dl}	double-layer capacitance
CE	counter electrode
CM	modified carbon
CPE	constant-phase element
CV	cyclic voltammetry
DFT	density functional theory
DOS	density of states
DPV	differential pulse voltammetry
DRT	distribution of relaxation times
E^{eq}	equilibrium potential
e.g.	exempli gratia
eCO_2RR	electrochemical CO_2 reduction reaction
ECSA	electrochemically active surface area
EDX	energy-dispersive X-ray spectroscopy
EELS	electron energy loss spectroscopy
EIS	electrochemical impedance spectroscopy
E_{onset}	onset-potential
Eq.	equation
eV	electron volt
geo	geometrical surface area
H-cell	h-type divided electrochemical cell
HER	hydrogen evolution reaction
H-H bond	hydrogen-hydrogen bond
H_{opd}	hydrogen overpotential deposition
HOR	hydrogen oxidation reaction
H_{upd}	hydrogen underpotential deposition
i.e.	id est

LSV	linear sweep voltammetry
M	catalyst active site
Me	metal
MEA	membrane electrode assembly
Me-H bond	metal-hydrogen bond
MO	metal oxide
MOF	metal-organic framework
η_{10}	overpotential at 10 mA cm^{-2}
$Nm^3\ h^{-1}$	normal cubic metres per hour
OCP	open circuit potential
OER	oxygen evolution reaction
O-O bond	oxygen-oxygen bond
ORR	oxygen reduction reaction
PEMWE	proton exchange membrane water electrolysis
R_{ct}	charge transfer resistance
RDE	rotating disk electrode
RE	reference electrode
RHE	reversible hydrogen electrode
R_p	polarization resistance
SAC	single-atom catalyst
SEM	scanning electron microscope
SOWE	solid oxide water electrolysis
SQWV	square wave voltammetry
STEM	scanning transmission electron microscopy
V_{RHE}	potential versus reversible hydrogen electrode
vs.	versus
WE	working electrode
wt %	weight percentage
XANES	X-ray absorption near edge structure
XAS	X-ray absorption spectroscopy
XPS	X-ray photoelectron spectroscopy
XRD	X-ray diffraction

Table of Contents

List of Figures

List of Tables

1. Introduction

1.1. Contemporary Energy Management and Transition

Energy is an indispensable part of daily life and manufacturing. The International Energy Agency (IEA) reported in 2024, that the global energy demand had increased by 2.2%, faster than the average rate of the past decade, due to rapid technological and industrial development [1]. Traditionally, consuming energy in the form of electricity requires gas, oil, and other fuels as primary energy carriers [2]. Gas and oil face the problem of uneven distribution around the world, which leads to price issues [3]. Additionally, fossil reserves are declining in the long term, and producing energy from fossil fuels damages the environment and enhances the greenhouse effect [4]. The world now faces the challenge of using more intermittent renewable energy sources such as solar and wind power.

In detail, traditional resources include fossil fuels (coal, natural gas, and oil) and nuclear power [5]. Nuclear power has several drawbacks, including waste disposal, safety risks, and costs [6]. In contrast, renewable resources are natural resources that can be replenished in a relatively short period of time, making them virtually inexhaustible on human timescales. Renewable resources are a promising solution for minimizing environmental impacts, health hazards, safety risks, and energy prices. However, they depend heavily on weather, location, and time. The availability of this type of energy depends significantly on regions with high sunlight density and suitable weather conditions. Often, these places are not the same as where the energy is needed. Therefore, the energy must be transported using a material that can store the produced surplus energy [7]. The most essential points in solving the energy crisis are achieving energy sustainability, reducing the cost of energy production, improving energy storage and efficiency, and transporting the stored energy [8].

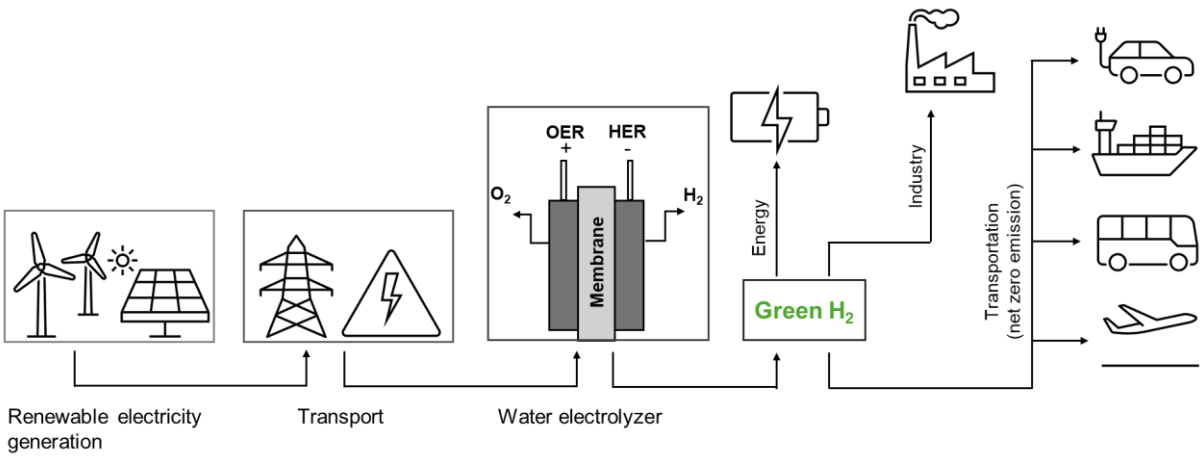

Figure 1. Green hydrogen production from water electrolysis using renewable energy, along with H_2 utilization strategies.

Hydrogen has the potential to be a key energy carrier for a sustainable economy. It can be stored for later use, transported, and converted into electricity as well as heat for industrial and transportation use (see Fig. 1) [9]. Furthermore, green hydrogen, can easily be produced from water

using electrolysis or photocatalysis with renewable energy. It does not cause environmental problems, produce pollutants, or affect human health [10]. On the other hand, there are still challenges with respect to efficiency of its generation and storage, which must be overcome for implementing a hydrogen economy [11].

1.2. Hydrogen Production

As discussed before, using hydrogen as a secondary energy source could be a viable solution for meeting global energy demands in a sustainable way [12]. According to the report from the International Renewable Energy Agency (IRENA) in late 2021, nearly 47% of the global hydrogen production comes from natural gas, 27% from coal, and 22% from oil (as a byproduct of oil refining). Only around 4% comes from electrolysis. Depending on the technological process, energy source, and environmental impact, hydrogen is distinguished by six main color codes i.e., blue, grey, brown/black, turquoise, and green (see Fig. 2).

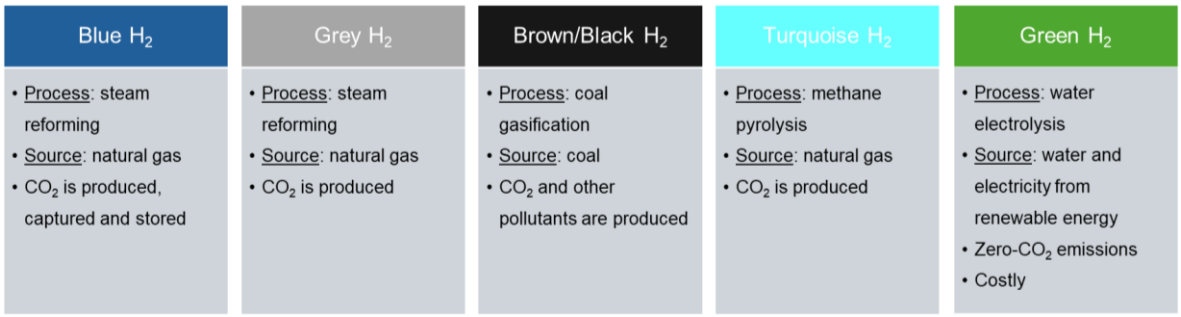

Figure 2. Color coding for classification of the origin of hydrogen [13].

Blue hydrogen (H_2) is commonly produced through two main processes: the steam methane reforming process (SMR) and autothermal reforming of methane (ATR) [14]. Although CO_2 is produced during blue H_2 production, carbon capture and storage technologies can be used to store it [15], meaning blue H_2 does not necessarily produce CO_2 emissions. However, the long-term impacts of storage remain uncertain, and potential leakage could harm both environment and climate.

Grey hydrogen is obtained by different methods: steam methane reforming, partial oxidation, or autothermal reforming [13c]. It is commonly used in the petrochemical industry and in ammonia production [16]. The main issue with grey H_2 is the significant amount of CO_2 emitted during H_2 production, estimated at around 830 Mt yearly [17].

Brown/black hydrogen is produced from coal with the colors referring to the types of lignite (brown) and bituminous (black) coal [17]. This method is considered the least environmentally friendly method of hydrogen production [13c]. There are two main methods of forming brown/black H_2: coal gasification and co-gasification of coal and biomass [17]. Coal gasification's main advantage lies in its ability to efficiently convert various carbon-based raw materials or waste into valuable gaseous products, such as CO, H_2, CH_4, and others [13c].

Turquoise hydrogen is produced through a thermal process called methane pyrolysis, whereby natural gas is broken down into H_2 and solid carbon [13c]. The process can be CO_2-neutral if the carbon remains permanently bound and does not convert to other carbon-based products during further processing. However, the extraction of raw material and natural gas itself contribute to emissions. Therefore, turquoise hydrogen is not usually completely climate-neutral throughout the entire production process and the downstream processing of carbon as a byproduct [18].

Green hydrogen, also known as "clean hydrogen", "renewable hydrogen", or "low-carbon hydrogen", is produced through water electrolysis using electricity from renewable energy sources [10, 13b, 13c, 19]. Using renewable energy for green hydrogen production eliminates CO_2 emissions, making it a vital part of the transition to more sustainable energy and transportation infrastructure [20]. IRENA has stated that low-carbon hydrogen is essential to achieving net-zero emissions by 2050. Unfortunately, green hydrogen currently accounts for only a small portion of total global hydrogen production due to technological and economic challenges [10, 21]. As of May 2024, 54 countries have reported national hydrogen strategies and roadmaps, including ambitious targets for large-scale electrolyzer capacity of 287 GW by 2050. This represents a promising step toward achieving future net-zero carbon goals.

There are two main methods for generating green H_2: water electrolysis and photocatalysis. Electrolysis is the more mature technology and is already implemented in various industrial applications [10, 13c, 22]. It is considered the most promising method for producing green hydrogen, provided the electricity powering the water electrolyzer comes entirely from renewable sources (see the next chapter for the main theory of water electrolysis). In the case of photocatalysis, semiconductor photocatalysts (typically TiO_2-based) produce an electron-hole pair when exposed to light, and H_2 can be obtained through a reduction reaction [23]. This method allows solar energy to be converted and stored as chemical energy, which is one of the key advantages of green hydrogen production [23b]. Consequently, photocatalytic water splitting is considered one of the cleanest methods of producing hydrogen, as it relies solely on sunlight to split water directly into H_2 and O_2 [13c]. However, the method is still in its infancy and very far from being economically viable.

1.3. Water Electrolysis

Water electrolysis, the process through which water is splitted into hydrogen (H_2) and oxygen (O_2) *via* electrolysis, has been studied for over 200 years [12c, 22, 24]. In 1789, J.R. Deiman and A.P. van Troostwijk conducted one of the earliest experiments involving electricity and water [25]. They used an electrostatic generator to discharge electricity through gold wires submerged in water, resulting in the release of gases [26]. A significant breakthrough occurred in 1800 when Alessandro Volta invented the voltaic pile [27]. Soon after, William Nicholson and Anthony Carlisle used this new device to split water through electrolysis and successfully identified the resulting gases as hydrogen (H_2) and oxygen (O_2) [22]. As electrochemistry advanced, Faraday's law of electrolysis established a proportional relationship between electrical energy consumption and gas production, enabling a scientific definition and formal description of water electrolysis [22]. Currently, water electrolysis technology is grouped into two main categories: low-temperature and high-temperature water electrolysis [20, 28]. Alkaline water electrolysis (AWE) and proton

exchange membrane (PEM) water electrolysis (PEMWE) are low-temperature water electrolysis technologies that are currently the most popular in research and industry due to their efficiency (Fig. 3) [20, 29]. High temperature water electrolysis technology will be discussed later in the Section 1.3.2.

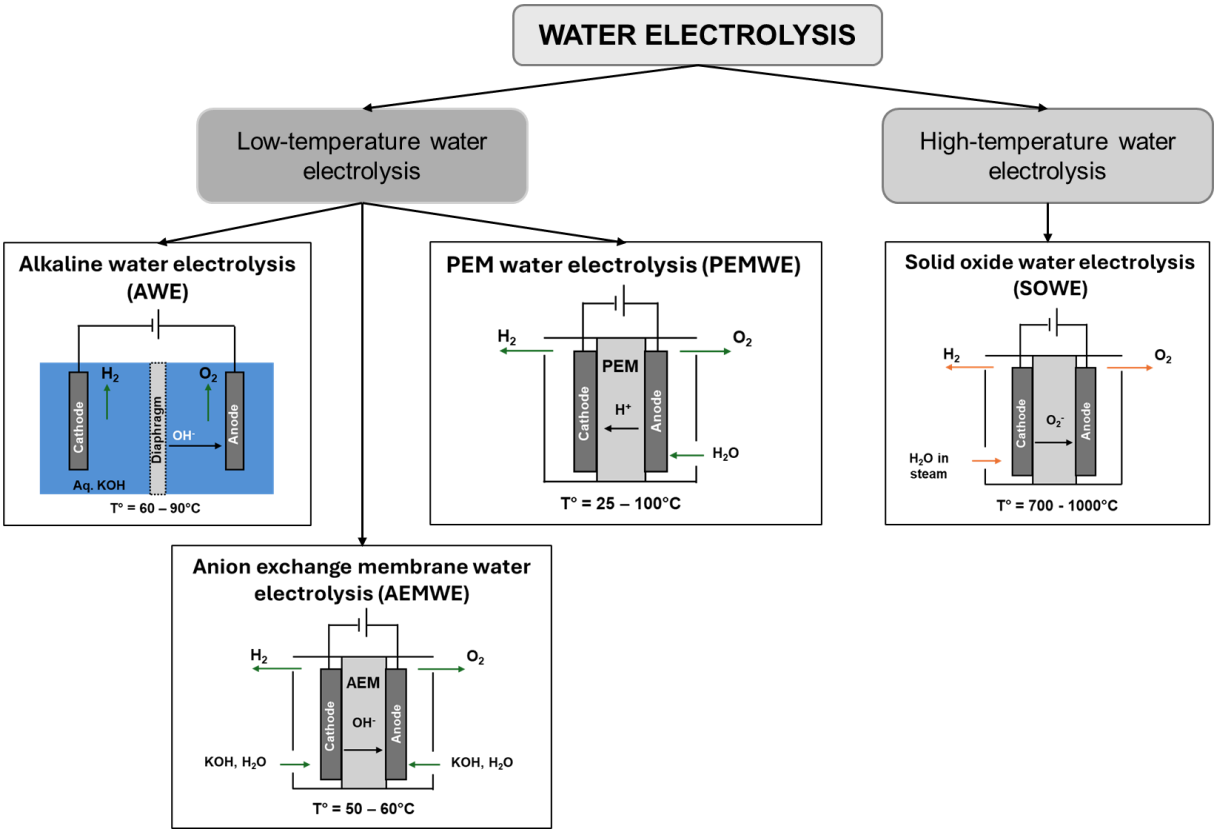

Figure 3. Schematic illustration of the working principle of different water electrolysis processes [28, 30].

1.3.1. Low-Temperature Water Electrolysis

Low-temperature electrochemical water splitting consists of two half-reactions: the hydrogen evolution reaction (HER) and the oxygen evolution reaction (OER). These reactions occur in alkaline (AWE) and acidic (PEMWE) conditions [20, 29a]. During alkaline electrolysis [31], four moles of water are reduced to form two molecules of H_2 and four moles of hydroxide ions (OH^-). The H_2 product is eliminated from the cathode surface, while the remaining OH^- ions are transferred through the separator to the anode chamber. At the anode, four moles of OH^- are discharged to produce one molecule of oxygen gas (O_2) and two moles of water (H_2O). In the case of the acidic electrolysis process [32], two moles of water are oxidized at the anode surface to produce one mole of oxygen gas (O_2) and four moles of protons (H^+). These protons are then transferred through the proton exchange membrane (PEM) to the cathode side, where they are reduced to form H_2 gas at the cathode surface.

1.3.1.1. Hydrogen Evolution Reaction (HER)

The general HER mechanism in alkaline and acidic media is illustrated by three reaction steps, as shown below [33]:

Under alkaline conditions:

$H_2O + e^- \rightleftharpoons H_{ads} + OH^-$ (Volmer step) (1)

$H_{ads} + H_2O + e^- \rightleftharpoons H_2 + OH^-$ (Heyrovsky step) (2a)

$2H_{ads} \rightleftharpoons H_2$ (Tafel step) (2b)

Under acidic conditions:

$H^+ + e^- \rightleftharpoons H_{ads}$ (Volmer step) (3)

$H^+ + H_{ads} + e^- \rightleftharpoons H_2$ (Heyrovsky step) (4a)

$2H_{ads} \rightleftharpoons H_2$ (Tafel step) (4b)

Under alkaline conditions [33a, 34], the Volmer step (1) involves dissociating a water molecule and subsequently adsorbing hydrogen onto an active site on the electrode or catalyst surface. Then, the target product H_2 is generated *via* an electrochemical process (Heyrovsky step, 2a) and/or a chemical process (Tafel step, 2b). Under acidic conditions [33c], the first step is the Volmer step (3), which produces adsorbed hydrogen (H_{ads}). Then, HER can proceed *via* the Heyrovsky step (4a), the Tafel step (4b), or both to produce H_2. At low overpotentials, the HER mechanism follows the Volmer step, which is then followed by the Heyrovsky and Tafel steps, the latter two occur in parallel. At high overpotentials, however, the Tafel step becomes insignificant, and the reaction predominantly proceeds through the Volmer–Heyrovsky pathway [33a, 35]. Electrocatalyst activity toward HER is strongly influenced by the strength of the Me–H bond, often leading to a "volcano-type" relationship between the reaction rate (exchange current density) and the Me-H bonding energy (see Fig. 4) [36]. Figure 4 illustrates the case of pure metals under alkaline (Fig. 4-left) and acidic (Fig. 4-right) conditions.

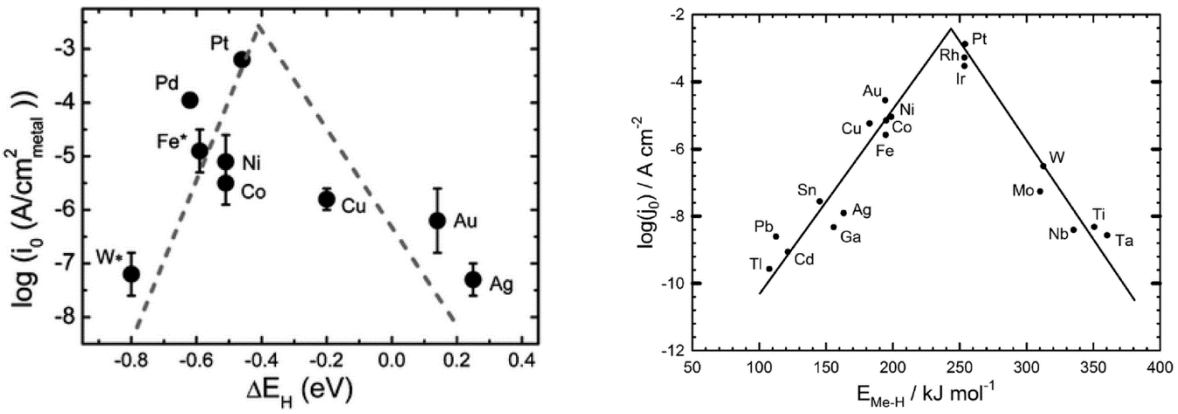

Figure 4. Volcano plots for HER in (left) alkaline solution (reprinted from ref. [37]) and (right) acidic solution (reprinted from ref. [38]).

It clearly demonstrates that platinum (Pt) metal exhibits the highest HER performance under both conditions with a Me-H binding energy close to the optimum, allowing for an efficient transition from reactants through intermediates to products. Metals on the left side of the volcano plots exhibit weaker Me–H bonds, which limit the adsorption of hydrogen atoms on the available active sites. For example, Ag and Cu demonstrate poor HER performance in an alkaline environment [39]. On the other hand, metals on the right form Me–H bonds that are too strong. This hinders the

formation of H–H bonds and the subsequent desorption of produced H_2 [35]. However, the dependence of HER current density on Me–H bond strength is not the only factor governing the efficiency of HER catalysts [40]. Other key factors influencing the catalytic activity include the position of the *d*-band center and its interaction with hydrogen [40-41]. Figure 5a shows a typical density of states for a transition metal in which the broad *s*-band is half-filled and the *d*-states form narrower bands [42]. The *d*-band center plays a crucial role in determining the surface's ability to adsorb other species. Thus, a shift in the *d*-band center relative to the Fermi level indicates a variation in adsorption energy (Fig. 5b). Specifically, the greater the upward shift, the stronger the binding energy between the metal and the adsorbate (Fig. 5c) [33a, 42-43]. Density functional theory calculations can determine the position of the d-band center, resulting in the prediction of promising catalysts [43-44].

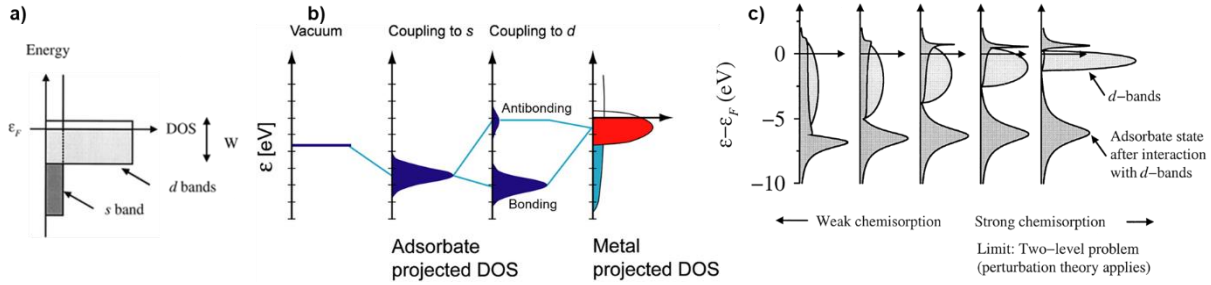

Figure 5. (a) Schematic illustration of density of state of a transition metal, showing the broad *s* band and the narrow *d* bands around the Fermi level (adapted from ref. [42], ε_F is the Fermi level energy and DOS stands for the density of states). (b) Bond formation at a transition-metal surface (adapted from ref. [45]). (c) The d-band center theory of adsorbed molecules on the surface of metal catalysts (adapted from ref. [42])

Another important factor contributing to the catalyst is hydrogen interaction in two states of adsorbed hydrogen: (i) H_{upd} (underpotential deposition, a strongly adsorbed state) and (ii) H_{opd} (overpotential deposition, a weakly adsorbed state). The latter is the more reactive state [33a, 40, 46].

In an acid environment, HER is a relatively straightforward process, consisting of the reduction of H^+ to an adsorbed hydrogen atom (H_{ads}) and the subsequent formation of H_2 [47]. In neutral/alkaline medium, the HER requires the dissociation of water molecules (H_2O) into a hydroxyl ion (OH^-) and H_{ads}, which is often considered the rate-limiting step in alkaline HER due to the breaking of a strong covalent bond (O-H) [48]. This results in slower kinetics of HER in neutral/alkaline medium than that under acidic conditions [33a, 46a]. Consequently, volcano plots offer a theoretical means of comparing pure metals using a single descriptor: the Me–H bond strength. However, for more complicated catalysts, such as metallic oxides, mixed metallic oxides, and alloys, the discussion becomes significantly more complex.

To study different electrocatalysts, it is important to define performance criteria such as overpotential at a given current density, Tafel slope, mass activity or current density at a specific potential, Faradaic efficiency, charge transfer, ECSA, and stability [49]. Based on these parameters and the testing protocol, the studied catalysts can be compared to published materials. Table 1 lists the recently reported electrocatalysts for HER under acidic and alkaline conditions over the last five years, as well as commercial catalysts, according to activity and stability. It can be concluded that the development of HER electrocatalysts follows the trend of reducing the loading

with expensive Pt group metals, for example by using carbon as supports/additives or Pt-free catalysts. However, poor catalyst stability remains a particular challenge for the long-term, large-scale implementation of HER and commercialization of water electrolysis for hydrogen production. This is due to the catalyst dissolution, corrosion, and bubble formations under harsh conditions such as acidic and alkaline electrolytes, leads to degradation of catalytic activity and efficiency [49-50].

Table 1. Summary of state-of-the-art catalysts for HER including key performance parameters.

Catalyst	Year reported	Working electrode (WE) - Electrolyte	η_{10} (mV)	Tafel slope (mV dec^{-1})	Stability test	Refs.
Commercial catalysts						
Commercial 20% PtRu/C	2016	GC – 0.1 M KOH	30	-	5000 cycles (between +0.0 and -0.4 V vs. RHE)	[51]
Commercial 20% Pt/C			42	-	-	
Commercial 20% Pt/C	2017	GC - 0.5 M H_2SO_4	35	30	-	[52]
Low- and non- Pt based catalysts						
Pt@MG NWs (*Pt on a nano engineered metallic glass (MG) surface*)	2021	GCE - 0.5 M H_2SO_4	48.5	19.8	at η_{500} for 500 hours	[53]
NFC@CNSs-700 (*Ni-Fe-Co@carbon nanosheets*)	2021	GC-RDE - 1.0 M KOH	213	115.1	at 20 mA cm^{-2} for 50 hours	[54]
CPF-Fe/Ni (*conjugated phthalocyanine framework (CPF) containing single atomic Ni/N/C and Fe/N/C*)	2023	GC-RDE - 1.0 M KOH	42	94.1	at η_{10} for 200 hours	[55]
		GC-RDE - 0.5 M H_2SO_4	23	169.5	at η_{10} for 200 hours	
WCU4-EPy (*tungsten-based carbide materials*)	2024	GC-RDE - 0.1 M NaOH	45	42	at 5 mA cm^{-2} for 15 hours	[56]
$PtTe_2$	2024	GC-RDE - 1.0 M KOH	108	98	1000 cycles (between -1.0 and 0.5 V vs. RHE)	[57]
Mo-CoO_x@MXene-Al (*MXene-Al: Al oxyhydroxide-terminated MXene*)	2022	GC-RDE - 1.0 M KOH	150	34	at 10 mA cm^{-2} for 25 hours	[58]
Ru_{NPs}-$RuCr_{APs}$-N-C (Ru_{NPs}: *Ru nanoparticles;* $RuCr_{APs}$: *RuCr atom pairs; N-C: nitrogen-doped carbon*)	2024	GC-RDE - 1.0 M KOH	31	53	at -0.1 V vs. RHE, for 20 hours	[59]
Pt/H_xMoO_3@CC (*Pt/hydrogenated* MoO_3 *on carbon cloth*)	2024	CC - 0.5 M H_2SO_4	11	58	at η_{10} for 12 hours	[60]
N-doped Ru/Mo_2C ($MCNR_x$)	2024	GC-RDE - 1.0 M KOH	35	36.5	at η_{10} for 50 hours	[61]
		GC-RDE - 0.5 M H_2SO_4	44	13.5	at η_{10} for 50 hours	
Mo2.8-Ru@CNT (*CNT: carbon nanotube*)	2025	GC-RDE - 0.5 M H_2SO_4	35	48	at 500 mA cm^{-2} for more than 100 hours	[62]
η_{10}: overpotential at 10 mA cm^{-2}; GC: glassy carbon; CC: carbon cloth; GC-RDE: glassy carbon rotating disk electrode						

1.3.1.2. Oxygen Evolution Reaction (OER)

Compared to the HER process, which involves two electron transfers, the OER process requires four electrons to form O-O bonds. This complex four electron process is generally associated with a higher overpotential than the HER process, and can therefore be considered the bottleneck of the water splitting process [63]. The general OER mechanisms in alkaline and acidic conditions are presented below:

Under alkaline conditions [64]:

$$M + OH^- \rightleftharpoons MOH + e^- \quad (5)$$

$$MOH + OH^- \rightleftharpoons MO + H_2O + e^- \quad (6)$$

$$2MO \rightleftharpoons 2M + O_2 \quad (7)$$

$$MO + OH^- \rightleftharpoons MOOH + e^- \quad (8a)$$

$$MOOH + OH^- \rightleftharpoons M + O_2 + H_2O + e^- \quad (8b)$$

Under acidic conditions [65]:

$$M + H_2O \rightleftharpoons MOH + H^+ + e^- \quad (9)$$

$$MOH \rightleftharpoons MO + H^+ + e^- \quad (10)$$

$$MO + H_2O \rightleftharpoons MOOH + H^+ + e^- \quad (11)$$

$$MOOH \rightleftharpoons M + O_2 + H^+ + e^- \quad (12)$$

In general, the OER can be described as a four-step process, as presented by reactions 5-8b under alkaline conditions and reactions 9-12 under acidic conditions. Each step of the reaction sequence can be influenced by OER catalysts [63-65]. The first step of the two proposed OER mechanisms involves the dissociation of H_2O in acidic electrolytes or the OH^- coordination in alkaline electrolytes. Under both conditions, M-OH is formed *via* the one-electron oxidation of OH^- adsorbed on the active site of the catalyst (M). In reactions 6 and 10, M-OH converts to M-O when a proton and an electron are removed. Then, two different paths of O_2 formation are possible. The first path occurs in alkaline media and is described by the transformation of M-O species that recombine to generate an O_2 molecule and a free M active site in reaction 7. On the other hand, the more common process under both conditions is transformation of M-O into M-OOH through one-electron oxidation in reactions 8a and 11. Finally, M-OOH undergoes a one-electron transfer process in reactions 8b and 12 to release an O_2 molecule and recover the initial active site M. The entire classical OER process contains three adsorbed reaction intermediates, which are *OH, *O, and *OOH [66].

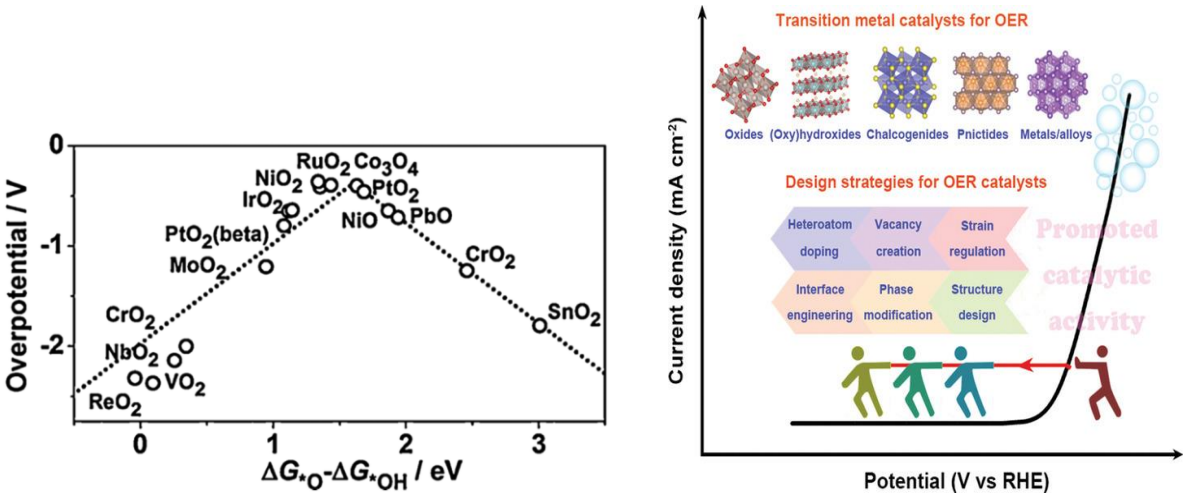

Figure 6. (Left) Volcano plot for OER on metal oxides (adapted from ref. [67]). (Right) Transition metal-based electrocatalysts for OER performance (taken from ref. [68]).

An ideal OER catalyst would have an equal change in Gibbs free reaction energy for each intermediate at the active site, and the OER reaction would start only slightly above the equilibrium potential of 1.23 V vs. RHE. However, actual catalysts require significant overpotentials for OER at reasonable rates [69]. It has been observed that both *OH and *OOH have a single bond between the oxygen atom and the catalyst surface and principally prefer the same

type of binding site [66]. Therefore, the volcano plot in Figure 6 (left) shows different single transition-metal oxides with their activity descriptor for the OER being the difference in energies of MO and MOH ($\Delta G_{MO} - \Delta G_{MOH}$) [70]. The rate-determining step of the OER usually occurs in the linear scaling relation between the difference in energies of MO and MOOH ($\Delta G_{MOOH} = \Delta G_{MOH} + 3.2 \pm 0.2$ eV) [71]. The deviation in the offset ±0.2 eV depends on a function of the exchange correlation functional used in the Density Functional Theory (DFT) calculations or on the class of materials [64]. This scaling relation lays the foundation for constructing an overpotential-dependent volcano plot for the OER over transition-metal oxides [71b].

Metallic oxides and oxyhydroxides are the most common OER catalysts in both alkaline and acidic conditions because they are thermodynamically more stable than other compounds at OER potential (see Fig. 6, right) [68, 72]. In the volcano plot (see Fig. 6, left), RuO_2 and IrO_2 are state-of-the-art OER catalysts, occupying the highest positions at the top of the volcano plot [73]. Under acidic conditions, iridium (Ir) is the most stable OER catalyst. Meanwhile, ruthenium (Ru) plays an important role in terms of high activity [74]. It's high electrocatalytic ability toward OER in an acidic environment of Ru is due to its transition from a low valence state to a stable Ru(IV) state during OER [75]. However, the long-term stability, cost, and rarity of Ir significantly impact its commercialization [76]. Therefore, cheaper and more abundant alternatives, such as Co, Ni, and Fe offer a significant advantage for AWE over the expensive and rare materials used for OER in PEMWE [29b, 73, 77]. Their multivalent oxidation states (II/III/IV) are responsible for their excellent OER activities [78]. Particularly, M(IV) containing species have been confirmed as the catalytic sites for cobalt-based catalysts [79], whereas M(III) containing species are active sites for iron and nickel [80]. Furthermore, mixed oxides of Ni, Co, and Fe (particularly $CoFeO_x$, $FeNiO_x$, and $CoFeNiO_x$) exhibit exceptional OER performance under alkaline conditions [81]. To select appropriate catalysts for applications, the key electrochemical parameters are to be measured to compare with those reported for other catalysts. Based on a review of literature, the critical parameter is the overpotential at a specific current density (preferably at 10 mA cm^{-2}). Basically, overpotential is estimated by the difference in potential compared to the expected OER equilibrium potential of 1.23 V vs. RHE, with a minor difference indicating high catalytic activity. In addition, the Tafel slope and the mass activity *via* catalyst loading provide essential information for identifying the catalytic ability. Finally, stability of the catalyst is also an important aspect. Tables 2 and 3 summarize the performance of state-of-the-art Co-, Ni-, and Fe-based, as well as Ru- and Ir- based OER electrocatalysts from the past five years. Although, these candidates are significantly cheaper than the precious metals (Ru and Ir) used in PEM electrolysis, issues related to the cost of materials are foreseeable in the future. Thus, a shortage of the rare Co metal can be expected due to the increasing demand for the Li-ion battery production [82] and the small number of deposits [83]. Further issues are related to the poor environmental footprint of Co and Ni mining [84]. Consequently, reducing the metal content while minimizing performance loss is important for improving the sustainability of Co-and Ni-based catalysts. The Table 2 also contains two examples that were developed in this work. A detailed discussion can be found in sections 3.1 and 3.2.

In the case of PEMWE, replacing or reducing Ir with cheaper, non-toxic metals has continuously been the key challenge in the field of electrochemical materials development as well as for large-scale PEM water electrolysis[85].

Table 2. Summary of reported catalysts for OER that include Co-, Ni-, and/or Fe oxides.

Catalyst	Year reported	WE - electrolyte	η_{10} (mV)	Mass activity at 1.56 V_{RDE}	Tafel slope (mV dec^{-1})	Stability test	Refs.
$Fe_{55}Co_{22.5}Ni_{22.5}$	2020	metal-alloy pellets 1.0 M NaOH	314	-	36	at 500 mA cm^{-2} for 50 hours	[86]
FeCoNiP@NC (*NC: nitrogen-doped carbon*)	2020	CP 1 M KOH	266	-	36	at 1.50 V vs. RHE for 25 hours	[87]
$Ni_{2.5}Co_5C_2O_4$	2021	CP 1 M KOH	330	~3 A g^{-1}	113	at 10 mA cm^{-2} for 24 hours	[88]
$(Co_{0.9}Ni_{0.1})_2B$	2021	GC 1 M KOH	371	~27 A g^{-1}	77	at 10 mA cm^{-2} for 8 hours	[89]
NiO/Co_3O_4	2022	GC-RDE 1 M KOH	330	~43 A g^{-1}	63	at 1.56 V vs. RHE for 48 hours	[90]
CoFe-$LDH_{0.5}$ fiber	2022	CC 1 M KOH	267	~80 A g^{-1}	56	at 1.53 V vs. RHE for 30 hours	[91]
Fe-$NiWO_4$	2023	CC 1 M KOH	230	~450 A g^{-1}	48	at 1.46 V vs. RHE for 30 hours	[92]
$NiCoO_2$/rGAs (*rGAs: reduced graphene aerogels*)	2024	GC 1 M KOH	258	~70 A g^{-1}	68	at 1.49 V vs. RHE for 10 hours	[93]
MnCo-OOH	2024	GC 1 M KOH	250	-	99	at 1.60 V vs. RHE for 12 hours	[94]
CoNiFe (2:2:1)/M (this work see section 3.1)	2024	GC-RDE 1 M KOH	291	~343 A g^{-1}	32	in AWE test: 10 $mg_{catalyst}$ cm^{-2}; at on-off 400 mA cm^{-2} for 75 hours	[95]
$Co_{0.17}Fe_{0.25}Ni_{0.58}$	2025	Ni-plate 1 M KOH	250	~40 A g^{-1}	49	in AWE test: 3.5 $mg_{catalyst}$ cm^{-2}; at 1000 mA cm^{-2} for 24 hours	[96]
Co_5Fe_5MoO	2025	CP 1 M KOH	245	-	92	at 10 mA cm^{-2} for 35 days	[97]
CFS-2 (CoFe-Silicide)	2025	GC-RDE 1 M KOH	291	~49 A g^{-1}	65	1000 cycles (1.1 and 1.9 V_{RDE})	[98]
M-Fe-Co_3O_4	2025	Ni foam 1 M KOH	297	~7 A g^{-1}	74	at 1.55 V_{RDE} for 12 hours	[99]
60MO/CM (this work see section 3.2)	2025	GC-RDE 1 M KOH	297	~370 A g^{-1}_{CoNiFe}	35	in AWE test: 5 $mg_{catalyst}$ cm^{-2}; at on-off 400 mA cm^{-2} for 110 hours	[100]
LDH: layered double hydroxide; GP: graphite plate; CP: carbon paper; CC: carbon cloth; MWCNT: multi-walled carbon nanotubes; GC-RDE: glassy carbon rotating disk electrode							

Table 3. Summary of reported catalysts for OER that include Ru-, and Ir-catalysts.

Catalyst	Year reported	WE-Electrolyte	η_{10} (mV)	Mass activity at 1.5 V_{RHE}	Tafel slope (mV dec^{-1})	Stability test	Refs.
Commercial IrO_2 (Alfa Aesar)	2022	GC-RDE 0.5 M H_2SO_4	390	-	66	-	[101]
$Ce_{0.2}$-IrO_2@NPC (*NPC: N-doped porous carbon*)	2020	CP 0.5 M H_2SO_4	224	~188 A g^{-1}	56	at 10 mA cm^{-2} for 100 hours	[102]
S-doped M-$SrIrO_3$	2021	GC 0.5 M H_2SO_4	228	~27 A g^{-1}_{Ir}	58	at 10 mA cm^{-2} for 20 hours	[103]
Cu-RuO_2-300	2022	GC 0.5 M H_2SO_4	201	~128 A g^{-1}	55	at 10 mA cm^{-2} for 24 hours	[104]
Sr_2CaIrO_6	2022	GC-RDE 0.1 M $HClO_4$	250	~390 A g^{-1}_{Ir}	33	in PEMWE test: 0.4 mg_{Ir} cm^{-2}; at 2 A cm^{-2} for 450 hours.	[105]
Ni-RuO_2	2023	GC-RDE 0.1 M $HClO_4$	214	~260 A g^{-1}	43	in PEMWE test: ~3.1 mg cm^{-2}; at 0.2 A cm^{-2} for 1000 hours.	[106]
ZnNiCoIrMn	2023	GC-RDE 0.1 M $HClO_4$	237	611 A g^{-1}_{Ir}	46	at 10 mA cm^{-2} for 100 hours	[107]
$Nb_{0.1}Ru_{0.9}O_2$	2023	GC-RDE 0.5 M H_2SO_4	204	151 A g_{Ru}^{-1} (at 1.47 V_{RDE})	48	in PEMWE test: ~2.0 mg cm^{-2}; at 0.3 A cm^{-2} for 100 hours.	[108]
$Mo_{0.15}$-RuO_2	2024	GC-RDE 0.5 M H_2SO_4	147	~700 A g^{-1}	38	at 10 mA cm^{-2} for 20 hours	[109]
m-$Ir_{0.91}Ru_{0.09}O_{2-\delta}$	2024	GC-RDE 0.5 M H_2SO_4	180	~380 A g^{-1}	50	in PEMWE test: ~0.1 mg cm^{-2}; at 1.8 V for 256 hours.	[110]

$IrRuO_x/MnO_x$	2025	Au-RDE 0.05 M H_2SO_4	256	~633 A g^{-1}_{RuIr}	62	in PEMWE test: 0.37 mg_{IrRu} cm^{-2}; at 2 A cm^{-2} for 150 hours.	[111]
GC: glassy carbon; CP: carbon paper; GC-RDE: glassy carbon rotating disk electrode.							

1.3.1.3. Anion Exchange Membrane Water Electrolysis (AEMWE)

AEMWE is the most recent low-temperature water electrolysis technology, driven primarily by the development of sufficiently stable alkaline membranes in recent years [112]. AEM electrolysis is receiving more attention due to its potential to lower the cell voltage through a zero-gap design and resulting smaller interelectrode distance than AWE [28, 77b]. In an AEM electrolyzer, the anode and cathode are separated by the anion exchange membrane that allows anion (OH^-) transport (see Fig. 3). The reaction occurs in the same fashion as in an AWE:

$$(HER)\ 4H_2O + 4e^- \rightleftharpoons 2H_2 + 4OH^- \qquad (13) \qquad\qquad (OER)\ 4OH^- \rightleftharpoons H_2O + 2O_2 + 4e^- \qquad (14)$$

Unlike AWE, AEM water electrolysis enables a low concentration of OH^- in the electrolyte by using diluted KOH, K_2CO_3/$KHCO_3$ or deionized water [77b]. Additionally, a stable membrane with high ionic conductivity, catalysts, and ionomers, as well as operating temperature are essential [113]. In the following, critical components of AEM systems, such as HER/OER catalysts and the membrane will be discussed (also listed in Table 4).

Table 4. Comparison of the main characteristics of alkaline, PEM and AEM water electrolysis (taken from ref. [77b]).

	AWE	PEMWE	AEM
Electrolyte	Aqueous KOH (20–40 wt%)	Proton exchange ionomer (*e.g.* Nafion)	Anion exchange ionomer (*e.g.*, AS-4) + diluted caustic solution
Cathode	Ni, Ni–Mo alloys	Pt, Pt–Pd	Ni and Ni alloys
Anode	Ni, Ni–Co alloys	RuO_2, IrO_2	Ni, Fe, Co oxides
Half-cell separation	Diaphragm (Zirfon Perl 500 µm)	Nafion 117 (*e.g.* 180 µm)	AEM (20–100 µm)
Current density (A cm^{-2})	0.2–0.4	0.6–2.0	0.2–1.0
Cell voltage (V)	1.8–2.4	1.8–2.2	1.8–2.2
Cell area (m^2)	<4	<3	Lab testing cells
Operating temperature (°C)	60–80	50–80	50–60
Operating pressure (bar)	1–30	30–76	1–30
Production rate ($Nm^3\ h^{-1}$)	<760	<40	<1
Gas purity (vol%)	>99.5	>99.9999	>99.99
System response	Seconds	Milliseconds	-
Stack lifetime (h)	60k to 100k	20–60k	-
Technology status	Mature	Commercial	R&D

The HER and OER mechanism in AEM water electrolysis are closely related to these in AWE, as described in Figure 3. Therefore, this chapter will discuss recent electrocatalysts for HER and OER under alkaline conditions in AEMWE. Regarding HER electrocatalysts, Ni-based catalysts are state-of-the-art materials that used as alternatives to Pt-based cathodic catalysts. However, they have significantly inferior activity compared to Pt-based catalysts [114]. The activity and stability of Ni alone are relatively poor, therefore, combining Ni with other transition metals (*e.g.,* Cu, Mo, and Co), oxides, or sulfides, selenides, nitrides or phosphides has been identified as a promising

strategy to improve performance [115]. Nevertheless, using a Pt-free cathode in commercial AEM designs is a viable option, despite the fact that some remarkably high active and stable catalysts have been reported in half-cell systems [77b]. In other words, the achieved saving in energy consumption must be carefully considered in the context of the high price of Pt.

Similar to applications in HER, Ni-based catalysts are widely used for OER in AEM electrolysis [77b, 114, 116]. Recent research has shown that Ni–Fe catalysts are more active than pure Ni catalysts [117]. Furthermore, Co-based catalysts exhibit high activity and stability when used anodic materials in AEM [118]. As previously discussed, Fe is useful for enhancing catalytic activity toward O_2 evolution. The mechanistic details and active species have been heavily discussed in recent years [119]. $NiCoO_x$-based catalysts demonstrate excellent performance and stability in AEM electrolysis [120]. In conclusion, Ni, Co, and Fe-based OER catalysts remain state-of-the-art for AEM water splitting. Optimizing catalyst loadings and the catalyst/ionomer ratio is essential to improving cell performance.

Another crucial components of an AEM electrolyzer are the anion exchange membrane and the ionomer [77b]. They are typically created with a polymer backbone to which cationic groups are anchored, allowing anions to selectively pass through the pores [121]. These anion exchange groups commonly comprise quaternary ammonium salts connected to polymeric backbones, such as polystyrene, polysulfone, poly(ether sulfone), or poly(phenylene oxide), *via* benzylic methylene groups [121]. However, the main limiting factor of anion exchange materials is their instability at high pH and temperature, which significantly affects the long-term stability of AEM electrolyzer systems and operational temperature limits [122]. Consequently, significant research efforts have focused on developing advanced anion exchange materials that provide enhanced thermal and chemical stability in alkaline environments for electrochemical applications [77b].

1.3.1.4. Advantages/Disadvantages of Low-Temperature Water Electrolysis Technologies

Table 5 summarizes the advantages and disadvantages of the different low-temperature water electrolysis technologies. The main advantage of AWE is that noble metals are not required as catalysts. Abundant non-noble transition metals, such as Ni, Co, and Fe, are widely used as benchmark materials in AWE. This is beneficial for minimizing operating costs and ensuring long-term operational stability. However, the quality of H_2 production from AWE is lower than that from PEMWE due to gas crossover through the ceramic membrane. Low current densities, efficiency, and operational pressure are the main drawbacks of AWE [28, 123]. PEMWE can achieve high energy efficiency in producing H_2 thanks to its ability to operate at high current densities [124]. Its compact design, high H_2 purity, and ability to operate at high pressure are advantageous for industrial applications. However, the strongly acidic environment is corrosive and limits the durability of PEMWE. This requires the use of durable materials for the electrocatalysts, especially the anodic catalysts, which are made of platinum and iridium [125]. Other important components of PEMWE are per- and polyfluoroalkyl substances (PFAS), which are found in the membranes and ionomers that enable proton conductivity and reactant separation [126]. However, these PFAS compounds are not easily degraded in nature and therefore pose a high risk to the environment and to human health [127]. In the coming years, these fluorinated chemicals will increasingly be banned in further

areas of life. Alongside the problem of iridium scarcity, developing novel, fluorine-free membranes for PEMWE are therefore one of the challenges for long-term use. Consequently, the use of PEMWE incurs high capital costs due to the use of iridium, and its future is uncertain due to the rapid depletion of this resource [85] and impending PFAS bans [128]. Without further research and development, the cost of this technology may be expected to rise significantly in the future, making it unprofitable for producing green hydrogen.

Therefore, AEMWE was developed to combine the advantages of AWE and PEMWE technologies. Investment costs for materials are lower than for PEMWE, because AEMWE uses non-noble metal catalysts and cheaper anion exchange membrane [129]. Moreover, AEM electrolysis is highly efficient, enabling operating with less corrosive electrolytes and minimizing salt loading. However, AEMWE currently faces two main challenges: fast degradation of the anion exchange membrane and system optimization [112]. In conclusion, low-temperature water electrolysis is the primary technology for producing green hydrogen, and developing electrocatalysts remains a critical factor in optimizing the water electrolysis process [113].

Table 5. Advantages and disadvantages of different low-temperature water electrolysis technologies [113, 130].

	AWE	PEMWE	AEMWE
Advantages	✓ Low capital costs due to the use of non-noble metals as electrocatalysts ✓ Long-term operational stability ✓ Large-scale (MW stacks) ✓ Mature technology	✓ Compact design ✓ Fast response and start-up ✓ Dynamic operation ✓ High purity of H_2 production ✓ High current density ✓ High efficiency	✓ Compact cell design ✓ High efficiency ✓ Low costs ✓ Non-noble metal catalysts ✓ Weak corrosive electrolyte ✓ High operating pressure
Disadvantages	× Crossover of gases × Low current densities × Low efficiency × Low operational pressure × Inferior production rate	× High costs of PEMs and noble metals as electrocatalysts × Strong acidic corrosion environment × Limited durability	× Limited stability × Under development × Membrane degradation

1.3.2. High-Temperature Water Electrolysis

High-temperature water electrolysis is based on the solid oxide water electrolysis (SOWE) technology, which is considered as a promising approach to high efficient hydrogen production [131]. Solid oxide is used as an electrolyte, similar to that in the solid oxide fuel cell technology [132]. SOWE generally operates at high temperatures (700 - 1000 °C) and pressures. During the process, water steam is consumed and generates hydrogen and oxygen [113, 132b]. As described in Figure 3, two water molecules receive four electrons at the cathode, forming two moles of hydrogen gas in the gas phase and releasing two moles of O^{2-} ions. The H_2 product can then be eliminated from the cathode surface while the remaining O^{2-} ions are transferred through the membrane to the anode chamber. At the anode, two moles of O^{2-} are discharged to produce one mol of oxygen gas (O_2).

A solid oxide water electrolysis cell includes three main components: two porous electrodes (anode and cathode) and a dense ceramic electrolyte capable of conducting oxide ions (*e.g.,* O^{2-}) [28]. The most commonly used electrolyte is Yttrium-stabilized zirconia (YSZ), which contains 8 mol% of Yttrium as dopant in a dense zirconium dioxide (ZrO_2) [133]. It functions as a dense ionic

conductor allowing O^{2-} to transport [132b]. The YSZ electrolyte exhibits long stability and excellent performance at higher temperatures (700–850 °C), as well as high ionic conductivity (10^{-2} - 10^{-1} S cm^{-1}) [133]. The most advanced cathode material currently is Ni–YSZ, a nickel-YSZ cermet that combines high ion conductivity with the advantages of a non-noble metal catalyst [28, 133]. The most widely used anode catalysts are perovskite materials, *e.g.*, LSCF ($La_{0.58}Sr_{0.4}Co_{0.2}Fe_{0.8O3-\delta}$) and LSM ($(La_{1-x}Sr_x)_{1-y}MnO_{3-\delta}$ [134]. SOWE technology is advantageous due to its high energy efficiency when operating at higher temperatures with non-noble metal electrocatalysts [113]. However, achieving long-term stability with this technique remains a significant challenge [113]. Presently studied approaches to achieving better stability comprise tuning of existing electrode materials or replacing them with new perovskite materials. Moreover, improved durability can be achieved by increasing the electrolyte conductivity and optimizing of chemical and mechanical stability.

1.4. Electrochemical Reduction of CO_2

In addition to advancing green hydrogen production technologies to support the net-zero carbon goal, methods are being developed to convert CO_2 into valuable industrial products, such as C_1 products (CH_4, CO, HCOOH, and CH_3OH), as well as C_{2+} products (C_2H_2, C_2H_4, and EtOH), is an increasingly important approach [135]. There are three major strategies to reduce CO_2 to other chemicals: thermochemical, photochemical, and electrochemical pathways (see Fig. 7). The selection of catalysts and process parameters significantly affect the effectiveness of CO_2 reduction [135].

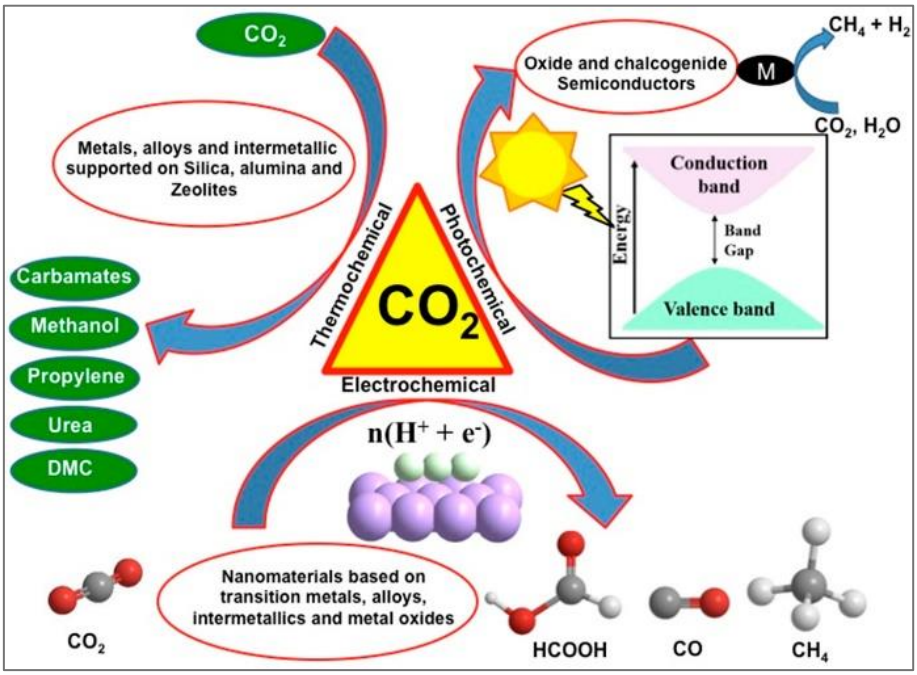

Figure 7. Different methods employed for the CO_2 reduction to various products (taken from ref. [135]).

Of the three methods mentioned above, electrochemical reduction of CO_2 (eCO_2RR) is the most promising due to its ability to operate at room temperature and pressure in an aqueous

electrolyte, its high product selectivity, its high operating flexibility, and its use of inexpensive energy input [136]. However, low CO_2 solubility, limited mass transfer, poor catalyst stability, and commercialization remain challenging issues that need improvement for this method [136d]. In a CO_2 cell, CO_2 is typically reduced to various products at the cathode *via* CO_2 electrochemical reduction (eCO_2RR), while H_2O is oxidized at the anode *via* the oxygen evolution reaction (OER), as shown in the following reaction equations [136c]:

Cathode: $$xCO_2 + nH^+ + ne^- \rightleftharpoons products + yH_2O \quad (13)$$

$$2H^+ + 2e^- \rightleftharpoons H_2 \quad (14)$$

Anode: $$2H_2O \rightleftharpoons O_2 + 4H^+ + 4e^- \ (E^{eq} = 1.23\ V\ vs.RHE) \quad (15)$$

The OER principally involves multiple reaction steps, as discussed previously in the water electrolysis section. In the case of eCO_2RR at the cathode, more than ten possible reaction steps can occur, depending on factors such as the catalysts used, the applied potential, and the products formed as reported in the literature [137]. Additionally, the hydrogen evolution reaction (HER) generates H_2, which is a concurrent side reaction. This section provides an overview of the principle of the electrochemical CO_2 reduction reaction and of electrocatalysts for converting CO_2 to C_{2+} products.

1.4.1. Comparison between Homogeneous and Heterogeneous Catalysis

Th eCO_2RR process has been developed in parallel in the fields of homogeneous and heterogeneous electrocatalysis. In the homogeneous case, the catalyst acts as a redox shuttle between the electrode and CO_2, replacing direct electron transfer with homogeneous electron transfer in solution - a process commonly referred to as indirect electrolysis (see Fig. 8 left) [138]. Homogeneous catalysts are typically well-defined structures comprising a metal center and organic ligands [139]. According to the literature, noble metals such as Ru, Ir, Rh, and Os demonstrate outstanding catalytic performance [140]. However, complexes of transition metals (Co, Ni, Fe, Cu, and Mn) have emerged as a promising alternative to noble metals for the homogeneous electrochemical CO_2 reduction [141].

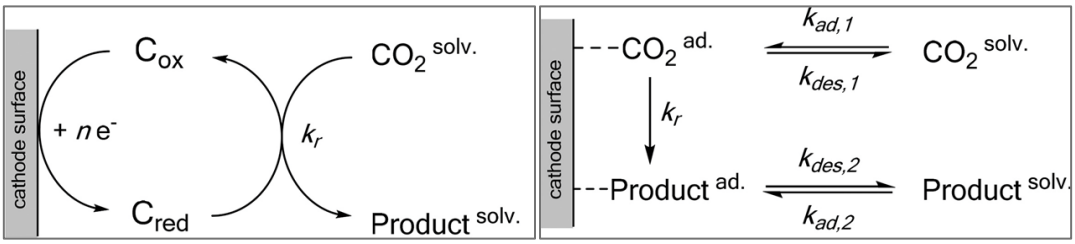

Figure 8. Electrochemical CO_2 reduction *via* homogeneous (left) and heterogeneous (right) catalysis (taken from ref. [138]).

In heterogeneous eCO_2RR catalysis (see Fig. 8 right), the reaction can be summarized in three steps: (1) CO_2 from the electrolyte chemisorbs onto the active surface of the electrocatalyst, (2)

electrons transfer to break C-O bonds or form C-H bonds, and (3) the products desorb from the cathodic surface [139]. With a suitable catalyst, CO_2RR can begin at a low overpotential. On the electrode surface, CO_{2ad} reacts to form products through different pathways, depending on the number of electron transfers [142]. The intermediates formed in these steps include *COOH, *OCOH, *CO, and *COH [142]. Understanding the formation of these intermediates is key to the rational designing and tuning of active sites for the development of electrocatalysts for eCO_2RR. Recently, eCO_2RR has been found to be sufficiently effective selective for preparing value-added multi-carbon products, such as ethylene (C_2H_4), ethanol (C_2H_5OH), and *n*-propanol (*n*-C_3H_7OH), which are of particular interest to the chemical industry [143]. Among the various types of materials, copper-based catalysts demonstrate great potential for converting CO_2 to C_{2+} products [144]. However, Cu-based catalysts still suffer from many drawbacks, including high overpotential, poor selectivity, and poor stability, which limits their practical application [145]. Therefore, the development of advanced Cu-based catalysts with superior CO_2RR performance for C_{2+} products is of pivotal importance (*vide infra*) [146].

1.4.2. Copper-Based Electrocatalysts for CO_2RR

Metallic copper catalysts face challenges including low selectivity due to various active sites, as well as poor stability due to surface restructuring under catalytic condition [147]. A particular challenge is the HER as a process that competes with eCO_2RR. It has been reported that the selectivity toward desired products can be improved by incorporating a second metal [148]. The class of single-atom catalysts (SACs) is another heterogeneous system which offer advantages like outstanding performance with high efficiency and selectivity [149]. However, the limited number of active sites can be a major problem for reactions requiring high catalytic site density [150]. Moreover, SACs also face stability issues, thus single atoms usually tend to migrate on the surface to form aggregates, leading to cluster or nanoparticle formation [150-151].

Molecular catalysts with well-defined active sites offer a promising opportunity for electrocatalytic applications for eCO_2RR [152]. First, the enable a precise structural tuning through the choice of appropriate ligands. Second, with stable and well-defined active sites, mechanistic studies and established structure-activity relationships are facilitated [138, 152]. Consequently, well-defined molecular Cu catalysts are promising electrocatalysts for both homogeneous and heterogeneous eCO_2RR approaches, the latter requiring heterogenization (attachment to the electrode surface) [153]. The C-C coupling step has been identified as crucial for generating C_{2+} products, which often depends on the proximity of Cu sites [154]. Interestingly, it has been demonstrated that establishing the correct Cu···Cu distance is essential for C-C coupling generation [153b, 155]. Nevertheless, the electronic conductivity, (reduced) surface Cu density, mass transfer between molecular units, and structural stability of molecular Cu electrocatalysts still require improvement [147, 155].

Cu-based metal-organic frameworks (MOFs), which show various advantages such as well-defined active centers, high active surface areas, and high intensity of active sites with uniform Cu···Cu distance, have been explored as high-potential catalysts for converting CO_2 to C_{2+} products [156]. However, similar to molecular catalysts, many MOF materials show poor

conductivity, which limits their ability to facilitate electron transfer during the electrochemical CO_2 reduction reaction [157].

In conclusion, both molecular catalysts and MOF-derived catalysts exhibit well-defined active sites and a C-C coupling process at the atomic level. However, major challenges related to stability need to be addressed. Consequently, this work focusses on developing molecular Cu catalysts that are capable of efficient C-C coupling between adsorbed CO_2 reduction intermediates and on improving the catalyst stability for practical applications.

1.5. Electroanalytical Methods and Test Cells Applied to Study OER and eCO₂RR Processes

1.5.1. Electroanalytical Methods

As shown in Figure 9, a variety of electroanalytical methods is available to study electrochemical phenomena under different conditions. Electrochemical methods are also powerful tools for studying the activity and durability of catalysts in specific reactions, such as HER, ORR, HOR, OER, and eCO_2RR [158].

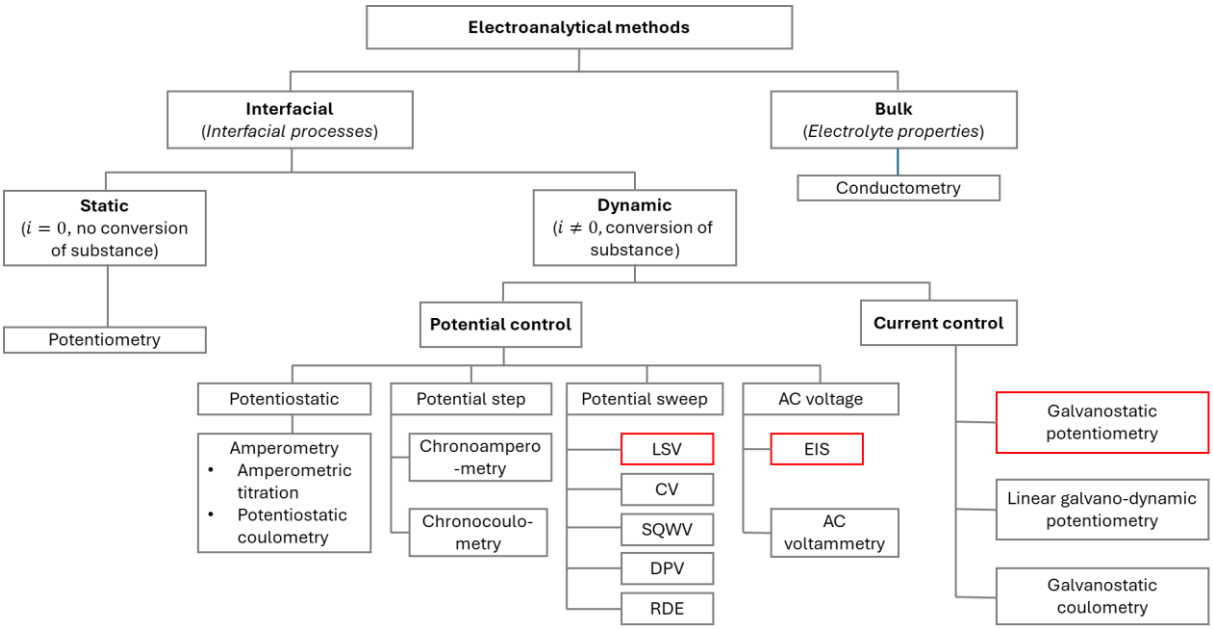

Figure 9. Overview of relevant electroanalytical methods [158].

Electroanalytical methods can be categorized into two main groups depending on whether the focus is on the interfacial processes or the electrolyte properties (see Fig. 9). Interfacial electrochemical methods analyze phenomena occurring at the interface between an electrode and an electrolyte. This is important for studying the electrochemical processes such as electron transfer, adsorption, and chemical steps on or close to the electrode surface [159]. The interfacial methods can be further classified as static or dynamic, depending on whether a current is passed through the electrochemical cell. Static methods include potentiometry, which measures potential without current flow and maintains a stable interface [160]. In contrast, dynamic methods enable the study of the electrode-electrolyte interface during the conversion of substances by

passing a current [160-161]. Dynamic methods are crucial for understanding and characterizing various electrochemical processes, such as energy storage, corrosion, and catalysis [161]. This section will discuss selected methods that were used to study the heterogeneous OER and eCO_2RR processes (chapter 3), namely linear sweep voltammetry (LSV), electrochemical impedance spectroscopy (EIS), and galvanostatic potentiometry.

1.5.1.1. Linear-Sweep Voltammetry

A standard electrode reaction consists of three typical steps: (1) mass transport of reactants to the electrode surface, (2) a redox reaction at the electrode surface, and (3) the mass transport of products away from the electrode surface. Voltammetry is a microanalysis technique, so only a negligible part of the analyte species in the solution is modified by the process occurring at the electrode. Voltammetry can be categorized into two broad classifications: stationary electrode voltammetry and forced convection voltammetry. Stationary electrode voltammetry is a technique which is carried out in a resting solution and in which the working electrode (WE) is not exposed to any forced convection. This approach stands in contrast to forced convection voltammetry, wherein the electrode or solution is instationary (*e.g.,* rotated electrodes or stirred solutions) to enhance mass transport. The discussion will encompass both techniques.

Firstly, in stationary electrode voltammetry, it is assumed that the transfer of the analyte species proceeds only *via* diffusion, since the analyte solution is quite (unstirred) and the supporting electrolyte concentration is high compared to the analyte concentration. The latter ensures that ion migration contributes only in a negligible way to transport of charged analytes/intermediates [162]. Linear sweep voltammetry (LSV) is a common voltammetry technique used to study the dynamic behavior and kinetics of electrochemical systems [162]. In LSV, the potential of the working electrode is ramped from an initial potential to a final potential at a sweep rate, resulting in current responses. That allows to study the redox potential, diffusion of the analyte, as well as coupled chemical steps [162]. Under certain preconditions, quantitative information on kinetics and thermodynamics of electrochemical processes can then be obtained. If the potential changes linearly in only one direction (anodic – to higher potentials; cathodic – to lower potentials), the resulting *i(E)* profiles represent a linear sweep voltammogram (LSV) [163]. This result can be used to characterize the performance of electrocatalysts and the rate of the reaction. Such performance criteria include the overpotential at a given current density, the Tafel slope, as well as the mass activity or the current density at a specific potential. The LSV current is mainly governed by the Butler-Volmer Equation (Eq. 16, kinetic control) [164] and the Cottrell Equation (Eq. 17, diffusion control) [165]:

$$j(E) = j_0 \cdot \left[e^{\frac{\alpha n F}{RT}(E - E^{eq})} - e^{-\frac{(1-\alpha) n F}{RT}(E - E^{eq})} \right] \qquad (16)$$

Where:

$j(E)$ is the total current density	E^{eq} is the equilibrium potential
j_0 is the exchange current density	$E\text{-}E^{eq}$ is the overpotential
α is the transfer coefficient ($0 < \alpha < 1$)	R is the gas constant
F is the Faraday constant	T is the absolute temperature

$$j(t) = \frac{nF\sqrt{D_s}}{\sqrt{\pi}} c_s^* \frac{A}{\sqrt{t}} \quad (17)$$

Where:

j(t) is the total current density

n is the number of electrons (to reduce/oxidize one molecule of analyte *s*)

F is the Faraday constant

D_s is the diffusion coefficient for analyte *s*

c_s^* is initial concentration of the reducible analyte *s*

A is the area of the (planar) electrode

t is the time

On the other hand, the use of LSV can be considered for forced convection voltammetry, in which convection is the principal mode of mass transport to control the diffusion layer thickness near the electrode and the fast achievement of a steady state at the electrode. This way the depletion of the analyte concentration at the electrode changes with current flow is controlled [166]. Compared to migration or diffusion, convection is the most efficient form of mass transport, dominating in forced-convection voltammetry [166]. Convection is defined as the movement of a solution relative to an electrode, which results in efficient mass transport. In this context, there are two extremes that rely on convection: (1) an electrode moving through an otherwise still solution and (2) a solution moving past a stationary electrode [166]. These two scenarios are also referred to as hydrodynamic electrodes. It should be noted that despite strong convection, mass transfer through the boundary layer is still limited by diffusion.

One of the most commonly employed hydrodynamic electrodes is the rotating disc electrode (RDE) [167]. The basis of any RDE analysis is the three-electrode voltammetry cell, which consists of an RDE as the working electrode (WE), a counter electrode (CE), and a reference electrode (RE). During measurement, the RDE is immersed in the analyte solution, which moves radially over the disc's surface as it rotates [166-167]. Rotating the electrode at a controlled speed during the reaction ensures well-defined diffusion and convection profiles. The RDE voltammetry current consists of kinetic contribution (i_k) and a diffusion-controlled current (i_{lim}), follows the Koutecký-Levich equation (Eq. 18):

$$\frac{1}{i} = \frac{1}{i_k} + \frac{1}{i_{lim}} = \frac{1}{i_k} + \frac{1}{0.62nFA \cdot D_s^{3/2} \cdot \omega^{1/2} \cdot \nu^{-1/6} \cdot c_s^*} \quad (18)$$

Where:

i is the total current

i_k is the kinetic current

i_{lim} is the limiting current

n is the number of electrons (to reduce/oxidize one molecule of analyte *s*)

F is the Faraday constant

D_s is the diffusion coefficient for analyte *s*

c_s^* is initial concentration of the reducible analyte *s*

A is the area of the (planar) electrode

ω is the rotation frequency of the electrode

v is the solution viscosity

According to the Koutecký-Levich equation (Eq. 18), the limiting current at an RDE is directly proportional to the analyte concentration and square root of the rotation frequency (*ω*) [168]. Additionally, the LSV measurements using an RDE enable the accurate estimation of kinetic currents, which allows to estimate the Tafel slope and the exchange current density (given by the Butler-Volmer equation (Eq.16)). Furthermore, the RDE is useful for analyzing reactions involving strong gas evolution (*e.g.*, OER or HER), as the rotation facilitates removal of gas bubbles from the working electrode surface [169]. On the other hand, the group of convection-based systems also comprises fixed electrodes with a moving solution (*e.g.* flow cells and channel electrodes) [166].

1.5.1.2. Electrochemical Impedance Spectroscopy

Electrochemical impedance spectroscopy (EIS) is another important method for studying electrocatalysts, wherein the response of an electrochemical system to a small-amplitude sinusoidal perturbation of the working electrode potential is measured. Since the individual processes such as charging of the electrochemical double layer, (pore) diffusion, electron transfer, and chemical steps occur on different timescales, the contributions to the overall cell resistance can be resolved and quantified by systematical variation of the alternating voltage frequency. EIS can therefore provide insights both into interfacial and bulk properties, as well as reaction mechanisms [170].

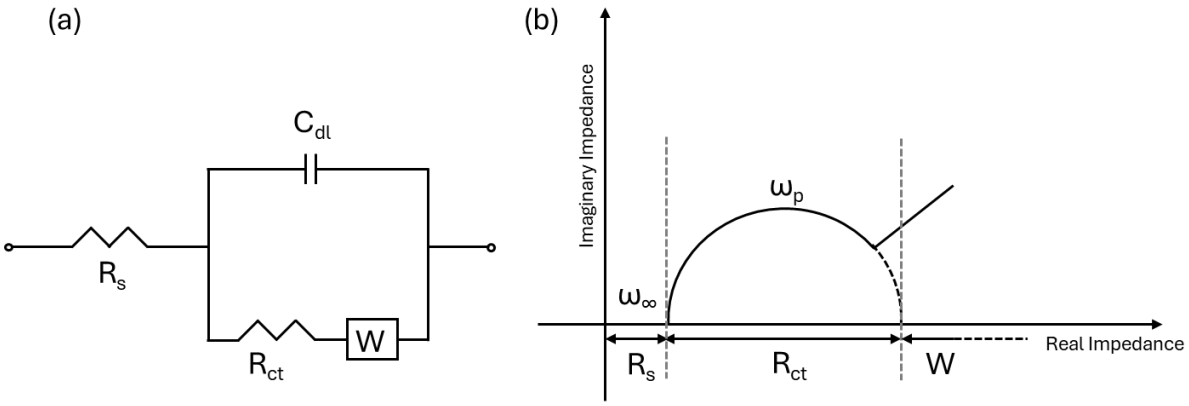

Figure 10. (a) A simplified equivalent electrical circuit of a half-cell. (b) Impedance Nyquist plot corresponds to the circuit (a).

Figure 10a describes a simplified equivalent electrical circuit of an electrolytic half-cell which consists of an electrolyte resistance between RE and WE (R_s) in series with parallel combination of the double-layer capacitance (C_{dl}) and an impedance of a Faradaic reaction (*incl.* a charge transfer resistance (R_{ct}) in series with a diffusion impedance (W, Warburg impedance)) [171]. In most practical cases, the transfer functions obtained in EIS measurements do not strictly follow the

expected theoretical patterns but rather show definite distortions. Therefore, a constant phase element (CPE) is often used to replace C_{dl} [172]. In circumstances where charge transfer is challenging (low overpotential), R_{ct} exerts a regulatory influence over the impedance of the Faradaic reaction. Conversely, W controls the Faradaic reaction when charge transfer is facile (high overpotential). EIS measurements produce so-called Nyquist (see in Fig. 10b) or Bode plots, which are used to obtain information about resistance and capacitance (fundamental electrical properties), as well as reaction rates, diffusion, and charge transfer processes [173]. This measurement is usually performed at open-circuit potential (OCP) to obtain preliminary information about the properties of the electrocatalyst.

Charge transfer resistance (R_{ct}), often referred to as polarization resistance (R_p) in the literature, is a pivotal parameter in electrochemical systems, denoting the resistance to the transfer of charge across the interface between an electrode and an electrolyte. This phenomenon reflects the kinetics of electron transfer reactions and plays a significant role in determining the overall efficiency of electrochemical processes. In the context of electrocatalysis, it directly impacts the rate that chemical reactions occur on the electrode surface. Lower R_{ct} values are generally indicative of faster electron transfer rates, which can enhance the performance of a catalytic system. This is particularly critical in studies of electrocatalytic OER and eCO_2RR processes. In this work, EIS measurements were carried out at different potentials, *i.e.*, at OCP, at the current onset and during OER or eCO_2RR [174]. A detailed discussion of this relatively complex method is beyond the scope of this thesis and can be found elsewhere [171, 175].

1.5.1.3. Galvanostatic Potentiometry

Galvanostatic potentiometry is an electrochemical technique in which a constant current (galvanostatic) is applied to an electrochemical cell and the resulting potential (potentiometry) is measured over time. It is sometimes also referred to as chronopotentiometry, in which it is essentially measured how the potential changes when a fixed current is applied. This method is used to study electrode processes, reaction mechanisms, and the kinetics of electrochemical reactions. In this study, this method is used to evaluate the stability of electrocatalysts for OER and eCO_2RR processes. Increases in the potential can indicate degradation, other instability issues with the material or system being tested, as well as bubble accumulation on the surface [176]. The applied current density is a critical parameter, since it influences the rate of electrochemical reactions and potential changes.

In conclusion, applying electrochemical methods to study the properties of reactions and electrode materials is essential to electrochemical research and electrocatalyst development. In addition to selecting the appropriate electrochemical analysis methods, the analysis of the electrocatalyst performance on the device level has also a great significance and is usually achieved under practically relevant conditions, *i.e.*, continuous operation in a flow cell with two-electrode configuration under galvanostatic control.

1.5.2. Electrochemical Test Cells from Laboratory to Industrial Application

In general, a standard electrochemical cell encompasses electrodes (cathode, anode), and an electrolyte. Depending on the research goal, a reference electrode and a porous membrane may need to be introduced, and the electrochemical cell may need to be modified to adapt the reaction conditions. In order to apply potentials or currents to the system, a potentiostat is required. This section discusses the advantages and disadvantages of the electrochemical cells commonly used to study OER and eCO_2RR processes.

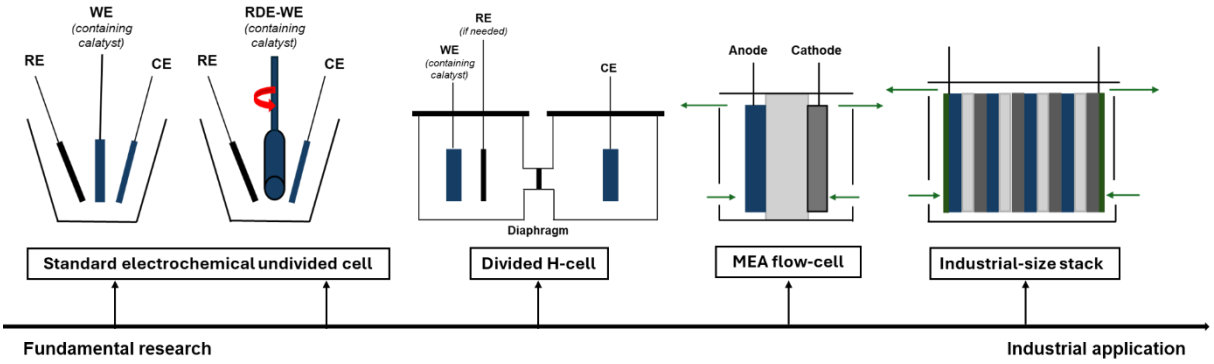

Figure 11. Schematic illustration of different types of test cells for studying OER and eCO_2RR processes.

Figure 11 illustrates typical electrochemical cells used in the OER and eCO_2RR processes from the laboratory to industrial scales. The first standard electrochemical undivided cell for fundamental research is a simple cell comprising a working electrode (WE, which typically contains the catalyst being studied), a counter electrode (CE), and a reference electrode (RE). The RE enables precise control and measurement of the WE's potential, which is crucial for many electrochemical techniques. Moreover, the three-electrode configuration is commonly used in fundamental studies of electrochemical processes and in screening electrode materials [177]. However, the RE must have stable and reliable voltage, and be non-polarizable, particularly during long-term studies [178].

An undivided cell with a rotating disc electrode (RDE) is considered superior to the WE in the first cell for strong gas evolution reactions (*e.g.,* HER, OER) since rotation at a controlled speed during the reaction ensures well-defined diffusion and convection profiles, enabling accurate kinetic currents and estimation of the exchange current densities (j_0) [179]. Furthermore, reproducible measurements can be obtained when the RDE setup conditions are well controlled, which is effective for studying electrocatalyst activity [180]. However, the small electrode surface area of an RDE may not be suitable for long-term experiments especially when quantification of product is desired, since only small conversions can be achieved. Furthermore, the gaseous products may form bubbles that adhere to the surface, blocking the material's pores and obscuring the actual activity of the catalyst [176].

When carrying out experiments with significant conversion of reactant ("bulk electrolysis"), undivided cells face the challenge that products from one electrode can react with reactants or products of the other as well as at the other electrode, which can potentially interfere with the

desired reaction [181]. The divided cell design separates the working electrode (WE) and the counter electrode (CE) into two chambers, which are divided by a separator such as a porous membrane or a diaphragm [182]. The reference electrode can be installed in the same chamber as the working electrode. While this design facilitates the identification and quantification of reaction products, supporting electrolyte ions pass through the separator, potentially along with reactants/products, leading to cross-contamination [182]. The H-type cell is the most common type of divided cell used for laboratory-scale HER/OER testing and eCO_2RR studies [183]. However, the main drawback of the H-type batch cell is that reactant concentrations decrease over time (instationary operation).

A membrane electrode assembly (MEA) flow electrochemical cell is a device in which the electrodes are separated by a membrane and the reactants flow continuously through this cell. MEA designs, particularly those with zero-gap configurations, can achieve high current densities and improve overall performance [184]. By eliminating the need for a bulk electrolyte between the electrodes, MEA's designs can minimize Ohmic losses. The flow field design of a MEA cell allows for the efficient delivery of reactants and the removal of products, thereby optimizing reaction conditions. Implementing a new catalyst into a MEA flow cell is an important step toward industrialization.

An industrial-size stack is a modular unit consisting of multiple individual MEAs connected in series with respect to the electric current and in parallel with respect to the electrolyte flow, to achieve higher efficiency, particularly for green hydrogen production [185] and CO_2 reduction [186]. However, high efficiency, long stability, high scalability, and cost-effectiveness remain major challenges for industrial applications [187]. To achieve these goals, it is necessary to focus on developing highly active, robust, and cost-effective electrocatalysts as well as other cell components.

2. Objectives of PhD Work

The development of highly active, stable, and affordable electrocatalysts is one of the key factors in improving the efficiency of small molecule conversion processes. This thesis focuses specifically on the water oxidation reaction and the CO_2 reduction reaction, with the three major objectives discussed in the following.

1. Producing green hydrogen through water electrolysis using electricity generated from renewable sources is a promising step toward achieving future net-zero carbon goals. Although hydrogen is the product of interest, the OER is the bottleneck of water splitting process. Hence, developing highly active and stable OER electrocatalysts is one of the keys to further improve the overall efficiency of water electrolysis. Rather than using noble metals such as Ir, and Ru as electrocatalysts for OER in PEMWE, earth-abundant alternatives such as Co, Ni, Fe, and Mn can be used as anodic electrocatalysts in AWE. Mixed oxides of Co, Ni, and Fe have emerged as promising candidates for OER have been studied over the past decade. Thermal treatment is a crucial step in synthesizing metal oxide catalysts and significantly influences their structure, composition, and catalytic activity. Controlling the atmosphere during treatment, allows the presence of defects, such as oxygen vacancies, to be easily tailored, thereby enhancing further catalytic activity. Based on the state of the art briefly outlined here and discussed in detail in section 1, three specific objectives can be derived for studies on $CoNiFeO_x$-based OER electrocatalysts:
    i. Investigating the molar ratio of Co : Ni : Fe to optimize a well-balanced ratio in $CoNiFeO_x$
    ii. Studying the impact of the thermal treatment conditions on the intrinsic properties affecting the OER by:
        - Using electroanalytical methods (*e.g.,* LSV, EIS, chronopotentiometry, CV) under RDE conditions
        - Analyzing the structural properties of catalysts by XRD, XPS, XAS, SEM, EDX, STEM, EELS, and BET of material before and after electrolysis
    iii. Evaluating activity and stability of catalysts under MEA conditions to facilitate the practical applications

2. Although CoNiFe oxides are significantly cheaper than the noble metals used in PEMWE, the limited availability of Co and the exceptionally poor environmental impact of Co and Ni mining remain challenges to scale up AEM water electrolysis capacities. Consequently, reducing the metal content while minimizing performance loss is a worthy goal for further improving the $CoNiFeO_x$ system. A further major objective is therefore to explore the use of Vulcan XC-72R carbon black (VC) as additive, which offers various advantages (*e.g.,* excellent conductivity, high purity and porosity, and low cost) and may serve to "dilute" $CoNiFeO_x$ while maintaining its catalytic performance. In this context, it is also necessary to investigate how the carbon's hydrophobic properties can be influenced and how the carbon additive should be added to the trimetallic oxide catalyst. The first issue can be approached by applying an oxidative pretreatment of VC. To address the second issue, carbon can be introduced during the sol-gel step and the ink formulation step, respectively. To determine the effects on

performance and stability, electrochemical studies under RDE tests and studies in an AEM electrolyzer are to be analyzed, and the structural properties are examined as outlined above.

3. In addition to developing OER catalysts for the alkaline medium, attention must be paid to the cathodic half-cell with electrochemical reduction reactions, such as the hydrogen evolution reaction (HER), and the CO_2 reduction reaction (eCO_2RR). Another focus will therefore be an investigation into some aspects of Cu-catalyzed eCO_2RR, since eCO_2RR has gained attention as a potential strategy for closing the carbon cycle, addressing the energy crisis, and producing valuable fuels and chemicals. Molecular Cu catalysts with well-defined active sites have emerged as promising candidates for converting CO_2 to C_{2+} products. Alongside the development of highly active materials, it is crucial to gain a better understanding the effect of the local reaction environment, such as the liquid-electrode interface. To support this purpose, this work is to use EIS technique to gain insight into the mechanism of a specific eCO_2RR process with special focus on the role of the supporting electrolyte cation.

3. Results and Discussion

3.1. Oxygen-Deficient Annealing Boosts Performance of CoNiFe Oxide Electrocatalyst in Oxygen Evolution Reaction

The Co, Ni, and Fe metallic oxides were synthesized *via* a simple sol-gel method followed by a thermal treatment step. First, an investigation of different stoichiometric molar ratios of Co : Ni : Fe was carried out to obtain optimal catalysts. As mentioned in the introduction, effective electrocatalysts for OER require low overpotential, high mass activity and current density, a small Tafel-slope, a low polarization resistance, a high electrochemically active surface area (ECSA), excellent stability, good conductivity, low cost, and environmental friendliness [188]. In this work, the electrocatalytic performance of the materials toward OER was studied using linear sweep voltammetry (LSV) with a catalyst-coated glassy carbon RDE in a 1 M KOH electrolyte. Additionally, short-term stability tests were performed in galvanostatic mode at a current density of 10 mA cm^{-2} (geometrical surface area) for 15 minutes to observe the degradation of the materials. Other electrochemical parameters, such as polarization resistance (R_p) and ECSA were also studied using EIS and CV, respectively.

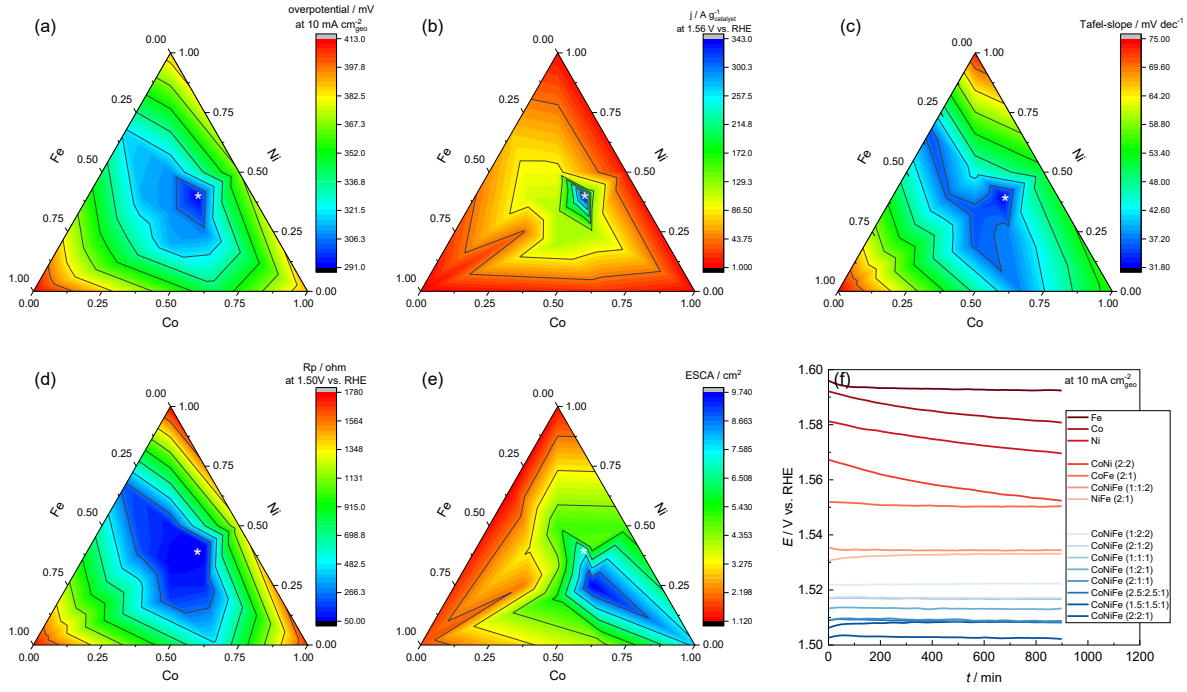

Figure 12. Summary of the electrochemical results for different molar ratios of CoNiFe catalysts. (a) Overpotential at 10 mA cm^{-2} (geometrical electrode surface area). (b) Mass activity calculated from the current density at 1.56 V vs. RHE and the catalyst loading on the electrode surface (~ 0.25 mg cm^{-2}). (c) Tafel slopes. (d) Polarization resistance (R_p) at 1.50 V vs. RHE. (e) ECSA, estimated from C_{dl} *via* CV measurements in the non-Faradaic potential region. (f) Short-term stability tests performed for 900 s at 10 mA cm^{-2}.

The dark blue region in Fig. 12 (a-e) represents high OER activity with a small overpotential at 10 mA cm^{-2}_{geo} (Fig. 12a), a high current density or specific mass activity at 1.56 V vs. RHE (Fig. 12b), a small Tafel slope (Fig. 12c), a small charge transfer resistance (Fig. 11d), and a large ECSA (Fig. 12e). Specifically, the monometallic oxides of Co, Ni, and Fe exhibit significantly poorer

performance and stability at 10 mA cm^{-2}_{geo}. In contrast, bimetallic oxides of CoNi, CoFe, and NiFe demonstrate significant improvement in OER performance, with the overpotential reduced by approximately 70 mV when Ni or Co is combined with Fe, as demonstrated in recent publications [81]. In comparison, nearly all trimetallic oxide samples indicate a better performance region in the triangle plots, as well as excellent stability. A well-balanced molar ratio of Co : Ni : Fe influences the catalytic performance of OER under alkaline conditions. In particular, samples with a high Fe concentration exhibit poorer OER activity than those with a higher Co and Ni content.

Of the various samples, CoNiFe with a molar ratio of 2:2:1 (noted as * in Fig. 12) was identified as the optimal catalyst in this study, demonstrating the smallest overpotential at 10 mA cm^{-2}_{geo} (η_{10} = 291 mV), and the highest mass activity at 1.56 V vs. RHE (~ 343 A $g^{-1}_{catalyst}$) which is over five times higher than the NiFe sample. Additionally, CoNiFe (2:2:1) also exhibits the lowest Tafel slope of 32 mV dec^{-1} within the CoNiFe series, though the difference with other representatives is only a few mV dec^{-1}. Interestingly, all the trimetallic oxide samples show similar Tafel slopes between 30 and 40 mV dec^{-1}, demonstrating the high value of trimetallic mixed oxides. Moreover, CoNiFe (2:2:1) exhibits the smallest polarization resistance (R_p) obtained at the initial OER stage of 1.50 V vs. RHE, reflecting rapid OER kinetics. Regarding the ECSA results in Fig. 12e, however, CoNiFe (2:2:1) is not the material with the highest value. Samples with a high Co concentration tend to exhibit a higher ECSA, indicating that performance optimization is not directly linked to enhance surface area.

In addition to the metal ratio, oxide vacancies or defects may also contribute to the catalytic activity [189]. The second study was focused on the influence of oxygen defects, which can be controlled *via* the gas phase during thermal treatment (see Fig. 13). CoNiFe (2:2:1) was pyrolyzed at 300 °C under three different annealing atmospheres: oxygen-rich (A; air), oxygen-deficient (M; 1 vol% air in argon), and reducing (H; 5 vol% H_2 in argon). The letters A, M, or H are used to denote the conditions of the thermal treatment (*e.g.*, CoNiFe (2:2:1)/M).

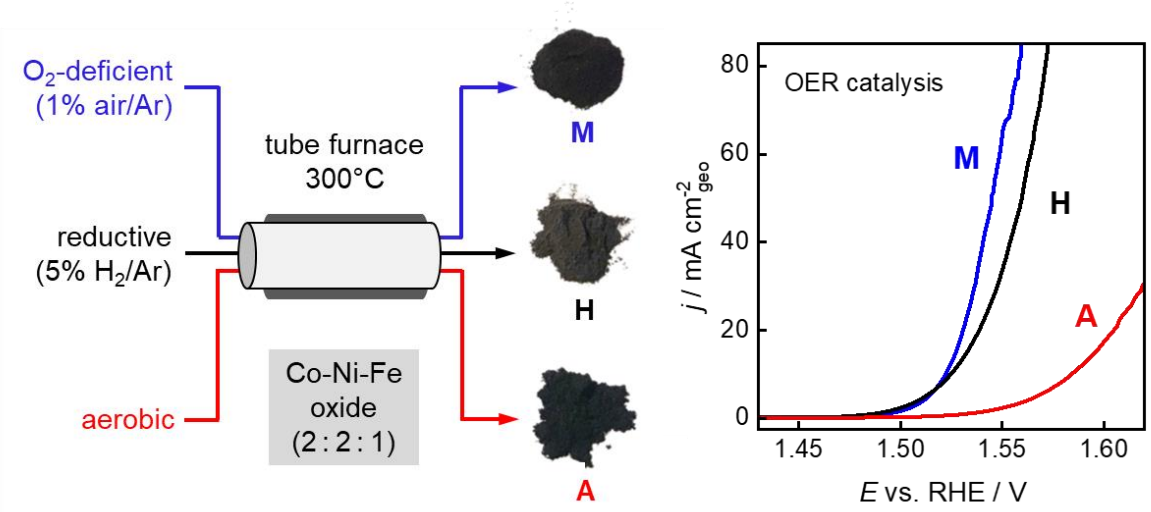

Figure 13. Summary of study on the influence of thermal treatment and metal ratio on the performance of $CoNiFeO_x$-based OER electrocatalysts [95].

This investigation has been discussed in detail in our publication [95]. This section will provide a brief overview of the study. Regarding the polarization curves of samples M, H, and A (see Fig. 13),

oxygen-deficient conditions (M; 1 vol% air in argon) lead to the best results in terms of activity. In contrast, reducing conditions (H; 5 vol% H_2 in argon) produce significantly poorer results. The lowest activity is observed for materials whose thermal treatment was carried out under aerobic conditions (A; air). In addition, CoNiFe (2:2:1)/M indicates excellent long-term stability at 100 mA cm^{-2} for 50 hours in RDE studies (see Fig. 14a) and under on-off conditions at 400 mA cm^{-2} for over 75 hours in electrolyzer studies (see Fig. 14b).

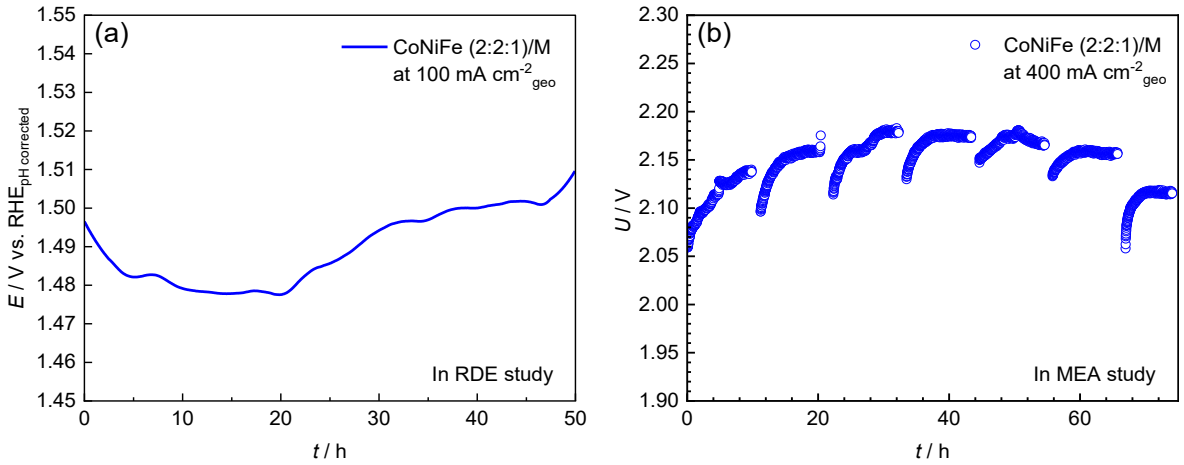

Figure 14. Durability tests for CoNiFe (2:2:1)/M. (a) On a GC RDE (1M KOH, ω = 1800 rpm) at a current density of 100 mA cm^{-2} for 50 hours. (b) In an electrolyzer (Ni foam substrate, 1 M KOH, 50 °C) at an on-off current density of 400 mA cm^{-2}.

Besides electrochemical analysis, structure characterization techniques such as SEM, TEM, XRD, and XPS were applied to characterize CoNiFe (2:2:1)/M,H,A before and after electrolysis at 10 mA cm^{-2} for one hour. The three as-prepared catalysts showed completely different structural properties due to the different oxygen content in the gas phase during the thermal treatment. As shown in Fig. 14a, the XRD results indicate that the sample A exhibits a highly crystalline character with relatively sharp reflection peaks that align well with the planes of Fe_3O_4 (magnetite) and Co_3O_4. In contrast, the PXRD pattern of CoNiFe (2:2:1)/H does not show any reflection peaks, indicating an amorphous structure. CoNiFe (2:2:1)/M exhibites both amorphous and crystalline structural components, with reflection peaks corresponding to the planes of CoO, NiO, and FeO. After electrolysis, all three samples became almost completely amorphous (see Fig. 15b).

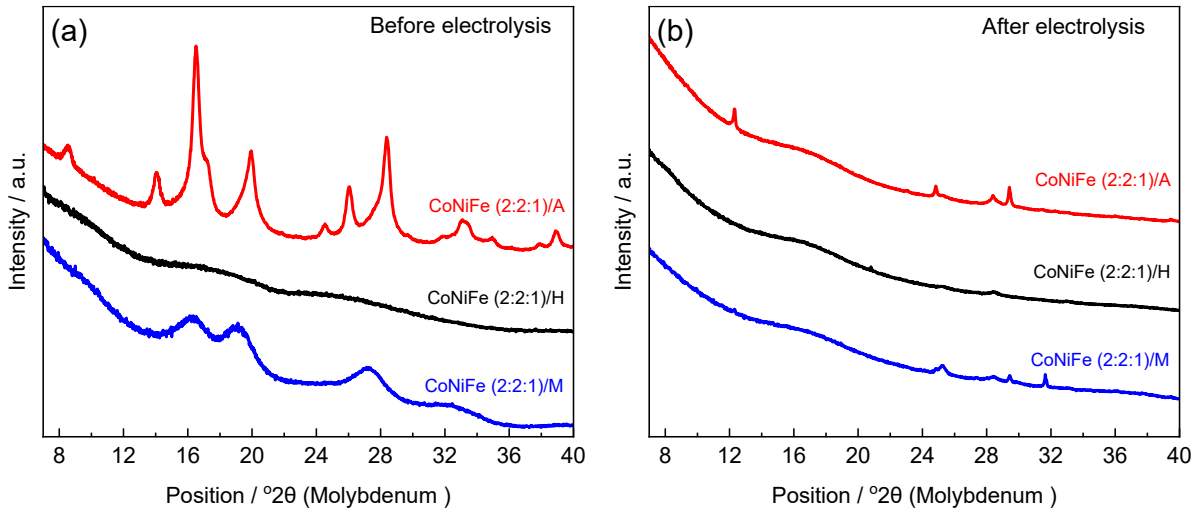

Figure 15. Powder X-ray diffraction patterns of CoNiFe (2:2:1)/M, CoNiFe (2:2:1)/H, and CoNiFe (2:2:1)/A. (a) Fresh catalysts (powder) before electrolysis. (b) Used catalysts after one hour stability tests at 10 mA cm^{-2}_{geo}.

According to XPS analysis, the metals on the surface are in different oxidation states. Surface-bound oxygen predominantly exists as hydroxide and, to a lesser extent, as lattice oxygen. Figure 16a shows that the samples M and H have the lowest oxidation state of Co (as well as Ni and Fe), while the aerobic sample (A) shows the formation of a higher oxidation state (*e.g.,* Co_3O_4) [95]. However, post-electrolysis XPS characterization reveals that all metals exist in their most highly oxidized form (see Fig. 16b). Interestingly, oxygen defects were successfully formed by a thermal treatment step, as observed in the XPS data in the O 1s region (see Fig. 16c). Sample H predominantly exhibits high intensity of defective oxide, while sample M shows the presence of both defective and lattice oxides (the intensity of the metal hydroxides/defective oxides peak is higher). On the other hand, the XP spectra (O 1s) for sample A likely exhibits lattice oxygen. After electrolysis, the high-resolution XP spectra for O 1s region of the three as-prepared materials tend to resemble the shape of sample CoNiFe (2:2:1)/M (see Fig. 16d), indicating a high concentration of surface oxygen vacancies in all three samples. Consequently, the mixed metal oxide electrocatalysts ($CoNiFeO_x$) tend to oxidize to a higher oxidation state of Co, Ni, and Fe under strong OER conditions in an alkaline environment, with their structural converting into that of the sample M.

To further explore the metal states, *in situ* XAS was performed on the CoNiFe (2:2:1)/M sample in a flow cell using a 0.1 M KOH electrolyte at various applied potentials (see Fig. 17). First, the analysis shows that **Co** is more readily oxidized to high valence state (shifts to higher photon energies) than Fe and Ni. The presence of Co^{3+}/Co^{4+} indicates an average oxidation state of 3.02 in the OER region (at 1.614 V vs. RHE), which is may be assigned to Co_3O_4 or β-CoOOH phases [79]. In contrast, the **Ni** state appears stable at potential steps. During the OER process, Ni mostly indicates the coexistence of Ni^{2+} and Ni^{3+}, which could be related to the formation of α-$Ni(OH)_2$ (at OCP) and the main active phase for OER in alkaline conditions, β-NiOOH (in the OER region) [80a, 80b]. The oxidation state of **Fe** is almost always +III [80c]. Further *in situ* spectroscopic techniques are required for a deeper study of the mechanistic aspects of the $CoNiFeO_x$ electrocatalyst.

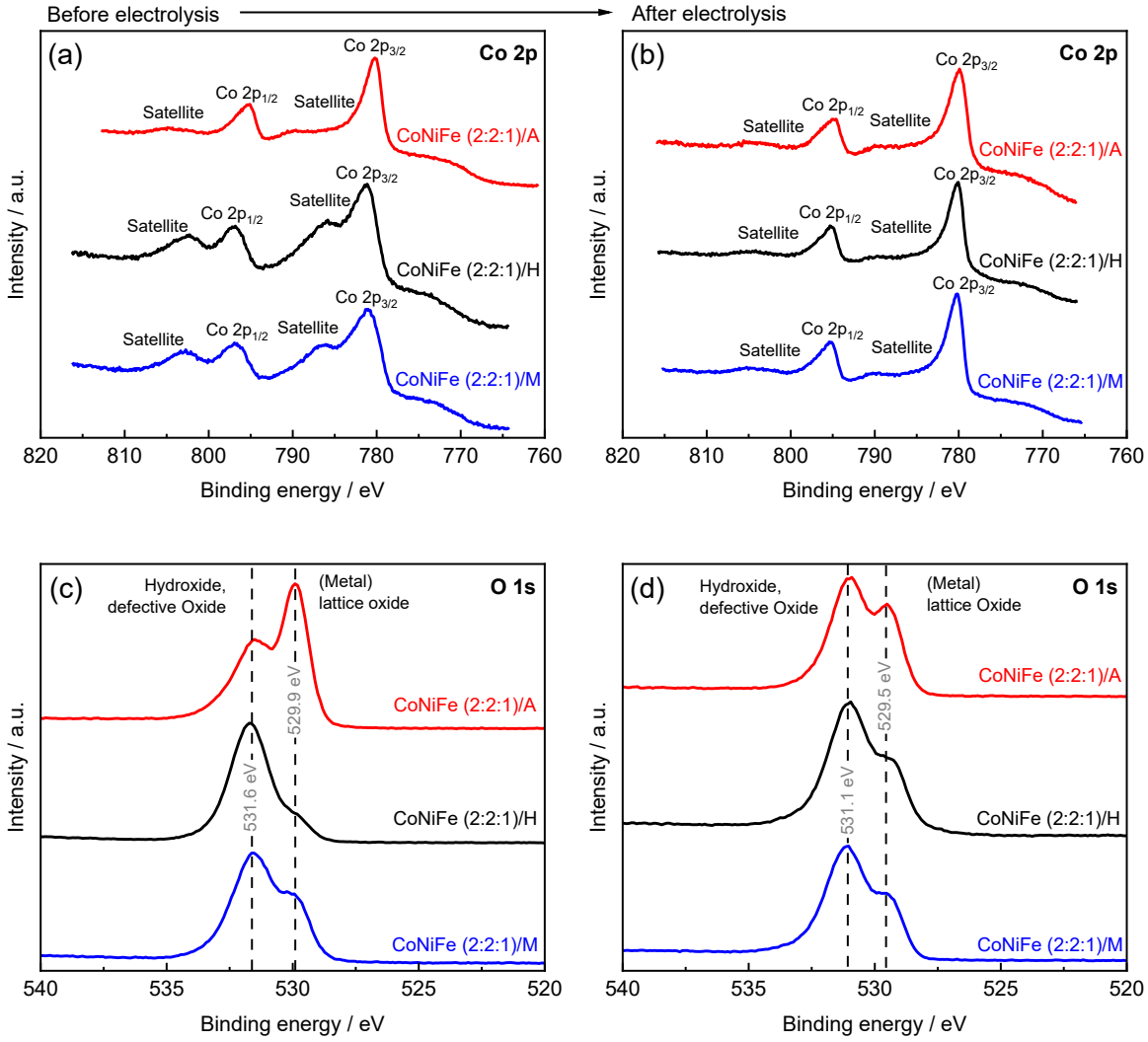

Figure 16. XP spectra (Co 2p and O 1s) of CoNiFe (2:2:1)/M,H,A. (left) Before electrolysis and (right) after stability tests for 1 h at 10 mA cm^{-2}_{geo}.

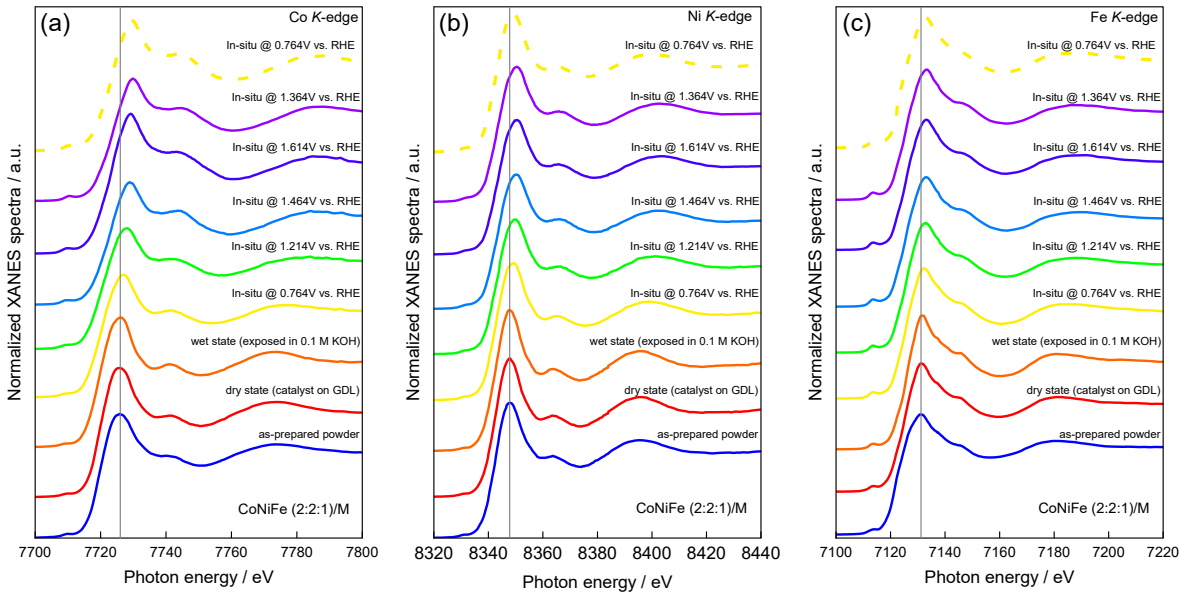

Figure 17. *In situ* K-edge XANES spectra of CoNiFe (2:2:1)/M. (a) Co K-edge. (b) Ni K-edge. and (c) Fe K-edge.

3.2. *Pre-Treated Carbon Additive Enables Reduction of Metal Loading in $CoNiFeO_x$ OER Electrocatalysts While Maintaining Performance*

The trimetallic oxides catalyst CoNiFe (2:2:1)/M has been studied and shown to have high activity and excellent stability both under RDE and MEA conditions [95]. However, due to the rapid development of Li-ion batteries, the global demand for Co and Ni has significantly increased [82]. Furthermore, Co and Ni mining has an exceptionally poor environmental footprint [84]. Consequently, reducing the metal content while minimizing the performance loss is a worthy goal for improving Co- and Ni-based catalysts.

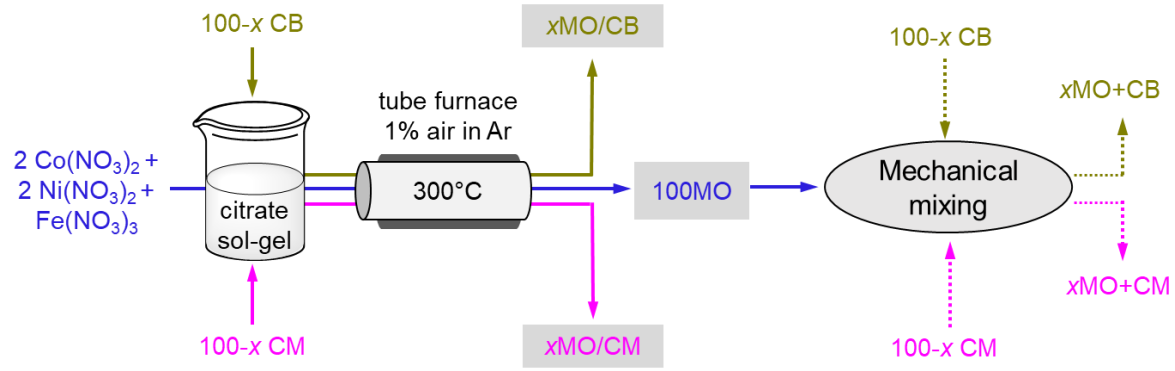

Figure 18. Schematic illustration of the preparation of catalyst 100MO and the xMO/CB, xMO/CM, xMO+CB, and xMO+CM series. MO = metal oxide. Metal oxide content (wt. %): x = 100, 80, 60, 40, 20. CB = unmodified carbon black. CM = pre-treated carbon black.

Following the synthesis of the optimal catalyst CoNiFe (2:2:1)/M (named 100MO in this work) in the first paper, Vulcan carbon black (CB) and modified carbon black (CB) were added to the metallic catalysts *via* two different methods: (1) mixing MO with carbon particles after thermal treatment using a mortar (xMO+CB and xMO+CM) and (2) adding carbon during synthesis before thermal treatment (xMO/CB and xMO/CM) as shown in Fig. 18 [100].

To study the electrochemical catalytic activity, the materials were examined using an RDE to obtain the main OER parameters, including η_{10}, j_{CoNiFe} at 1.56 V vs. RHE *via* metal oxide (MO) content, Tafel slope, R_p, ECSA, and durability. This method was similar to that described in the previous paper [95]. The following section discusses the influence of the carbon additives (CB and CM) at different mass ratios relative to the MO content, as well as the impact of the composite preparation approach (see Fig. 18). Firstly, carbon particles must be added during the sol-gel process, rather than only during ink preparation. As shown in Fig. 19, samples *x*MO+CB and *x*MO+CM exhibit low mass activity at 1.56 V vs. RHE and high overpotential at 10 mA cm^{-2}. In contrast, the materials *x*MO/CB and *x*MO/CM show promising performance despite having the same metal oxide loading content. One possible explanation can be the strong interaction between the metal oxide and the carbon particles through a chemical process followed by thermal treatment. This interaction allows the carbon to contribute effectively to the current flow as a conductivity-enhancing additive.

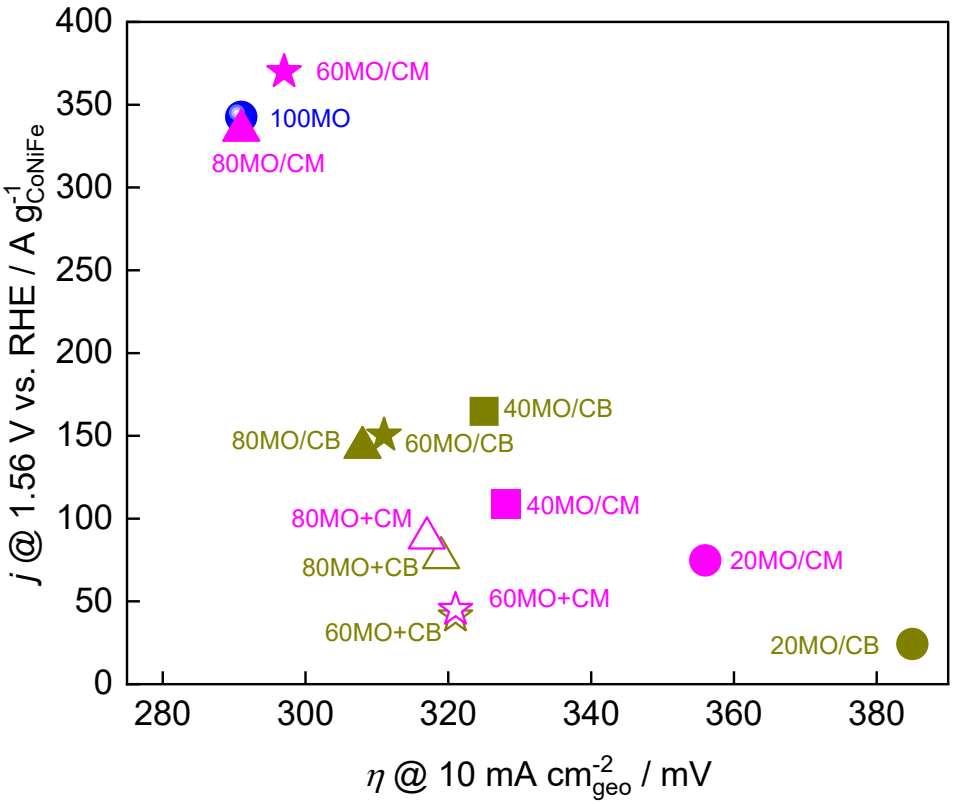

Figure 19. Comparison of overpotential and mass activity between 100MO and the MO-carbon composite series.

Secondly, oxidative pretreatment of hydrophobic carbon black particles is recommended, as evidenced by the high OER activity of samples 80MO/CM and 60MO/CM in the top left corner of Figure 19. Most samples in the MO/CM series perform better than those in the MO/CB series. One plausible explanation can be that the enhanced, more hydrophilic surface enables stronger binding to the metal oxide during composite formation. Specifically, a high metal oxide content (80 and 60 wt%) within the composite is necessary for good catalytic activity. Among the xMO/CM samples, 60MO/CM is the most promising candidate for OER and is comparable to the sample without carbon addition (100MO), as shown in the RDE study. Reducing the metal oxide content by 40% achieved the highest mass activity at 1.56 V corresponding to a metal content related one of approximately. 370 A g^{-1}, and a small overpotential of 297 mV at 10 mA cm^{-2}_{geo}. Furthermore, 60MO/CM exhibits comparable OER activity to 100MO as shown by the other electrochemical parameters such as the Tafel slope, R_p, and has an even higher ECSA [100].

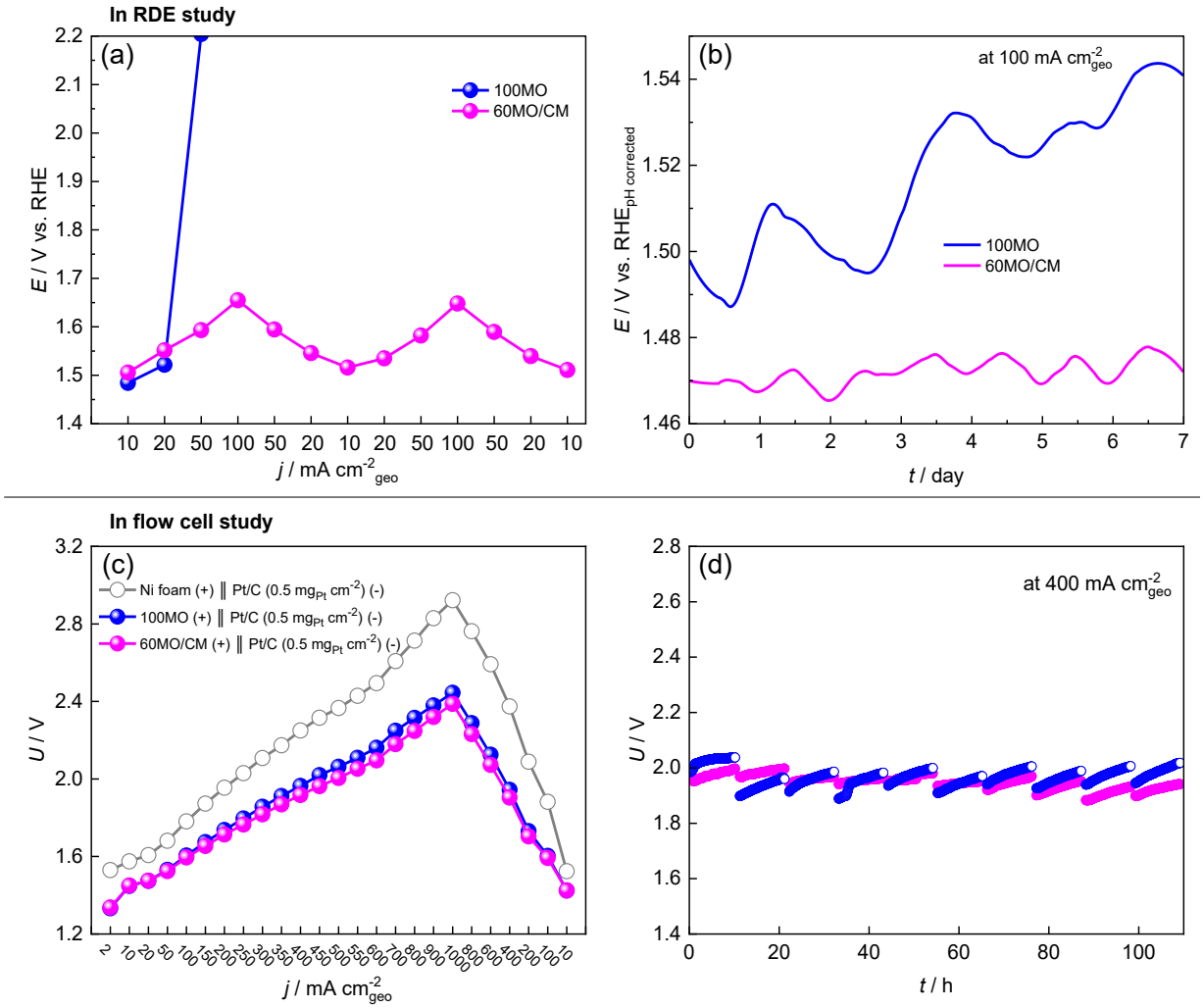

Figure 20. Durability studies for 100MO and 60MO/CM under RDE conditions (top: 1 M KOH, ω = 1800 rpm) and in the flow cell electrolyzer (bottom: 1 M KOH, 50 °C). (a) Stepwise chronopotentiometric stability test carried out at 10, 20, 50, and 100 mA cm^{-2}_{geo} (3 h for each step). (b) Chronopotentiometric stability tests recorded at 100 mA cm^{-2}_{geo} for 100MO and 60MO/CM on glassy carbon (all measured potentials are pH-corrected). (c) Cell voltage acquisition at various current densities ranging from 2 mA cm^{-2}_{geo} to 1000 mA cm^{-2}_{geo} (10 minutes per each point) and step-scanning back to 10 mA cm^{-2}_{geo}. (d) Stability tests using 100MO and 60MO/CM as OER catalysts, respectively, at 400 mA cm^{-2}_{geo}.

Indeed, durability is the next crucial factor in electrocatalyst design. As shown in Figure 20b, 60MO/CM exhibits a stable profile with a potential increase rate of ~ 0.2 μV h^{-1} for seven days of long-term stability on a GC RDE. By contrast, 100MO exhibits a higher potential increase of ~ 1.8 μV h^{-1} after beginning at a higher η_{100} value of 262 mV (see Fig. 20b). To further probe stability under high stress, an on-off chronopotentiometric analysis was carried out with 3-h intervals and current densities of 10, 20, 50, and 100 mA cm^{-2} at ω = 1800 rpm for (see Fig. 20a). Despite the harsh conditions and significant gas bubble formation, 60MO/CM exhibits stable plateaus during the three-hour intervals. In contrast, 100MO is much less stable under these conditions; in several trials, the experiment had to be terminated prematurely due to potential overloads at the 50 mA cm^{-2} current density step. While RDE conditions are well suited for studying and comparing catalyst properties, they cannot fully describe the long-term stability of catalysts, as discussed in the introduction.

A flow AEM electrolyzer was set-up with two electrodes separated by an anion exchange membrane (electrolyte: 1.0 M KOH; T = 50 °C). The catalysts studied were deposited on the surface of Ni foam by spray coating with a catalyst mass loading of 5 mg cm^{-2}_{geo}. The anolyte and the catholyte were purged through the divided cell separately. Concerning the short stress test results depicted in Figure 20c, bare Ni foam shows significantly higher potentials at every current density compared to catalyst loaded electrode (100MO and 60MO/CM). At the back scan, cell voltages at applied current densities pose improvement compared to the forward scan, confirming the excellent OER activity of 100MO and 60MO/CM under practically relevant conditions. More specifically, 60MO/CM performs somewhat better than 100MO. Long-term stability tests were carried out at 400 mA cm^{-2} with ten intervals of ten hours each (see Fig. 20d). 60MO/CM performs high activity and excellent stability by minor increasing in cell voltage within and between the 10 h intervals. Improvement in cell voltage is observed during the stress tests for 60MO/CM which is not seen in the case of 100MO. In summary, 60MO/CM shows a better long-term stability than its carbon-free counterpart (100MO).

To further discuss the importance of the carbon additive in this study, two different methods were applied to control the metal oxide content loaded on the GC RDE surface, rather than introducing carbon to the $CoNiFeO_x$ system. 60MO-1 was prepared by reducing the mass of material by 40 % and increasing the Nafion-content in the mixture. The ink volume used for the drop casting was the same as that used for electrode preparation to maintain the same catalyst layer thickness on the WE surface. Conversely, 60MO-2 was prepared using the original 100MO ink with only a small amount of ink dropped onto the WE surface resulting in a loading of 60% MO. This method affected the thickness of the catalyst layer on the WE surface.

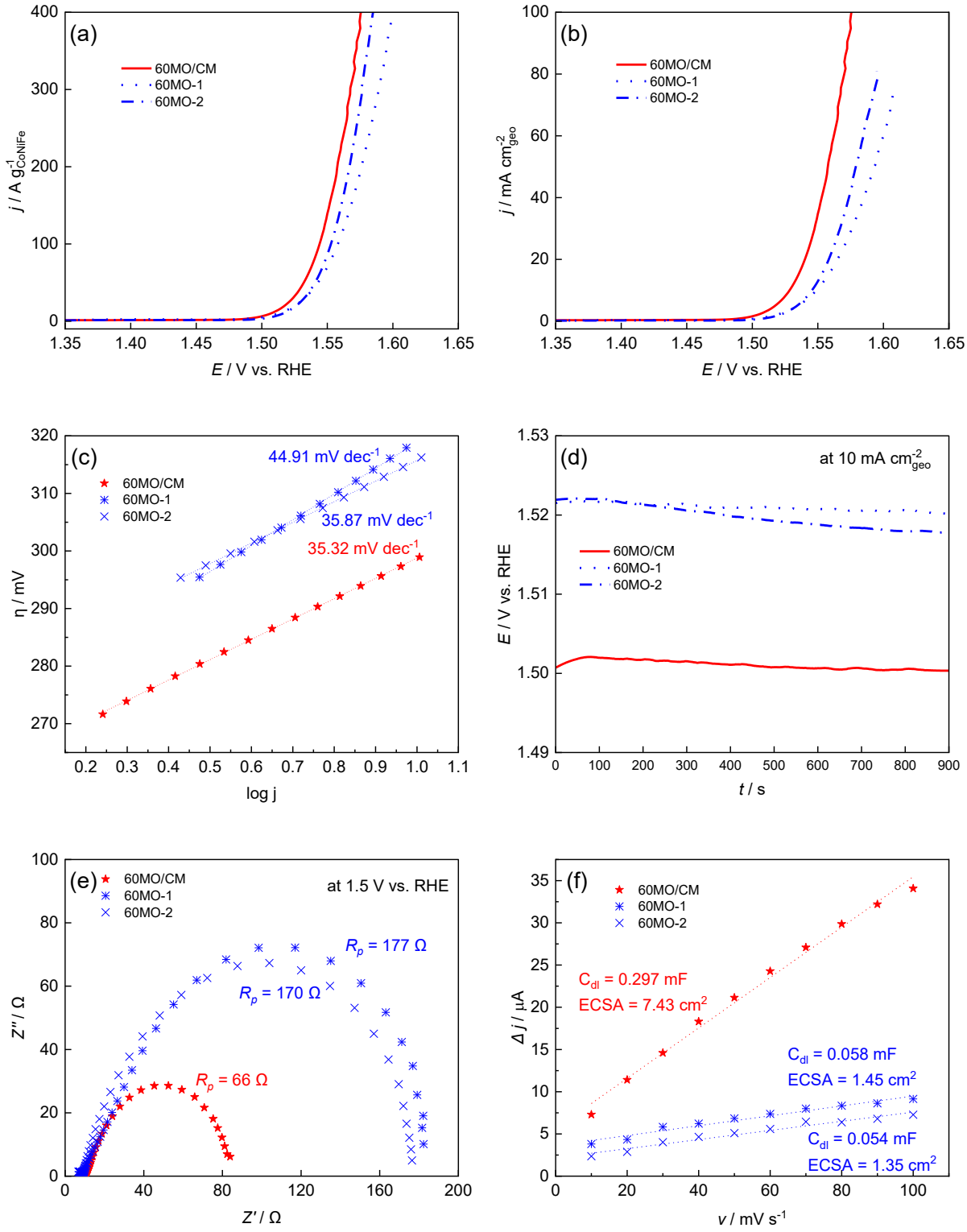

Figure 21. (a, b) OER polarization curves measured in 1 M KOH solution (v = 1 mV s^{-1}, ω = 1800 rpm, iR-drop corrected) showing the mass related current densities (a) and the current density with respect to the geometrical electrode surface area (b). (c) Tafel slope from LSVs in Fig. 21b. (d) Chronopotentiometric profiles recorded at 10 mA cm^{-2} (ω = 1800 rpm). (e) Electrochemical impedance spectra (Nyquist plots) recorded for 60MO/CM, 60MO-1, and 60MO-2 at 1.5 V vs. RHE. (f) Estimation of double layer capacitance (C_{dl}) and electrochemically active surface area (ECSA).

As shown in Figures 21a and 21b, the electrocatalytic performance of the different approaches to reducing the metal content is compared. Sample 60MO/CM, in which the $CoNiFeO_x$ content was reduced by the adding modified carbon (CM) during synthesis exhibits significantly higher performance than methods that do not involve the addition of carbon. Sample 60MO-1 exhibits a low mass activity, corresponding to the MO content loading on the electrode surface, of ~ 110 A g^{-1}_{CoNiFe} at 1.56 V vs. RHE, compared to ~. 149 A g^{-1}_{CoNiFe} for 60MO-2. These values are around 2.5 times smaller than those of 60MO/CM (~ 370 A g^{-1}_{CoNiFe}). Furthermore, sample 60MO/CM achieves a small η_{10} of 297 mV; however, samples 60MO-1 and 60MO-2 show higher overpotentials at 10 mA cm^{-2}, of 319 mV and 314 mV, respectively. This is further confirmed by the short stability test shown in Fig. 21d. Regarding other electrochemical OER parameters (Tafel slope, R_p, and ECSA), carbon-free samples exhibit poorer OER activity than samples containing carbon (see Fig. 21c, e, and f). These experiments confirm the advantages of adding carbon to trimetallic oxides electrocatalysts in view of maintaining high OER activity and improving outstanding long-term stability under alkaline conditions. Interestingly, 60MO-2 shows better performance than 60MO-1 despite both having lower OER activity than 60MO/CM. This suggests that thinner catalyst layer improves the anodic electrochemical reaction.

For structural characterization, XRD, XPS, SEM, STEM, and EDX were applied before and after electrolysis. As discussed in the manuscript, the samples containing carbon additives (60MO/CM and 60MO/CB) and sample without carbon (100MO) exhibited similar, less crystalline XRD patterns, showing three typical diffraction signals at 16.3°, 19.1°, and 27.3°, corresponding to the planes of CoO, NiO, and FeO, respectively. XPS results confirmed that the impact of added carbon on the surface metal oxide composition and valence states was negligible. SEM/EDX and STEM/EELS analyses revealed homogeneous mixing of carbon and metal oxides *via* the sol-gel method, as well as an even distribution of all three metals across the surface. Adding carbon to metallic oxides successfully improved the specific surface area, mesopore volume, and conductivity (as determined by BET and conductivity measurements). After stability tests, 60MO/CM exhibited behavior similar to that of sample 100MO, as discussed in the previous section. Notably, the XP spectra in the O1s region are different. The addition of carbon appears to alter the ratio of lattice oxygen to hydroxide/defective oxygen during OER. The hydroxide peak is clearly visible for all samples, both before and after electrolysis. However, to better understand sample 60MO/CM, *in situ* XAS measurements were carried out under the same conditions as for sample 100MO (see Fig. 22).

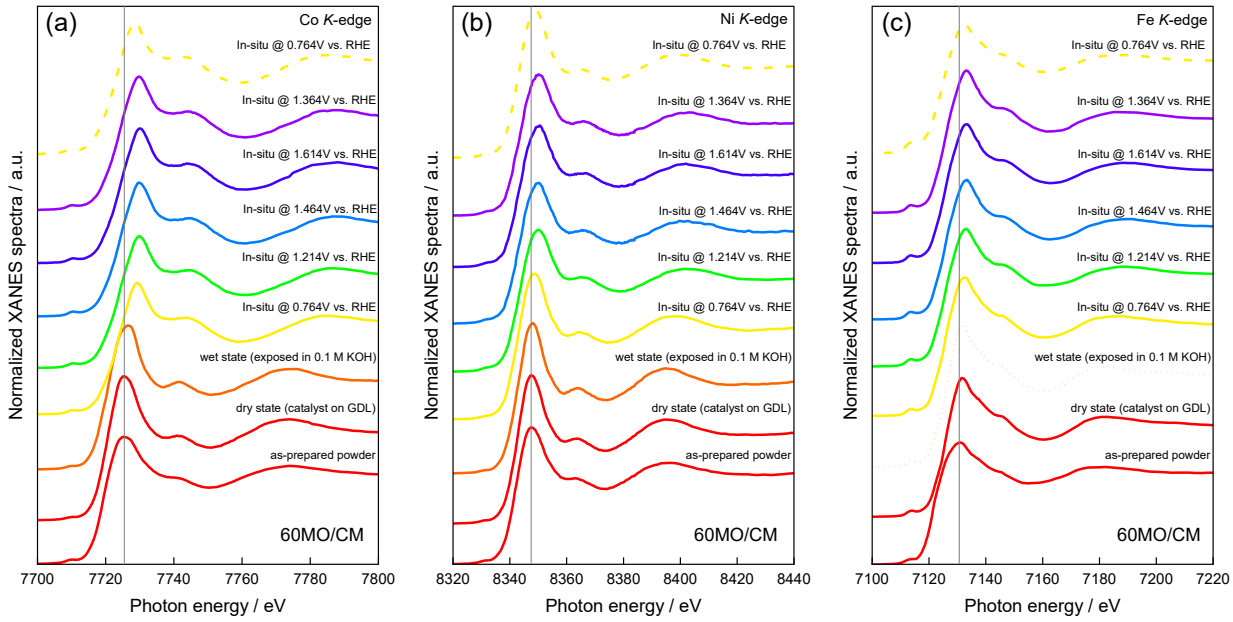

Figure 22. *In situ* K-edge XANES spectra of 60MO/CM. (a) Co K-edge. (b) Ni K-edge. and (c) Fe K-edge.

Similar to sample 100MO, the oxidation state of **Co** in sample 60MO/CM is more depended on the electrode potential than Fe and Ni. When scanned from the OCP to the OER region, Co always remains at a higher oxidation state than in sample100MO, forming an active phase (*e.g.,* Co_3O_4 or β-CoOOH). Consequently, carbon appears to influence the metal oxidation state [190]. In the OER region, Co exhibits an oxidation state of 3.2, which confirms the presence of Co^{4+} in the system [79]. Unlike in sample 100MO, Co in sample 60MO/CM is reduced to the lower-energy Co^{3+} form when scanning back to the OCP. As with sample 100MO, **Ni** exists primarily in the Ni^{2+} and Ni^{3+} states during OER process [80a, 80b]. The oxidation state of **Fe** is almost always +III [80c]. Finally, the presence of carbon affects the striking difference in Co oxidation states. While for 100MO it increases from 2.5 to 3.0, in 60MO/CM it exhibits significantly higher values at OCP (3.1) and under OER conditions (3.3). In conclusion, Fe maintains an oxidation state +III over a wide potential range. Furthermore, a significant proportion of Co(IV) centers are present under OER conditions, while Ni exists in a lower oxidation state. Interestingly, the two investigated catalysts exhibit clear differences in the redox behavior of Co, with significantly higher oxidation states in 60MO/CM than in 100MO. This large difference under potential bias indicates that carbon strongly influences the electronic structure of the metal oxide. This is likely due to improved charge transfer through the material, which may influence the OER activity of individual sites at elevated potentials.

3.3. Heterogenized Copper(II) Phenanthroline Catalysts for Electroreduction of CO_2 to C_2 Compounds: Substitution on the Ligand Causes Structural Changes to the Molecular Framework and Stability Enhancement

In addition to developing OER catalysts for alkaline media, attention has been given to the cathodic half-cell, where electrochemical reduction reactions occur, such as the hydrogen evolution reaction (HER), and the CO_2 reduction reaction (eCO_2RR). Molecular Cu catalysts with

well-defined structure have been gained attention as promising candidates for generating C_{2+} from CO_2 with high efficiency. However, the formation of nanoclusters during eCO_2RR undermines the advantages of the molecular framework. Therefore, this work focuses on developing of molecular Cu complexes that, incorporate the phenanthroline framework as the ligand, resulting in promising electrocatalysts for electrochemical conversion of CO_2 to C_2H_4 production in eCO_2RR.

A brief history of material development shows that, **Cat2**, a heterogenized binuclear hydroxo-bridged phenanthroline Cu(II) complex (see Fig. 23) with a short Cu···Cu distance exhibits high selectivity for CO_2-to-C_2H_4 conversion. Discussion of the structural characterization confirmed that the molecular structure was preserved during electrolysis. However, long-term operation remains challenges for **Cat2**, since the formation of CuO_x particles has been observed under potential bias and accompanied by leaching of catalyst into the electrolyte solution [153b].

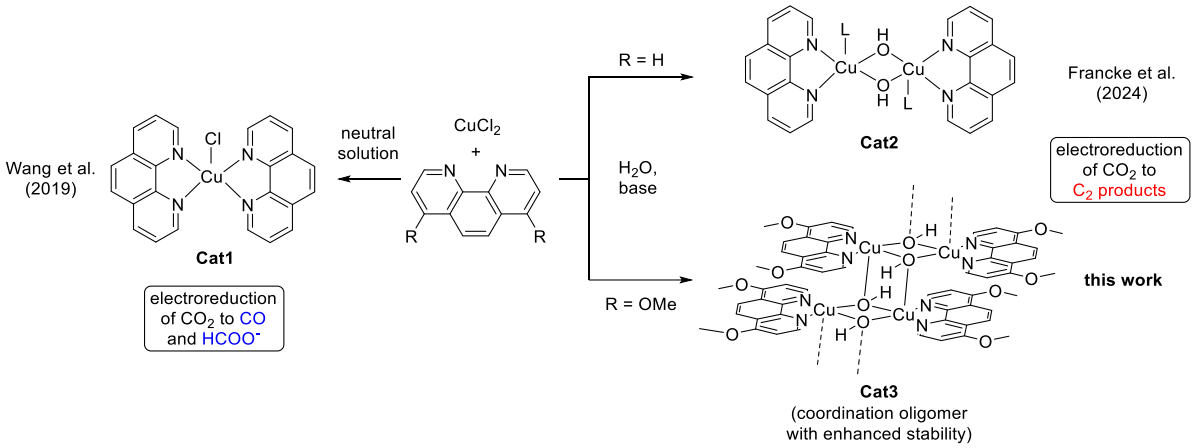

Figure 23. Mono, bi- and oligonuclear Cu phen compounds as molecular catalysts for eCO_2RR. **Cat2**: Binuclear Cu phenanthroline complex [153b]. **Cat3**: heterogenized molecular Cu(II) phenanthroline catalysts.

In the development of molecular copper complexes for CO_2RR, a heterogenized molecular Cu(II) phenanthroline catalyst has been studied. With no observation of catalyst leaching in the H-cell tests and no change of the Cu coordination environment in *in situ* XAS studies, **Cat3** exhibits potentially for long-term stable operation. In particular, **Cat3** enables the selective formation of C_{2+} products at high current densities in an MEA electrolyzer, highlighting the potential as a CO_2RR catalyst for industrially relevant applications.

This discussion focuses on the impact of supporting electrolyte cations on eCO_2RR. **Cat2** and **Cat3** demonstrate superior performance in CO_2RR when $CsHCO_3$ is used as the electrolyte solution rather than $KHCO_3$ [153b]. To understand the benign effect of Cs^+ cations on the reactivity of **Cat3** for eCO_2RR, EIS measurements were carried out at a frequency range of 100 kHz to 1 Hz at -1.2 V vs. RHE in an H-type divided cell. This potential enables significant C_{2+} products formation, while minimizing the strong gas bubble generation that would occur at higher potentials/current densities.

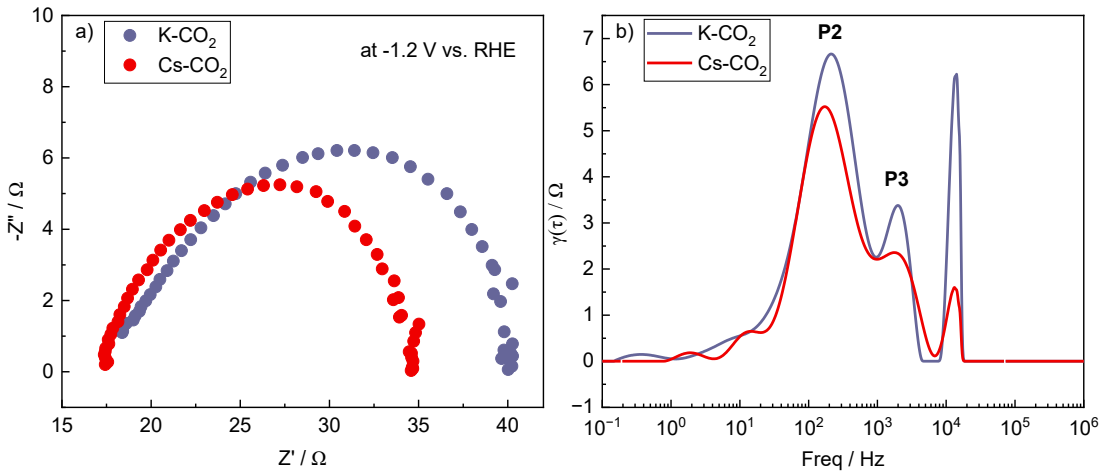

Figure 24. Results of the EIS analysis of **Cat3** on carbon paper in the H-type cell at -1.2 V vs. RHE. (a) Nyquist plot. (b) Distribution of relaxation time (DRT). K-CO_2: CO_2 saturated in 0.1 M $KHCO_3$ solution. Cs-CO_2: CO_2 saturated in 0.1 M $CsHCO_3$ solution.

As shown in Figure 24a, while the electrolyte resistance of both $CsHCO_3$ and $KHCO_3$ is comparable, the Cs^+ tends to lower the polarization resistance, suggesting enhanced reaction kinetics due to smaller charge transfer resistance. To further elucidate these complex interface dynamics, the distribution of relaxation times (DRT) was used to analyze the EIS data [191]. In theory, this approach allows the deconvolution of individual transport and kinetic contributions based on their characteristic relaxation frequencies.

A DRT analysis was performed using the RelaxIS web-tool, with the standard setting of a regularization parameter of 10^{-3} [192]. The extracted DRT profiles are shown in Figure 24b. At -1.2 V vs. RHE, sharp and prominent peaks appear near 10^2 Hz and 10^3 Hz, which were previously assigned to eCO_2RR-related electron transfer (P2) and the coupled chemical bicarbonate/CO_2 equilibrium (P3) [191a]. Particularly, in a 0.1 M $CsHCO_3$ electrolyte, both peaks contribute less than in a 0.1 M $KHCO_3$ electrolyte, which suggests that the enhanced eCO_2RR reactivity may be due to improved electron transfer kinetics and a more favorable bicarbonate/CO_2 equilibrium (resulting in better local CO_2 availability).

The benign effect of Cs^+ ions has also been reported for eCO_2RR processes on other catalysts [193]. While a clear impact on the charge transfer kinetics could be demonstrated using the EIS technique, further studies are needed to obtain a clearer picture of the role of the counter ion in this particular example.

4. Conclusion of This Work

This work describes the development of high-performance heterogeneous electrocatalysts for water oxidation and carbon dioxide reactions toward sustainable energy conversion including a detailed analysis of the influence of synthesis parameters and additives on the catalyst performance.

First, an effective method of synthesizing highly active mixed metal oxide electrocatalysts is introduced. This approach is based on a simple sol-gel process combined with thermal treatment and a well-balanced molar metal ratio. $CoNiFeO_x$ with an optimal stoichiometry of Co : Ni : Fe = 2 : 2: 1, treated under oxygen-deficient conditions (M; 1 vol% air in argon), exhibits high activity and excellent stability for OER in alkaline media under both RDE and MEA electrolyzer conditions. The impact of thermal treatment conditions on the structural properties of the catalysts was clarified using advanced characterization techniques, such as XRD, XPS, SEM, and STEM. As a results of the oxygen-deficient conditions during thermal treatment, the optimal CoNiFe (2:2:1)/M catalyst has an amorphous structure, and low metallic oxidation states. It also contains both lattice oxide and a higher density of defective oxide. During OER, the material became completely amorphous and exhibited higher metallic oxidation states, while retaining both lattice oxide and a higher density of defective oxide. *In situ* XANES data confirmed the behavior of Co, Ni, and Fe during OER in an alkaline environment. In summary, the formation of these structural properties in the catalyst material already offers advantages for excellent OER performance. Nevertheless, detailed mechanistic studies have to be carried out in the future to better understand the catalyst's behavior, the structure of the active site, and the catalytic mechanism. Therefore, application of further in situ spectroscopic techniques, ideally in tandem with computational (quantum chemical) analysis, are necessary.

Furthermore, to minimize the metal content, a carbon additive was introduced. The carbon precursors, untreated Vulcan carbon black (CB) and acid-treated carbon black (CM), were introduced into the trimetallic oxide catalyst ($CoNiFeO_x$) *via* mechanical mixing and during the sol-gel process, respectively. Adding carbon during the sol-gel process resulted in higher OER catalytic activity than mixing through ink formulation due to formed stronger interactions between the metal oxide and carbon particles. Additionally, the oxidative pre-treatment of hydrophobic carbon black particles and a sufficiently high metal oxide content (80 and 60 wt%) are required for optimal catalytic activity. Catalyst 60MO/CM, which has a metal oxide content of 60 wt% mixed with 40 wt% pre-treated carbon during the sol-gel process, is the most promising candidate for both RDE and flow AEM electrolysis studies. Notably, under practically relevant conditions in an AEM flow electrolyzer, 60MO/CM demonstrated remarkably high OER performance, even surpassing the 100MO sample with 100 wt% metal oxide content. This suggests that adding carbon during synthesis not only reduces metal loading but also enhances stability in the flow cell electrolyzer.

Lastly, a new class of molecular copper(II) phenanthroline catalysts has been developed and studied for the eCO_2RR process. Cu-based molecular catalysts achieve high performance and selectivity toward C_{2+} products at high current densities in an MEA flow electrolyzer, enabling the application under practically relevant conditions. In this work, EIS measurements along with DRT analysis were performed to confirm the contribution of Cs^+ to improved electron transfer kinetics

and a more favorable bicarbonate/CO_2 equilibrium. As conclusion, understanding and leveraging the intriguing cation impact will allow for better control of eCO_2RR processes in the future.

5. Outlook

This thesis focuses on developing mixed metallic oxide electrocatalysts with high activity and stability for the oxygen evolution reaction (OER) under alkaline condition. Due to their high catalytic performance for OER, $CoNiFeO_x$ catalysts could be used in other electrocatalytic processes, such as the anodic oxidation of biomass-derived alcohols or sugars. This process is currently being investigated in our laboratory and showing promising results (see Fig. 25).

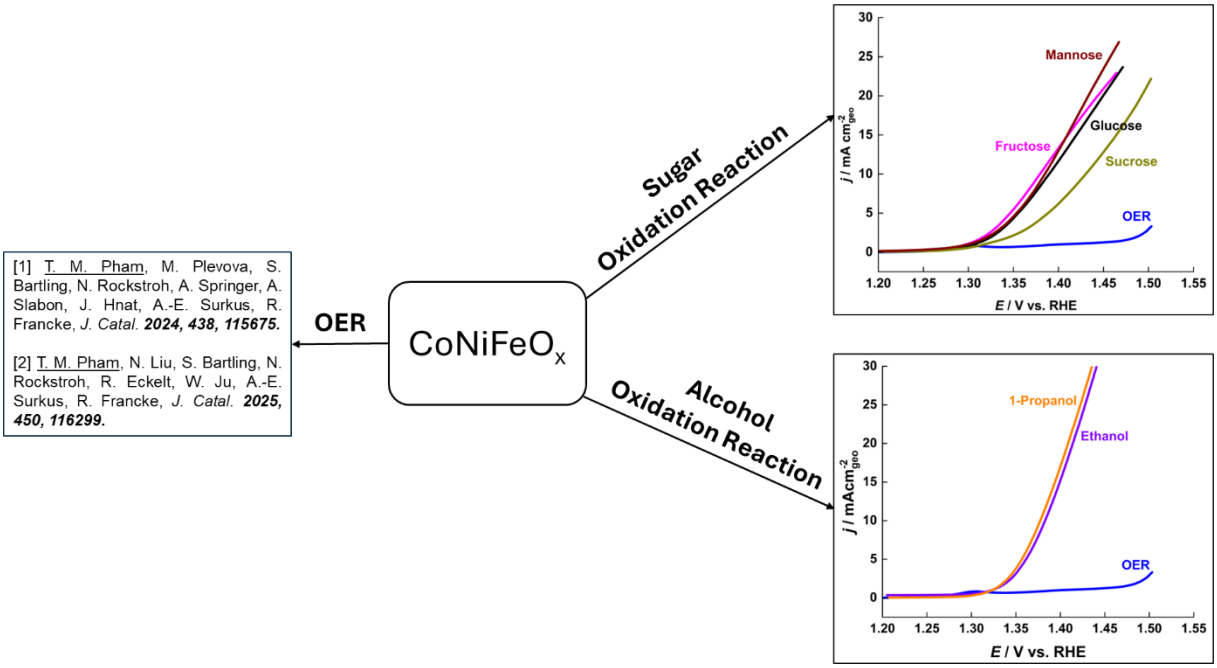

Figure 25. Initial results from the application of the developed OER catalysts for the oxidation of biomass-derived alcohols and sugars.

6. References

[1] IEA, Global Energy Review 2025, IEA, Paris https://www.iea.org/reports/global-energy-review-2025, **2025**.

[2] T. Kober, H. W. Schiffer, M. Densing, E. Panos, *Energy Strate Rev* **2020**, *31*, 100523.

[3] H. R. D. Sutoyo, I. G. A. G. Angga, H. Schümann, C. F. Berg, *Geoenergy Sci. Eng.* **2023**, *226*, 211759.

[4] a) N. Khan, E. Kalair, N. Abas, A. R. Kalair, A. Kalair, *Eng. Sci. Technol. Int. J.* **2019**, *22*, 185-214; b) S. Kumar, R. Srivastava, J. Koh, *J. CO2 Util.* **2020**, *41*, 101251.

[5] M. Zerta, P. R. Schmidt, C. Stiller, H. Landinger, *Int. J. Hydrogen Energy* **2008**, *33*, 3021-3025.

[6] R. Raineri, J. Binder, A. Cohen, A. Muller, *Energies, Vol. 18*, **2025**.

[7] S. Sharma, S. Agarwal, A. Jain, *Energies, Vol. 14*, **2021**.

[8] M. A. Rosen, I. Dincer, M. Kanoglu, *Energy Policy* **2008**, *36*, 128-137.

[9] a) S. Dunn, *Int. J. Hydrogen Energy* **2002**, *27*, 235-264; b) S. G. Nnabuife, A. K. Hamzat, J. Whidborne, B. Kuang, K. W. Jenkins, *Int. J. Hydrogen Energy* **2025**, *107*, 218-240.

[10] S. Aslam, S. Rani, K. Lal, M. Fatima, T. Hardwick, B. Shirinfar, N. Ahmed, *Green Chem.* **2023**, *25*, 9543-9573.

[11] A. J. Martyr, D. R. Rogers, *Engine Testing (Fifth Edition)* (Eds.: A. J. Martyr, D. R. Rogers), Butterworth-Heinemann, Oxford, **2021**, pp. 191-215.

[12] a) M. Younas, S. Shafique, A. Hafeez, F. Javed, F. Rehman, *Fuel* **2022**, *316*, 123317; b) M. Neuwirth, T. Fleiter, P. Manz, R. Hofmann, *Energy Convers. Manag.* **2022**, *252*, 115052; c) T. Jordan, *Hydrogen Safety for Energy Applications* (Eds.: A. Kotchourko, T. Jordan), Butterworth-Heinemann, **2022**, pp. 25-115; d) T. Yusaf, M. Laimon, W. Alrefae, K. Kadirgama, D. Ramasamy, M. Kamal, B. Yousif, *Appl. Sci.* **2022**, *12*, 17.

[13] a) A. I. Osman, N. Mehta, A. M. Elgarahy, M. Hefny, A. Al-Hinai, A. a. H. Al-Muhtaseb, D. W. Rooney, *Environ. Chem. Lett.* **2022**, *20*, 153-188; b) P. Saha, F. A. Akash, S. M. Shovon, M. U. Monir, M. T. Ahmed, M. F. H. Khan, S. M. Sarkar, M. K. Islam, M. M. Hasan, D.-V. N. Vo, A. A. Aziz, M. J. Hossain, R. Akter, *Int. J. Green Energy* **2024**, *21*, 1383-1397; c) J. M. M. Arcos, D. M. F. Santos, *Gases, Vol. 3*, **2023**, pp. 25-46; d) M. Hermesmann, T. E. Müller, *Prog. Energy Combust. Sci.* **2022**, *90*, 100996.

[14] O. Massarweh, M. Al-khuzaei, M. Al-Shafi, Y. Bicer, A. S. Abushaikha, *J. CO2 Util.* **2023**, *70*, 102438.

[15] X. Wu, Y. Yu, Z. Qin, Z. Zhang, *Energy Procedia* **2014**, *63*, 1339-1346.

[16] R. Yukesh Kannah, S. Kavitha, Preethi, O. Parthiba Karthikeyan, G. Kumar, N. V. Dai-Viet, J. Rajesh Banu, *Bioresour. Technol.* **2021**, *319*, 124175.

[17] M. Newborough, G. Cooley, *Fuel Cells Bull.* **2020**, *2020*, 16-22.

[18] S. Schneider, S. Bajohr, F. Graf, T. Kolb, *ChemBioEng Rev.* **2020**, *7*, 150-158.

[19] Q. Hassan, S. Algburi, A. Z. Sameen, H. M. Salman, M. Jaszczur, *Int. J. Hydrogen Energy* **2024**, *50*, 310-333.

[20] M. El-Shafie, *Results Eng* **2023**, *20*, 101426.

[21] D. Franzmann, H. Heinrichs, F. Lippkau, T. Addanki, C. Winkler, P. Buchenberg, T. Hamacher, M. Blesl, J. Linßen, D. Stolten, *Int. J. Hydrogen Energy* **2023**, *48*, 33062-33076.

[22] T. Smolinka, H. Bergmann, J. Garche, M. Kusnezoff, *Electrochemical Power Sources: Fundamentals, Systems, and Applications* (Eds.: T. Smolinka, J. Garche), Elsevier, **2022**, pp. 83-164.

[23] a) Y. Zhou, R. Li, Z. Lv, J. Liu, H. Zhou, C. Xu, *Chin J Chem Eng.* **2022**, *43*, 2-13; b) S. Nishioka, F. E. Osterloh, X. Wang, T. E. Mallouk, K. Maeda, *Nat Rev Methods Primers* **2023**, *3*, 42.

[24] a) A. J. Shih, M. C. O. Monteiro, F. Dattila, D. Pavesi, M. Philips, A. H. M. da Silva, R. E. Vos, K. Ojha, S. Park, O. van der Heijden, G. Marcandalli, A. Goyal, M. Villalba, X. Chen, G. T. K. K. Gunasooriya, I. McCrum, R. Mom, N. López, M. T. M. Koper, *Nat. Rev. Methods Primers.* **2022**, *2*, 84; b) Y. D. Zi-You Yu, Xing-Yu Feng, Xingxing Yu, Min-Rui Gao,* and Shu-Hong Yu, *Adv. Mater.* **2021**, *33*.

[25] S. Trasatti, *J. Electroanal. Chem.* **1999**, *476*, 90-91.
[26] R. de Levie, *J. Electroanal. Chem.* **1999**, *476*, 92-93.
[27] C. J. Brockman, *J. Chem. Educ.* **1927**, *4*, 770.
[28] H. L. S. Shiva Kumar, *Energy Rep.* **2022**, *8*, 21.
[29] a) W. Li, H. Tian, L. Ma, Y. Wang, X. Liu, X. Gao, *Mater. Adv.* **2022**, *3*, 5598-5644; b) M. Schalenbach, G. Tjarks, M. Carmo, W. Lueke, M. Mueller, D. Stolten, *J. Electrochem. Soc.* **2016**, *163*, F3197.
[30] Y. Sugawara, S. Sasidharan, M. Shoji, I. Rajith, G. P. K., K. Hidenori, A. G. M., T. and Yamaguchi, *J. Chem. Eng. Japan* **2023**, *56*, 2210195.
[31] H. Tüysüz, *Acc. Chem. Res.* **2024**, *57*, 558-567.
[32] T. Wang, X. Cao, L. Jiao, *Carbon Neutrality* **2022**, *1*, 21.
[33] a) M. Ďurovič, J. Hnát, K. Bouzek, *J. Power Sources* **2021**, *493*, 229708; b) M. R. G. de Chialvo, A. C. Chialvo, *J. Electroanal. Chem.* **1994**, *372*, 209-223; c) M. Zeng, Y. Li, *J. Mater. Chem. A* **2015**, *3*, 14942-14962; d) A. Raveendran, M. Chandran, R. Dhanusuraman, *RSC Adv.* **2023**, *13*, 3843-3876.
[34] Y. Zheng, Y. Jiao, A. Vasileff, S.-Z. Qiao, *Angew. Chem. Int. Ed.* **2018**, *57*, 7568-7579.
[35] F. M. Sapountzi, J. M. Gracia, C. J. Weststrate, H. O. A. Fredriksson, J. W. Niemantsverdriet, *Prog. Energy Combust. Sci.* **2017**, *58*, 1-35.
[36] S. J. Gutić, A. S. Dobrota, E. Fako, N. V. Skorodumova, N. López, I. A. Pašti, in *Catal., Vol. 10*, **2020**.
[37] W. Sheng, M. Myint, J. G. Chen, Y. Yan, *Energy Environ. Sci.* **2013**, *6*, 1509-1512.
[38] H. Wendt, E. V. Spinacé, A. Oliveira Neto, M. Linardi, *Quim. Nova* **2005**, *28*.
[39] N. Behrooz, A. Ghaffarinejad, N. Sadeghi, *J. Electroanal. Chem.* **2016**, *782*, 1-8.
[40] P. Quaino, F. Juarez, E. Santos, W. Schmickler, *Beilstein J. Nanotechnol.* **2014**, *5*, 846-854.
[41] P. Quaino, E. Santos, G. Soldano, W. Schmickler, *Adv. Phys. Chem.* **2011**, *2011*, 851640.
[42] B. Hammer, J. K. Nørskov, *Adv. Catal., Vol. 45*, Academic Press, **2000**, pp. 71-129.
[43] Z. Wang, S. Shen, J. Wang, W. Zhong, *Chem. Eur. J.* **2024**, *30*, e202402725.
[44] S. Bhattacharjee, U. V. Waghmare, S.-C. Lee, *Sci. Rep.* **2016**, *6*, 35916.
[45] J. K. Nørskov, F. Abild-Pedersen, F. Studt, T. Bligaard, *PNAS* **2011**, *108*, 937-943.
[46] a) N. M. Marković, P. N. Ross, *Surf. Sci. Rep.* **2002**, *45*, 117-229; b) M. Nakamura, T. Kobayashi, N. Hoshi, *Surf. Sci.* **2011**, *605*, 1462-1465.
[47] H. Hu, M. Qiao, Y. Pei, K. Fan, H. Li, B. Zong, X. Zhang, *Appl. Catal. A: Gen.* **2003**, *252*, 173-183.
[48] F. Safizadeh, E. Ghali, G. Houlachi, *Int. J. Hydrogen Energy* **2015**, *40*, 256-274.
[49] M. A. Qadeer, X. Zhang, M. A. Farid, M. Tanveer, Y. Yan, S. Du, Z.-F. Huang, M. Tahir, J.-J. Zou, *J. Power Sources.* **2024**, *613*, 234856.
[50] M. S. Goh, H. Shin, J. Lee, H. Jeong, M. Kang, *Appl. Surf. Sci.* **2025**, *696*, 162953.
[51] F. S. M. Ali, R. L. Arevalo, M. Vandichel, F. Speck, E.-L. Rautama, H. Jiang, O. Sorsa, K. Mustonen, S. Cherevko, T. Kallio, *Appl. Catal. B: Environ.* **2022**, *315*, 121541.
[52] Y.-Y. Ma, C.-X. Wu, X.-J. Feng, H.-Q. Tan, L.-K. Yan, Y. Liu, Z.-H. Kang, E.-B. Wang, Y.-G. Li, *Energy Environ. Sci.* **2017**, *10*, 788-798.
[53] Y. Yan, C. Wang, Z. Huang, J. Fu, Z. Lin, X. Zhang, J. Ma, J. Shen, *J. Mater. Chem. A* **2021**, *9*, 5415-5424.
[54] W. Yaseen, N. Ullah, M. Xie, B. A. Yusuf, Y. Xu, C. Tong, J. Xie, *Surf. Interfaces* **2021**, *26*, 101361.
[55] Y. Zang, D.-Q. Lu, K. Wang, B. Li, P. Peng, Y.-Q. Lan, S.-Q. Zang, *Nat. Commun.* **2023**, *14*, 1792.
[56] S. Díaz-Coello, D. Winkler, C. Griesser, T. Moser, J. L. Rodríguez, J. Kunze-Liebhäuser, G. García, E. Pastor, *ACS Appl. Mater. Interfaces* **2024**, *16*, 21877-21884.
[57] L. F. Mxakaza, V. Mashindi, C. E. Linganiso, N. Moloto, Z. N. Tetana, *ChemistryOpen* **2024**, *13*, e202400146.
[58] Z. Chen, H. Hu, L. Yin, Z. Zhao, J.-H. Choi, G. Liu, F. Geng, *Proc. Natl. Acad. Sci.* **2023**, *120*, e2209760120.

[59] P. Eskandari, S. Zhou, J. Yuwono, D. Gunawan, R. F. Webster, Z. Ma, H. Xu, R. Amal, X. Lu, *Adv. Mater.* **2025**, *n/a*, 2419360.
[60] Y. Liu, Y. Chen, C. Liang, Z. Liang, C. Fan, F. Wang, J. Lei, *Int. J. Hydrogen Energy* **2024**, *51*, 701-708.
[61] H. M. C. M. Jayawardana, B. A. Yusuf, S. Meng, Y. Li, H. Ren, Q. Nie, Y. Xu, J. Xie, M. Chen, *J. Alloys Compd.* **2024**, *997*, 174809.
[62] W. Xu, D. Zhang, T. Wang, J. Lai, L. Wang, *Appl. Catal. B: Environ. Energy* **2025**, *361*, 124626.
[63] Q. Liang, G. Brocks, A. Bieberle-Hütter, *JPhys Energy* **2021**, *3*, 026001.
[64] M. Plevová, J. Hnát, K. Bouzek, *J. Power Sources* **2021**, *507*, 230072.
[65] Z. Liu, X. Wang, G. Xie, J. Ge, *Chem. Eng. J.* **2024**, *499*, 155901.
[66] I. C. Man, H.-Y. Su, F. Calle-Vallejo, H. A. Hansen, J. I. Martínez, N. G. Inoglu, J. Kitchin, T. F. Jaramillo, J. K. Nørskov, J. Rossmeisl, *ChemCatChem* **2011**, *3*, 1159-1165.
[67] K. Liu, P. Cao, W. Chen, C. I. Ezeh, Z. Chen, Y. Luo, Q. Liu, H. Zhao, Z. Rui, S. Gao, Z. Yin, X. Sun, X. Yu, *Mater Adv* **2022**, *3*, 1359-1400.
[68] K. Zhang, R. Zou, *Small* **2021**, *17*, 2100129.
[69] H. Dau, C. Limberg, T. Reier, M. Risch, S. Roggan, P. Strasser, *ChemCatChem* **2010**, *2*, 724-761.
[70] V. Viswanathan, H. A. Hansen, *Top. Catal.* **2014**, *57*, 215-221.
[71] a) X. Huang, J. Wang, H. B. Tao, H. Tian, H. Xu, *Chem. Sci.* **2019**, *10*, 3340-3345; b) K. S. Exner, *ACS Appl. Energy Mater.* **2019**, *2*, 7991-8001.
[72] a) T.-W. Chen, S.-M. Chen, G. Anushya, R. Kannan, P. Veerakumar, M. M. Alam, S. Alargarsamy, R. Ramachandran, *Nanomaterials, Vol. 13*, **2023**; b) F. Song, L. Bai, A. Moysiadou, S. Lee, C. Hu, L. Liardet, X. Hu, *J. Am. Chem. Soc.* **2018**, *140*, 7748-7759; c) *ACS Energy Lett.* **2017**, *2*, 1937-1938.
[73] C. C. L. McCrory, S. Jung, I. M. Ferrer, S. M. Chatman, J. C. Peters, T. F. Jaramillo, *J. Am. Chem. Soc.* **2015**, *137*, 4347-4357.
[74] a) S. Cherevko, S. Geiger, O. Kasian, N. Kulyk, J.-P. Grote, A. Savan, B. R. Shrestha, S. Merzlikin, B. Breitbach, A. Ludwig, K. J. J. Mayrhofer, *Catal. Today* **2016**, *262*, 170-180; b) S. Cherevko, A. R. Zeradjanin, A. A. Topalov, N. Kulyk, I. Katsounaros, K. J. J. Mayrhofer, *ChemCatChem* **2014**, *6*, 2219-2223; c) O. Kasian, S. Geiger, P. Stock, G. Polymeros, B. Breitbach, A. Savan, A. Ludwig, S. Cherevko, K. J. J. Mayrhofer, *J. Electrochem. Soc.* **2016**, *163*, F3099.
[75] a) C. Angelinetta, S. Trasatti, L. D. Atanososka, R. T. Atanasoski, *J. Electroanal. Chem. Interf. Electrochem.* **1986**, *214*, 535-546; b) R. Kötz, S. Stucki, *Electrochim. Acta* **1986**, *31*, 1311-1316; c) H. Over, Y. D. Kim, A. P. Seitsonen, S. Wendt, E. Lundgren, M. Schmid, P. Varga, A. Morgante, G. Ertl, *Science* **2000**, *287*, 1474-1476.
[76] a) R. Sen, S. Das, A. Nath, P. Maharana, P. Kar, F. Verpoort, P. Liang, S. Roy, *Front. Chem.* **2022**, *Volume 10 - 2022*; b) M. Clapp, C. M. Zalitis, M. Ryan, *Catal. Today* **2023**, *420*, 114140.
[77] a) J. Mohammed-Ibrahim, *J. Power Sources* **2020**, *448*, 227375; b) H. A. Miller, K. Bouzek, J. Hnat, S. Loos, C. I. Bernäcker, T. Weißgärber, L. Röntzsch, J. Meier-Haack, *Sustain. Energy Fuels* **2020**, *4*, 2114-2133; c) M. Schalenbach, O. Kasian, K. J. J. Mayrhofer, *Int. J. Hydrogen Energy* **2018**, *43*, 11932-11938; d) M. Schalenbach, A. R. Zeradjanin, O. Kasian, S. Cherevko, K. J. J. Mayrhofer, *Int. J. Electrochem. Sci.* **2018**, *13*, 1173-1226.
[78] L. Han, S. Dong, E. Wang, *Adv. Mater.* **2016**, *28*, 9266-9291.
[79] D. Friebel, M. Bajdich, B. S. Yeo, M. W. Louie, D. J. Miller, H. Sanchez Casalongue, F. Mbuga, T.-C. Weng, D. Nordlund, D. Sokaras, R. Alonso-Mori, A. T. Bell, A. Nilsson, *Phys. Chem. Chem. Phys.* **2013**, *15*, 17460-17467.
[80] a) D. K. Bediako, B. Lassalle-Kaiser, Y. Surendranath, J. Yano, V. K. Yachandra, D. G. Nocera, *J. Am. Chem. Soc.* **2012**, *134*, 6801-6809; b) S.-Y. Lee, I.-S. Kim, H.-S. Cho, C.-H. Kim, Y.-K. Lee, *Appl. Catal. B: Environ.* **2021**, *284*, 119729; c) M. Görlin, P. Chernev, J. Ferreira de Araújo, T. Reier, S. Dresp, B. Paul, R. Krähnert, H. Dau, P. Strasser, *J. Am. Chem. Soc.* **2016**,

138, 5603-5614; d) N. Li, D. K. Bediako, R. G. Hadt, D. Hayes, T. J. Kempa, F. von Cube, D. C. Bell, L. X. Chen, D. G. Nocera, *Proc. Natl. Acad. Sci.* **2017**, *114*, 1486-1491; e) L. Calvillo, F. Carraro, O. Vozniuk, V. Celorrio, L. Nodari, A. E. Russell, D. Debellis, D. Fermin, F. Cavani, S. Agnoli, G. Granozzi, *J. Mater. Chem. A* **2018**, *6*, 7034-7041.

[81] a) M. Yu, E. Budiyanto, H. Tüysüz, *Angew. Chem. Int. Ed.* **2022**, *61*, e202103824; b) R. A. Krivina, Y. Ou, Q. Xu, L. P. Twight, T. N. Stovall, S. W. Boettcher, *Acc. Mater. Res.* **2021**, *2*, 548-558.

[82] a) P. Kalungi, Z. Yao, H. Huang, *Materials, Vol. 17*, **2024**; b) M. Li, J. Lu, *Science* **2020**, *367*, 979-980.

[83] S. van den Brink, R. Kleijn, B. Sprecher, A. Tukker, *Resour. conserv. recycl.* **2020**, *156*, 104743.

[84] a) E. M. Mervine, R. K. Valenta, J. S. Paterson, G. M. Mudd, T. T. Werner, I. Nursamsi, L. J. Sonter, *Nat. Commun.* **2025**, *16*, 481; b) S. H. Farjana, N. Huda, M. A. P. Mahmud, *J. Sustain. Min.* **2019**, *18*, 150-161.

[85] C. Minke, M. Suermann, B. Bensmann, R. Hanke-Rauschenbach, *Int. J. Hydrogen Energy* **2021**, *46*, 23581-23590.

[86] F. Le Formal, L. Yerly, E. Potapova Mensi, X. Pereira Da Costa, F. Boudoire, N. Guijarro, M. Spodaryk, A. Züttel, K. Sivula, *ACS Catal.* **2020**, *10*, 12139-12147.

[87] J. Sun, S. Li, Q. Zhang, J. Guan, *Sustain. Energy Fuels* **2020**, *4*, 4531-4537.

[88] S. Ghosh, R. Jana, S. Ganguli, H. R. Inta, G. Tudu, H. V. S. R. M. Koppisetti, A. Datta, V. Mahalingam, *Nanoscale Adv.* **2021**, *3*, 3770-3779.

[89] J. Schuch, S. Klemenz, P. Schuldt, A.-M. Zieschang, S. Dolique, P. Connor, B. Kaiser, U. I. Kramm, B. Albert, W. Jaegermann, *ChemCatChem* **2021**, *13*, 1772-1780.

[90] D. Nam, J. Kim, *Int. J. Hydrogen Energy* **2022**, *47*, 16900-16907.

[91] S. Nagappan, A. Karmakar, R. Madhu, S. S. Selvasundarasekar, S. Kumaravel, K. Bera, H. N. Dhandapani, D. Sarkar, S. M. Yusuf, S. Kundu, *ACS Appl. Energy Mater.* **2022**, *5*, 11483-11497.

[92] H. N. Dhandapani, R. Madhu, A. De, M. A. Salem, B. Ramesh Babu, S. Kundu, *Inorg. Chem.* **2023**, *62*, 11817-11828.

[93] D. Guo, J. Xu, G. Liu, X. Yu, in *Molecules, Vol. 29*, **2024**.

[94] R. Alotaibi, M. S. Amer, P. Arunachalam, S. G. Alshammari, in *Catalysts, Vol. 14*, **2024**.

[95] T. M. Pham, M. Plevova, S. Bartling, N. Rockstroh, A. Springer, A. Slabon, J. Hnat, A.-E. Surkus, R. Francke, *J. Catal.* **2024**, *438*, 115675.

[96] R. P. Antony, R. Zerdoumi, S. Saddeler, O. A. Krysiak, L. Banko, A. Ludwig, W. Schuhmann, *ChemCatChem* **2025**, *17*, e202401749.

[97] T. Cheng, F. Wu, C. Chen, X. Zhang, M. Zhang, L. Cui, Y. Dai, B. Hou, Y. Tian, J. Zhu, in *Molecules, Vol. 30*, **2025**.

[98] Z. Han, Y. Zhang, T. Lv, X. Tan, Q. Wang, Y. Wang, C. Meng, *J. Colloid Interface Sci.* **2025**, *682*, 1-10.

[99] J. Liu, H. Sun, L. Wang, Y. Huang, Y. Cao, *J. Alloys Compd.* **2025**, *1013*, 178391.

[100] T. M. Pham, N. Liu, S. Bartling, N. Rockstroh, R. Eckelt, W. Ju, A.-E. Surkus, R. Francke, *J. Catal.* **2025**, 116299.

[101] S. Park, M. Shviro, H. Hartmann, J. Mayer, M. Carmo, D. Stolten, *ACS Appl. Nano Mater.* **2022**, *5*, 4062-4071.

[102] Y. Wang, S. Hao, X. Liu, Q. Wang, Z. Su, L. Lei, X. Zhang, *ACS Appl. Mater. Interfaces* **2020**, *12*, 37006-37012.

[103] M. You, L. Gui, X. Ma, Z. Wang, Y. Xu, J. Zhang, J. Sun, B. He, L. Zhao, *Appl. Catal. B: Environ. Energy* **2021**, *298*, 120562.

[104] Y.-Y. Feng, S. Si, G. Deng, Z.-X. Xu, Z. Pu, H.-S. Hu, C.-B. Wang, *J. Alloys Compd.* **2022**, *892*, 162113.

[105] M. Retuerto, L. Pascual, J. Torrero, M. A. Salam, Á. Tolosana-Moranchel, D. Gianolio, P. Ferrer, P. Kayser, V. Wilke, S. Stiber, V. Celorrio, M. Mokthar, D. G. Sanchez, A. S. Gago, K. A. Friedrich, M. A. Peña, J. A. Alonso, S. Rojas, *Nat. Commun.* **2022**, *13*, 7935.

[106] Z.-Y. Wu, F.-Y. Chen, B. Li, S.-W. Yu, Y. Z. Finfrock, D. M. Meira, Q.-Q. Yan, P. Zhu, M.-X. Chen, T.-W. Song, Z. Yin, H.-W. Liang, S. Zhang, G. Wang, H. Wang, *Nat. Mater.* **2023**, *22*, 100-108.
[107] J. Kwon, S. Sun, S. Choi, K. Lee, S. Jo, K. Park, Y. K. Kim, H. B. Park, H. Y. Park, J. H. Jang, H. Han, U. Paik, T. Song, *Adv. Mater.* **2023**, *35*, 2300091.
[108] H. Liu, Z. Zhang, J. Fang, M. Li, M. G. Sendeku, X. Wang, H. Wu, Y. Li, J. Ge, Z. Zhuang, D. Zhou, Y. Kuang, X. Sun, *Joule* **2023**, *7*, 558-573.
[109] Y. Zhang, J. Dong, T. Sun, X. Zhang, J. Chen, L. Xu, *Small* **2024**, *20*, 2305889.
[110] K. Qin, H. Yu, W. Zhu, Y. Zhou, Z. Guo, Q. Shao, Y. Wu, X. Wang, Y. Li, Y. Ji, F. Liao, Y. Liu, Z. Kang, M. Shao, *Adv. Funct. Mater.* **2024**, *n/a*, 2402226.
[111] J. Kang, S. Möhle, X. Wang, M. M. Kovács, K. N. N. Nasralla, J. Schmidt, S. Selve, D. Dworschak, P. Strasser, *Adv. Energy Mater.* **2025**, *n/a*, 2405758.
[112] N. Du, C. Roy, R. Peach, M. Turnbull, S. Thiele, C. Bock, *Chem. Rev.* **2022**, *122*, 11830-11895.
[113] S. Shiva Kumar, H. Lim, *Energy Reports* **2022**, *8*, 13793-13813.
[114] Q. Xu, L. Zhang, J. Zhang, J. Wang, Y. Hu, H. Jiang, C. Li, *EnergyChem* **2022**, *4*, 100087.
[115] a) S. Kamali, M. Zhiani, H. Tavakol, *Renew. Energy* **2020**, *154*, 1122-1131; b) I. Vincent, E.-C. Lee, H.-M. Kim, *RSC Adv.* **2020**, *10*, 37429-37438; c) A. Shahroudi, M. Esfandiari, S. Habibzadeh, *RSC Adv.* **2022**, *12*, 29440-29468; d) Y. Zhang, Y. Jiang, A. Abdukayum, X. Xie, S. Gao, X. Liu, L. Zhang, Q. Liu, G. Hu, *Mater. Today Energy* **2024**, *44*, 101641; e) W.-F. Chen, K. Sasaki, C. Ma, A. I. Frenkel, N. Marinkovic, J. T. Muckerman, Y. Zhu, R. R. Adzic, *Angew. Chem. Int. Ed.* **2012**, *51*, 6131-6135.
[116] E. Cossar, F. Murphy, E. A. Baranova, *J. Chem. Technol. Biotechnol.* **2022**, *97*, 1611-1624.
[117] a) E. Cossar, A. Oyarce Barnett, F. Seland, E. A. Baranova, *Catalysts, Vol. 9*, **2019**; b) Y. Han, J. Wang, Y. Liu, T. Li, T. Wang, X. Li, X. Ye, G. Li, J. Li, W. Hu, Y. Deng, *Carbon neutraliz.* **2024**, *3*, 172-198.
[118] a) A. W. Tricker, J. K. Lee, J. R. Shin, N. Danilovic, A. Z. Weber, X. Peng, *J. Power Sources* **2023**, *567*, 232967; b) C.-Y. Kwon, J.-Y. Jeong, J. Yang, Y. S. Park, J. Jeong, H. Park, Y. Kim, S. M. Choi, *Front. Chem.* **2020**, *Volume 8 - 2020*; c) M. J. Jang, J. Yang, J. Lee, Y. S. Park, J. Jeong, S. M. Park, J.-Y. Jeong, Y. Yin, M.-H. Seo, S. M. Choi, K. H. Lee, *J. Mater. Chem. A* **2020**, *8*, 4290-4299.
[119] S. Anantharaj, S. Kundu, S. Noda, *Nano Energy* **2021**, *80*, 105514.
[120] K. W. Ahmed, S. Habibpour, Z. Chen, M. Fowler, *J. Energy Storage* **2024**, *79*, 110149.
[121] J. R. Varcoe, P. Atanassov, D. R. Dekel, A. M. Herring, M. A. Hickner, P. A. Kohl, A. R. Kucernak, W. E. Mustain, K. Nijmeijer, K. Scott, T. Xu, L. Zhuang, *Energy Environ. Sci.* **2014**, *7*, 3135-3191.
[122] J. R. Varcoe, R. C. T. Slade, *Fuel Cells* **2005**, *5*, 187-200.
[123] S. A. Grigoriev, V. N. Fateev, D. G. Bessarabov, P. Millet, *Int. J. Hydrogen Energy* **2020**, *45*, 26036-26058.
[124] a) H. Ju, S. Badwal, S. Giddey, *Appl. Energy* **2018**, *231*, 502-533; b) W. Xu, K. Scott, *Int. J. Hydrogen Energy* **2010**, *35*, 12029-12037.
[125] A. Gupta, Y. M. Chellehbari, S. Shahgaldi, *J. Power Sources* **2025**, *630*, 236088.
[126] P. von Tettau, P. Thiele, P. Mauermann, M. Wick, S. Tinz, S. Pischinger, *J. Power Sources* **2025**, *630*, 236104.
[127] a) S. E. Fenton, A. Ducatman, A. Boobis, J. C. DeWitt, C. Lau, C. Ng, J. S. Smith, S. M. Roberts, *Environ. Toxicol. Chem.* **2021**, *40*, 606-630; b) R. Dhore, G. S. Murthy, *Bioresour Technol* **2021**, *341*, 125808.
[128] X. Lim, *Nature* **2023**, *620*, 24-27.
[129] I. Vincent, D. Bessarabov, *Renew. Sustain. Energy Rev.* **2018**, *81*, 1690-1704.
[130] a) S. E. Hosseini, M. A. Wahid, *Int. J. Energy Res.* **2020**, *44*, 4110-4131; b) M. Benghanem, A. Mellit, H. Almohamadi, S. Haddad, N. Chettibi, A. M. Alanazi, D. Dasalla, A. Alzahrani, in *Energies, Vol. 16*, **2023**.
[131] A. Hauch, R. Küngas, P. Blennow, A. B. Hansen, J. B. Hansen, B. V. Mathiesen, M. B. Mogensen, *Science* **2020**, *370*, eaba6118.

[132] a) A. Brisse, J. Schefold, M. Zahid, *Int. J. Hydrogen Energy* **2008**, *33*, 5375-5382; b) M. A. Laguna-Bercero, *J. Power Sources* **2012**, *203*, 4-16.
[133] A. Nechache, S. Hody, *Renew. Sustain. Energy Rev.* **2021**, *149*, 111322.
[134] F. Tietz, D. Sebold, A. Brisse, J. Schefold, *J. Power Sources* **2013**, *223*, 129-135.
[135] S. C. Peter, *ACS Energy Lett.* **2018**, *3*, 1557-1561.
[136] a) S. Garg, M. Li, A. Z. Weber, L. Ge, L. Li, V. Rudolph, G. Wang, T. E. Rufford, *J. Mater. Chem. A* **2020**, *8*, 1511-1544; b) O. G. Sánchez, Y. Y. Birdja, M. Bulut, J. Vaes, T. Breugelmans, D. Pant, *Curr. Opin. Green Sustain. Chem.* **2019**, *16*, 47-56; c) G. Leonzio, A. Hankin, N. Shah, *Chem. Eng. Res. Des.* **2024**, *208*, 934-955; d) K. Wiranarongkorn, K. Eamsiri, Y.-S. Chen, A. Arpornwichanop, *J. CO2 Util.* **2023**, *71*, 102477.
[137] a) J. Qiao, Y. Liu, F. Hong, J. Zhang, *Chem. Soc. Rev.* **2014**, *43*, 631-675; b) K. P. Kuhl, E. R. Cave, D. N. Abram, T. F. Jaramillo, *Energy Environ. Sci.* **2012**, *5*, 7050-7059; c) K. P. Kuhl, T. Hatsukade, E. R. Cave, D. N. Abram, J. Kibsgaard, T. F. Jaramillo, *J. Am. Chem. Soc.* **2014**, *136*, 14107-14113.
[138] R. Francke, B. Schille, M. Roemelt, *Chem. Rev.* **2018**, *118*, 4631-4701.
[139] S. Zhang, Q. Fan, R. Xia, T. J. Meyer, *Acc. Chem. Res.* **2020**, *53*, 255-264.
[140] a) C. M. Bolinger, N. Story, B. P. Sullivan, T. J. Meyer, *Inorg. Chem.* **1988**, *27*, 4582-4587; b) P. Kang, C. Cheng, Z. Chen, C. K. Schauer, T. J. Meyer, M. Brookhart, *J. Am. Chem. Soc.* **2012**, *134*, 5500-5503; c) Z. Chen, C. Chen, D. R. Weinberg, P. Kang, J. J. Concepcion, D. P. Harrison, M. S. Brookhart, T. J. Meyer, *Chem. Commun.* **2011**, *47*, 12607-12609; d) M. R. M. Bruce, E. Megehee, B. P. Sullivan, H. Thorp, T. R. O'Toole, A. Downard, T. J. Meyer, *Organometallics* **1988**, *7*, 238-240.
[141] a) C. Liu, T. R. Cundari, A. K. Wilson, *J. Phys. Chem. C* **2012**, *116*, 5681-5688; b) M. Abdinejad, M. N. Hossain, H.-B. Kraatz, *RSC Adv.* **2020**, *10*, 38013-38023.
[142] C. Yang, Y. Wang, L. Qian, A. M. Al-Enizi, L. Zhang, G. Zheng, *ACS Appl. Energy Mater.* **2021**, *4*, 1034-1044.
[143] a) C. Choi, S. Kwon, T. Cheng, M. Xu, P. Tieu, C. Lee, J. Cai, H. M. Lee, X. Pan, X. Duan, W. A. Goddard, Y. Huang, *Nat. Catal.* **2020**, *3*, 804-812; b) F. Pan, Y. Yang, *Energy Environ. Sci.* **2020**, *13*, 2275-2309; c) J. Yu, J. Wang, Y. Ma, J. Zhou, Y. Wang, P. Lu, J. Yin, R. Ye, Z. Zhu, Z. Fan, *Adv. Funct. Mater.* **2021**, *31*, 2102151.
[144] J. Yan, W. Song, Z. Zhao, M. Zhang, Y. Wu, L. Zhang, *Int. J. Hydrogen Energy* **2024**, *89*, 664-685.
[145] a) J. Durst, A. Rudnev, A. Dutta, Y. Fu, J. Herranz, V. Kaliginedi, A. Kuzume, A. A. Permyakova, Y. Paratcha, P. Broekmann, T. J. Schmidt, *Chimia (Aarau)* **2015**, *69*, 769-776; b) C. W. Li, M. W. Kanan, *J. Am. Chem. Soc.* **2012**, *134*, 7231-7234; c) C. T. Dinh, T. Burdyny, M. G. Kibria, A. Seifitokaldani, C. M. Gabardo, F. P. García de Arquer, A. Kiani, J. P. Edwards, P. De Luna, O. S. Bushuyev, C. Zou, R. Quintero-Bermudez, Y. Pang, D. Sinton, E. H. Sargent, *Science* **2018**, *360*, 783-787.
[146] D. Gao, R. M. Arán-Ais, H. S. Jeon, B. Roldan Cuenya, *Nat. Catal.* **2019**, *2*, 198-210.
[147] M. S. Hussain, S. Ahmed, M. Irshad, S. S. Bibi, M. Asif, F. Sher, M. K. Khan, *Nano Mater. Sci.* **2024**.
[148] D. Higgins, A. T. Landers, Y. Ji, S. Nitopi, C. G. Morales-Guio, L. Wang, K. Chan, C. Hahn, T. F. Jaramillo, *ACS Energy Lett.* **2018**, *3*, 2947-2955.
[149] C. Gao, J. Low, R. Long, T. Kong, J. Zhu, Y. Xiong, *Chem. Rev.* **2020**, *120*, 12175-12216.
[150] H. Jeong, S. Shin, H. Lee, *ACS Nano* **2020**, *14*, 14355-14374.
[151] D. Bhalothia, A. Beniwal, P. Kumar Saravanan, P.-C. Chen, T.-Y. Chen, *ChemElectroChem* **2024**, *11*, e202400034.
[152] L. Sun, V. Reddu, A. C. Fisher, X. Wang, *Energy Environ. Sci.* **2020**, *13*, 374-403.
[153] a) K. Kim, P. Wagner, K. Wagner, A. J. Mozer, *Energy amp; Fuels* **2022**, *36*, 4653-4676; b) N. Liu, S. Bartling, A. Springer, C. Kubis, O. S. Bokareva, E. Salaya, J. Sun, Z. Zhang, S. Wohlrab, A. M. Abdel-Mageed, H.-Q. Liang, R. Francke, *Adv. Mater.* **2024**, *36*, 2309526.

[154] S. Nitopi, E. Bertheussen, S. B. Scott, X. Liu, A. K. Engstfeld, S. Horch, B. Seger, I. E. L. Stephens, K. Chan, C. Hahn, J. K. Nørskov, T. F. Jaramillo, I. Chorkendorff, *Chem. Rev.* **2019**, *119*, 7610-7672.
[155] N. Liu, W. Ju, R. Francke, *Curr. Opin. Electrochem.* **2025**, *49*, 101598.
[156] L.-X. Liu, C. Qin, T. Deng, L. Sun, Z. Chen, X. Han, *J. Mater. Chem. A* **2024**, *12*, 26421-26438.
[157] O. Ogunbanjo, P. Rodríguez, P. Anderson, *Mater. Chem. Front.* **2025**, *9*, 1650-1680.
[158] P. Malhotra, *Analytical Chemistry: Basic Techniques and Methods* (Ed.: P. Malhotra), Springer International Publishing, Cham, **2023**, pp. 131-160.
[159] M. Wang, Z. Feng, *Chem. Commun.* **2021**, *57*, 10453-10468.
[160] E. Bartosińska, P. Kozlík, A. Kubíčková, J. Heřt, J. Fischer, T. Křížek, *Talanta* **2021**, *226*, 122141.
[161] H. Shin, J. M. Yoo, Y.-E. Sung, D. Y. Chung, *JACS Au* **2022**, *2*, 2222-2234.
[162] in *Fundamentals of Electroanalytical Chemistry*, **2001**, pp. 131-194.
[163] a) Y. Uchida, E. Kätelhön, R. G. Compton, *J. Electroanal. Chem.* **2018**, *823*, 465-473; b) N. Leslie, J. Mauzeroll, *Encyclopedia of Solid-Liquid Interfaces (First Edition)* (Eds.: K. Wandelt, G. Bussetti), Elsevier, Oxford, **2024**, pp. 461-478.
[164] E. J. F. Dickinson, A. J. Wain, *J. Electroanal. Chem.* **2020**, *872*, 114145.
[165] J. C. Myland, K. B. Oldham, *Electrochem. Commun.* **2004**, *6*, 344-350.
[166] *Fundamentals of Electroanalytical Chemistry*, **2001**, pp. 195-236.
[167] J. J. Jarju, M. C. Figueiredo, Y. V. Kolen'ko, *Frontiers of Nanoscience, Vol. 18* (Eds.: A. J. Wain, E. J. F. Dickinson), Elsevier, **2021**, pp. 343-420.
[168] H. Chen, E. Kätelhön, R. G. Compton, *Anal. Chem.* **2023**, *95*, 12826-12834.
[169] M. Fathi Tovini, A. Hartig-Weiß, H. A. Gasteiger, H. A. El-Sayed, *J. Electrochem. Soc.* **2021**, *168*, 014512.
[170] a) S. Wang, J. Zhang, O. Gharbi, V. Vivier, M. Gao, M. E. Orazem, *Nat Rev Methods Primers* **2021**, *1*, 41; b) *Electrochemical Impedance Spectroscopy*, **2017**, pp. 89-127.
[171] J. R. Macdonald, W. B. Johnson, *Impedance Spectroscopy*, **2018**, pp. 1-20.
[172] Z. Lukács, T. Kristóf, *Electrochim. Acta* **2020**, *363*, 137199.
[173] M. Gaberšček, *Curr. Opin. Electrochem.* **2022**, *32*, 100917.
[174] a) Y. Lu, W. Wang, F. Xie, *J. Electroanal. Chem.* **2020**, *871*, 114281; b) A. Sacco, *J. CO2 Util.* **2018**, *27*, 22-31.
[175] a) M. C. H. McKubre, D. D. Macdonald, B. Sayers, J. R. Macdonald, *Impedance Spectroscopy*, **2018**, pp. 107-174; b) N. Bonanos, B. C. H. Steele, E. P. Butler, J. R. Macdonald, W. B. Johnson, W. L. Worrell, G. A. Niklasson, S. Malmgren, M. Strømme, S. K. Sundaram, M. C. H. McKubre, D. D. Macdonald, G. R. Engelhardt, E. Barsoukov, B. E. Conway, W. G. Pell, N. Wagner, C. M. Roland, R. S. Eisenberg, *Impedance Spectroscopy*, **2018**, pp. 175-478.
[176] H. A. El-Sayed, A. Weiß, L. F. Olbrich, G. P. Putro, H. A. Gasteiger, *J. Am. Chem. Soc.* **2019**, *166*, F458.
[177] A. R. Woldu, A. H. Shah, H. Hu, D. Cahen, X. Zhang, T. He, *Int. J. Energy Res.* **2020**, *44*, 548-559.
[178] J. Costard, M. Ender, M. Weiss, E. Ivers-Tiffée, *J. Electrochem. Soc.* **2017**, *164*, A80.
[179] C. Du, Q. Tan, G. Yin, J. Zhang, *Rotating Electrode Methods and Oxygen Reduction Electrocatalysts* (Eds.: W. Xing, G. Yin, J. Zhang), Elsevier, Amsterdam, **2014**, pp. 171-198.
[180] M. F. Tesch, S. Neugebauer, P. V. Narangoda, R. Schlögl, A. K. Mechler, *Energy Adv.* **2023**, *2*, 1823-1830.
[181] J. Lodh, S. Paul, H. Sun, L. Song, W. Schöfberger, S. Roy, *Front. Chem.* **2023**, *10 - 2022*.
[182] S. Katipamula, N. M. White, K. M. Waldie, *Chem Catalysis* **2023**, *3*, 100561.
[183] a) D. Cheng, H. H. Ngo, W. Guo, S. W. Chang, D. D. Nguyen, S. Zhang, S. Deng, D. An, N. B. Hoang, *Bioresour. Technol.* **2022**, *346*, 126588; b) C. Ampelli, F. Tavella, D. Giusi, A. M. Ronsisvalle, S. Perathoner, G. Centi, *Catal. Today* **2023**, *421*, 114217.
[184] B. Martindale, *Nat. Catal.* **2020**, *3*, 966-966.

[185] G. Sakas, A. Ibáñez-Rioja, S. Pöyhönen, A. Kosonen, V. Ruuskanen, P. Kauranen, J. Ahola, *Renew. Energy* **2024**, *225*, 120266.
[186] L. Ge, H. Rabiee, M. Li, S. Subramanian, Y. Zheng, J. H. Lee, T. Burdyny, H. Wang, *Chem* **2022**, *8*, 663-692.
[187] T. Stracensky, H. Xu, *Electrochem. Soc. Interface* **2024**, *33*, 55.
[188] A. Higareda, D. L. Hernández-Arellano, L. C. Ordoñez, R. Barbosa, N. Alonso-Vante, *Catalysts* **2023**, *13*, 1346.
[189] a) S. S. Kalanur, I.-H. Yoo, I.-S. Cho, H. Seo, *Electrochim. Acta* **2019**, *296*, 517-527; b) J. Yao, D. Xu, X. Ma, J. Xiao, M. Zhang, H. Gao, *J. Power Sources* **2022**, *524*, 231068; c) K. Zhu, F. Shi, X. Zhu, W. Yang, *Nano Energy* **2020**, *73*, 104761.
[190] M. Görlin, J. Ferreira de Araújo, H. Schmies, D. Bernsmeier, S. Dresp, M. Gliech, Z. Jusys, P. Chernev, R. Kraehnert, H. Dau, P. Strasser, *J. Am. Chem. Soc.* **2017**, *139*, 2070-2082.
[191] a) Q. Chen, A. Kube, D. Kopljar, K. A. Friedrich, *ACS Energy Letters* **2024**, *9*, 6096-6103; b) S. Dierickx, A. Weber, E. Ivers-Tiffée, *Electrochim. Acta* **2020**, *355*, 136764; c) S. W. Lee, T. H. Nam, S. H. Lee, T. Ishihara, J. T. S. Irvine, T. H. Shin, *Energy Environ. Sci.* **2025**, *18*, 1205-1213.
[192] T. H. Wan, M. Saccoccio, C. Chen, F. Ciucci, *Electrochim. Acta* **2015**, *184*, 483-499.
[193] a) M. R. Singh, Y. Kwon, Y. Lum, J. W. Ager, III, A. T. Bell, *J. Am. Chem. Soc.* **2016**, *138*, 13006-13012; b) J. Resasco, L. D. Chen, E. Clark, C. Tsai, C. Hahn, T. F. Jaramillo, K. Chan, A. T. Bell, *J. Am. Chem. Soc.* **2017**, *139*, 11277-11287; c) S. Ringe, E. L. Clark, J. Resasco, A. Walton, B. Seger, A. T. Bell, K. Chan, *Energy Environ. Sci.* **2019**, *12*, 3001-3014; d) L. D. Chen, M. Urushihara, K. Chan, J. K. Nørskov, *ACS Catalysis* **2016**, *6*, 7133-7139; e) M. C. O. Monteiro, F. Dattila, B. Hagedoorn, R. García-Muelas, N. López, M. T. M. Koper, *Nat. Catal.* **2021**, *4*, 654-662.

Appendix

Appendix 1. Publications of This Work

The following publications form the basis for this cumulative thesis. Additional publications are listed in the appendix.

I. T.M. Pham, M. Plevova, S. Bartling, N. Rockstroh, A. Springer, A. Slabon, J. Hnat, A.-E. Surkus, R. Francke, Oxygen-deficient annealing boosts performance of CoNiFe oxide electrocatalyst in oxygen evolution reaction, *J. Catal.*, 438 (**2024**) 115675. DOI: 10.1016/j.jcat.2024.115675

II. T.M. Pham, N. Liu, S. Bartling, N. Rockstroh, R. Eckelt, W. Ju, A.-E. Surkus, R. Francke, Pre-treated carbon additive enables reduction of metal loading in CoNiFe oxide-based OER electrocatalysts while maintaining performance, *J. Catal.*, 450 (**2025**) 116299. DOI: 10.1016/j.jcat.2025.116299

III. N. Liu, T.M. Pham, Y. Han, O.S. Bokareva, S. Bartling, A. Springer, A. Spannenberg, C. Kubis, J. Weiss, D.E. Doronkin, W. Ju, R. Francke, Heterogenized Copper(II) Phenanthroline Catalysts for Electroreduction of CO2 to C2 Compounds: Substitution on the Ligand Causes Structural Changes to the Molecular Framework and Stability Enhancement, *Adv. Mater.*, n/a (**2025**) e13702. DOI: 10.1002/adma.202513702

Publication 1

Oxygen-deficient annealing boosts performance of CoNiFe oxide electrocatalyst in oxygen evolution reaction

Trang Minh Pham, Michaela Plevova, Stephan Bartling, Nils Rockstroh, Armin Springer, Adam Slabon, Jaromir Hnat*, Annette-Enrica Surkus*, Robert Francke*.

DOI: 10.1016/j.jcat.2024.115675

Abstract: Mixed oxides of transition metals have emerged as promising catalysts for the oxygen evolution (OER) reaction in alkaline water electrolysis. Since OER is significantly slower than hydrogen evolution, developing stable and easily accessible materials that effectively promote OER is one of the keys to improving overall efficiency. In this context, we present a promising method for preparing Co-Ni-Fe oxides which is based on a straightforward sol-gel procedure. Key to success is a thermal treatment under oxygen-deficient atmosphere, which renders superior electrocatalytic properties compared to a treatment under reductive and aerobic conditions, respectively. Attractive performance characteristics are thereby obtained, *e.g.*, a η_{10} value of 291 mV and a Tafel slope of 32 mV dec^{-1}. The impact of the annealing conditions on the material properties has been elaborated using cyclic voltammetry, impedance spectroscopy, and structural analyses. Stability and strong performance under practical conditions was confirmed in long-term studies using an AEM electrolyzer.

Author contribution: I planned and performed experimental works, including synthesis, optimization of catalysts as well as electrochemical measurements. In addition, I evaluated all analytical data, wrote the first draft of the manuscript and supporting information. My contribution approximately amounts to 75%.

Signature of the student

(Trang Minh Pham)

Signature of the supervisor

(Prof. Dr. Robert Francke)

Journal of Catalysis 438 (2024) 115675

Contents lists available at ScienceDirect

Journal of Catalysis

journal homepage: www.elsevier.com/locate/jcat

Research article

Oxygen-deficient annealing boosts performance of CoNiFe oxide electrocatalyst in oxygen evolution reaction

Trang Minh Pham [a], Michaela Plevova [b], Stephan Bartling [a], Nils Rockstroh [a], Armin Springer [c], Adam Slabon [d,e], Jaromir Hnat [b,*], Annette-Enrica Surkus [a,*], Robert Francke [a,*]

[a] Leibniz Institute for Catalysis, Albert-Einstein-Straße 29a, Rostock 18059, Germany
[b] University of Chemistry and Technology Prague, Technická 5, Prague 16628, Czechia
[c] Medical Biology and Electron Microscopy Center, University Medical Center Rostock, Strempelstraße 14, Rostock 18057, Germany
[d] Chair of Inorganic Chemistry, University of Wuppertal, Gaußstraße 20, Wuppertal 42119, Germany
[e] Wuppertal Center for Smart Materials & Systems, University of Wuppertal, Rainer-Gruenter-Straße 21, Wuppertal 42119, Germany

ARTICLE INFO

Keywords:
Alkaline water electrolysis
Oxygen evolution reaction
Electrocatalyst
Cobalt
Nickel
Iron
Oxygen vacancy

ABSTRACT

Mixed oxides of transition metals have emerged as promising catalysts for the oxygen evolution (OER) reaction in alkaline water electrolysis. Since OER is significantly slower than hydrogen evolution, developing stable and easily accessible materials that effectively promote OER is one of the keys to improving overall efficiency. In this context, we present a promising method for preparing Co-Ni-Fe oxides which is based on a straightforward sol–gel procedure. Key to success is a thermal treatment under oxygen-deficient atmosphere, which renders superior electrocatalytic properties compared to a treatment under reductive and aerobic conditions, respectively. Attractive performance characteristics are thereby obtained, *e.g.*, a η_{10} value of 291 mV and a Tafel slope of 32 mV dec^{-1}. The impact of the annealing conditions on the material properties has been elaborated using cyclic voltammetry, impedance spectroscopy, and structural analyses. Stability and strong performance under practical conditions were confirmed in long-term studies using an AEM electrolyzer.

1. Introduction

The production of green hydrogen through water electrolysis using electricity generated from renewable sources is one of the most promising strategies toward achieving a carbon–neutral economy [1–3]. Water electrolysis represents an effective and well-established water splitting process consisting of two half-cell reactions, the cathodic hydrogen evolution reaction (HER) and the anodic oxygen evolution reaction (OER). Although hydrogen is the product of interest, considerable efforts are devoted to the development of OER catalysts. This can be attributed primarily to the fact that the four-electron process is much slower than HER and can therefore be considered as the bottleneck of the water splitting process [4–6]. Hence, the development of electrocatalysts that effectively promote OER, resulting in low overpotential, high current density, high mass activity, and excellent stability is one of the keys to further improve the overall efficiency of water electrolysis [7,8].

Compared to the widely used PEM water electrolysis, electrochemical H_2 production under alkaline conditions represents a promising alternative [9–13]. This is mainly due to the fact that instead of expensive metals such as Ir and Ru, earth-abundant alternatives such as Co, Ni, Fe, and Mn can be used as anodic electrocatalysts [14–18]. These metals have been employed as oxides or oxyhydroxides [19–21], chalcogenides [22–25], and phosphides [26,27]. Among these catalytic systems, mixed oxides of Ni, Co, and Fe (in particular $CoFeO_x$, $FeNiO_x$, and $CoFeNiO_x$) show outstanding performance for OER [28]. The remarkable catalytic properties have been ascribed to the volcano-type dependence of the activity from the binding energies between catalysts and oxygen intermediates, wherein mixed oxides of Co, Ni, and Fe are located near the top of the volcano curve [29–31]. Consequently, these materials have been continuously studied over the past decade [17,28,32–35]. In these studies, the mixed oxides often exhibit low overpotentials (290–400 mV) during electrolysis at 10 mA cm_{geo}^{-2} in 1 M KOH or NaOH. The activity can often be further enhanced by introduction of oxygen vacancies, which has been achieved by various methods such as partial chemical reduction under wet-chemical conditions, thermal annealing under reducing atmosphere, cation/anion doping, plasma treatment, and laser ablation [36,37]. However, despite

* Corresponding authors.
E-mail addresses: jaromir.hnat@vscht.cz (J. Hnat), annette-enrica.surkus@catalysis.de (A.-E. Surkus), robert.francke@catalysis.de (R. Francke).

https://doi.org/10.1016/j.jcat.2024.115675
Received 5 April 2024; Received in revised form 18 July 2024; Accepted 25 July 2024
Available online 26 July 2024

all advances made, poor electrical conductivity and limited long-term stability still represent major challenges for the development of truly efficient electrocatalysts for alkaline OER [7–13].

In the present work, a synthetic protocol is disclosed, which involves a thermal treatment of a precursor material under oxygen-deficient conditions. The resulting CoNiFe oxide catalysts exhibit substantially increased OER activity. A comparison between mixed metal oxides with various compositions revealed that the catalyst precursor with a molar Co:Ni:Fe ratio of 2:2:1 renders the best results in 1 M KOH when analyzed with rotating disc electrode measurements [17]. Under these conditions, an overpotential (η) of merely 291 mV at 10 mA cm_{geo}^{-2}, a small Tafel slope of 32 mV dec^{-1}, and excellent stability for at least 50 h at 100 mA cm_{geo}^{-2} were achieved. The material with the optimum metal ratio was further tested in an AEM electrolyzer under galvanostatic conditions, where it showed stable performance for ~ 75 h at 400 mA cm_{geo}^{-2}. The study indicates a path towards improving OER activity by using CoNiFe oxides with a well-balanced oxygen content and metal ratio.

2. Results and discussion

2.1. Synthesis and materials characterization

The mixed metal oxides investigated in this study were synthesized from the corresponding nitrate salts in the presence of citric acid using a sol–gel approach, followed by thermal treatment at 300 °C. Tuning of the structural properties was achieved by varying the metal ratio and the oxygen content of the annealing atmospheres during thermal treatment, whereby an oxygen-rich (A; air), an oxygen-deficient (M; 1 vol% air in argon), and a reducing (H; 5 vol% H_2 in argon) atmosphere, respectively, were applied (for details, see the Experimental Section and Table S1 in the SI). In the following, the mixed metal oxides are abbreviated as CoNiFe (*x*:*y*:*z*), with *x*:*y*:*z* as the respective stoichiometric ratio between the metals. To indicate the conditions of the thermal treatment, the letters A, M or H are added to the abbreviation (*e.g.*, CoNiFe (2:2:1)/M).

For structural characterization of the as-prepared materials, powder X-ray diffraction (PXRD), X-ray photoelectron spectroscopy (XPS), scanning electron microscopy (SEM), energy dispersive X-ray spectroscopy (EDX), scanning transmission electron microscopy (STEM), and electron energy loss spectroscopy (EELS) were performed. As shown exemplarily in Fig. 1a, XRD patterns of CoNiFe (2:2:1)/M, CoNiFe (2:2:1)/H, and CoNiFe (2:2:1)/A clearly differ from each other, although these materials have the same Co:Ni:Fe ratio. CoNiFe (2:2:1)/A, the sample that was thermally treated under air, exhibits a highly crystalline character, with relatively sharp reflection peaks at 14.0°, 16.5°, 19.9°, 26.0° and 28.4° that align well with the (220), (222), (400), (422) and (511) planes of Fe_3O_4 (magnetite) and Co_3O_4 (for details, see Fig. S1). In contrast, the PXRD pattern does not show any reflection peaks in the case of CoNiFe (2:2:1)/H, the sample pyrolyzed under H_2 (5 vol% H_2 in Ar), indicating an amorphous structure. The structure of CoNiFe (2:2:1)/M, the material treated under oxygen-deficient atmosphere, can be classified between amorphous and crystalline, with broad reflection peaks at 16.3°, 19.1°, and 27.3° that correspond well with the (111), (200), and (220) planes of CoO, NiO, and FeO.

The recorded XP spectra provide valuable information on the elemental composition on the sample surfaces and valence states of the CoNiFe (2:2:1) series. The rather complex system as well as the strong overlap of photoelectron lines and Auger peaks complicate a convincing deconvolution of the obtained spectra so that only a qualitive analysis is given here. For CoNiFe (2:2:1)/M, CoNiFe (2:2:1)/H, and CoNiFe (2:2:1)/A, the Co 2p and O 1s regions are shown exemplarily in Fig. 1b and 1c, while the results of the Ni 2p and Fe 2p regions are listed in Fig. S3 and Table S4. The Co 2p region of all CoNiFe (2:2:1) samples

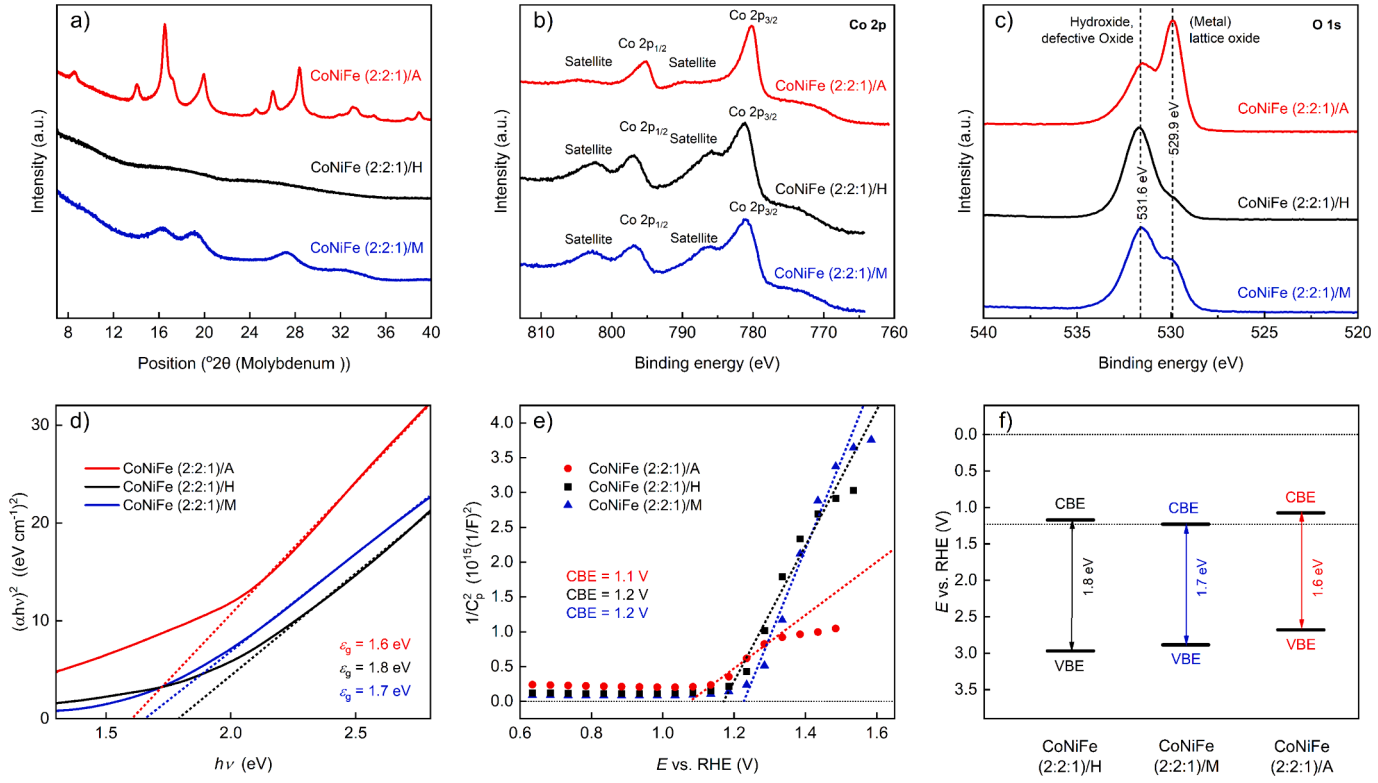

Fig. 1. Structural characterization of CoNiFe (2:2:1)/M, CoNiFe (2:2:1)/H, and CoNiFe (2:2:1)/A. (a) Powder X-ray diffraction patterns. (b), (c) XP spectra (Co 2p and O 1s). (d) Estimation of optical band gaps (ε_g) from Tauc plots (direct allowed transition). (e) Mott-Schottky plots (frequency: 1500 Hz). The positive slopes indicate that all three materials are n-type semiconductors, *i.e.* the V_{FB} value represents in the Mott-Schottky approximation the corresponding conducting band edge (CBE). (f) Energy schemes of CoNiFe oxide materials constructed from the estimated ε_g values and conducting band edges (CBE).

contains two main peaks associated with Co $2p_{3/2}$ and Co $2p_{1/2}$ orbitals, and two main satellite peaks each. The shoulders at lower binding energies are probably caused by Auger peaks of Fe and Ni which are present in this region. CoNiFe (2:2:1)/M and CoNiFe (2:2:1)/H exhibit the Co $2p_{3/2}$ peak at 781.1 eV and 781.2 eV, respectively. Together with the pronounced satellite features, this suggests the presence of Co^{2+} as CoO or $Co(OH)_2$. In contrast, the Co $2p_{3/2}$ peak is slightly shifted to a lower binding energy (780.2 eV) in CoNiFe (2:2:1)/A and only very weak satellite features can be observed, thus clearly suggesting the formation of higher oxidation states such as observed for Co_3O_4 [38], which is also in agreement with XRD and STEM-EELS results. In general, the observed Co 2p binding energies are slightly shifted to higher values compared to the literature reference of monometallic oxides. This might be caused by the interaction with other elements present such as Ni and Fe. Only minor differences in the Ni 2p (mainly Ni^{2+}) and Fe 2p spectra of the three samples can be found and will be discussed in detail in the SI.

The high-resolution scans of the O 1s regions for all three samples (Fig. 1c) show two peaks with binding energies of 529.9 eV and 531.6 eV, respectively, corresponding to lattice metal–oxygen ($M-O_x$) and to metal hydroxides/defective oxides, respectively [39,40]. For sample CoNiFe (2:2:1)/M, both peaks are pronounced, while the intensity of the metal hydroxides/defective oxides peak is higher. In contrast, CoNiFe (2:2:1)/H exhibits only a very small signal for lattice oxygen, while the hydroxide/defective oxide signal is very strong. This result is not surprising and reflects the anaerobic conditions of the thermal treatment. For CoNiFe (2:2:1)/A, on the other hand, the peak ratio is inverted in favor of lattice oxygen, which can be ascribed to the aerobic thermal treatment. In principle, the ratio between the signal intensities can be considered as an indicator for the relative amount of surface oxygen vacancies, whereby a higher hydroxide / lattice oxide ratio reflects a larger density of surface oxygen vacancies [41,42].

SEM analysis of the as-prepared powder samples of the CoNiFe (2:2:1) series shows that all three mixed metal oxides exist as microparticles without significant morphological differences despite the distinct thermal treatment conditions (Fig. S4-S6). EDX mapping indicates that Co, Ni, Fe, and O are uniformly distributed on the material surface. A more detailed examination using STEM coupled to EDX and EELS reveals significant structural differences between the materials (Fig. S7-S12). In agreement with the results of SEM analysis, a uniform distribution of Co, Ni, and Fe with only minor variations in their ratio was observed for CoNiFe (2:2:1)/A and CoNiFe (2:2:1)/M (for the latter material, STEM images are shown exemplarily in Fig. 2). In contrast, CoNiFe (2:2:1)/H exhibits nanodomains on the bulk, which are enriched with metallic Ni (Fig. S7 and S8) according to EELS and EDX. Further differences between the three samples became apparent upon detailed EELS analysis. Taken together, the respective EEL spectra (Fe, Co, and Ni L edge, O K edge) reflect the different preparation procedures of CoNiFe (2:2:1) well, showing a material with completely oxidized metals in CoNiFe (2:2:1)/A, the presence of metallic Ni in CoNiFe (2:2:1)/H and the presence of non-oxidic Ni and Co in the case of CoNiFe (2:2:1)/M in agreement with XPS analysis. A more detailed discussion of the EELS results is provided in the SI.

The electronic band energy diagrams, including the corresponding conduction band edge (CBE) and valence band edge (VBE), for the prepared catalysts were elucidated based on combined UV–Vis (Fig. S13) and Mott-Schottky analyses [43,44]. The corresponding Tauc plots were constructed for the electronic band gap estimation (Fig. 1d). The band gaps vary significantly with values of 1.7, 1.8, and 1.6 eV for CoNiFe (2:2:1)/M, CoNiFe (2:2:1)/H, and CoNiFe (2:2:1)/A, respectively. Mott-Schottky analysis was performed in 0.5 M Na_2SO_4 aqueous electrolyte (Fig. 1e, S14a-c) to estimate the flat band potentials (V_{FB}). For all samples, the positive slopes indicate n-type semiconducting behavior with V_{FB} values, which were obtained by extrapolation of the curves, of 1.23, 1.17, and 1.07 V vs. RHE for CoNiFe (2:2:1)/M, CoNiFe (2:2:1)/H, and CoNiFe (2:2:1)/A, respectively. Since all materials are n-type semiconductors, these V_{FB} values represent the corresponding CBEs in the Mott-Schottky approximation (Fig. 1f). The shift of the V_{FB}, as a consequence of different atmosphere during annealing, is generally known for semiconducting materials and confirms the influence on the physical properties of the prepared materials [45–47].

2.2. OER activity evaluation

The electrocatalytic performance of CoNiFe oxides toward the OER was investigated by linear sweep voltammetry (LSV) using a glassy carbon RDE in a 1 M KOH electrolyte. The catalysts were applied to the electrode via drop-casting of an ink that also contained Nafion binder (for details, see the Experimental Section). In the following, the influence of the gas atmosphere during thermal treatment and the metal ratio on the activity of the mixed metal oxides is discussed. Furthermore, a comparison with the corresponding bimetallic oxides including commercially available Co_2NiO_x illustrates the benefits of the trimetallic system.

Fig. 3a shows the OER polarization curves for CoNiFe (2:2:1) oxides annealed under different gas atmospheres along with commercial Co_2NiO_x. Upon comparison between the LSVs, a pronounced effect of the thermal treatment conditions becomes evident. CoNiFe (2:2:1)/M, the catalyst treated under oxygen-deficient conditions, shows significantly higher OER catalytic ability than CoNiFe (2:2:1)/H and CoNiFe (2:2:1)/A, the materials heated under reducing atmosphere and under air, respectively. With 291 mV, CoNiFe (2:2:1)/M achieves the lowest overpotential (η_{10}) at 10 mA cm_{geo}^{-2} among the candidates in Fig. 3a,

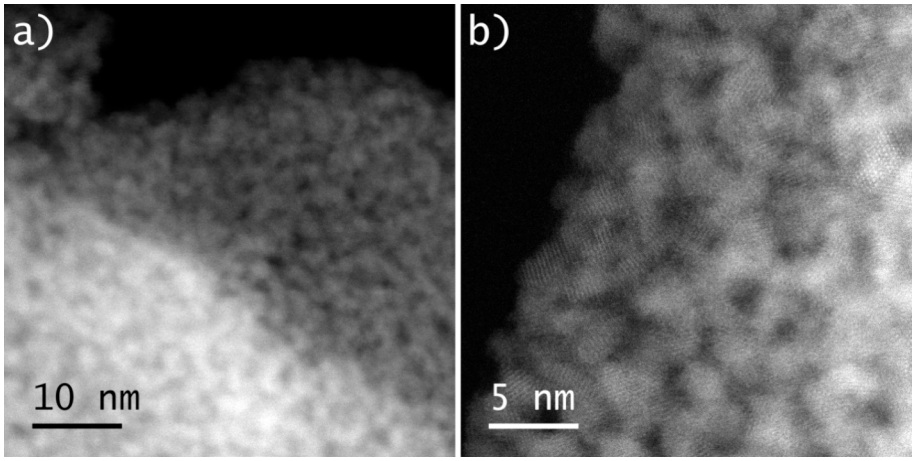

Fig. 2. TEM images illustrating nanoscopic CoNiFe (2:2:1)/M.

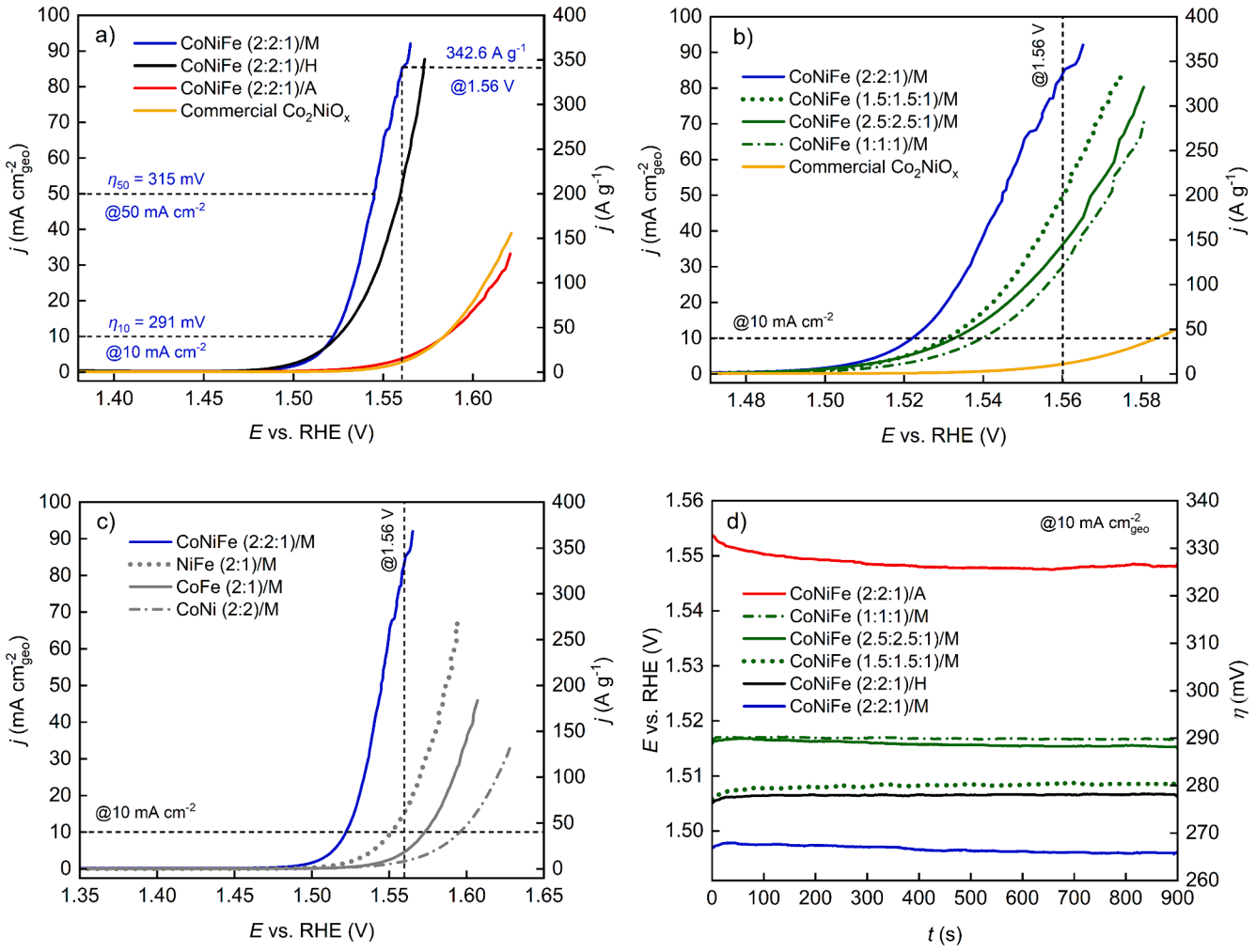

Fig. 3. (a-c) OER polarization curves obtained with different catalysts in 1 M KOH solution ($v = 1$ mV s^{-1}, $\omega = 1800$ rpm, *iR* drop corrected). (a) Influence of the gas phase composition during the thermal treatment of the active materials. (b) Influence of the molar metal ratio. (c) Comparison with bimetallic oxides. (d) Chronopotentiometric profiles recorded at 10 mA cm^{-2}_{geo} at 1800 rpm.

whereas CoNiFe (2:2:1)/A, and commercially available Co_2NiO_x exhibit the highest η_{10} values (Table 1). Moreover, the mass activity of CoNiFe (2:2:1)/M at 1.56 V vs. RHE ($\eta = 330$ mV) is 343 A g^{-1}, which is more than 30 times higher than for Co_2NiO_x (10 A g^{-1}). With 32 mV dec^{-1}, CoNiFe (2:2:1)/M exhibits the lowest Tafel slope within the CoNiFe (2:2:1) series, albeit the differences to some other representatives are only a few mV dec^{-1} (Fig. S16a, Table 1). Interestingly, all iron-containing trimetallic samples in the M series show similar Tafel

Table 1
Summary of electrochemical properties of OER electrocatalysts extracted from LSVs (Fig. 3a-c, S15a, and S17a), Tafel plots (Fig. S15b, S16a-c, S17b) impedance spectra (Fig. 4e, f, S17d, S18 and S19), and ECSA analysis (Fig. S20, and S21).

Sample	Onset potential[a,b] (V)	Overpotential[b] at 10 mA cm^{-2}_{geo} (mV)	Mass activity [b] at 1.56 V[a] (A $g^{-1}_{catalyst}$)	Tafel slope (mV dec^{-1})	R_P at 1.5V[a] (Ω)	ECSA[c] (cm^2)
CoNiFe (1:1:1)/M	1.48 ± 0.006	310 ± 2.4	117.7 ± 5.6	35.6 ± 0.14	64.8	4.15 ± 0.10
CoNiFe (1.5:1.5:1)/M	1.47 ± 0.006	299 ± 2.3	224.4 ± 17.3	35.0 ± 0.16	59.6	6.55 ± 0.15
CoNiFe (1:2:2)/M	1.47 ± 0.002	313 ± 1.6	106.0 ± 3.4	36.6 ± 0.25	181.2	3.35 ± 0.10
CoNiFe (2:1:2)/M	1.48 ± 0.002	313 ± 8.0	119.0 ± 6.6	36.1 ± 0.38	147.2	5.58 ± 0.23
CoNiFe (2:2:1)/M	**1.45 ± 0.003**	**291 ± 3.9**	**342.6 ± 17.1**	**32.0 ± 0.15**	**54.9**	**7.20 ± 0.07**
CoNiFe (2.5:2.5:1)/M	1.46 ± 0.004	305 ± 2.8	135.5 ± 9.3	35.4 ± 0.13	60.6	4.78 ± 0.16
CoNiFe (2:2:1)/H	1.46 ± 0.003	296 ± 1.9	223.4 ± 24.5	37.4 ± 0.17	81.9	4.18 ± 0.12
CoNiFe (2:2:1)/A	1.49 ± 0.001	349 ± 5.0	17.9 ± 3.0	50.7 ± 0.22	1246.3	2.34 ± 0.25
CoNi (2:2)/M	1.50 ± 0.003	366 ± 7.6	9.9 ± 1.3	51.7 ± 0.13	1278.4	4.95 ± 0.07
CoFe (2:1)/M	1.49 ± 0.003	343 ± 3.4	19.6 ± 4.2	38.0 ± 0.13	504.4	4.15 ± 0.11
NiFe (2:1)/M	1.48 ± 0.001	319 ± 3.0	70.7 ± 8.7	35.7 ± 0.25	210.4	1.13 ± 0.07
Commercial Co_2NiO_x	1.50 ± 0.002	361 ± 7.0	10.1 ± 2.3	41.5 ± 0.58	2366.10	1.45 ± 0.10

[a] All potentials are *iR* drop corrected and reported vs. RHE.
[b] Mean values obtained from at least five measurements.
[c] Geometrical electrode surface area: 0.113 cm^2.

slopes between 30 and 40 mV dec^{-1}, while CoNi (2:2)/M is positioned much higher at 51.7 mV dec^{-1}. Similarly for the bimetallic catalysts the most active are the ones containing iron.

The rather amorphous character of CoNiFe (2:2:1)/M may serve as an explanation for the superior performance compared to crystalline CoNiFe (2:2:1)/A, as an increasing density of structural defects has been discussed as one of the keys for the improvement of OER catalysts in water electrolysis [48–50]. In this context, the higher activity of CoNiFe (2:2:1)/M compared to CoNiFe(2:2:1)/H is somewhat unexpected, as the latter has a much more pronounced amorphous character according to the XRD results. A possible explanation could be Ni accumulation in certain nanodomains triggered by the reductive thermal treatment (H), as discussed above in connection with EELS analysis. However, great care must be taken when interpreting the results, as the material structures change significantly under operating conditions (see section 2.3).

Next, the influence of the metal ratio was explored. The LSVs of some mixed metal oxides with different molar ratios between Co, Ni, and Fe, all subjected to thermal treatment under oxygen-deficient atmosphere (M), are depicted in Fig. 3b and Fig. S17a. The OER performance data of all prepared materials are listed in Table 1. A comparison shows that all trimetallic oxides are significantly more active than commercial Co_2NiO_x and that deviation from the 2:2:1 ratio leads to a performance decrease. Within the series depicted in Fig. 3b, the OER activities increase in the order CoNiFe (1:1:1)/M<CoNiFe (2.5:2.5:1)/M<CoNiFe (1.5:1.5:1)/M<CoNiFe (2:2:1)/M. Similarly, CoNiFe (1:2:2)/M and CoNiFe (2:1:2)/M show significantly inferior performance compared to CoNiFe (2:2:1)/M (Fig. S17a). Among all tested materials, CoNiFe (2:2:1)/M exhibits the smallest η_{10} value, the highest mass activity, and the smallest Tafel slope (Table 1). A comparison with OER electrocatalysts from the literature (Table S12) shows that CoNiFe (2:2:1)/M is a highly competitive material.

Another focus of the investigations involved a comparison with the corresponding bimetallic systems, all synthesized under the same conditions (Fig. 3c and Fig. S15a). The LSVs and all extracted performance parameters clearly demonstrate the benefit of the trimetallic systems over the bimetallic ones. For example, the mass activity at 1.56 V vs. RHE of CoNiFe (2:2:1)/M is 35, 17, and 5 times higher than that of CoNi (2:1)/M, CoFe (2:1)/M, and NiFe (2:1)/M, respectively (Table 1). A further significant loss of performance was observed when testing the monometallic systems (Fig. S15a). Similar trends have already been observed in previous studies on the Co-Ni-Fe system, in which the mixed oxides were prepared using other synthetic methods [51,52]. Earlier, the improved performance of the tri- and bimetallic systems over the monometallic oxides has been ascribed to a synergistic stabilization of active oxidation states, whereby the Ni(II)/Ni(III) couple ($Ni(OH)_2$/NiOOH) has been proposed as the active site [53–55]. In more recent publications, the high activity of mixed metal oxide catalysts has been ascribed to various synergistic effects between metal centers [56–58]. While the exact nature of the active site is still a subject of debate, it should also be noted that even small Fe impurities were found to have a performance-enhancing effect on the OER activity [59–61].

In the case of the monometallic (NiO_x) electrocatalyst, formation of NiOOH can be observed *via* cyclic voltammetry in resting solution as a pre-peak of the OER process at 1.46 V (see Fig. S22) [62]. Likewise, the CV of CoNiFe(2:2:1)/M shows such a pre-peak, but with a cathodic shift of 70 mV. Accordingly, assignment to a stabilized NiOOH species appears tempting. However, without further information, *e.g.*, from *in situ* spectroscopic measurements, no conclusive statement can be made [63].

Chronopotentiometric measurements were carried out at 10 mA cm_{geo}^{-2} for 15 min to assess the short-term stability of the materials under mild stress (Fig. 3d, S15c, S17c, and Table S6). Except for CoNiFe (2:2:1)/A, the tested mixed metal oxides show only small potential changes during the test. Consistent with the η_{10} values read out from the LSVs, the potentiometric profiles start at comparable overpotentials. Again, the CoNiFe (2:2:1)/M shows superior behavior exhibiting the lowest starting potential, and no significant change in the overpotential during the measurement.

Following the short-term tests shown in Fig. 3d, CoNiFe (2:2:1)/M, CoNiFe (2:2:1)/H, CoNiFe (2:2:1)/A, and commercial Co_2NiO_x were subjected to long-term chronopotentiometric measurements (10 mA cm_{geo}^{-2}, 50 h). As shown in Fig. 4a, a particularly high stability was observed for CoNiFe (2:2:1)/M, with the smallest starting potential (η_{10} = 269 mV) and a potential increase of only 9 mV after 50 h. The potentiometric profile of CoNiFe (2:2:1)/H is slightly elevated to higher potentials, but still relatively close to CoNiFe (2:2:1)/M, while CoNiFe (2:2:1)/A exhibits a much higher starting potential (η_{10} = 321 mV) with similar potential increase after 50 h (9 mV). In contrast, commercial Co_2NiO_x exhibits a much stronger change (59 mV) after starting at a higher η_{10} value (332 mV).

To analyze the stability at higher stress, further long-term measurements were carried out (see Fig. 4b). For this purpose, the most promising candidate, CoNiFe (2:2:1)/M, was subjected to chronopotentiometric analyses for a duration of 50 h at 50 mA cm_{geo}^{-2} and 100 mA cm_{geo}^{-2}, respectively (ω = 1800 rpm). Despite harsh conditions and strong bubble formation [64,65], the catalyst exhibits a remarkable stability. While initial η_{50} and η_{100} values are 266 and 268 mV, respectively, η increases by only 23 and 38 mV after 50 h. Monitoring of the electrolyte pH showed a slight decrease during the experiment. Correction of the measured profiles for the pH drift (Fig. S24) suggests that the increase of the working electrode potentials in Fig. 4b is associated with pH changes rather than with catalyst degradation. Furthermore, it is possible that formation of nano- and microbubbles within the catalyst pores that cannot be removed by electrode rotation contribute to potential changes [66].

Since in alkaline water electrolyzers, the catalyst is frequently applied to Ni supports [28], a chronopotentiometric control experiment was carried out at 50 mA cm^{-2} in which a Ni RDE was used instead of the glassy carbon electrode (Fig. 4c). In both cases, the electrode was loaded with CoNiFe (2:2:1)/M. The resulting chronopotentiometric profile shows improved characteristics compared to the glassy carbon support, *i.e.*, a lower initial η_{50} value (258 mV) and a smaller potential increase (only 4 mV). Consequently, Ni seems to be ideally suited as a support for CoNiFe (2:2:1)/M, calling for performance evaluation in an alkaline water electrolyzer under practical conditions (*vide infra*). Additional LSVs were recorded after the potentiometric measurements both for the Ni and the glassy carbon support (Fig. 4d). The fact that the curves measured before and after the 50 h stress tests almost match each other confirm the excellent stability of CoNiFe (2:2:1)/M.

To gain an understanding of the activity trends that occur when the synthesis conditions and the metal ratio are varied, electrochemical impedance spectroscopy (EIS) measurements were carried out (Fig. 4e, f) and the electrochemically active surface areas (ECSAs) were determined (Table 1) by measuring the double-layer capacitance (C_{dl}) in the non-Faradaic potential range using cyclic voltammetry (CV) (Fig. S20 and S21). The EIS spectra recorded at 1.5 V vs. RHE using the catalysts from the CoNiFe (2:2:1) series and commercial Co_2NiO_x are shown in Fig. 4e (further EIS results obtained at η_{10} and the onset potentials are summarized in Fig. S18 and Table S7). The results show the same trend as the Tafel slopes, *i.e.*, that the performance increases in the order CoNiFe (2:2:1)/A<CoNiFe (2:2:1)/H<CoNiFe (2:2:1)/M. This indicates that annealing, *i.e.*, phase formation, under oxygen-deficient conditions may augment OER kinetics. Compared to the trimetallic oxides, R_P is much higher in the case of Co_2NiO_x. Within the trimetallic oxide series, on the other hand, the influence of the metal ratio on R_P is relatively moderate (Fig. 4f and S18). In terms of active surface area, the ECSA values increase in the order CoNiFe (2:2:1)/A<CoNiFe (2:2:1)/H<CoNiFe (2:2:1)/M as well (a more detailed discussion is provided in the SI). Taken together, CoNiFe (2:2:1)/M exhibits both the lowest polarization resistance (R_P) and the highest ECSA among all tested materials. The reason of the outstanding performance thus seems to be a combination of both fast OER kinetics at 1.5 V vs. RHE and high specific

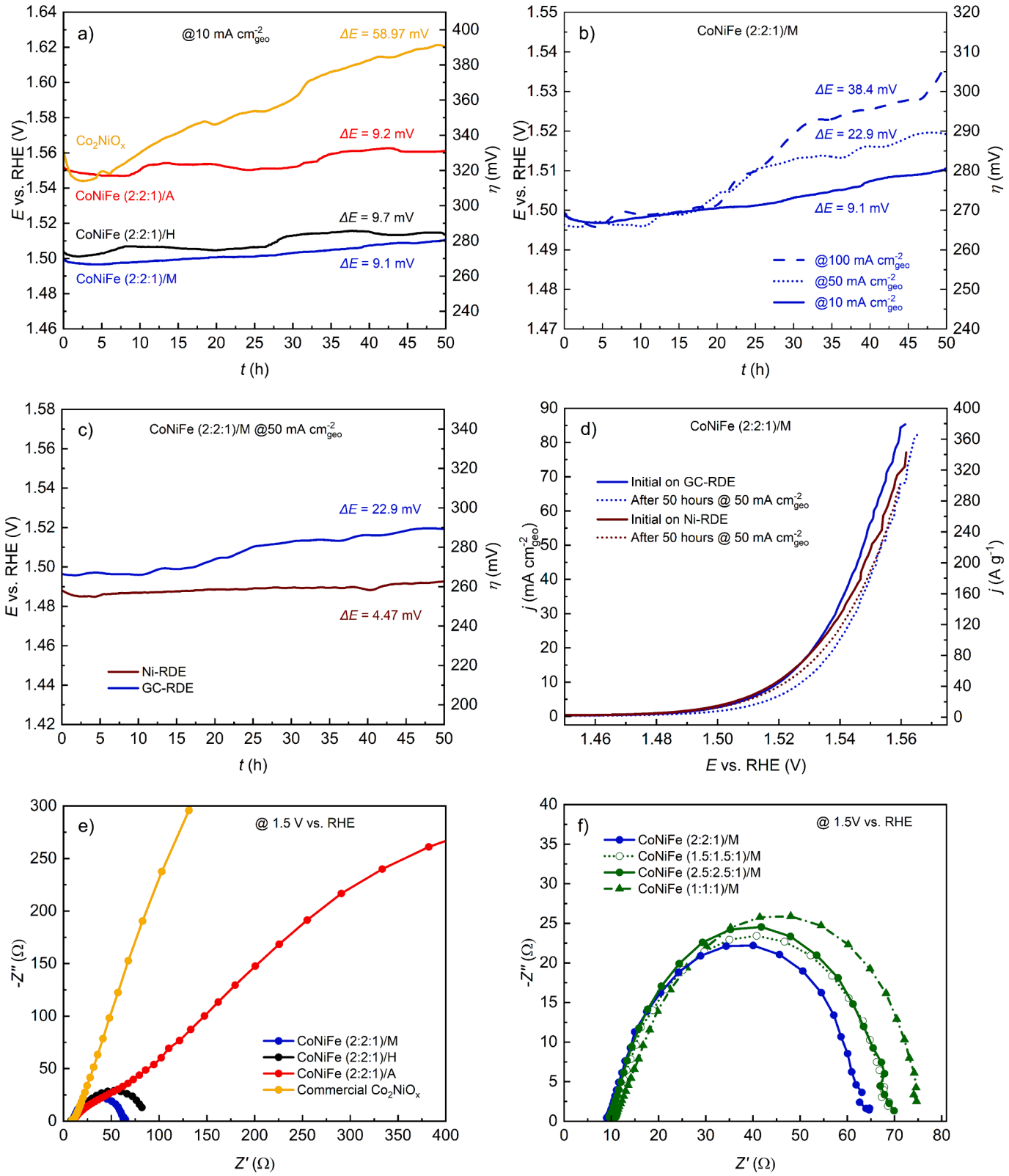

Fig. 4. (a-c) Chronopotentiometric long-term stability tests (RDE, 1 M KOH, $\omega = 1800$ rpm). (a) Comparison within the CoNiFe (2:2:1) series (GC RDE). (b) Influence of the current density (GC RDE). (c) Comparison between a Ni and a GC RDE used as support for CoNiFe (2:2:1)/M. (d) LSV curves ($v = 1$ mV s^{-1}, $\omega = 1800$ rpm, *iR* drop corrected) obtained for CoNiFe (2:2:1)/M on GC RDE and Ni RDE before and after galvanostatic stability test (50 h, 50 mA cm^{-2}). (e, f) Electrochemical impedance spectra (Nyquist plots) of mixed metal oxides from Fig. 3a and 3b, recorded at 1.5 V vs. RHE.

surface area.

2.3. Characterization of used electrocatalysts

To obtain a better understanding of structural changes which CoNiFe (2:2:1)/M, H, and A undergo during the stability tests shown in Fig. 4a-c, additional electroanalytical experiments were performed (Fig. 5 and Table 2). A first indication of occurred alterations can be derived from comparing LSVs recorded before and after 50 h potentiometric analysis at 10 mA cm_{geo}^{-2} (Fig. 5a). While CoNiFe (2:2:1)/M shows only minor profile changes and a η_{10} shift of merely 5 mV, more pronounced changes are observed for CoNiFe (2:2:1)/A ($\Delta\eta_{10}$ = 30 mV) and CoNiFe (2:2:1)/H ($\Delta\eta_{10}$ = 11 mV). The high structural integrity of CoNiFe (2:2:1)/M is manifested in stability tests at 50 and 100 mA cm_{geo}^{-2}, after which only relatively small deviations of the LSVs can be observed (Fig. 5b). ICP OES analysis of the electrolyte solution was carried out after the measurements, whereby the Co, Ni, and Fe contents were below the detection limit.

Further indications can be derived from the change in ECSA before and after long-term measurements (Table 2 and Fig. S25). In the case of the best performing CoNiFe (2:2:1)/M catalyst, a small decrease in ECSA of only 15 % is observed. In contrast, the materials CoNiFe (2:2:1)/H and CoNiFe (2:2:1)/A show stronger losses in ECSA of 54 %, and 58 %, respectively, as result of stronger structural changes. In relation to the ECSA, the H-sample shows the highest activity, indicating that the outstanding performance of the M sample is not due to a higher intrinsic rate. Regarding the polarization resistance (Fig. S26, Table S10), both CoNiFe (2:2:1)/M and CoNiFe (2:2:1)/H experience only moderate increases after the stability tests at 10 mA cm^{-2}, whereas CoNiFe (2:2:1)/A shows a strongly enhanced R_P value. As with the freshly prepared electrodes, R_P increases in the order CoNiFe (2:2:1)/M<CoNiFe (2:2:1)/H<CoNiFe (2:2:1)/A.

To analyze the structural changes that occur under operating conditions, PXRD, SEM-EDX, and XPS measurements were performed. According to PXRD, used CoNiFe (2:2:1)/M and CoNiFe (2:2:1)/A samples exhibit an increased amorphous character compared to the fresh materials, whereas CoNiFe (2:2:1)/H shows hardly any characteristic reflection peaks either before or after the electrochemical test (Fig. S27). The morphology and element distribution of CoNiFe (2:2:1)/M, the best performing material, were studied by SEM-EDX. Both after currentless contact with 1 M KOH and after positive polarization at 10 mA cm_{geo}^{-2} in the same electrolyte, the porosity was significantly enhanced compared to the as-prepared material (Fig. S29a-d and Fig. S30a-d). EDX confirmed that the metals were still evenly distributed and that their stoichiometry did not change significantly (Fig. S29e-i and Fig. S30e-i, Table S11).

XPS of all materials after electrolysis (Fig. 5c, d and S28) point toward an oxidic nature of Co, Ni, and Fe. XP spectra in the region of Co

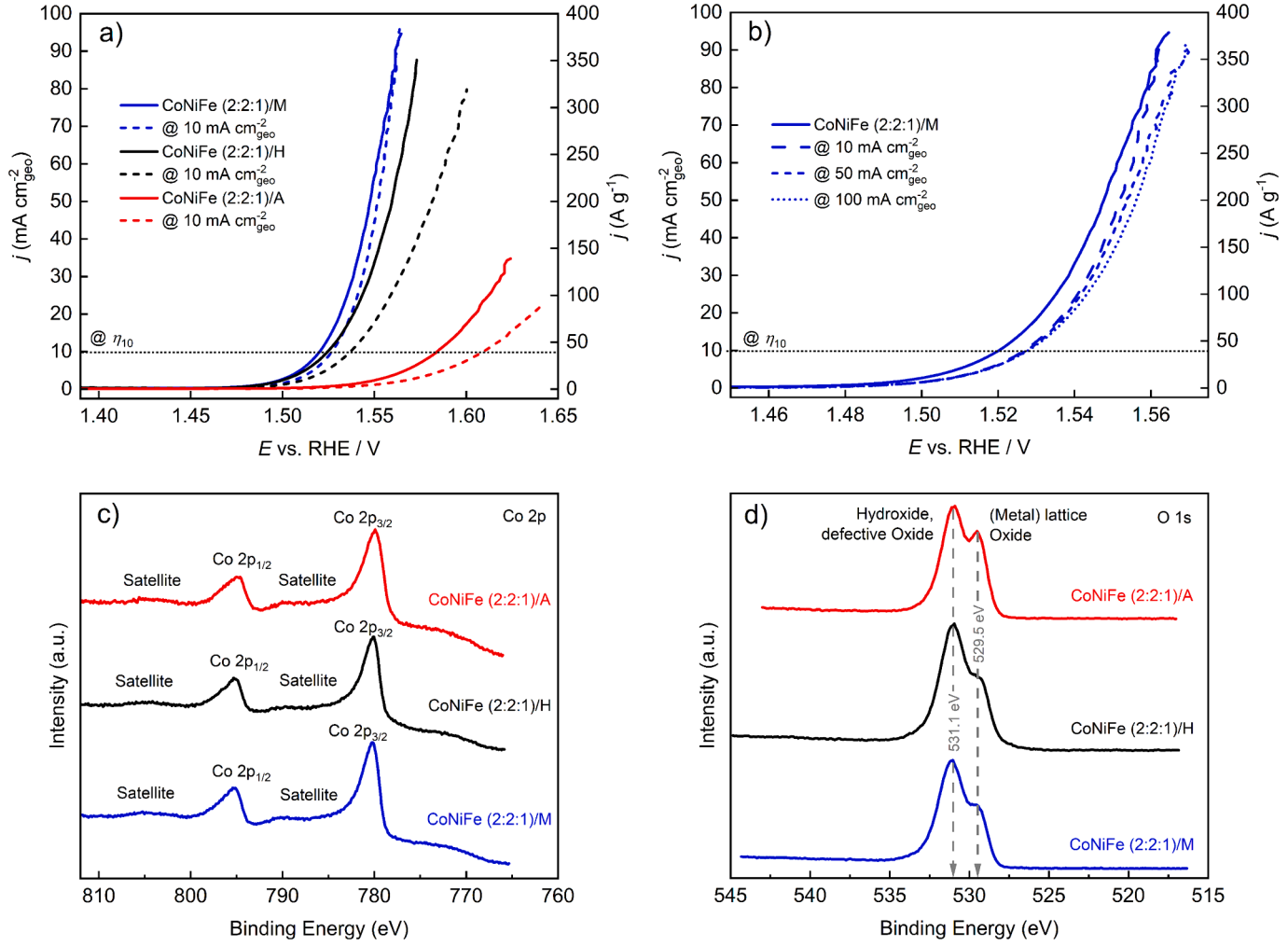

Fig. 5. (a) OER polarization curves of CoNiFe (2:2:1)/M, CoNiFe (2:2:1)/H, and CoNiFe (2:2:1)/A recorded before and after 50 h electrolysis at 10 mA cm_{geo}^{-2} (v = 1 mV s^{-1}, ω = 1800 rpm, *iR* drop corrected). (b) OER polarization curves of CoNiFe (2:2:1)/M before and after 50 h stability tests at 10 mA cm_{geo}^{-2}, 50 mA cm_{geo}^{-2}, and 100 mA cm_{geo}^{-2}, respectively. (c-d) XP spectra (Co 2p and O 1s) of CoNiFe (2:2:1)/M, CoNiFe (2:2:1)/H, and CoNiFe (2:2:1)/A after stability tests for 1 h at 10 mA cm_{geo}^{-2} (for electrolysis conditions see Experimental Section).

Table 2
Summary of changes in electrochemical properties of CoNiFe (2:2:1) catalysts after 50 h stability tests at 10 mA cm_{geo}^{-2} (Fig. 5a-b, S25, S26).

Sample	η_{10} before stability test (mV)	η_{10} after stability test (mV)	ECSA[a] before stability test (cm^2)	ECSA[a] after stability test (cm^2)	R_P before stability test (Ω)	R_P after stability test (Ω)
CoNiFe (2:2:1)/M	291.0	295.8	7.20 ± 0.074	6.13 ± 0.190	55.0	70.9
CoNiFe(2:2:1)/H	296.0	307.0	4.18 ± 0.12	1.92 ± 0.070	81.9	97.1
CoNiFe(2:2:1)/A	349.0	379.0	2.34 ± 0.25	0.97 ± 0.066	1246.3	2436.5

[a] Geometrical electrode surface area: 0.113 cm^2.

2p, Ni 2p, and Fe 2p show the tendency to adapt the shape of as-prepared CoNiFe (2:2:1)/A (compare Fig. 1b) for all CoNiFe (2:2:1) oxides, reflecting the strongly oxidizing conditions during the electrochemical tests. The binding energy at main peaks associated with metal oxide-$2p_{3/2}$ and metal- $2p_{1/2}$ orbitals, and main satellite peaks, are almost identical among the three materials. In contrast, XP spectra of O 1s for the three mixed metal oxides Co:Ni:Fe (2:2:1)/M, H, A in Fig. 5d show the opposite trend; after electrochemical tests they resemble more the spectrum of fresh CoNiFe (2:2:1)/M (compare Fig. 1c). The high-resolution XP spectra of O 1s of the used materials again exhibit two main peaks with binding energies of 529.5 eV and 531.1 eV. The hydroxide peak is now the strongest for all samples in contrast to the results of the samples before electrolysis, reflecting a high amount of surface oxygen vacancies in all three materials. While it is frequently argued that oxygen vacancies enhance the activity of metal oxide catalysts [37], it is known that lattice oxygen can also play a critical role in alkaline OER [7]. Since anodic polarization of the three materials leads to a convergence of the XP (Fe 2p, Co 2p, Ni 2p, O 1s) spectra, the outstanding catalytic activity of CoNiFe (2:2:1)/M can therefore not be attributed to the structural features of the material surface revealed by XPS alone. Together with the observed progression of the ECSA values, however, a conclusive explanation can be offered. Thus, in the case of the A and H samples, anodic polarization appears to cause *in situ* surface activation and associated strong restructuring, which is particularly well illustrated by the XPS results (cf. Fig. 5d with Fig. 1c) and the strong diminishing in ECSA (Table 2). While restructuring seems to render

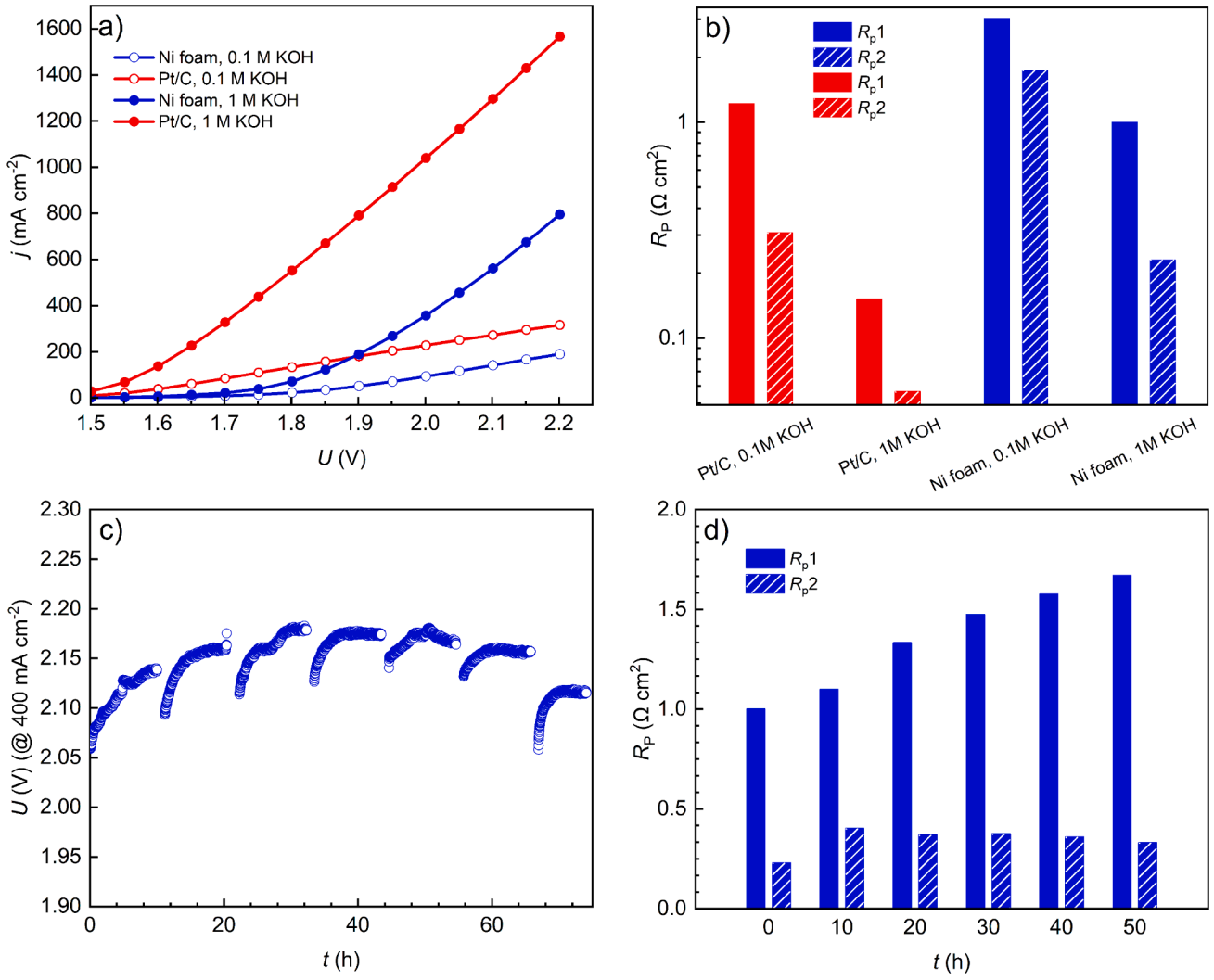

Fig. 6. Results of the alkaline water electrolyzer studies using CoNiFe (2:2:1)/M as the anode catalyst. (a) Load curves obtained with two different cathodes at 50 °C at different KOH concentrations. (b) Polarization resistances evaluated from EIS spectra that correspond with the measurements in Fig. 6a (EIS spectra recorded at U=1.8 V). (c) Stability experiment at 400 mA cm^{-2} current density using a Ni foam cathode (1 M KOH, 50 °C). (d) Polarization resistances evaluated from EIS spectra for stability measurement (measured at 1.8 V).

improved intrinsic activity, concommittant reduction in ECSA leads to a smaller number of active sites. On the other hand, the M sample appears to experience the smallest surface changes during OER. Consequently, it seems advantageous to introduce the catalytic activity by the oxygen-deficient thermal treatment as in the case of CoNiFe (2:2:1)/M, and not by *in situ* electrochemical activation as in the cases of the A and H samples.

2.4. Studies in an alkaline water electrolyzer

The catalyst with the best performance in the RDE studies, CoNiFe (2:2:1)/M, was studied in an alkaline water electrolyzer under practice-related conditions in a two-electrode arrangement. For this purpose, the catalyst was deposited on a Ni foam electrode that was separated from the cathode by an anion-selective polymer membrane (PSEBS-CM-DABCO, for details see the Experimental Section). Fig. 6a and b show load curves and corresponding EIS data resulting from short-term measurements, whereby R_P1 and R_P2 correspond to polarization resistances in series with the system resistance (R_S; detailed equivalent circuits are shown in Fig. S31). Firstly, a CoNiFe (2:2:1)/M−modified Ni foam anode was tested in combination with a bare Ni foam cathode to use the most simplified system. As follows from Fig. 6a, the performance in 0.1 M KOH was relatively poor, achieving only 22.5 mA cm_{geo}^{-2} at 1.8 V cell voltage (U). However, the shape of the load curve indicates that the performance is limited by the Ohmic resistance of the electrolysis cell. Increasing the KOH concentration from 0.1 to 1 M rendered a significant improvement of the electrolyzer performance (71.2 mA cm_{geo}^{-2} at 1.8 V) due to both, lower R_s (Fig. S32) and R_p values (Fig. 6b). Decreasing R_P values with increasing KOH concentration is also in line with concentration dependent OER polarization curves recorded under RDE conditions (Fig. S23, Table S8).

Despite the significant improvement of the performance, the achieved current density at 1.8 V is still below typical values reported in the literature [9]. Therefore, the bare Ni foam cathode was replaced by Ni foam modified with Pt/C catalyst (for details, see the Experimental Section), leading to an increase of the current density to 133.4 mA cm_{geo}^{-2} at 1.8 V in 0.1 M KOH. Obviously, both R_p values shown in Fig. 6b decreased when using the Pt/C cathode. Since water electrolysis was performed in a two-electrode arrangement, it was not possible to assign R_p1 and R_p2 values specifically to OER or hydrogen evolution reaction (HER), respectively. However, the fact that using the Pt/C-modified cathode decreases both R_p values indicates that the overall performance of the alkaline water electrolysis was hindered by the HER in the case of the bare Ni foam cathode. Finally, increasing the KOH concentration to 1 M further improved the performance, achieving 551.8 mA cm_{geo}^{-2} at 1.8 V. This result exceeds by far most of the results presented in the literature [9].

To analyze the impact of the CoNiFe (2:2:1)/M catalyst, the measurement was repeated in 1 M KOH using a Pt/C cathode and a bare Ni foam anode. The corresponding load curves and EIS analysis are shown in Fig. S33 and Fig. S34, respectively. Direct comparison shows that about 13.5 % higher current density was achieved when using modified Ni foam. The EIS data suggests that the improvement was achieved due to reduced polarization resistance, as a result of enhanced electrode kinetics. However, it seems that under the applied electrolysis conditions, the true performance of the CoNiFe (2:2:1)/M catalyst can still be hindered by the HER at the counter electrode.

After establishing the high activity of the CoNiFe (2:2:1)/M catalyst under the conditions of the alkaline water electrolysis, the next step was to analyze its stability. To simplify the system, a bare Ni foam cathode was used again. The results of the stability test performed at a constant current density of 400 mA cm^{-2} are shown in Fig. 6c. The cell voltage shows an increase at the beginning of the experiment (first 20 h) from 2.06 to 2.16 V (+4.9 %). This period is followed by a stable voltage plateau at 2.16 V±0.01 V (±0.5 %) up to 65 h. During the last period, the cell voltage decreased to 2.11 V. The initial increase of the cell voltage can be due to the stabilization of the system, including formation of the surface layers on the electrodes or achieving equilibrium in the ratio gas/liquid phase within the cell.

EIS shows that during the stability experiment, the R_s value that corresponds to the Ohmic resistance of the cell slightly decreased from 0.27 Ω cm^2 to 0.24 Ω cm^2 (11 %) (Fig. S35). This can be explained by the additional activation of the polymer membrane under constant current load. The R_p values show a different trend, whereby R_p1 increases during stability test, while R_p2 remains stable. As discussed before, it is not possible to assign the R_p values specifically to OER and HER due to the setup used. However, the results obtained from the short-term experiments suggest that HER represents the performance limiting factor when bare Ni foam is used as cathode. Considering the R_p values shown in Fig. 6d, it is likely that the increasing resistance R_p1 corresponds to the HER process at the Ni foam cathode.

To evaluate the structural integrity of CoNiFe (2:2:1)/M during alkaline water electrolysis, SEM-EDX and XRD measurements were performed prior to and after the stability test. SEM images of the fresh anode and anode after stability test are shown in Fig. S36. From SEM imaging, it is clearly visible that the catalyst layer after the experiment is still present and that shape, size, and number of the catalyst particles is not significantly affected by the stability test. The stability is confirmed by EDX mapping (Fig. S37), where it is possible to see homogeneous distribution of all three metals. Finally, comparing the XRD pattern of a freshly prepared electrode with a pattern of an electrode after the stability test (Fig. S38) shows appearance of a new NiO phase. This is likely connected with the oxidation of the Ni foam that was used as catalyst support. However, the XRD patterns clearly show that the phase composition of the catalyst was not affected by the stability test. Taken together, the results of the electrochemical studies and the structural characterizations testify excellent stability of the CoNiFe (2:2:1)/M catalyst under practice-related conditions.

3. Conclusion

In the present study, a promising approach for the preparation of highly active mixed metal oxide electrocatalysts is presented, which is based on a straightforward sol–gel process in combination with an oxygen-deficient thermal treatment and a well-balanced molar metal ratio. The influence of the thermal treatment conditions on the catalytic properties of CoNiFe oxides toward alkaline OER was analyzed in comparative electrochemical studies. Treatment of the materials under oxygen-deficient conditions (M; 1 vol% air in argon) leads to the best results in terms of activity and stability, while reducing conditions (H; 5 vol% H_2 in argon) render significantly poorer results. The by far lowest activity and stability were observed for materials whose thermal treatment was carried out under aerobic conditions (A; air). Through systematic variation of the molar metal ratio, CoNiFe (2:2:1)/M was identified as the best candidate under RDE conditions, with a η_{10} value of 291 mV, a mass activity of 343 A $g_{catalyst}^{-1}$ at 1.56 V vs. RHE, a Tafel slope of only 32.0 mV dec^{-1}, and negligible changes of the overpotential in long-term potentiometric measurements at 100 mA cm^{-2}. Furthermore, CoNiFe (2:2:1)/M exhibits the lowest polarization resistance (R_P) and the highest electrochemically active surface area (ECSA) among all tested materials. In view of R_P and ECSA, the material only deteriorates marginally when exposed to electrolytic conditions.

While SEM measurements confirm a homogeneous metal distribution within all materials, XRD, STEM, and XPS analyses show a clear influence of the thermal treatment conditions on the crystallinity and surface chemistry. The optimized catalyst, CoNiFe (2:2:1)/M, exhibits a rather amorphous character with crystalline fractions. According to XPS analysis, the metals on the surface are present in different oxidation states, whereby surface-bound oxygen predominantly exists as hydroxide, to a lesser extent also as lattice oxygen. However, post-electrolysis XPS characterization shows that anodic polarization causes a surface restructuring and thereby an alignment of the structural properties

between the M, H, and A materials. Consequently, the oxidative conditions lead to a situation in which all metals exist in their highest oxidation states and where the distribution between the oxygen species assumes the one of as-prepared CoNiFe (2:2:1)/M. In contrast, the influence of the greatly increased active surface area on the performance of CoNiFe (2:2:1)/M is evident. It is particularly important to note that for this material, the ECSA only diminishes marginally during OER, as opposed to the A and H candidates. Thus, CoNiFe (2:2:1)/A and CoNiFe (2:2:1)/H seem to lose a considerable portion of ECSA as a result of their electrochemical activation, which reduces the number of active sites compared to the M sample. In contrast, the M sample experiences much less dramatic changes of the surface properties upon OER. Consequently, it appears beneficial to introduce catalytic activity by the oxygen-deficient thermal treatment as in the case of CoNiFe (2:2:1)/M, and not merely by electrochemical activation as in the cases of the A and H samples. A deeper analysis of mechanistic aspects requires a combination of additional (*in situ*) spectroscopic techniques and is currently underway.

Finally, the suitability of the optimized catalyst under practical conditions was confirmed by studies using an alkaline water electrolyzer in a two-electrode arrangement. Application of CoNiFe (2:2:1)/M to a nickel mesh anode that was separated from a Ni foam cathode by an anion exchange membrane enabled an average cell voltage of ~ 2.1 V at a current density of 400 mA cm^{-2}. Stability of the device for at least 70 h was demonstrated. These promising results call for an in-depth analysis under practical water splitting conditions as well as for studies on other electrocatalytic applications (*e.g.*, anodic oxidation of biomass-derived alcohols), both of which will be carried out in our laboratory in the near future.

4. Experimental section

Materials. All chemicals were of analytical grade and used without further purification. Cobalt(II) nitrate hexahydrate ($Co(NO_3)_2{\cdot}6H_2O$) was purchased from ThermoFisher GmbH (Karlsruhe, Germany). Nickel (II) nitrate hexahydrate ($Ni(NO_3)_2{\cdot}6H_2O$), iron(III) nitrate nonahydrate ($Fe(NO_3)_3{\cdot}9H_2O$), nickel(II) cobalt(II) oxide (Co_2NiO_x, nanopowder, <150 nm particle size) and citric acid ($C_6H_8O_7$) were obtained from Sigma-Aldrich. Potassium hydroxide solution (KOH, 0.999–1.001 M at 20 °C) was purchased from AppliChem. Ethanol (EtOH, abs., > 99.5 %) was obtained from Walter-CMP. Nafion solution (D-521) was purchased from Alfa Aesar. Throughout all experiments, deionized water was used.

Preparation of CoNiFe oxides. For preparation of the mixed metal oxide precursors, a sol–gel protocol reported by Polyakov and co-workers was adapted [67–69]. A mixture of x mol $Co(NO_3)_2{\cdot}6H_2O$, y mol $Ni(NO_3)_2{\cdot}6H_2O$, z mol $Fe(NO_3)_3{\cdot}.9H_2O$, and ($x + y + z = 0.03$) mol citric acid was dissolved completely in 60 mL deionized water using a magnetic stirrer at room temperature. For variation of the molar metal ratio, the sum of x ,y and z remained constant. The homogeneous solution was concentrated through stirring at 75 °C for 24 h, resulting in a gel that was dried at 110 °C for 17 h. The light brown solid was ground using a ball mill for 10 min to obtain a powder. The precursor material was subjected to thermal treatment in a horizontal tubular furnace (HTM Reetz) at 300 °C for 3 h, whereby a temperature ramp of 5 K min^{-1} was used to achieve the treatment temperature. Samples with the index A were heated under air with a flow rate ($\dot{V}$) of 25 mL min^{-1}, while materials with the index H and M were pyrolyzed in 5 vol% H_2 / argon ($\dot{V}$ = 25 mL min^{-1}) and in 1 vol% air / argon ($\dot{V}$ = 5 mL min^{-1}), respectively. Details on all studied samples are summarized in Table S1. Results of elemental analysis are provided in Table S2.

Materials characterization: Elemental analysis for carbon, hydrogen and nitrogen was carried out using a TruSpec Micro CHNS analyzer (Leco). The metal contents of the samples were measured using atomic absorption spectroscopy (AAS) on a contra 800 D device (Analytik Jena). For analysis of the electrolyte after long-term stability tests, ICP OES measurements were carried out using a Varian/Agilent 715-ES spectrometer.

Powder X-ray diffraction patterns were recorded using a Stoe Stadi P transmission diffractometer equipped with a DECTRIs Mythen2 1 K detector applying Ge(1 1 1) monochromatized Mo Kα1 radiation (50 kV, 40 mA, 0.70930 Å). The samples were ground to a fine powder and placed between two plastic wraps before the measurement. Peak positions and profile were fitted with the Pseudo-Voigt function using the HighScore Plus software package (Panalytical). Phase identification was achieved by using the PDF-2 database of the International Center of Diffraction Data (ICDD).

The XPS (X-ray Photoelectron Spectroscopy) measurements were performed on an ESCALAB 220iXL (Thermo Fisher Scientific) with monochromated Al Kα radiation (E=1486.6 eV). Samples were prepared on a stainless-steel holder with conductive double-sided adhesive carbon tape. The measurements were performed with charge compensation using a flood electron system combining low energy electrons and Ar^+ ions ($p_{Ar} = 1 \times 10^{-7}$ mbar). The electron binding energies are referenced to the C 1s core level of carbon at 284.8 eV (C–C and C–H bonds).

The morphology of the electrode surface before and after electrolysis was studied with electron microscopy. Scanning electron microscopy (SEM, equipped with EDX) was performed using a MERLIN® VP Compact (Zeiss, Germany) microscope. Scanning transmission electron microscopy (STEM) investigations were carried out on a probe aberration-corrected JEM-ARM200F (JEOL, corrector: CEOS) at an accelerating voltage of 200 kV. The microscope is equipped with a JED-2300 (JEOL) energy-dispersive X-ray spectrometer (for EDX) having a silicon drift detector (dry SD60GV). Electron energy-loss spectroscopy (EELS) was done with an Enfinium ER (Gatan) electron energy-loss (EEL) spectrometer. For STEM imaging, a High-Angle Annular Dark Field (HAADF) and an Annular Bright Field (ABF) detector were employed, while an Annular Dark Field (ADF) detector was used for position control during EELS acquisition. Dual EELS was performed at a camera length of 4 cm, an illumination semi angle of 27.8 mrad and a filter entrance aperture semi angle of 41.3 mrad using the low loss region for compensation of energy shifts during acquisition. The solid samples were deposited without any pre-treatment onto a holey carbon-supported Cu grid (mesh 300) and subsequently transferred to the microscope. The specific surface area and pore volume were determined by N_2 adsorption and calculated using BET and BJH methods, respectively. Diffuse reflectance UV–vis spectra were obtained using an AvaSpec 2048 fiber optical spectrometer (Avantes BV) equipped with an AvaLight-DHS light source and an FCR-19UV200-2-ME reflection probe by using $BaSO_4$ as white standard reference material.

Electroanalytical Experiments: All experiments were performed in a three-electrode arrangement using an Autolab PGSTAT 302 N (Metrohm). A glassy carbon rotating disk electrode [17] (diameter: 3.8 mm, geometrical surface area: 0.113 cm^2) was used as the working electrode (WE). For the preparation of the coated working electrode, catalyst inks were prepared by dispersion of 5 mg catalyst in 1 mL of a mixture of 0.1 M KOH, Nafion, EtOH, and H_2O (1:2:45:45 in relation to the volumes of the pure components). The ink was sonicated for 45 min at room temperature. A defined amount of catalyst suspension was slowly dropped on the working electrode surface and dried for an hour under air to achieve a catalyst loading on the electrode surface area of 0.25 mg cm^{-2}. An Ag/AgCl (3 M KCl) electrode and a Pt rod electrode were used as reference electrode (RE) and counter electrode (CE), respectively. All reported potentials are *iR* drop corrected. The uncompensated resistance R was determined by electrochemical impedance spectroscopy (EIS) at the open-circuit potential (OCP) from 20 kHz to 200 Hz with alternating current perturbation of 5 mV. All recorded potentials were converted to RHE.

All linear sweep voltammograms (LSVs) were recorded using a scan rate of 1 mV s^{-1} and a rotation rate of 1800 rpm. EIS analysis of the electrocatalysts was carried out at 1.50 V vs RHE, at OER onset, and at η_{10} scanning the frequency range from 10 kHz to 0.01 Hz and applying

an amplitude of 5 mV. The electrochemically active surface area (ECSA) was estimated by measuring the double layer capacitance in the non-Faradaic region using cyclic voltammetry without electrode rotation (for details, see the SI).

For Mott-Schottky analysis, FTO supports were coated by drop-casting 100 μL of a Nafion-free ink (5 mg catalyst in 1 mL EtOH/H_2O 1:1, v/v). EIS measurements were performed at 100 Hz, 1000 Hz, 1500 Hz, and 2000 Hz, respectively, in the potential range between 0 V and 1 V vs Ag/AgCl (3 M KCl) in 50 mV steps.

For structural characterization of used materials, a Nafion-free ink of the catalyst was deposited onto a glassy carbon plate (1 cm^2, material loading: 0.25 mg cm^{-2}). Anodic polarization of the materials was carried out at 10mA cm^{-2}_{geo} for 1 h in a resting 1 M KOH electrolyte. After the electrochemical test, KOH was removed by rinsing the plates with deionized water. The plates with used catalyst could be investigated directly by SEM. For XRD and XPS, the material was removed from the plates.

Studies in alkaline water electrolyzer. For electrolysis tests, the catalyst ink was prepared by mixing the catalyst powder with chloromethylated poly(styrene-ethylene/butylene-styrene) block copolymer (PSEBS-CM) acting as the polymer binder of the catalyst layer. Chloroform (10 mL) was used as a solvent/dispersant. The catalyst to binder ratio (wt/wt) was 90:10. The prepared catalyst ink was rested for 16 h prior to the catalyst layer deposition. The catalyst layer was deposited on the surface of the support (Ni foam) using the sonicated dispersion deposition method. The catalyst load was 10 mg cm^{-2}. After deposition of the catalyst layer, the electrodes were immersed in a solution of 10 wt% DABCO (1,4-diazabicyclo[2.2.2]octane) in ethanol at room temperature for 48 h in order to introduce DABCO functional groups to the PSEBS-CM [70,71]. After activation, the electrode was immersed in 0.1 M KOH solution to load the polymer binder with OH^- ions. Bare Ni foam and Ni foam modified by Pt/C (0.5 mg Pt cm^{-2}), respectively, were used as cathodes. The anion-selective polymer membrane PSEBS-CM-DABCO (thickness in dry state: 60 μm) was used as separator between anode and cathode. Electrolysis was carried out at 50 °C using 0.1 M and 1 M KOH, respectively, as the electrolyte. Activation of fresh electrodes was achieved by polarization at constant cell voltage (1.9 V) for 20 h. After the activation procedure, the short-term measurement of the load curves followed in the cell voltage range between 1.5 and 2.2 V. The load curve measurement was accompanied by EIS measurement at cell voltages in the range from 1.5 to 1.8 V. The maximum amplitude of the perturbing signal was 10 mV. The frequency range was 100 kHz – 0.1 Hz. The equivalent circuits used for EIS spectra evaluation are shown in Fig. S31. The top circuit was used in the case of bare Ni foam cathode, the bottom one in the case of the Pt/C cathode.

The stability test was performed in 1 M KOH electrolyte at 50 °C and a current density of 400 mA cm^{-2}. Bare Ni foam was used as a cathode. The stability test was composed of 10 h constant current measurement, followed by the load curve and EIS measurements. The procedure was successfully repeated six times. During the seventh cycle, the cell was short-circuited.

Prior to and after the stability test, XRD and SEM-EDX were used to investigate possible differences in the catalyst. For XRD analysis, a PANanalytical X'Pert PRO with Cobalt lamp was used in the range from 6 to 110 °2θ. For SEM analysis, a Hitachi S4700 scanning electron microscope with EDX detector was used.

CRediT authorship contribution statement

Trang Minh Pham: Writing – review & editing, Validation, Investigation, Data curation. **Michaela Plevova:** Investigation, Data curation. **Stephan Bartling:** Writing – review & editing, Investigation. **Nils Rockstroh:** Writing – review & editing, Investigation. **Armin Springer:** Investigation. **Adam Slabon:** Writing – review & editing, Validation, Conceptualization. **Jaromir Hnat:** Writing – original draft, Visualization, Supervision, Conceptualization. **Annette-Enrica Surkus:** Writing – original draft, Supervision, Methodology, Data curation, Conceptualization. **Robert Francke:** Writing – review & editing, Visualization, Supervision, Conceptualization.

Declaration of competing interest

The authors declare that they have no known competing financial interests or personal relationships that could have appeared to influence the work reported in this paper.

Data availability

Data will be made available on request.

Acknowledgements

The authors thank Dr. Henrik Lund and Kathleen Schubert (both Leibniz Institute for Catalysis) for XRD measurements. Valuable contributions through BET measurements by Reinhard Eckelt (Leibniz Institute for Catalysis) are appreciated. T.M.P. is grateful for the RoHan project between Rostock University, Leibniz Institute for Catalysis (Germany) and Hanoi University of Science and Technology, funded by the German Academic Exchange Service (DAAD), No. 57315854 and the Federal Ministry for Economic Cooperation and Development (BMZ) within the framework of the "SDG Graduate School" for financial support. R.F. acknowledges financial support by the German Research Foundation (DFG, Heisenberg Professorship, FR 3848/4-1). The authors thank and commemorate Dr. Mykola Polyakov, a good friend and colleague who passed away so young, for all joint work concerning OER material development.

Appendix A. Supplementary data

Supplementary data to this article can be found online at https://doi.org/10.1016/j.jcat.2024.115675.

References

[1] Z.-Y. Yu, Y. Duan, X.-Y. Feng, X. Yu, M.-R. Gao, S.-H. Yu, Clean and Affordable Hydrogen Fuel from Alkaline Water Splitting: Past, Recent Progress, and Future Prospects, Adv. Mater. 33 (2021) 2007100.
[2] H.L.S. Shiva Kumar, An overview of water electrolysis technologies for green hydrogen production, Energy Rep. 8 (2022) 21.
[3] M. Neuwirth, T. Fleiter, P. Manz, R. Hofmann, The future potential hydrogen demand in energy-intensive industries - a site-specific approach applied to Germany, Energy Convers. Manag. 252 (2022) 115052.
[4] X. Xie, L. Du, L. Yan, S. Park, Y. Qiu, J. Sokolowski, W. Wang, Y. Shao, Oxygen Evolution Reaction in Alkaline Environment: Material Challenges and Solutions, Adv. Funct. Mater. 32 (2022) 2110036.
[5] A.J. Shih, M.C.O. Monteiro, F. Dattila, D. Pavesi, M. Philips, A.H.M. da Silva, R. E. Vos, K. Ojha, S. Park, O. van der Heijden, G. Marcandalli, A. Goyal, M. Villalba, X. Chen, G.T.K.K. Gunasooriya, I. McCrum, R. Mom, N. López, M.T.M. Koper, Water electrolysis, Nat. Rev. Methods Primers 2 (2022) 84.
[6] J. Zhang, Q. Zhang, X. Feng, Support and Interface Effects in Water-Splitting Electrocatalysts, Adv. Mater. 31 (2019) 1808167.
[7] E. Fabbri, T.J. Schmidt, Oxygen Evolution Reaction—The Enigma in Water Electrolysis, ACS Catal. 8 (2018) 9765–9774.
[8] M. Chatenet, B.G. Pollet, D.R. Dekel, F. Dionigi, J. Deseure, P. Millet, R.D. Braatz, M.Z. Bazant, M. Eikerling, I. Staffell, P. Balcombe, Y. Shao-Horn, H. Schäfer, Water electrolysis: from textbook knowledge to the latest scientific strategies and industrial developments, Chem. Soc. Rev. 51 (2022) 4583–4762.
[9] H.A. Miller, K. Bouzek, J. Hnat, S. Loos, C.I. Bernäcker, T. Weißgärber, L. Röntzsch, J. Meier-Haack, Green hydrogen from anion exchange membrane water electrolysis: a review of recent developments in critical materials and operating conditions, Sustain. Energy Fuels 4 (2020) 2114–2133.
[10] S. Wang, A. Lu, C.-J. Zhong, Hydrogen production from water electrolysis: role of catalysts, Nano Converg. 8 (2021).
[11] M. Schalenbach, O. Kasian, K.J.J. Mayrhofer, An alkaline water electrolyzer with nickel electrodes enables efficient high current density operation, Int. J. Hydrogen Energy 43 (2018) 11932–11938.
[12] M. Schalenbach, A.R. Zeradjanin, O. Kasian, S. Cherevko, K.J.J. Mayrhofer, A Perspective on Low-Temperature Water Electrolysis – Challenges in Alkaline and Acidic Technology, Int. J. Electrochem. Sci. 13 (2018) 1173–1226.

[13] M. Schalenbach, G. Tjarks, M. Carmo, W. Lueke, M. Mueller, D. Stolten, Acidic or Alkaline? Towards a New Perspective on the Efficiency of Water Electrolysis, J. Electrochem. Soc. 163 (2016) F3197.
[14] M.A. Khan, H. Zhao, W. Zou, Z. Chen, W. Cao, J. Fang, J. Xu, L. Zhang, J. Zhang, Recent Progresses in Electrocatalysts for Water Electrolysis, Electrochem. Energy Rev. 1 (2018) 483–530.
[15] C. Minke, M. Suermann, B. Bensmann, R. Hanke-Rauschenbach, Is iridium demand a potential bottleneck in the realization of large-scale PEM water electrolysis? Int. J. Hydrogen Energy 46 (2021) 23581–23590.
[16] A. Li, Y. Sun, T. Yao, H. Han, Earth-Abundant Transition-Metal-Based Electrocatalysts for Water Electrolysis to Produce Renewable Hydrogen, Chem. Eur. J. 24 (2018) 18334–18355.
[17] F. Song, L. Bai, A. Moysiadou, S. Lee, C. Hu, L. Liardet, X. Hu, Transition Metal Oxides as Electrocatalysts for the Oxygen Evolution Reaction in Alkaline Solutions: An Application-Inspired Renaissance, J. Am. Chem. Soc. 140 (2018) 7748–7759.
[18] C. Karacan, F.P. Lohmann-Richters, G.P. Keeley, F. Scheepers, M. Shviro, M. Müller, M. Carmo, D. Stolten, Challenges and important considerations when benchmarking single-cell alkaline electrolyzers, Int. J. Hydrogen Energy 47 (2022) 4294–4303.
[19] T. Wu, X. Ren, Y. Sun, S. Sun, G. Xian, G.G. Scherer, A.C. Fisher, D. Mandler, J. W. Ager, A. Grimaud, J. Wang, C. Shen, H. Yang, J. Gracia, H.-J. Gao, Z.J. Xu, Spin pinning effect to reconstructed oxyhydroxide layer on ferromagnetic oxides for enhanced water oxidation, Nat. Commun. 12 (2021) 3634.
[20] R.A. Krivina, Y. Ou, Q. Xu, L.P. Twight, T.N. Stovall, S.W. Boettcher, Oxygen Electrocatalysis on Mixed-Metal Oxides/Oxyhydroxides: From Fundamentals to Membrane Electrolyzer Technology, Acc. Mater. Res. 2 (2021) 548–558.
[21] J. Yuan, X. Cheng, C. Lei, B. Yang, Z. Li, K. Luo, K.H. Koko Lam, L. Lei, Y. Hou, K. K. Ostrikov, Bimetallic Oxyhydroxide as a High-Performance Water Oxidation Electrocatalyst under Industry-Relevant Conditions, Eng. 7 (2021) 1306–1312.
[22] J. Yin, J. Jin, H. Lin, Z. Yin, J. Li, M. Lu, L. Guo, P. Xi, Y. Tang, C.-H. Yan, Optimized Metal Chalcogenides for Boosting Water Splitting, Adv. Sci. 7 (2020) 1903070.
[23] Y. Zhao, S. Wei, K. Pan, Z. Dong, B. Zhang, H.-H. Wu, Q. Zhang, J. Lin, H. Pang, Self-supporting transition metal chalcogenides on metal substrates for catalytic water splitting, J. Chem. Eng. 421 (2021) 129645.
[24] Y. Liu, Y. Guo, Y. Liu, Z. Wei, K. Wang, Z. Shi, A Mini Review on Transition Metal Chalcogenides for Electrocatalytic Water Splitting: Bridging Material Design and Practical Application, Energy Fuels 37 (2023) 2608–2630.
[25] M. Wang, L. Zhang, Y. He, H. Zhu, Recent advances in transition-metal-sulfide-based bifunctional electrocatalysts for overall water splitting, J. Mater. Chem. A 9 (2021) 5320–5363.
[26] F. Yu, H. Zhou, Y. Huang, J. Sun, F. Qin, J. Bao, W.A. Goddard, S. Chen, Z. Ren, High-performance bifunctional porous non-noble metal phosphide catalyst for overall water splitting, Nat. Commun. 9 (2018) 2551.
[27] J. Joo, T. Kim, J. Lee, S.-I. Choi, K. Lee, Morphology-Controlled Metal Sulfides and Phosphides for Electrochemical Water Splitting, Adv. Mater. 31 (2019) 1806682.
[28] M. Yu, E. Budiyanto, H. Tüysüz, Principles of Water Electrolysis and Recent Progress in Cobalt-, Nickel-, and Iron-Based Oxides for the Oxygen Evolution Reaction, Angew. Chem. Int. Ed. 61 (2022) e202103824.
[29] Z.W. Seh, J. Kibsgaard, C.F. Dickens, I. Chorkendorff, J.K. Nørskov, T.F. Jaramillo, Combining theory and experiment in electrocatalysis: Insights into materials design, Science 355 (2017) eaad4998.
[30] I.C. Man, H.-Y. Su, F. Calle-Vallejo, H.A. Hansen, J.I. Martínez, N.G. Inoglu, J. Kitchin, T.F. Jaramillo, J.K. Nørskov, J. Rossmeisl, Universality in Oxygen Evolution Electrocatalysis on Oxide Surfaces, ChemCatChem 3 (2011) 1159–1165.
[31] R. Subbaraman, D. Tripkovic, K.-C. Chang, D. Strmcnik, A.P. Paulikas, P. Hirunsit, M. Chan, J. Greeley, V. Stamenkovic, N.M. Markovic, Trends in activity for the water electrolyser reactions on 3d M(Ni Co, Fe, Mn) hydr(oxy)oxide catalysts, Nat. Mater. 11 (2012) 550–557.
[32] C.C.L. McCrory, S. Jung, I.M. Ferrer, S.M. Chatman, J.C. Peters, T.F. Jaramillo, Benchmarking Hydrogen Evolving Reaction and Oxygen Evolving Reaction Electrocatalysts for Solar Water Splitting Devices, J. Am. Chem. Soc. 137 (2015) 4347–4357.
[33] B.H.R. Suryanto, Y. Wang, R.K. Hocking, W. Adamson, C. Zhao, Overall electrochemical splitting of water at the heterogeneous interface of nickel and iron oxide, Nat. Commun. 10 (2019) 5599.
[34] G.A. Gebreslase, M.V. Martínez-Huerta, M.J. Lázaro, Recent progress on bimetallic NiCo and CoFe based electrocatalysts for alkaline oxygen evolution reaction: A review, J. Energy Chem. 67 (2022) 101–137.
[35] Y. Pi, Q. Shao, P. Wang, F. Lv, S. Guo, J. Guo, X. Huang, Trimetallic Oxyhydroxide Coralloids for Efficient Oxygen Evolution Electrocatalysis, Angew. Chem. Int. Ed. 56 (2017) 4502–4506.
[36] K. Zhu, T. Wu, M. Li, R. Lu, X. Zhu, W. Yang, Perovskites decorated with oxygen vacancies and Fe–Ni alloy nanoparticles as high-efficiency electrocatalysts for the oxygen evolution reaction, J. Mater. Chem. A 5 (2017) 19836–19845.
[37] K. Zhu, F. Shi, X. Zhu, W. Yang, The roles of oxygen vacancies in electrocatalytic oxygen evolution reaction, Nano Energy 73 (2020) 104761.
[38] M.C. Biesinger, B.P. Payne, A.P. Grosvenor, L.W.M. Lau, A.R. Gerson, R.S.C. Smart, Resolving surface chemical states in XPS analysis of first row transition metals, oxides and hydroxides: Cr, Mn, Fe, Co and Ni, Appl. Surf. Sci. 257 (2011) 2717–2730.
[39] M. Cheng, H. Fan, Y. Song, Y. Cui, R. Wang, Interconnected hierarchical NiCo2O4 microspheres as high-performance electrode materials for supercapacitors, Dalton Trans. 46 (2017) 9201–9209.
[40] P. Salunkhe, M.A. AV, D. Kekuda, Investigation on tailoring physical properties of Nickel Oxide thin films grown by dc magnetron sputtering, Mater. Res. Express 7 (2020) 016427.
[41] Z. Wang, W. Wang, L. Zhang, D. Jiang, Surface oxygen vacancies on Co3O4 mediated catalytic formaldehyde oxidation at room temperature, Catal. Sci. Technol. 6 (2016) 3845–3853.
[42] Z. Xiao, Y.-C. Huang, C.-L. Dong, C. Xie, Z. Liu, S. Du, W. Chen, D. Yan, L. Tao, Z. Shu, G. Zhang, H. Duan, Y. Wang, Y. Zou, R. Chen, S. Wang, Operando Identification of the Dynamic Behavior of Oxygen Vacancy-Rich Co3O4 for Oxygen Evolution Reaction, J. Am. Chem. Soc. 142 (2020) 12087–12095.
[43] S.S. Kalanur, I.-H. Yoo, I.-S. Cho, H. Seo, Effect of oxygen vacancies on the band edge properties of WO3 producing enhanced photocurrents, Electrochim. Acta 296 (2019) 517–527.
[44] M. Ertl, Z. Ma, T. Thersleff, P. Lyu, S. Huettner, P. Nachtigall, J. Breu, A. Slabon, Mössbauerite as Iron-Only Layered Oxyhydroxide Catalyst for WO3 Photoanodes, Inorg. Chem. 58 (2019) 9655–9662.
[45] Z. Ma, O. Linnenberg, A. Rokicinska, P. Kustrowski, A. Slabon, Augmenting the Photocurrent of CuWO4 Photoanodes by Heat Treatment in the Nitrogen Atmosphere, J. Phys. Chem. C 122 (2018) 19281–19288.
[46] T.W. Kim, Y. Ping, G.A. Galli, K.-S. Choi, Simultaneous enhancements in photon absorption and charge transport of bismuth vanadate photoanodes for solar water splitting, Nat. Commun. 6 (2015) 8769.
[47] Y. Tang, N. Rong, F. Liu, M. Chu, H. Dong, Y. Zhang, P. Xiao, Enhancement of the photoelectrochemical performance of CuWO4 films for water splitting by hydrogen treatment, Appl. Surf. Sci. 361 (2016) 133–140.
[48] R.V. Mom, L.J. Falling, O. Kasian, G. Algara-Siller, D. Teschner, R.H. Crabtree, A. Knop-Gericke, K.J.J. Mayrhofer, J.-J. Velasco-Vélez, T.E. Jones, Operando Structure–Activity–Stability Relationship of Iridium Oxides during the Oxygen Evolution Reaction, ACS Catal. 12 (2022) 5174–5184.
[49] J. Park, S. Lee, S. Kim, Recent advances in amorphous electrocatalysts for oxygen evolution reaction, Front. Chem. 10 (2022).
[50] T. Guo, L. Li, Z. Wang, Recent Development and Future Perspectives of Amorphous Transition Metal-Based Electrocatalysts for Oxygen Evolution Reaction, Adv. Energy Mater. 12 (2022) 2200827.
[51] F. Le Formal, L. Yerly, E. Potapova Mensi, X. Pereira Da Costa, F. Boudoire, N. Guijarro, M. Spodaryk, A. Züttel, K. Sivula, Influence of Composition on Performance in Metallic Iron–nickel–cobalt Ternary Anodes for Alkaline Water Electrolysis, ACS Catal. 10 (2020) 12139–12147.
[52] H. Zhang, J. Zheng, Y. Chao, K. Zhang, Z. Zhu, Surface engineering of FeCo-based electrocatalysts supported on carbon paper by incorporating non-noble metals for water oxidation, New J. Chem. 42 (2018) 7254–7261.
[53] R.D.L. Smith, M.S. Prévot, R.D. Fagan, S. Trudel, C.P. Berlinguette, Water Oxidation Catalysis: Electrocatalytic Response to Metal Stoichiometry in Amorphous Metal Oxide Films Containing Iron, Cobalt, and Nickel, J. Am. Chem. Soc. 135 (2013) 11580–11586.
[54] F. Le Formal, N. Guijarro, W.S. Bourée, A. Gopakumar, M.S. Prévot, A. Daubry, L. Lombardo, C. Sornay, J. Voit, A. Magrez, P.J. Dyson, K. Sivula, A Gibeon meteorite yields a high-performance water oxidation electrocatalyst, Energy Environ. Sci. 9 (2016) 3448–3455.
[55] L. Trotochaud, S.L. Young, J.K. Ranney, S.W. Boettcher, Nickel-Iron Oxyhydroxide Oxygen-Evolution Electrocatalysts: The Role of Intentional and Incidental Iron Incorporation, J. Am. Chem. Soc. 136 (2014) 6744–6753.
[56] F. Dionigi, J. Zhu, Z. Zeng, T. Merzdorf, H. Sarodnik, M. Gliech, L. Pan, W.-X. Li, J. Greeley, P. Strasser, Intrinsic Electrocatalytic Activity for Oxygen Evolution of Crystalline 3d-Transition Metal Layered Double Hydroxides, Angew. Chem. Int. Ed. 60 (2021) 14446–14457.
[57] M. Görlin, P. Chernev, J. Ferreira de Araújo, T. Reier, S. Dresp, B. Paul, R. Krähnert, H. Dau, P. Strasser, Oxygen Evolution Reaction Dynamics, Faradaic Charge Efficiency, and the Active Metal Redox States of Ni–Fe Oxide Water Splitting Electrocatalysts, J. Am. Chem. Soc. 138 (2016) 5603–5614.
[58] Z. Yu, Y. Bai, G. Tsekouras, Z. Cheng, Recent advances in Ni-Fe (Oxy)hydroxide electrocatalysts for the oxygen evolution reaction in alkaline electrolyte targeting industrial applications, Nano Select 3 (2022) 766–791.
[59] M.T. de Groot, Alkaline water electrolysis: with or without iron in the electrolyte? Curr. Opin. Chem. Eng. 42 (2023) 100981.
[60] I. Spanos, J. Masa, A. Zeradjanin, R. Schlögl, The Effect of Iron Impurities on Transition Metal Catalysts for the Oxygen Evolution Reaction in Alkaline Environment: Activity Mediators or Active Sites? Catal. Lett. 151 (2021) 1843–1856.
[61] S. Anantharaj, S. Kundu, S. Noda, "The Fe Effect": A review unveiling the critical roles of Fe in enhancing OER activity of Ni and Co based catalysts, Nano Energy 80 (2021) 105514.
[62] J. Gallenberger, H. Moreno Fernández, A. Alkemper, M. Li, C. Tian, B. Kaiser, J. P. Hofmann, Stability and decomposition pathways of the NiOOH OER active phase of NiOx electrocatalysts at open circuit potential traced by ex situ and in situ spectroscopies, Catal. Sci. Technol. 13 (2023) 4693–4700.
[63] A.M. Ullman, C.N. Brodsky, N. Li, S.-L. Zheng, D.G. Nocera, Probing edge site reactivity of oxidic cobalt water oxidation catalysts, J. Am. Chem. Soc. 138 (2016) 4229–4236.
[64] X. Zhao, H. Ren, L. Luo, Gas Bubbles in Electrochemical Gas Evolution Reactions, Langmuir 35 (2019) 5392–5408.
[65] D. Zhang, K. Zeng, Evaluating the Behavior of Electrolytic Gas Bubbles and Their Effect on the Cell Voltage in Alkaline Water Electrolysis, Ind. Eng. Chem. Res. 51 (2012) 13825–13832.

[66] H.A. El-Sayed, A. Weiß, L.F. Olbrich, G.P. Putro, H.A. Gasteiger, OER Catalyst Stability Investigation Using RDE Technique: A Stability Measure or an Artifact? J. Am. Chem. Soc. 166 (2019) F458.
[67] M. Polyakov, A.-E. Surkus, A. Maljusch, S. Hoch, A. Martin, Impact of the Co: Cu Ratio in CoCu-Containing Oxidic Solids on their Activity for the Water-Splitting Reaction, ChemElectroChem 4 (2017) 2109–2116.
[68] D. Hollmann, N. Rockstroh, K. Grabow, U. Bentrup, J. Rabeah, M. Polyakov, A.-E. Surkus, W. Schuhmann, S. Hoch, A. Brückner, From the Precursor to the Active State: Monitoring Metamorphosis of Electrocatalysts During Water Oxidation by In Situ Spectroscopy, ChemElectroChem 4 (2017) 2117–2122.
[69] T. Swathi, G. Buvaneswari, Application of NiCo2O4 as a catalyst in the conversion of p-nitrophenol to p-aminophenol, Mater. Lett. 62 (2008) 3900–3902.
[70] J. Hnát, M. Plevová, J. Žitka, M. Paidar, K. Bouzek, Anion-selective materials with 1,4-diazabicyclo[2.2.2]octane functional groups for advanced alkaline water electrolysis, Electrochim. Acta 248 (2017) 547–555.
[71] M. Plevová, J. Hnát, J. Žitka, L. Pavlovec, M. Otmar, K. Bouzek, Optimization of the membrane electrode assembly for an alkaline water electrolyser based on the catalyst-coated membrane, J. Power Sources 539 (2022) 231476.

Publication 2

Pre-treated carbon additive enables reduction of metal loading in CoNiFe oxide-based OER electrocatalysts while maintaining performance

Trang Minh Pham, Na Liu, Stephan Bartling, Nils Rockstroh, Reinhard Eckelt, Wen Ju, Annette-Enrica Surkus*, Robert Francke*.

DOI: 10.1016/j.jcat.2025.116299

Abstract: Mixed oxides (MO) of Co, Ni, and Fe have emerged as promising catalysts for the oxygen evolution reaction (OER) in alkaline water electrolysis (AWE). Although they are significantly cheaper than the precious metal catalysts used for proton exchange membrane (PEM) water splitting, the limited availability of Co and the exceptionally poor environmental footprint of Co and Ni mining remain challenges for scaling up AWE capacities. In this context, we present a promising approach toward reducing the metal content while preserving the catalytic performance. Based on a recent work on $CoNiFeO_x$ OER catalysts from our group, admixture of pre-treated Vulcan carbon XC-72R (VC) at different synthesis stages in various loadings was evaluated in view of material structure and electrocatalytic activity. Attractive performance characteristics were obtained for the optimized MO-VC composite material, *e.g.*, a mass activity of 370 A g^{-1}_{CoNiFe} at 1.56 V vs. RHE and a Tafel slope of 39.0 mV dec^{-1}. Stable long-term performance under practical AWE conditions was confirmed in an anion exchange membrane (AEM) electrolyzer. An understanding of the effect of carbon admixture was achieved by combining *in situ* X-ray absorption spectroscopy, analysis of the electrochemically active surface area, as well as electrochemical impedance spectroscopy. The results point toward a benign impact of carbon admixture on the electronic structure of the MO domains under potential bias.

Author contribution: I planned and performed experimental works, including synthesis, optimization of catalysts as well as electrochemical measurements under both RDE and MEA conditions. In addition, I evaluated all analytical data, wrote the first draft of the manuscript and supporting information. My contribution approximately amounts to 75%.

Signature of the student

(Trang Minh Pham)

Signature of the supervisor

(Prof. Dr. Robert Francke)

Journal of Catalysis 450 (2025) 116299

Contents lists available at ScienceDirect

Journal of Catalysis

journal homepage: www.elsevier.com/locate/jcat

Research article

Pre-treated carbon additive enables reduction of metal loading in CoNiFe oxide-based OER electrocatalysts while maintaining performance

Trang Minh Pham, Na Liu, Stephan Bartling, Nils Rockstroh, Reinhard Eckelt, Wen Ju, Annette-Enrica Surkus *, Robert Francke *

Leibniz Institute for Catalysis, Albert-Einstein-Straße 29a, Rostock 18059, Germany

ARTICLE INFO

Keywords:
Alkaline water electrolysis
Oxygen evolution reaction
Electrocatalyst
Cobalt
Nickel
Iron
Carbon additive
Metal content

ABSTRACT

Mixed oxides (MO) of Co, Ni, and Fe have emerged as promising catalysts for the oxygen evolution reaction (OER) in alkaline water electrolysis (AWE). Although they are significantly cheaper than the precious metal catalysts used for proton exchange membrane (PEM) water splitting, the limited availability of Co and the exceptionally poor environmental footprint of Co and Ni mining remain challenges for scaling up AWE capacities. In this context, we present a promising approach toward reducing the metal content while preserving the catalytic performance. Based on a recent work on $CoNiFeO_x$ OER catalysts from our group, admixture of pre-treated Vulcan carbon XC-72R (VC) at different synthesis stages in various loadings was evaluated in view of material structure and electrocatalytic activity. Attractive performance characteristics were obtained for the optimized MO-VC composite material, *e.g.*, a mass activity of 370 A g^{-1}_{CoNiFe} at 1.56 V vs. RHE and a Tafel slope of 39.0 mV dec^{-1}. Stable long-term performance under practical AWE conditions was confirmed in an anion exchange membrane (AEM) electrolyzer. An understanding of the effect of carbon admixture was achieved by combining *in situ* X-ray absorption spectroscopy, analysis of the electrochemically active surface area, as well as electrochemical impedance spectroscopy. The results point toward a benign impact of carbon admixture on the electronic structure of the MO domains under potential bias.

1. Introduction

Hydrogen production through electrochemical water splitting powered by renewable energy is considered as one of the key building blocks in establishing a carbon–neutral economy [1–3]. Although it is the cathodic hydrogen evolution reaction (HER) that leads to the product of interest, considerable efforts are devoted to the development of catalysts for the anodic oxygen evolution reaction (OER). This is primarily caused by the slow kinetics of the four-electron OER, which represents the bottleneck of the water splitting process [4–7]. Consequently, developing OER electrocatalysts towards low overpotentials, high mass activity, and improved stability is one of the keys to further optimizing the efficiency of water electrolysis [8,9].

Compared to the already well-established proton exchange membrane (PEM) water splitting, alkaline water electrolysis (AWE) is a less prevalent but promising alternative, since instead of expensive Ir- and Ru-based catalysts, cheaper and readily available alternatives such as Co, Ni and Fe can be employed [10–13]. Recently, significant progress has been made in the field of AWE through the development of increasingly stable anion exchange membranes (AEM), with the prospect of establishing efficient and durable AEM electrolyzers in the foreseeable future [10,14]. This development has given fresh impetus to AWE research, bringing OER electrocatalysts based on Ni, Co and Fe into the focus [15–18]. The three metals are usually applied as oxides or oxyhydroxides, with $CoFeO_x$, $FeNiO_x$ and $CoFeNiO_x$ showing particularly good OER performance [19,20]. The outstanding catalytic properties were deduced from a volcano-type relationship between activity and binding energies of oxygen intermediates, whereby mixed Co, Ni, and Fe oxides are located near the top of the volcano curve [21–23].

In a recent paper, we have presented a promising and straightforward method for preparing Co-Ni-Fe oxides as OER electrocatalysts based on a citrate sol–gel approach (Fig. 1) [24]. It was found that the key to strong catalytic performance is thermal treatment under oxygen-deficient atmosphere (M), which renders superior electrocatalytic properties compared to reductive (H) and aerobic conditions (A), respectively. A comprehensive study on the impact of the metal

* Corresponding authors.
E-mail addresses: annette-enrica.surkus@catalysis.de (A.-E. Surkus), robert.francke@catalysis.de (R. Francke).

https://doi.org/10.1016/j.jcat.2025.116299
Received 27 March 2025; Received in revised form 26 May 2025; Accepted 23 June 2025
Available online 26 June 2025

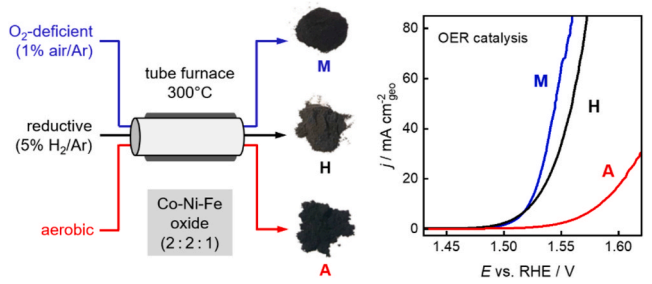

Fig. 1. Summary of our previous study on the influence of thermal treatment and metal ratio on the performance of $CoNiFeO_x$-based OER electrocatalysts [24].

composition showed that Co : Ni : Fe in a ratio 2 : 2 : 1 (denoted as CoNiFe (2:2:1)/M in our previous work) renders optimum performance. Using the optimized material, attractive performance characteristics were obtained, *e.g.*, an overpotential of 291 mV at 10 mA cm^{-2} (η_{10}) and a Tafel slope of 32 mV dec^{-1}. The combined results of electroanalytical studies and structural characterization suggest that performance enhancement through oxygen-deficient annealing can be mostly ascribed to a higher electrochemically active surface area, which does not significantly diminish under OER conditions in contrast to samples prepared by reductive and aerobic treatment, respectively.

Although Co-, Ni-, and Fe-based OER electrocatalysts are significantly cheaper than the precious metals used in PEM electrolysis, issues related to cost of materials are also foreseeable in the future. Thus, a shortage of the rare Co metal can be expected due to the increasing demand for production of Li ion batteries [25,26] and limited number of deposits [27]. Further issues are associated with the exceptionally poor environmental footprint of Co and Ni mining [28,29]. Consequently, reducing the metal content while minimizing the loss of performance is a worthy goal for further improvement of our $CoNiFeO_x$ system. In this context, carbon-based materials as widespread supports for HER [30–34] and ORR [35] catalysts are interesting candidates that may enable cost-effective "dilution" of the mixed metal oxide. In fact, the use of carbon-supported OER catalysts in alkaline media has already been successfully demonstrated by others [36–40]. Depending on the materials investigated, positive properties such as excellent electrical conductivity and high porosity at a low price are usually emphasized [41]. On the other hand, a fundamental challenge is that carbon becomes thermodynamically unstable at potentials higher than its equilibrium potential of 0.207 V vs. the reversible hydrogen electrode (RHE) [42]. However, recent studies have suggested that the carbon oxidation reaction (COR) is effectively suppressed when working in alkaline environment [43] and that COR can be further reduced by combining carbon with a highly effective OER electrocatalyst ("activity-durability coincidence" of OER in the presence of COR) [44,45]. Further works demonstrate that under certain conditions, passivation can stabilize graphitic carbon kinetically [46] and that metal oxide–carbon composites can work effectively as OER electrocatalysts in AEM water electrolysis for more than 1100 h at 200 mA cm^{-2} and 80 °C without performance loss [47]. In view of these encouraging findings, we opted to investigate the influence of carbon additives on the OER behavior of our $CoNiFeO_x$ system.

Herein, we present a study on the effect of "diluting" our $CoNiFeO_x$ electrocatalyst with Vulcan XC-72R carbon black (VC). The latter was selected as a popular material from battery and fuel cell research with excellent electrochemical properties, i.e., high electric conductivity (31 ± 5 S cm^{-1}), high purity, low sulfur contamination, good processability, and high BET surface area (207 ± 4 m^2 g^{-1}) [38,48–51]. In addition, VC showed good performance and particularly low susceptibility toward COR in several recent OER and ORR studies [45,48–50]. To mitigate the hydrophobicity of the material [52] and to explore potential benefits on OER performance [51] including higher surface area and better interaction with the OER catalyst, oxidative pre-treatment of VC was applied and evaluated. A further focus of our study is the impact of the composite preparation method, whereby carbon was introduced during the sol–gel step and during ink-preparation, respectively. The effects of VC modification and composite preparation method were monitored by electroanalytical studies under RDE conditions as well as through structural characterization before and after electrolysis. Despite significant reduction of the metal content in the as-prepared materials, a stable performance was achieved. Finally, high activity and stability of the optimized $CoNiFeO_x$–VC composite was demonstrated at practically relevant current density in an AEM electrolyzer.

2. Results and discussion

2.1. Catalyst preparation

The composite materials studied in this work consist of a mixed CoNiFe oxide and conductive Vulcan XC-72R carbon black particles. The metal oxide component is based on the catalyst material from our previous study with best OER performance [24], CoNiFe (2:2:1)/M, whereby 2:2:1 refers to the stoichiometric ratio between the three metals and M for the oxygen-deficient thermal treatment of the catalyst precursor. The precursors were prepared from the corresponding metal nitrates in presence of citric acid using our sol–gel approach (Fig. 2) [24]. Either unmodified carbon black (CB, particle size of 20–50 nm) or carbon black pre-treated with aq. HNO_3 (CM) [53] was added to the metal nitrate solution prior to gel formation. The precursors were subjected to the same thermal treatment conditions as in the previous report (300 °C, 1 vol% air in argon).

To systematically study the impact of the reduced metal content, composites with various mass ratios between CoNiFe oxide and carbon additive were prepared (for details, see the Experimental Section and Table S1 in the SI). In the following, the different materials are denoted as MO/CB or MO/CM, whereby MO refers to the mixed oxide (CoNiFe (2:2:1)/M), CB to carbon black, and CM to carbon black pre-treated with aq. HNO_3. In addition, each sample denomination contains a number *x* that represents the mass percentage of metal oxide in the material (*e.g.*, 60MO/CM). The compositions of the materials determined by elemental analysis are summarized in Table S2. After thermal treatment, inks were prepared from the MO-carbon composites and a binder, followed by deposition on the electrode surface for electrochemical studies. For comparison, catalyst series *x*MO + CB and *x*MO + CM were prepared by mixing MO with carbon particles *after* thermal treatment using a mortar. The resulting mixtures were then used for ink preparation and electrode coating under the same conditions.

2.2. Structural characterization

Structural characterization of the as-prepared composite materials was carried out using powder X-ray diffraction (PXRD), X-ray photoelectron spectroscopy (XPS), scanning electron microscopy (SEM), energy-dispersive X-ray spectroscopy (EDX), scanning transmission

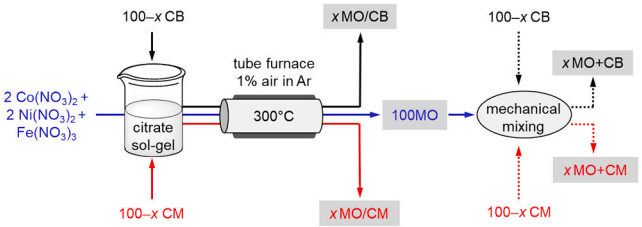

Fig. 2. Schematic illustration of the preparation of catalyst 100MO and the xMO/CB, xMO/CM, xMO + CB, and xMO + CM series. MO = metal oxide. Metal oxide content (wt. %): x = 100, 80, 60, 40, 20. CB = unmodified carbon black. CM = pre-treated carbon black.

electron microscopy (STEM), electron energy loss spectroscopy (EELS), Raman spectroscopy (RS), X-ray absorption spectroscopy (XAS), and Fourier transform infrared (FTIR) spectroscopy. As exemplarily shown in Fig. 3a, PXRD patterns of 100MO (corresponds to CoNiFe (2:2:1)/M in ref. [24]), 60MO/CB, and 60MO/CM exhibit similar patterns with broad diffraction peaks at 16.3°, 19.1°, and 27.3° that are typical for the (111), (200), and (220) planes of CoO, NiO, and FeO (for details, see Fig. S2). An additional peak at 11.1° occurs for the two carbon-containing samples, which indicates the presence of graphite oxide [54,55]. The presence of graphitic domains is confirmed for both the CB and the CM samples by characteristic Raman bands at 1310 cm^{-1} and 1595 cm^{-1} (Fig. S20a-b), whereby the former reflects the well-ordered bonding environment of sp^2-hybridized carbon and the latter is caused by defects in the graphitic structure [56].

XPS was carried out to provide information about the valence states and chemical composition of the catalyst surface. Due to the strong overlap of photoelectron lines and intense Auger peaks we focus on a qualitative analysis here. For 100MO, 60MO/CB, and 60MO/CM, the Co 2p and O 1s regions are shown exemplarily in Fig. 3b and c, while the Ni 2p, Fe 2p, and C 1s regions are summarized in Fig. S7 and Table S4. The Co 2p region of the catalyst with (CM and CB) and without carbon is composed of two main peaks associated with Co $2p_{3/2}$ and Co $2p_{1/2}$ orbitals together with two intense satellite features on the high binding energy side of each peak. As discussed in our previous work [24], the shoulders at lower binding energies are probably caused by Auger peaks of Fe and Ni which are present in this region. All catalysts show the Co $2p_{3/2}$ peak at 781.1 eV together with pronounced satellite features, which suggests the presence of Co^{2+} probably as CoO or $Co(OH)_2$ [57]. However, compared to the literature dealing with monometallic oxides [57], the observed Co 2p binding energies are slightly shifted to higher values here. The interaction with other elements present in this catalyst (Ni and Fe) probably leads to this shift. The Ni 2p (mainly Ni^{2+}) and Fe 2p spectra of the three catalysts are discussed in detail in the SI.

The high-resolution scans of the O 1s regions for all three samples (Fig. 3c) show a similar shape with two main peaks at binding energies of 529.9 eV and 531.6 eV, respectively, corresponding to lattice metal–oxygen ($M–O_x$) and to metal hydroxides/defective oxides, respectively [58,59]. All samples present a much stronger signal for hydroxides/defective oxides than for lattice oxide (the presence of M–OH is further confirmed for all three samples by FTIR spectroscopy, see Fig. S20c). While for samples 100MO and 60MO/CM the same binding energies are observed for both peaks, 60MO/CB shows a slightly higher binding energy for the second peak at 531.8 eV.

According to the XPS results, the impact of added carbon on the surface metal oxide composition (and valence states) seems to be negligible, which is in line with results obtained by K-edge XAS. Within the Co K edge regime, 100MO and 60MO/CM exhibit basically the same XANES profile (Fig. 3d). A similar outcome is also observed for the Ni

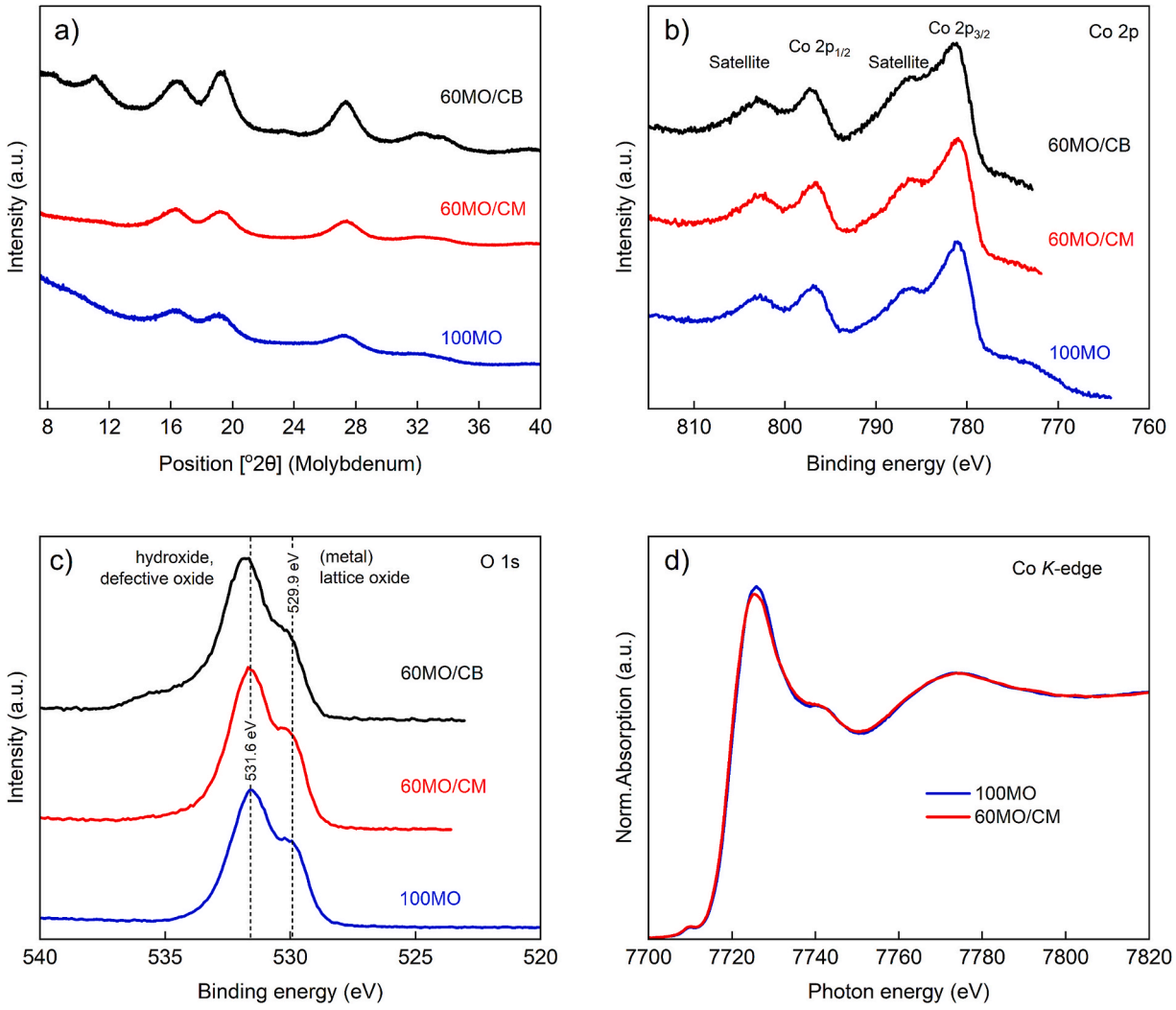

Fig. 3. Structural characterization of 100MO (blue), 60MO/CM (red), and 60MO/CB (black). (a) Powder X-ray diffraction patterns. (b) Co 2p and (c) O 1s XP spectra. (d) Co K-edge XANES analysis. (For interpretation of the references to colour in this figure legend, the reader is referred to the web version of this article.)

and Fe K edge when comparing the data of 100MO and 60MO/CM (Fig. S45). The oxidation states of the three metals within both as-prepared materials are ~2.3 (Co), ~2.1 (Ni), and ~2.0 (Fe) according to XANES analysis (Figs. S44 and S45). Consequently, the electronic structures of the mixed metal oxide component within 60MO/CM powder seem to resemble as-prepared 100MO.

SEM analysis was performed for 60MO/CM, 60MO/CB, 60MO + CM, 60MO + CB, and 100MO (Figs. S8–S12). The samples in which the carbon particles were added only after thermal treatment (60MO + CM and 60MO + CB) show a strong segregation into different domains, which is shown exemplarily for 60MO + CB in Fig. 4a (bright domains are caused by backscattering of electrons through elements with high atomic number, here likely by Co, Ni, and Fe). In contrast, composites that were prepared by adding carbon during the sol–gel step do not show such separated domains, as exemplified for 60MO/CM in Fig. 4b. Samples 60MO/CM and 60MO/CB were additionally examined using STEM coupled to EDX and EELS (Figs. S13–S19). The exemplary STEM image of 60MO/CM in Fig. 4c shows a homogeneous distribution of the elements Co, Ni, Fe, and C across the particle (see EDX mappings in Figs. 4e–g and S14c). Fig. 4d clearly shows nanocrystalline domains of $CoNiFeO_x$ present on carbon. In principle, formation of a $CoNiFeO_x$/carbon composite could be confirmed by electron microscopic techniques, with the main structural features of the metal oxide found in 100MO being retained. A detailed discussion of the findings is provided in the SI.

Specific surface area (S) and conductivity of the as-prepared materials were investigated using BET analysis (Table S3) and impedance spectroscopy (Table S6). With higher carbon content, both the xMO/CM and xMO/CB series show increased S_{BET} (up to 211 $m^2\ g^{-1}$) compared to 100 MO (80 $m^2\ g^{-1}$), although the surface-increasing effect becomes

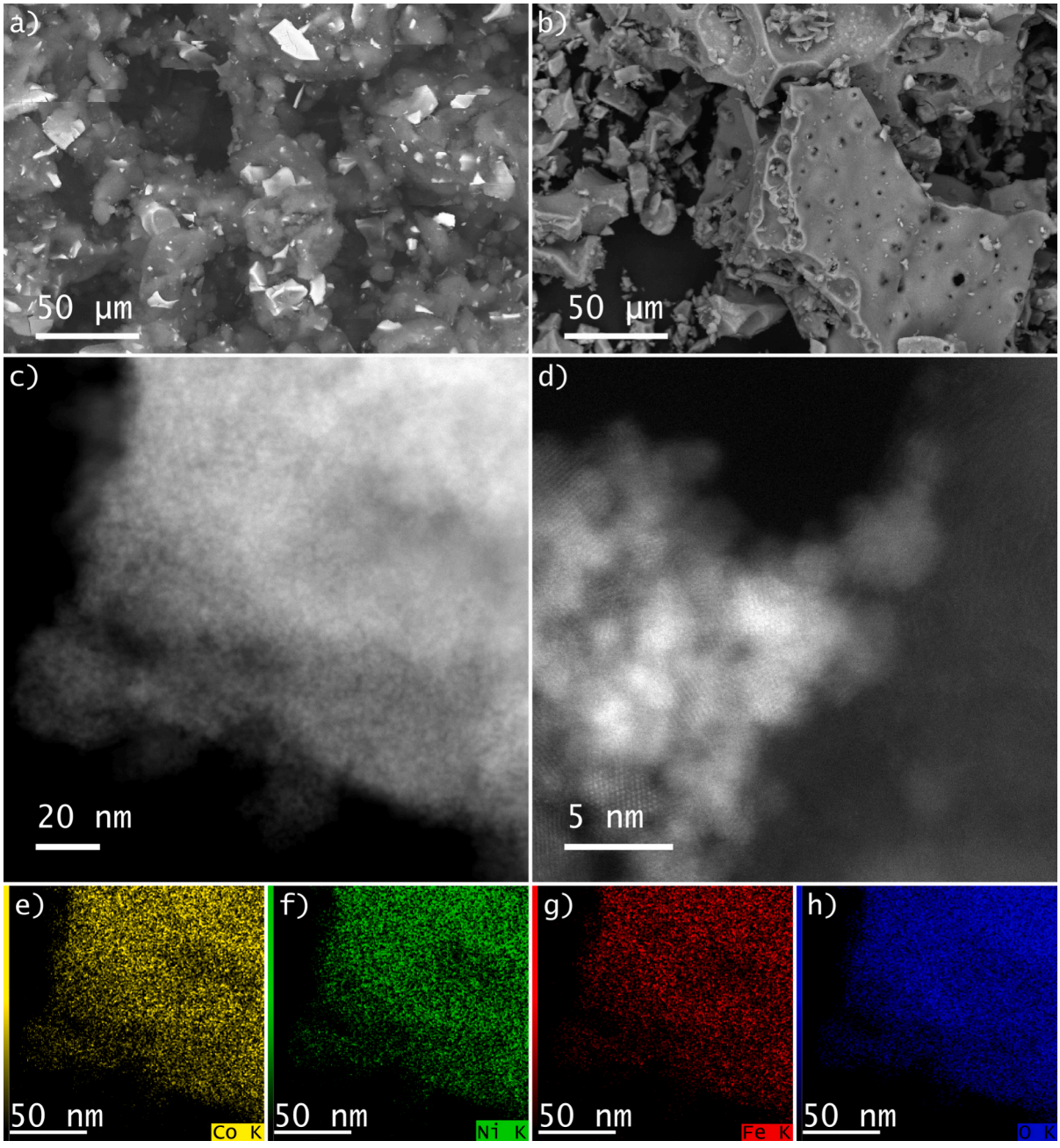

Fig. 4. Top row: SEM images of as-prepared 60MO + CM (a) and 60MO/CM (b) (BSE detector). Central row: STEM-HAADF images of 60MO/CM at different magnifications (c, d). Bottom row: EDX elemental mapping of image (c) showing the distribution of Co (e), Ni (f), Fe (g), and O (h).

significantly pronounced only below $x = 60$. Furthermore, an increase in average pore size d (up to 49 nm) and mesopore volume V_m (up to 0.56 $cm^3\ g^{-1}$) with increasing CB or CM content is clearly visible. This effect is stronger for MO-carbon composites that were prepared by mechanical mixing (xMO + CB and xMO + CM) than for the samples that were prepared by adding carbon during the sol–gel process (xMO/CB and xMO/CM).

The S_{BET}, V_m, and d values of selected samples, i.e., 60MO/CB, 60MO/CM, 60MO + CB, 60MO + CM, and 100MO are summarized in Table 1 along with the electrical conductivity of the as-prepared powders (for details on conductivity analysis, see the Experimental Section). A comparison of the conductivities shows that CM renders lower values than CB, which is likely due to the oxidative pre-treatment and the resulting decrease of the fraction of sp^2-hybridized (graphitic) carbon [53]. Moreover, it becomes clear that mechanical mixing of MO and carbon particles (60MO + CB and 60MO + CM) is beneficial for conductivity compared to adding carbon during the sol–gel step (60MO/CB and 60MO/CM).

2.3. OER performance evaluation under RDE conditions

The electrocatalytic study was initiated with linear sweep voltammetry (LSV) using a glassy carbon RDE in a 1.0 M KOH electrolyte. The electrode was coated *via* drop-casting of a Nafion-containing ink (for details, see the Experimental Section). In the following, the influence of the carbon additives (CB, CM) in different mass ratios relative to MO is discussed along with the impact of the composite preparation approach (compare Fig. 2). More specifically, addition of carbon particles at the beginning of the sol–gel procedure (MO/CB and MO/CM series) is compared to mechanical mixing of as-prepared $CoNiFeO_x$ with carbon particles using a mortar, followed by preparation of catalyst ink (MO + CB and MO + CM series). For all measurements, the same mass of $CoNiFeO_x$/C composite was applied to the electrode surface, resulting in varying metal oxide loadings depending on the degree of "dilution" with carbon.

LSVs were recorded at 1800 rpm ($\nu = 1$ mV s^{-1}) for composites with different MO content (80 %, 60 %, 40 %, and 20 %) for series MO/CB, MO/CM, MO + CB, and MO + CM. While all results are summarized in Figs. S21, S23, and S24, exemplary LSVs of 60MO/CB, 60MO/CM, 60MO + CB, and 60MO + CM are shown in Fig. 5a-b together with the LSV of pure metal oxide catalyst (100MO). Fig. 5a shows the mass specific activity related to the metal oxide content, whereas in Fig. 5b, the current density was calculated with respect to the geometrical electrode surface area. The current densities at 1.56 V vs. RHE and overpotentials at 10 mA cm^{-2}_{geo} extracted from the LSVs of the four composite series are summarized in Fig. 5c. Mass specific activities, current densities and overpotentials (η_{10}) are summarized in Table S6 for all catalysts.

At first glance, a comparison of the different samples shows that most carbon composites perform significantly worse than the pure metal oxide (Fig. 5c). However, some of the "carbon-diluted" materials have a performance comparable to 100MO despite significantly lower metal content. Although 100MO renders the highest current density (Fig. 5b), catalyst 60MO/CM, for example, provides a higher mass activity (A g^{-1}_{CoNiFe}) at 1.56 V with only 60 % metal oxide content (Fig. 5a). When comparing 60MO/CM with 60MO + CM and 60MO/CB with 60MO + CB, it becomes apparent that introducing the carbon already during the sol–gel process leads to better results than only during ink preparation (Fig. 5-b). For example, the mass specific activity at 1.56 V drops by almost 80 % when replacing 60MO/CM with 60MO + CM, while η_{10} increases by more than 20 mV. A possible explanation for the superior performance of the MO/CM and MO/CB materials is that a more intimate mixing of the two components is achieved with the integrated sol–gel process and heat treatment, leading to improved contact between the MO and CM domains (see also SEM images in Fig. 4a-b, Fig. S9, and Fig. S11), and allowing the carbon to effectively contribute to current flow as conductivity-enhancing additive. Superior performance of the MO/CM and MO/CB materials is also reflected by the Tafel slopes (Fig. 5d and Fig. S25).

A further prerequisite for good performance is the chemical pretreatment of carbon particles, as 60MO/CM performs significantly better than 60MO/CB (Fig. 5-b). This trend is also confirmed by comparing the activities and overpotentials of other congeners of the MO/CB and MO/CM series (see Fig. 5c) and the Tafel slopes in Figs. 5d and S25. A possible explanation is that the increased and more hydrophilic surface allows a stronger binding to the metal oxide during composite formation. Moreover, a sufficiently high MO content within the composite is required for good catalytic activity. While very good results can be achieved with 80MO/CM and 60MO/CM, the overpotentials and current densities are significantly worse for 40MO/CM and 20MO/CM (Fig. 5c). Finally, it should be noted that despite the good mass specific activity, the admixture of carbon does in principle decrease the geometrical LSV current density under RDE conditions (Fig. 5b). This may be attributed to a decrease of the number of active sites by "dilution" with carbon.

From Fig. 5c, it can be concluded that the group located at the top left of the diagram (60MO/CM, 80MO/CM, and 100MO) exhibits the most promising catalytic properties. Catalyst 60MO/CM represents a particularly auspicious candidate, as it achieves a high mass specific activity of 369.9 A g^{-1}_{CoNiFe} at 1.56 V and a small η_{10} of 297 mV at low metal oxide content. This impression is further confirmed by chronopotentiometric profiles recorded at 10 mA cm^{-2}_{geo} (Fig. 5e; further measurements are summarized in Figs. S21d, S23d, S24d, and Table S6). Again, 60MO/CM shows a behavior similar to 100MO and superior to 60MO/CB, starting at relatively low potential without significant changes within 15 min. Not surprisingly, the samples 60MO + CB and 60MO + CM show clearly inferior profiles compared to 100MO, 60MO/CM, and 60MO/CB (Fig. S21d).

Interestingly, long-term chronopotentiometric analysis at higher current density, i.e., 50 mA cm^{-2}_{geo} (Fig. S28a) and 100 mA cm^{-2}_{geo} (Fig. 5f), shows that 60MO/CM performs even better under high stress compared to 100MO. 60MO/CM starts at $\eta_{100} = 240$ mV and exhibits a stable profile with a potential increase of less than 5 mV after 7 days. In contrast, 100MO shows a stronger potential increase (~45 mV) after starting at a higher η_{100} value (262 mV). Since Ni foam is frequently used in AEM electrolyzers as OER catalyst support, the long-term measurement was repeated with 60MO/CB using a Ni RDE under otherwise identical conditions (Fig. 5f). Starting at a higher potential compared to the GC RDE, a similar potential was achieved after 7 days.

To further probe the performance of 60MO/CM at high stress, an on–off chronopotentiometric analysis with 3 h intervals was carried out with current densities of 10, 20, 50, and 100 mA cm^{-2}_{geo} at $\omega = 1800$ rpm (Fig. 5g). Despite harsh conditions and strong bubble formation, the catalyst exhibits stable plateaus during the 3 h intervals. In contrast, 100MO is much less stable under these conditions, as in several trials, the experiment had to be aborted due to potential overloads at the 50 mA cm^{-2}_{geo} step (see Fig. S29). In general, the potential-time profile can be affected both by catalyst degradation and by development of micro- and nanobubbles within the pores which cannot be removed by electrode

Table 1
Summary of surface areas (S_{BET}), mesopore volumes (V_m), average pore sizes (d), and conductivity values for selected materials.

Sample	S_{BET} [$m^2\ g^{-1}$]	V_m [$cm^3\ g^{-1}$]	d [nm]	conductivity [S cm^{-1}]
100MO	80.3	0.04	1.6	0
60MO + CB	106.7	0.36	49.0	28.9
60MO + CM	89.6	0.29	48.1	6.0
60MO/CB	91.1	0.17	3.3	3.3
60MO/CM	89.6	0.11	3.3	2.1

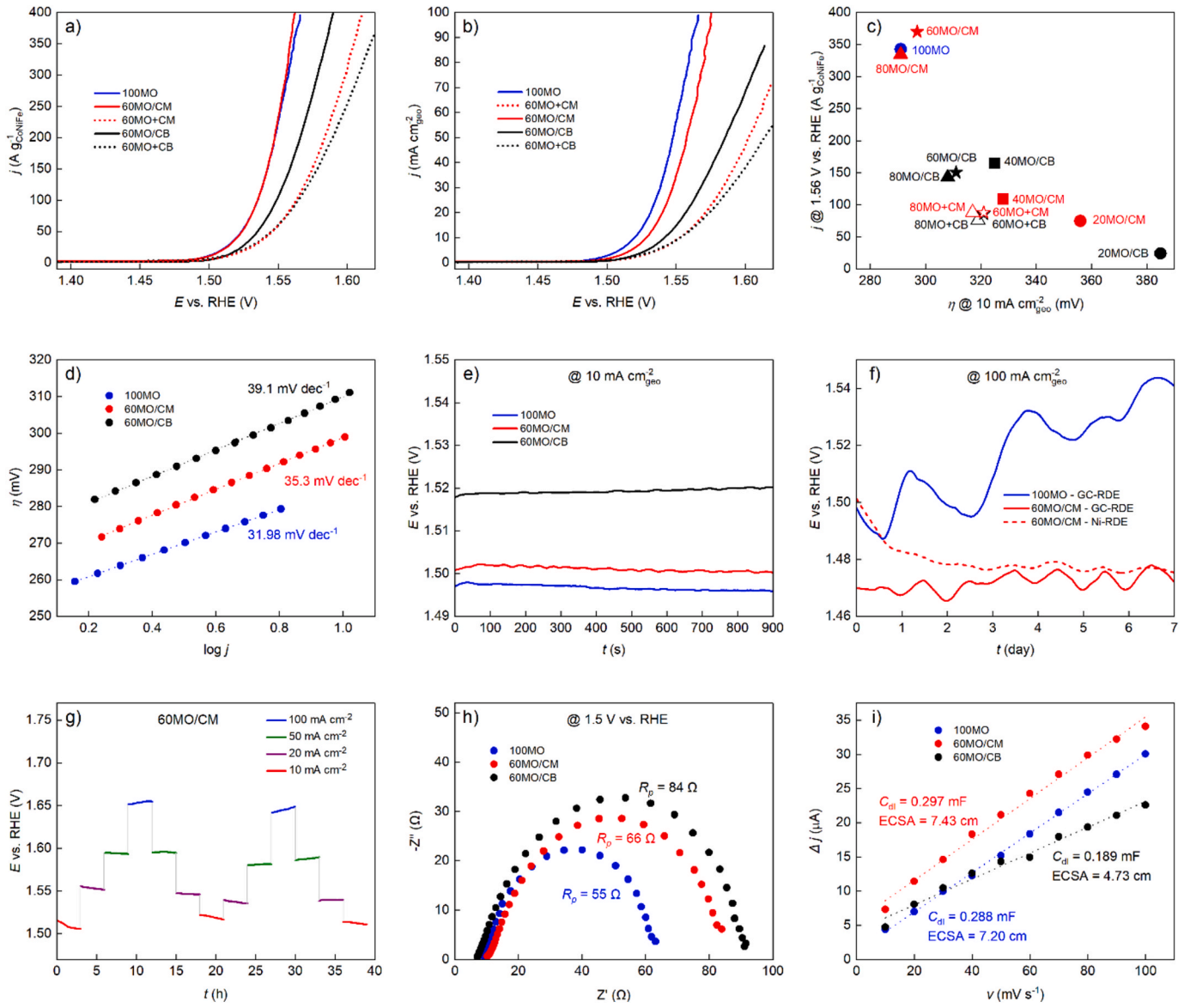

Fig. 5. (a-b) OER polarization curves measured in 1.0 M KOH solution (v = 1 mV s^{-1}, ω = 1800 rpm, iR drop corrected) showing the mass activity related to metal oxide content (a) and the current density with respect to the geometrical electrode surface area (b). (c) Comparison of overpotential and mass activity between 100MO and the MO-carbon composite series. (d) Tafel plots extracted from LSVs shown in Fig. 5b. (e) Chronopotentiometric profiles recorded at 10 mA cm^{-2}_{geo} (ω = 1800 rpm). (f) Chronopotentiometric stability tests recorded at 100 mA cm^{-2}_{geo} for 100MO and 60MO/CM on glassy carbon and Ni RDE, respectively (all measured potentials are pH corrected). (g) Stepwise chronopotentiometric stability test carried out at 10, 20, 50, and 100 mA cm^{-2}_{geo} (3 h for each step). (h) Electrochemical impedance spectra (Nyquist plots) recorded for 100MO, 60MO/CB, and 60MO/CM at 1.5 V vs. RHE. (i) Estimation of double layer capacitance (C_{dl}) and electrochemically active surface area (ECSA) via CV in the non-Faradaic regime (for details, see Figs. S22, S26, and S27).

rotation [60,61]. Based on the present data, it cannot be clearly inferred whether the superior long-term performance of 60MO/CM is due to a higher stability or to improved dissipation of gas bubbles. In view of this ambiguity, it should be noted that although RDE conditions are well suited for studying and comparing catalyst properties, the significance of the results is limited with respect to practical conditions in AEM electrolyzers [61]. Consequently, stability and performance of 60MO/CM was also evaluated in an AEM flow cell at 400 mA cm^{-2}_{geo} (see Section 2.5).

To explore the origins of the observed trends, further analytical techniques were applied. Electrochemical impedance spectroscopy (EIS) at 1.5 V (Figs. 5h, S21e, S23e, and S24e) was used to determine the charge transfer resistance R_P. CV was carried out with a stationary electrode in the non-Faradaic regime (Figs. 5i, S21f, S23f, and S24f) to determine the electrochemically active surface areas (ECSA) from the double-layer capacitance (C_{dl}). The R_P and ECSA values of 100MO, 60MO/CM, 60MO/CB, and other samples are summarized in Table S6. The Nyquist plots in Fig. 5h show the same trend as the Tafel slopes in Fig. 5d, i.e., that the charge transfer rate increases in the order 60MO/CB < 60MO/CM < 100MO. The corresponding R_P values obtained from EIS data fitting amount to 85 Ω, 66 Ω, and 55 Ω, indicating *i*) that the presence of carbon slows down OER kinetics at 1.5 V and *ii*), that the decelerating effect is less pronounced for CM than for CB. On the other hand, analysis of C_{dl} shows a slight increase of the ECSA for 60MO/CM compared to 100MO (7.43 cm^2 vs. 7.20 cm^2). In contrast, 60MO/CB exhibits a significantly smaller ECSA (4.73 cm^{-2}), suggesting that the stronger catalytic performance of 60MO/CM compared to 60MO/CB could be a result of the enhanced ECSA.

The better electronic conductivity of 60MO/CM and 60MO/CB

compared to 100MO (*cf.* Table 1) certainly supports the rate of charge transfer and counteracts the reduction in the number of catalytically active sites. Although the oxidative carbon pre-treatment reduces the conductivity of 60MO/CM compared to 60MO/CB (2.1 S cm^{-1} vs. 3.3 S cm^{-1}), it is still significantly higher than that of poorly conducting 100MO. However, interpreting the conductivity values should be exercised with care, since conductivity measurements were performed using dry powder, while ECSA and EIS measurements were carried out in contact with the alkaline electrolyte at potential bias [62]. Under these circumstances, the differences between the electronic conductivities of the powder samples can only serve as a qualitative indication. Overall, 60MO/CM exhibits high ECSA and good conductivity, both of which may partially compensate for the lower number of active centers compared to 100MO.

2.4. Characterization of used catalysts

To better understand the structural changes which 100MO, 60MO/CM, and 60MO/CB undergo under OER conditions, additional electroanalytical and spectroscopic experiments were performed after applying 10 mA cm^{-2}_{geo} for 1 h in 1.0 M KOH (RDE conditions). The first indication can be derived from the change in R_p before and after the galvanostatic measurements (Fig. S30 and Table 2). Surprisingly, the initially lowest polarization resistance of 100MO electrolysis rises by 16 Ω, which corresponds to a 29 % increase. On the other hand, the R_P value of 60MO/CM increases by only 3 Ω (5 %). A similarly small increase in R_P (+2 Ω) is observed for 60MO/CB, albeit at a significantly higher level. As a result, the post-electrolysis R_P values of the catalysts increase in the order 60MO/CM ≈ 100MO < 60MO/CB.

Regarding ECSA, 60MO/CM experiences a loss of 52 %, whereas the value for 100MO decreases by only 15 %. At a first glance, this result appears surprising, as 60MO/CM shows a stable potential-time profile, while the performance of 100MO deteriorates significantly during the galvanostatic stability test (Fig. 5f). However, it must be considered that the ECSA was determined *via* the double layer capacitance which also contains contributions from catalytically inactive carbon domains – the ECSA does therefore not directly translate to the number of active sites. Catalyst 60MO/CB suffers a further loss of 34 % from its already low initial ECSA value. Consequently, the post-electrolysis ECSA values decrease in the order 100MO > 60MO/CM > 60MO/CB (Fig. S31 and Table 2). This finding suggests that despite the decreasing ECSA, the number of active sites and/or OER microkinetics of 60MO/CM remain stable/gradually improve under stress. In contrast, 100MO seems to deteriorate in agreement with the results of the RDE stress test at 100 mA cm^{-2}_{geo} (Fig. 5f).

To analyze the structural changes that occurred under operating conditions, PXRD, SEM-EDX, STEM-EELS, XPS, and XAS measurements were performed. Compared to the pre-electrolysis PXRD results shown in Fig. 3a, used 60MO/CB and 60MO/CM show preserved but significantly broadened peaks around 16°, 19°, and 27° (Fig. 6a). In contrast, these signals vanish completely in the post-electrolysis PXRD pattern of 100MO, indicating that the material has become largely amorphous, whereby minor peaks around 25°, 30°, and 32° may suggest formation of crystalline FeO and Fe_3O_4 domains [24]. Morphology changes of samples 60MO/CB and 60MO/CM according to SEM (Figs. S33-35) and STEM (Fig. S36-43) analysis are comparable to 100MO, whereby EDX mapping indicates that Co, Ni, Fe, and C retain their distribution across the surface.

Table 2
Summary of changes in electrochemical properties of OER electrocatalysts after 1 h polarization at 10 mA cm^{-2}_{geo} in 1.0 M KOH.

Sample	R_P before stability test[a] (Ω)	R_P after stability test[a] (Ω)	ECSA before stability test (cm^2)	ECSA after stability test (cm^2)
100MO	54.9	70.9	7.20 ± 0.07	6.13 ± 0.20
60MO/CM	66.2	69.6	7.43 ± 0.30	3.60 ± 0.12
60MO/CB	84.4	86.4	4.73 ± 0.20	3.13 ± 0.12

[a] R_P measured at 1.5 V vs. RHE.

After the galvanostatic tests, the sample surfaces of 100MO, 60MO/CB, and 60MO/CM were investigated again by XPS. The results for Co 2p, Ni 2p and Fe 2p are shown in Fig. 6b and Fig. S32 (all binding energies are summarized in Table S10). For all samples with (CB and CM) and without carbon, very similar XP spectra can be observed and point toward an oxidic nature of Co, Ni, and Fe after the strongly oxidizing OER conditions. Especially for Co 2p in Fig. 6b, the small satellite features together with the binding energy of the Co $2p_{3/2}$ peak around 780.3 eV indicate the presence of Co as Co_3O_4 [57]. These findings are in line with *ex situ* Co/Ni/Fe *K*-edge XANES data obtained from post-electrolysis 60MO/CM (Fig. S46), which indicate an increase of the Co, Ni, and Fe oxidation states from 2.3 to 3.3, from 2.0 to 2.5, and from 2.0 to 2.9, respectively.

In the O 1s region in Fig. 6c, again two main peaks at binding energies of 529.5 eV and 531.1 eV can be observed. However, in the O 1s XP spectra for 60MO/CM, the peak at 529.5 eV is weaker compared to 100MO (blue), while it almost disappears in the case of sample 60MO/CB (Fig. 6c). The addition of carbon thus seems to change the ratio of lattice oxygen to hydroxide/defective oxygen after the OER. The hydroxide peak is strongly visible for all samples before and after electrolysis.

2.5. Studies in an AEM flow electrolyzer

To approach the industrial standard of alkaline water electrolysis, further studies were carried out in a flow AEM electrolyzer, in which two electrodes were separated by an anion exchange membrane (electrolyte: 1.0 M KOH; $T = 50$ °C; for further details, see the Experimental Section). 60MO/CM was studied as the most promising catalyst from the RDE measurements and compared to 100MO. OER catalysts were deposited on a Ni-foam layer by air spray-coating with a mass loading of 5 mg cm^{-2} related to the geometrical electrode surface area. The influence of the cathode material was investigated by using bare Ni foam as well as different loading of Pt on Vulcan carbon cloth electrodes (Fig. S53). To minimize limitation through HER, carbon cloth with a Pt loading of 0.5 mg cm^{-2} has been identified as a suitable cathode material.

Key results are summarized in Fig. 7. Stepwise increase of current density with a time interval of 10 min for every step was used to evaluate the short-stress stability. Bare Ni foam shows significantly higher potentials at every current density compared to catalyst-loaded electrodes (100MO and 60MO/CM on Ni-foam). With ca. 600 mV, the biggest voltage gap between bare Ni foam and catalyst-loaded electrodes is achieved at 1000 mA cm^{-2}_{geo}. During the reverse scan, cell voltages at 800, 600, 400, 200, 100, and 10 mA cm^{-2}_{geo} show significant improvement compared to the forward scan, confirming the excellent OER activity of 100MO and 60MO/CM under practically relevant conditions. Interestingly, 60MO/CM performs somewhat better than 100MO, which aligns with the RDE chronopotentiometric studies at high current density. The two samples exhibit the same potential at small current densities (2–50 mA cm^{-2}_{geo}), but 60MO/CM renders 50–80 mV lower cell voltages at higher current densities. The influence of the catalyst loading on the anode was also studied (Fig. S54) and is discussed in the Supporting Information.

Long-term stability tests were carried out at 400 mA cm^{-2}_{geo} with 10 intervals of 10 h each (Fig. 7b). During all intervals, the cell voltage is close to 2.0 V. Once more, 60MO/CM shows high activity and stability with little increase in cell voltage within and between the 10 h intervals. During the experiment, the starting voltage is reduced continuously for each 10 h interval. For example, the voltage at the beginning of the tenth

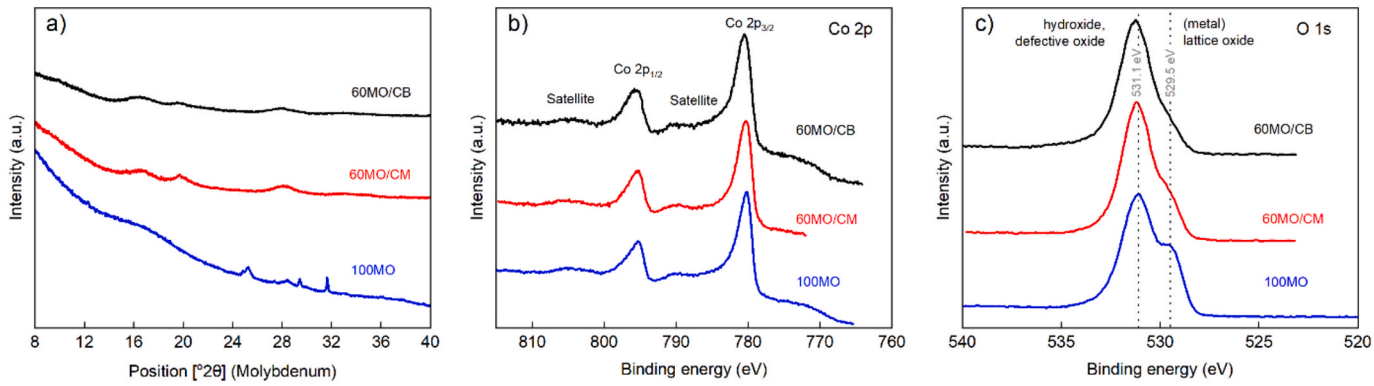

Fig. 6. (a) Powder X-ray diffraction patterns. (b) Co 2p and (c) O 1s XP spectra of 100MO, 60MO/CB, and 60MO/CM after stability tests (10 mA cm^{-2}_{geo}, 1 h, 1.0 M KOH, undivided cell).

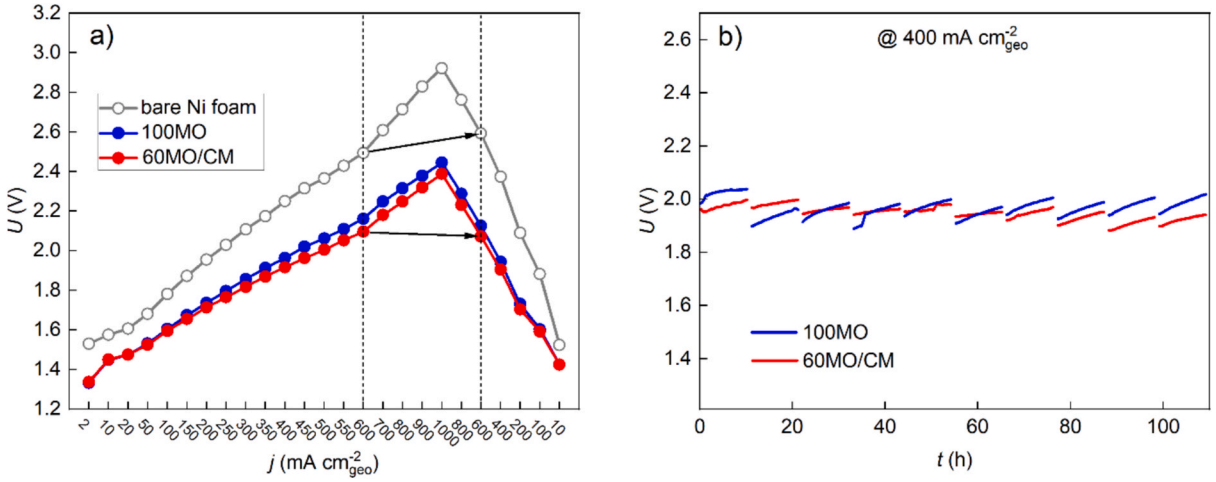

Fig. 7. Results of the flow AEM water electrolyzer studies using bare Ni foam, 100MO/CM on Ni foam, and 60MO/CM on Ni foam as the anode (1.0 M KOH, 50 °C). In all cases, Pt (0.5 mg cm^{-2}) on carbon cloth was used as the cathode. (a) Acquisition of cell voltages at various current densities from 2 mA cm^{-2}_{geo} to 1000 mA cm^{-2}_{geo} (10 min per each point) and step-scanning back to 10 mA cm^{-2}_{geo}. Arrows indicate the potential change during the reverse scan at 600 mA cm^{-2}_{geo}. (b) Stability experiments using 100MO and 60MO/CM, respectively, as OER catalysts at 400 mA cm^{-2}_{geo}.

interval is only 1.89 V and thereby 85 mV smaller compared to the first interval. In contrast, no improvement of the cell voltage is observed after 100 h of load test when 100MO is used. Moreover, compared to 60MO/CM, the pure metal oxide catalyst shows a significantly stronger potential increase during most of the 10 h intervals. Consequently, as in the step-scan experiments shown in Fig. 7a, 60MO/CM renders a better impression during long-term stability test than its carbon free counterpart 100MO.

2.6. *In situ* XAS analysis

To investigate the impact of CM additives on the structural evolution of $CoNiFeO_x$ catalysts (100MO and 60MO/CM) during the OER, *in situ* XAS measurements were conducted in a custom-made spectroelectrochemical (SEC) flow cell using a carbon paper anode as catalyst support. Experimental protocols for synchrotron and electrochemical settings are detailed in the Experimental Section. To optimize fluorescence signal quality, 0.1 M KOH (instead of 1.0 M) was used as standard electrolyte, with applied potentials recalibrated to the RHE scale. Analysis was focused on the K-edge absorption profiles of Co, Ni, and Fe in the 100MO and 60MO/CM catalysts under positive electrode polarization, probing their redox dynamics during OER.

Prior to *in situ* OER studies, reference spectra were recorded for the dry catalyst layer (after ink preparation, spray coating, and electrode mounting in the SEC cell) and for the wet state after exposing the electrode to electrolyte without potential bias (Fig. S48, Table S12). Notably, the Fe species in the 100MO and 60MO/CM materials exhibited a positive shift of the average oxidation state from 2.0 (as-prepared catalyst powder) to ~ 2.9 after spray-coating, likely caused by aerobic oxidation during the ink/spray process. In contrast, the K-edge profiles and average oxidation states for Co and Ni in 100MO and 60MO/CM remained relatively stable between the as-prepared and spray-deposited states.

Spectral evolution was analyzed at several selected critical potentials (Fig. S47) and the results are summarized in Figs. S49–S52 as well as Table S12. A comparison between the average oxidation states of 60MO/CM and 100MO at the OCP (0.76 V) as well as under OER conditions (1.61 V) is shown in Table 3. XANES spectra are shown exemplary for the Co K-edge in Fig. 8. Between 60MO/CM and 100MO, a similar progression of the mean oxidation states can be observed for Ni (from 2.3 to 2.5) and Fe (remains at ~3.0, see Table 3). In contrast, there is a striking difference regarding the Co oxidation states: While 100MO shows an increase from 2.5 to 3.0, 60MO/CM exhibits significantly higher values both at the OCP (3.1) and under OER conditions (3.3).

Based on the available data and a comparison with the literature, some tentative conclusions are possible. First, Fe shows no pronounced redox activity and seems to maintain oxidation state +III over a wide potential range. Although at this point, the task of Fe in our catalytic

Table 3
Summary of average metal oxidation states by XANES analysis (for details, see the Supporting Information).

Experiment	Average oxidation states for 60MO/CM			Average oxidation states for 100MO		
	Co	Ni	Fe	Co	Ni	Fe
Analysis of as-prepared catalyst powder	2.3	2.0	2.0	2.3	2.2	2.1
In situ measurement at OCP (0.76 V vs. RHE)	3.1	2.3	3.0	2.5	2.3	2.9
In situ measurement during OER (1.61 V vs. RHE)	3.3	2.5	3.0	3.0	2.5	2.9

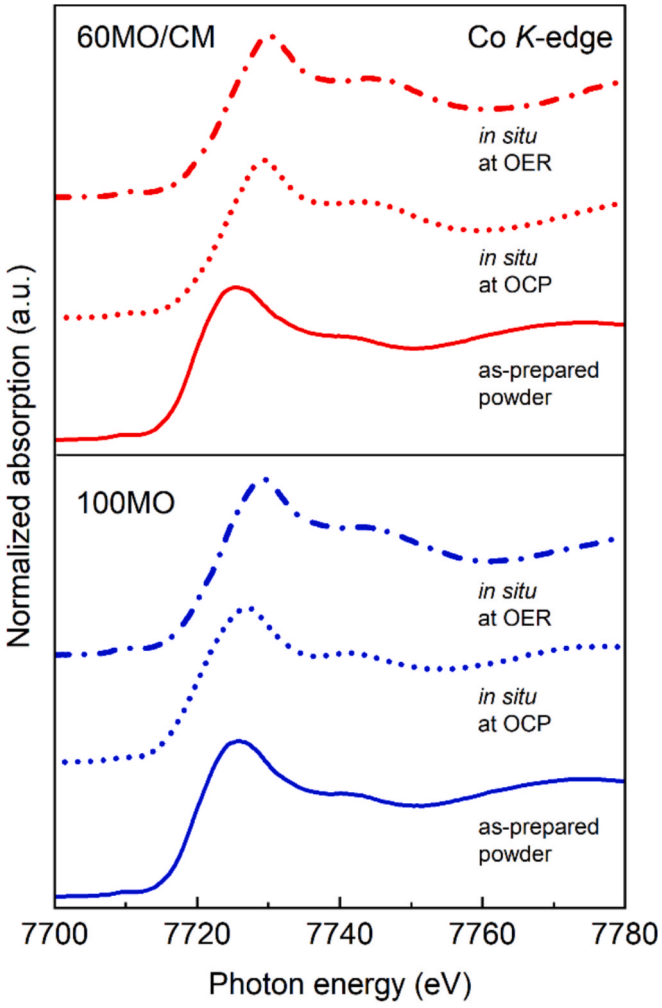

Fig. 8. *In situ* Co K-edge XANES spectra of 60MO/CM (top) and 100MO (bottom).

system cannot be unequivocally assigned, its role in mixed metal oxide OER catalysts is generally considered to be rather a performance promoter than an active site [63–65]. Second, a significant proportion of Co (IV) centers can be observed under OER conditions, while Ni is present in significantly lower oxidation states. The latter may be ascribed to the short lifetime of the Ni(IV) state [63]. Third, there is a clear difference in the redox behavior of Co between the two catalyst materials, reaching significantly higher oxidation states in 60MO/CM than in 100MO. This large difference under potential bias indicates that there is a strong influence of carbon on the electronic structure of the metal oxide, probably caused by improved charge transfer and likely influencing OER activity of the individual sites at elevated potentials.

3. Conclusion

Based on our previously reported CoNiFe oxide OER catalytic system [24], the effect of carbon black admixture and composite preparation procedure on the performance was investigated. Using RDE voltammetry and RDE chronopotentiometry, it was found that under three prerequisites, a significant reduction of metal loading is possible while maintaining high activity at low overpotentials:

1. The carbon particles must be already added during the sol–gel process and not only during ink preparation. A possible explanation is that a more intimate mixing of the two components is achieved through the sol–gel step and subsequent thermal treatment, leading to stronger interaction between metal oxide and carbon particles and allowing the carbon to effectively contribute to current flow as conductivity-enhancing additive. This rationale is supported by SEM analysis of as-prepared composites.
2. Oxidative pre-treatment of hydrophobic carbon black particles is required. A plausible explanation is that the enhanced and more hydrophilic surface enables a stronger binding to the metal oxide during composite formation.
3. A sufficiently high metal oxide content within the composite is necessary for good catalytic activity. While very good results can be achieved with 80 and 60 wt% metal oxide, activity significantly drops when reducing the content to 40 and 20 wt%, respectively.

Catalyst 60MO/CM was identified as the most promising candidate under RDE conditions: With 40 % reduced metal content, it achieved a η_{10} value of 297 mV, a mass activity of 370 A g^{-1}_{CoNiFe} at 1.56 V, a Tafel slope of only 39.0 mV dec^{-1}, and negligible changes of the overpotential in long-term potentiometric measurements at 100 mA cm^{-2}_{geo}. A comparison between the R_P values of the catalysts before and after chronopotentiometric tests shows that 100MO experiences a strong increase in charge transfer resistance, while 60MO/CM exhibits almost no change. Interestingly, this is *not* a result of the available surface area, as the ECSA of 60MO/CM decreases more than the value of 100MO. On the other hand, the electronic structure of the metal oxide domains experiences a strong influence through the CM component under OER conditions, as demonstrated by *in situ* XANES analysis. Taken together, these observations suggest that at elevated potentials, the carbon additive has a promoting effect on OER microkinetics, enabling the effective use of the composite materials despite lower metal loading. Excellent performance of 60MO/CM was also confirmed under practically relevant conditions in an AEM flow electrolyzer. Future studies should aim at improving the mechanistic understanding, including the interplay between carbon and metal oxide domains as well as their structural changes under OER conditions.

4. Experimental section

Materials for catalyst synthesis. All chemicals were of analytical grade and used without further purification. Cobalt(II) nitrate hexahydrate ($Co(NO_3)_2{\cdot}6H_2O$) was purchased from ThermoFisher GmbH (Karlsruhe, Germany). Nickel(II) nitrate hexahydrate ($Ni(NO_3)_2{\cdot}6H_2O$), iron(III) nitrate nonahydrate ($Fe(NO_3)_3{\cdot}9H_2O$), and citric acid ($C_6H_8O_7$) were obtained from Sigma-Aldrich. Vulcan carbon XC-72R (carbon black) was purchased from CABOT corporation and nitric acid (HNO_3, ~65 %) was ordered from Fisher Scientific. Potassium hydroxide solution (KOH, 0.999–1.001 M at 20 °C) was purchased from AppliChem. Ethanol (EtOH, abs., >99.5 %) was obtained from Walter-CMP. Nafion solution (D-521) was purchased from Alfa Aesar. Throughout all experiments, deionized water was used.

Preparation of modified carbon black (CM). For oxidative carbon treatment, a reported procedure was used [53]. Vulcan carbon XC72R (2 g) was added to 90 mL of an aq. 9 M HNO_3 solution. The mixture was

stirred at room temperature for 30 min and sonicated for 1 h (120 W, 35 kHz). Then, the mixture was heated to 90 °C and stirred for 3 h (650 rpm). After allowing the suspension to cool to room temperature, the treated carbon particles were separated by centrifugation and layered with deionized water. Centrifugation and addition of water were repeated until reaching pH 7. Finally, after removal of water by centrifugation, the black powder was dried at room temperature.

Preparation of MO-carbon composites by mechanical mixing. A defined amount of CoNiFe oxide prepared according to our previously published procedure (CoNiFe (2:2:1)/M) [24], carbon black (CB) or modified carbon (CM), as well as a small amount of ethanol (200 mg MO-carbon mixture in 2 mL ethanol) were mechanically mixed in a mortar until homogeneity of the sample was achieved. The resulting mixture was then dried in an oven at 45 °C to remove the alcohol and used for catalyst ink preparation according to the procedure described below. A summary of the prepared composites including the mass rations between MO and carbon additive is found in Table S1.

Preparation of MO-carbon composites via sol–gel synthesis. The synthesis of the composite is based on the sol–gel procedure of our previous work [24]. 12 mmol $Co(NO_3)_2{\cdot}6H_2O$, 12 mmol $Ni(NO_3)_2{\cdot}6H_2O$, and 6 mmol $Fe(NO_3)_3{\cdot}9H_2O$ were dissolved in 30 mL deionized water using a magnetic stirrer at room temperature. A solution of 30 mmol citric acid in 30 mL deionized water was added slowly to the solution using a dropping funnel. The resulting solution was then stirred for 30 min, followed by the addition of a defined amount of carbon (CB or CM, for details see Table S1). To improve dispersion of the particles, the mixture was sonicated for 45 min. The resulting dispersion was stirred at 250 rpm for 30 min at room temperature, followed by heating to 70 °C to achieve gel formation. Heating to 110 °C for 17 h in a drying oven yielded a xerogel, which was processed into a powder by grounding in a ball mill for 10 min. The precursor material was subjected to thermal treatment in a horizontal tubular furnace (HTM Reetz) at 300 °C for 3 h under an argon/1 vol% air atmosphere ($\dot{V}$ = 5 mL min^{-1}), whereby a temperature ramp of 5 K min^{-1} was used to achieve the treatment temperature. Results of elemental analysis are provided in Table S2.

Materials characterization: Elemental analysis for carbon, hydrogen, and nitrogen was carried out using a TruSpec Micro CHNS analyzer (Leco). The metal contents of the samples were measured using ICP OES analysis which was carried out using a Varian/Agilent 715-ES spectrometer.

Powder X-ray diffraction patterns were recorded using a Stoe Stadi P transmission diffractometer equipped with a DECTRIs Mythen2 1 K detector applying Ge(111) monochromatized Mo Kα1 radiation (50 kV, 40 mA, 0.70930 Å). The samples were ground to a fine powder and placed between two plastic wraps before the measurement. Peak positions and profile were fitted with the Pseudo-Voigt function using the HighScore Plus software package (Panalytical). Phase identification was achieved by using the PDF-2 database of the International Center of Diffraction Data (ICDD).

The XPS (X-ray Photoelectron Spectroscopy) measurements were performed on an ESCALAB 220iXL (Thermo Fisher Scientific) with monochromated Al Kα radiation (E = 1486.6 eV). Samples were prepared on a stainless-steel holder with conductive double-sided adhesive carbon tape. The measurements were performed with charge compensation using a flood electron system combining low energy electrons and Ar^+ ions ($p_{Ar} = 1 \times 10^{-7}$ mbar). The electron binding energies are referenced to the C 1s core level of carbon at 284.8 eV (C–C and C–H bonds) for 100MO, 284.5 eV for CB and 284.4 eV for CM as received from the measurement of pure CB and CM as reference samples (see Section 13 in the SI and Fig. S58 for details).

The morphology of the electrode surface before and after electrolysis was studied with electron microscopy. Scanning Electron Microscope (SEM) analysis was performed on a Thermo Fisher Scientific (Hillsboro, USA) Quattro S equipped with a Thermo Fisher Scientific UltraDry 60 M Energy Dispersive X-ray Spectrometer (EDXS) for elemental identification.

Scanning transmission electron microscopy (STEM) investigations were carried out on a probe aberration-corrected JEM-ARM200F (JEOL, corrector: CEOS) at an accelerating voltage of 200 kV. The microscope is equipped with a JED-2300 (JEOL) energy-dispersive X-ray spectrometer (for EDX) having a silicon drift detector (dry SD60GV). EDX elemental maps are depicted after applying net count fitting using the software Analysis Station (JEOL). Electron energy-loss spectroscopy (EELS) was done with an Enfinium ER (Gatan) electron energy-loss (EEL) spectrometer. For STEM imaging, a High-Angle Annular Dark Field (HAADF) and an Annular Bright Field (ABF) detector were employed, while an Annular Dark Field (ADF) detector was used for position control during EELS acquisition. Dual EELS was performed at a camera length of 4 cm, an illumination semi angle of 27.8 mrad and a filter entrance aperture semi angle of 41.3 mrad using the low loss region for compensation of energy shifts during acquisition. The solid samples were deposited without any pre-treatment onto a holey carbon-supported Cu grid (mesh 300) and subsequently transferred to the microscope.

Specific surface areas and pore volumes were determined by N_2 physisorption measurements on a Micromeritics ASAP 2020 apparatus at –196 °C and calculated using BET and BJH methods, respectively. Catalysts were degassed at 200 °C in vacuum for 4 h before analysis. Raman measurements were carried out at an excitation wavelength of 785 nm using a HORIBA iHR550 spectrometer equipped with a sapphire ball-probe (Marq Metrix). FTIR spectra were recorded using a Bruker Alpha-FTIR spectrometer in ATR mode.

Conductivity analysis. The composite was pressed into a pellet (diameter: 10 mm, height: 1.5 mm) at a pressure of 3 kbar. The pellet was placed between two gold-plated steel disk electrodes using a spring rate of 2.4 N mm^{-1} to obtain a stack pressure of approximately 0.6 bar. Estimation of specific conductivity was done by impedance spectroscopy (amplitude: 0.05 V, frequency range: 10 kHz to 1 kHz) at open circuit potential using the TSC Battery test cell from RHD Instruments.

Electroanalytical experiments. All experiments were performed in a three-electrode arrangement using an Autolab PGSTAT 302 N (Metrohm). A glassy carbon rotating disk electrode (diameter: 3.8 mm, geometrical surface area: 0.113 cm^2) was used as the working electrode (WE). For the preparation of the coated WE, catalyst inks were prepared by dispersing 5 mg catalyst in 1 mL of a mixture of 0.1 M KOH, Nafion solution, EtOH, and H_2O (1:2:45:45 in relation to the volumes of the pure components). The ink was sonicated for 45 min at room temperature. The catalyst suspension was slowly dropped on the working electrode surface and dried for an hour under air to achieve a catalyst loading on the electrode surface area of 0.25 mg cm^{-2}. An Ag/AgCl (3 M KCl) electrode and a Pt rod were used as reference electrode (RE) and counter electrode (CE), respectively. All reported potentials are *iR* drop corrected. The uncompensated resistance *R* was determined by electrochemical impedance spectroscopy (EIS) at the open-circuit potential (OCP) from 20 kHz to 200 Hz with alternating current perturbation of 5 mV. All recorded potentials were converted to RHE.

All linear sweep voltammograms (LSVs) were recorded using a scan rate of 1 mV s^{-1} and a rotation rate of 1800 rpm. EIS analysis of the electrocatalysts was carried out at 1.50 V vs RHE, at OER onset, and at η_{10} scanning the frequency range from 10 kHz to 0.01 Hz and applying an amplitude of 5 mV. The electrochemically active surface area (ECSA) was estimated by measuring the double layer capacitance in the non-Faradaic region using cyclic voltammetry without electrode rotation (for details, see the SI).

For structural characterization of used electrodes, anodic polarization of the materials (ink preparation without Nafion) was carried out at 10 mA cm_{geo}^{-2} for 1 h in a resting 1.0 M KOH electrolyte, followed by removal of the electrode from solution and rinsing with deionized water. SEM analysis was carried out directly on the electrode surface, whereas for STEM, XRD, and XPS, the catalyst material was removed from the glassy carbon disc.

Studies in alkaline flow electrolyzer. The experiments were carried out in a flow cell equipped with a catalyst-coated Ni foam current collector for the anodic (OER) reaction, an anion exchange membrane, and a Pt-loaded gas diffusion electrode for the cathodic HER process. The OER catalyst was applied to the Ni foam (Good Fellow, 60–100 PPI, 1.5 mm thickness) *via* spray-coating of a catalyst ink. The ink was prepared by adding 50 mg 100MO (or 60MO/CM) and 16 μL of an ethanolic 5 wt% Sustainion® XA-9 alkaline ionomer solution to 10 mL of a 3:1 (v/v) ethanol–water mixture, followed by ultrasonication at room temperature for 45 min, and resting for at least 16 h before using. The ink was applied to the Ni-foam (25 mm × 25 mm) by spray-coating at 75 °C until a catalyst loading of 5 mg cm^{-2} geometrical electrode surface area was achieved. As separator, a Fumasep anion exchange membrane (FAA-3-PK-130) was used. Prior to the experiment, the membrane was activated by storage in 1.0 M KOH solution for one hour. Depending on the experiment, two different types of gas diffusion cathodes were used. For studies with 0.2 mg cm^{-2} Pt loading, a Vulcan carbon cloth cathode (W1S1011, FuelCellStore) was used. For experiments with higher Pt loading, a Toray 060 sheet (25 mm × 25 mm) was spray-coated with an ink consisting of 7.5 mg Vulcan Carbon particles loaded with 50 % Pt (Umicore), 16 μL D-521 Nafion binder solution (Alfa Aesar), and 734 μL of a 1:1 (v/v) ethanol–water mixture until the desired loading was achieved. Electrolysis was carried out under galvanostatic conditions at 50 °C using tempered aq. 1.0 M KOH solutions as anolyte and catholyte, respectively. Anolyte and catholyte solutions were separately purged through the anode and cathode chambers, each with a flow rate of 80 mL min^{-1}.

XAS measurements. XAS K-edge spectra were recorded for Co, Ni, and Fe at BESSY II synchrotron (Helmholtz-Center Berlin, Germany) at Beamline KMC-3. The measurements were performed in transmission mode. The Co, Ni, and Fe K-edge spectra were measured from 7580 to 8290 eV, 8207 to 8922 eV, and 7009 to 8922 eV, respectively. To obtain Fe K-edge spectra, a servo system (PID controller) was needed to subtract counts coming from other elements that absorb at the same energy. Co-powder, Ni-powder, and Fe-foil were used as references, whereby the first real inflection points at 7708.4 eV (Co), 8331.6 eV (Ni), and 7111.4 eV (Fe), respectively, were used for energy calibration. Further reference materials used for Co were CoO (Co^{2+}), Co_3O_4 ($Co^{2.67+}$), and Co $(NO_3)_2{\cdot}6H_2O$ (Co^{2+}). Similarly, NiO (Ni^{2+}), $Ni(NO_3)_2$ $6H_2O$ (Ni^{2+}), as well as Fe_3O_4 ($Fe^{2.67+}$), and $Fe(NO_3)_3{\cdot}9H_2O$ (Fe^{3+}) were analyzed as references for Ni and Fe K-edges, respectively (Fig. S44).

All powders for *ex situ* measurements were mixed homogenously in a mortar with boron nitride (BN) as binder with the mass ratio of 1 : 10 (sample: binder). *In situ* measurements were carried out using a spectroelectrochemical flow cell. The OER catalyst was deposited on a carbon paper gas diffusion layer (GDL, 250 μm) at 70 °C with a mass loading of approximately 0.75 mg cm^{-2} by spray-coating with air flow. An Ag/AgCl electrode (saturated KCl, $E^0 = 0.197$ V) and a Pt-modified Vulcan carbon cloth (W1S1011, Pt loading: 0.2 mg cm^{-2}, FuelCellStore) served as the reference and the counter electrode, respectively. An anion exchange membrane (Sustainion® X37-50 Grade 60) was used as a separator. Measurements were carried out at room temperature using aq. 0.1 M KOH solutions as anolyte and catholyte (pumped separately through the anodic and cathodic half-cell with a flow rate of 20 mL min^{-1}). The back side of the working electrode was covered by a Teflon layer and orthogonally aligned to the X-ray beam.

CRediT authorship contribution statement

Trang Minh Pham: Validation, Writing – review & editing, Data curation, Investigation. **Na Liu:** Investigation. **Stephan Bartling:** Investigation, Writing – review & editing. **Nils Rockstroh:** Writing – review & editing, Investigation. **Reinhard Eckelt:** Investigation. **Wen Ju:** Conceptualization. **Annette-Enrica Surkus:** Supervision, Conceptualization, Writing – original draft, Data curation, Methodology. **Robert Francke:** Supervision, Visualization, Writing – review & editing, Conceptualization.

Declaration of competing interest

The authors declare that they have no known competing financial interests or personal relationships that could have appeared to influence the work reported in this paper.

Acknowledgements

The authors thank Dr. Henrik Lund and Kathleen Schubert for XRD measurements, and the Analytics Service Department (Leibniz Institute for Catalysis) for FTIR and EA/ICP measurements. The contributions through Raman measurements by Dr. Jana Weiss as well as fruitful discussion with Dr. Carsten Robert Kreyenschulte (both Leibniz Institute for Catalysis) are appreciated. The authors are also thankful to Tuyen Thanh Do (Leibniz Institute for Catalysis) for assistance in the laboratory. We are particularly grateful for the possibility to investigate our materials at BESSY II synchrotron (Helmholtz Center Berlin, Germany) at Beamline KMC-3, and for the kind support and productive guidance of PD Dr. Michael Haumann (FU Berlin).

This work has been supported by the RoHan Project funded by the German Academic Exchange Service (DAAD, No. 57315854 and 57560571) and the Federal Ministry for Economic Cooperation and Development (BMZ) within the framework 'SDG Bilateral Graduate School Programme'. R.F. acknowledges financial support by the German Research Foundation (DFG, Heisenberg Professorship, FR 3848/4-1).

Appendix A. Supplementary material

Supplementary data to this article can be found online at https://doi.org/10.1016/j.jcat.2025.116299.

Data availability

Data will be made available on request.

References

[1] A.J. Shih, M.C.O. Monteiro, F. Dattila, D. Pavesi, M. Philips, A.H.M. da Silva, R. E. Vos, K. Ojha, S. Park, O. van der Heijden, G. Marcandalli, A. Goyal, M. Villalba, X. Chen, G.T.K.K. Gunasooriya, I. McCrum, R. Mom, N. López, M.T.M. Koper, Water electrolysis, Nat. Rev. Methods Primers 2 (2022) 84.

[2] M. Neuwirth, T. Fleiter, P. Manz, R. Hofmann, The future potential hydrogen demand in energy-intensive industries – a site-specific approach applied to Germany, Energy Convers. Manage. 252 (2022) 115052.

[3] Y.D. Zi-You Yu, Xing-Yu Feng, Xingxing Yu, Min-Rui Gao*, Shu-Hong Yu, Clean and affordable hydrogen fuel from alkaline water splitting: past, recent progress, and future prospects, Adv. Mater. 33 (2021) 2007100.

[4] J. Song, C. Wei, Z.-F. Huang, C. Liu, L. Zeng, X. Wang, Z.J. Xu, A review on fundamentals for designing oxygen evolution electrocatalysts, Chem. Soc. Rev. 49 (2020) 2196–2214.

[5] J. Zhang, Q. Zhang, X. Feng, Support and interface effects in water-splitting electrocatalysts, Adv. Mater. 31 (2019) 1808167.

[6] X. Xie, L. Du, L. Yan, S. Park, Y. Qiu, J. Sokolowski, W. Wang, Y. Shao, Oxygen evolution reaction in alkaline environment: material challenges and solutions, Adv. Funct. Mater. 32 (2022) 2110036.

[7] C.C.L. McCrory, S. Jung, I.M. Ferrer, S.M. Chatman, J.C. Peters, T.F. Jaramillo, Benchmarking hydrogen evolving reaction and oxygen evolving reaction electrocatalysts for solar water splitting devices, J. Am. Chem. Soc. 137 (2015) 4347–4357.

[8] E. Fabbri, T.J. Schmidt, Oxygen evolution reaction—the enigma in water electrolysis, ACS Catal. 8 (2018) 9765–9774.

[9] M. Chatenet, B.G. Pollet, D.R. Dekel, F. Dionigi, J. Deseure, P. Millet, R.D. Braatz, M.Z. Bazant, M. Eikerling, I. Staffell, P. Balcombe, Y. Shao-Horn, H. Schäfer, Water electrolysis: from textbook knowledge to the latest scientific strategies and industrial developments, Chem. Soc. Rev. 51 (2022) 4583–4762.

[10] H.A. Miller, K. Bouzek, J. Hnat, S. Loos, C.I. Bernäcker, T. Weißgärber, L. Röntzsch, J. Meier-Haack, Green hydrogen from anion exchange membrane water electrolysis: a review of recent developments in critical materials and operating conditions, Sustain. Energy Fuels 4 (2020) 2114–2133.

[11] M. Schalenbach, O. Kasian, K.J.J. Mayrhofer, An alkaline water electrolyzer with nickel electrodes enables efficient high current density operation, Int. J. Hydrogen Energy 43 (2018) 11932–11938.

[12] M. Schalenbach, A.R. Zeradjanin, O. Kasian, S. Cherevko, K.J.J. Mayrhofer, A perspective on low-temperature water electrolysis – challenges in alkaline and acidic technology, Int. J. Electrochem. Sci. 13 (2018) 1173–1226.

[13] M. Schalenbach, G. Tjarks, M. Carmo, W. Lueke, M. Mueller, D. Stolten, Acidic or alkaline? Towards a new perspective on the efficiency of water electrolysis, J. Electrochem. Soc. 163 (2016) F3197.

[14] N. Du, C. Roy, R. Peach, M. Turnbull, S. Thiele, C. Bock, Anion-exchange membrane water electrolyzers, Chem. Rev. 122 (2022) 11830–11895.

[15] A. Li, Y. Sun, T. Yao, H. Han, Earth-abundant transition-metal-based electrocatalysts for water electrolysis to produce renewable hydrogen, Chem. Eur. J. 24 (2018) 18334–18355.

[16] F. Song, L. Bai, A. Moysiadou, S. Lee, C. Hu, L. Liardet, X. Hu, Transition metal oxides as electrocatalysts for the oxygen evolution reaction in alkaline solutions: an application-inspired renaissance, J. Am. Chem. Soc. 140 (2018) 7748–7759.

[17] G.A. Gebreslase, M.V. Martínez-Huerta, M.J. Lázaro, Recent progress on bimetallic NiCo and CoFe based electrocatalysts for alkaline oxygen evolution reaction: a review, J. Energy Chem. 67 (2022) 101–137.

[18] B.H.R. Suryanto, Y. Wang, R.K. Hocking, W. Adamson, C. Zhao, Overall electrochemical splitting of water at the heterogeneous interface of nickel and iron oxide, Nat. Commun. 10 (2019) 5599.

[19] M. Yu, E. Budiyanto, H. Tüysüz, Principles of water electrolysis and recent progress in cobalt-, nickel-, and iron-based oxides for the oxygen evolution reaction, Angew. Chem. Int. Ed. 61 (2022) e202103824.

[20] R.A. Krivina, Y. Ou, Q. Xu, L.P. Twight, T.N. Stovall, S.W. Boettcher, Oxygen electrocatalysis on mixed-metal oxides/oxyhydroxides: from fundamentals to membrane electrolyzer technology, Acc. Mater. Res. 2 (2021) 548–558.

[21] Z.W. Seh, J. Kibsgaard, C.F. Dickens, I. Chorkendorff, J.K. Nørskov, T.F. Jaramillo, Combining theory and experiment in electrocatalysis: insights into materials design, Science 355 (2017) eaad4998.

[22] I.C. Man, H.-Y. Su, F. Calle-Vallejo, H.A. Hansen, J.I. Martínez, N.G. Inoglu, J. Kitchin, T.F. Jaramillo, J.K. Nørskov, J. Rossmeisl, Universality in oxygen evolution electrocatalysis on oxide surfaces, ChemCatChem 3 (2011) 1159–1165.

[23] R. Subbaraman, D. Tripkovic, K.-C. Chang, D. Strmcnik, A.P. Paulikas, P. Hirunsit, M. Chan, J. Greeley, V. Stamenkovic, N.M. Markovic, Trends in activity for the water electrolyser reactions on 3d M(Ni,Co,Fe,Mn) hydr(oxy)oxide catalysts, Nat. Mater. 11 (2012) 550–557.

[24] T.M. Pham, M. Plevova, S. Bartling, N. Rockstroh, A. Springer, A. Slabon, J. Hnat, A.-E. Surkus, R. Francke, Oxygen-deficient annealing boosts performance of CoNiFe oxide electrocatalyst in oxygen evolution reaction, J. Catal. 438 (2024) 115675.

[25] P. Kalungi, Z. Yao, H. Huang, Aspects of nickel, cobalt and lithium, the three key elements for Li-ion batteries: an overview on resources, demands, and production, Materials 17 (2024) 4389.

[26] M. Li, J. Lu, Cobalt in lithium-ion batteries, Science 367 (2020) 979–980.

[27] S. van den Brink, R. Kleijn, B. Sprecher, A. Tukker, Identifying supply risks by mapping the cobalt supply chain, Resour. Conserv. Recy. 156 (2020) 104743.

[28] E.M. Mervine, R.K. Valenta, J.S. Paterson, G.M. Mudd, T.T. Werner, I. Nursamsi, L. J. Sonter, Biomass carbon emissions from nickel mining have significant implications for climate action, Nat. Commun. 16 (2025) 481.

[29] S.H. Farjana, N. Huda, M.A.P. Mahmud, Life cycle assessment of cobalt extraction process, J. Sus. Mining 18 (2019) 150–161.

[30] D. Balaji, J. Madhavan, M.S. AlSalhi, M.J. Aljaafreh, S. Prasad, P.L. Show, Carbon supported Ni3N/Ni heterostructure for hydrogen evolution reaction in both acid and alkaline media, Int. J. Hydrogen Energy 46 (2021) 30739–30749.

[31] J. Verma, S. Goel, Cost-effective electrocatalysts for hydrogen evolution reactions (HER): challenges and prospects, Int. J. Hydrogen Energy 47 (2022) 38964–38982.

[32] Y. Zhu, M. Klingenhof, C. Gao, T. Koketsu, G. Weiser, Y. Pi, S. Liu, L. Sui, J. Hou, J. Li, H. Jiang, L. Xu, W.-H. Huang, C.-W. Pao, M. Yang, Z. Hu, P. Strasser, J. Ma, Facilitating alkaline hydrogen evolution reaction on the hetero-interfaced Ru/RuO2 through Pt single atoms doping, Nat. Commun. 15 (2024) 1447.

[33] Y. Liu, Q. Wang, J. Zhang, J. Ding, Y. Cheng, T. Wang, J. Li, F. Hu, H.B. Yang, B. Liu, Recent advances in carbon-supported noble-metal electrocatalysts for hydrogen evolution reaction: syntheses, structures, and properties, Adv. Energy Mat. 12 (2022) 2200928.

[34] A.P. Murthy, J. Madhavan, K. Murugan, Recent advances in hydrogen evolution reaction catalysts on carbon/carbon-based supports in acid media, J. Power Sources 398 (2018) 9–26.

[35] S. Zaman, M. Wang, H. Liu, F. Sun, Y. Yu, J. Shui, M. Chen, H. Wang, Carbon-based catalyst supports for oxygen reduction in proton-exchange membrane fuel cells, Trends Chem. 4 (2022) 886–906.

[36] W. Cai, X. Zhang, J. Shi, J. Li, Z. Liu, S. Zhou, X. Jia, J. Xiong, K. Qu, Y. Huang, Contribution of carbon support in cost-effective metal oxide/carbon composite catalysts for the alkaline oxygen evolution reaction, Catal. Commun. 127 (2019) 5–9.

[37] S. Han, S. Liu, S. Yin, L. Chen, Z. He, Electrodeposited Co-doped Fe3O4 thin films as efficient catalysts for the oxygen evolution reaction, Electrochim. Acta 210 (2016) 942–949.

[38] P. Trogadas, T.F. Fuller, P. Strasser, Carbon as catalyst and support for electrochemical energy conversion, Carbon 75 (2014) 5–42.

[39] P. Stelmachowski, J. Duch, D. Sebastián, M.J. Lázaro, A. Kotarba, Carbon-based composites as electrocatalysts for oxygen evolution reaction in alkaline media, Materials 14 (2021) (2021) 4984.

[40] C.T. Alexander, A.M. Abakumov, R.P. Forslund, K.P. Johnston, K.J. Stevenson, Role of the carbon support on the oxygen reduction and evolution activities in LaNiO3 composite electrodes in alkaline solution, ACS Appl. Energy Mat. 1 (2018) 1549–1558.

[41] S. Sharma, B.G. Pollet, Support materials for PEMFC and DMFC electrocatalysts—a review, J. Power Sources 208 (2012) 96–119.

[42] P.T. Yu, W. Gu, J. Zhang, R. Makharia, F.T. Wagner, H.A. Gasteiger, Carbon-support requirements for highly durable fuel cell operation, in: F.N. Büchi, M. Inaba, T.J. Schmidt (Eds.) Polymer Electrolyte Fuel Cell Durability, Springer New York, New York, NY, 2009, pp. 29–53.

[43] S. Möller, S. Barwe, J. Masa, D. Wintrich, S. Seisel, H. Baltruschat, W. Schuhmann, Online monitoring of electrochemical carbon corrosion in alkaline electrolytes by differential electrochemical mass spectrometry, Angew. Chem. Int. Ed. 59 (2020) 1585–1589.

[44] J. Yang, S. Park, K.y. Choi, H.-S. Park, Y.-G. Cho, H. Ko, H.-K. Song, Activity-durability coincidence of oxygen evolution reaction in the presence of carbon corrosion: case study of $MnCo_2O_4$ spinel with carbon black, ACS Sus. Chem. Eng. 6 (2018) 9566–9571, https://doi.org/10.1021/acssuschemeng.8b01879.

[45] X. Wu, K. Zhao, X. Yan, X. Cao, L. Ke, Y. Zhao, L. Li, X. Jiang, N. Yan, Suppressing carbon corrosion via mechanically mixing transition metal phosphide clusters: a comparative in situ study in alkaline media, J. Mater. Chem. A 11 (2023) 17237–17245.

[46] Y. Sato, N. Yamada, S. Kitano, D. Kowalski, Y. Aoki, H. Habazaki, High-corrosion-resistance mechanism of graphitized platelet-type carbon nanofibers in the OER in a concentrated alkaline electrolyte, J. Mater. Chem. A 10 (2022) 8208–8217.

[47] Y.S. Park, G.H. Choi, J. Jung, C.-H. Ahn, S.S. Hwang, M.G. Nam, P.J. Yoo, A.S. Lee, Engineering durable anion exchange membrane water electrolyzers through suppressed electrochemical corrosion of a NiFe–graphitic carbon shell anode catalyst, ACS Catal. 14 (2024) 9969–9984.

[48] V.F. Mattick, X. Jin, R.E. White, K. Huang, Understanding the role of carbon in alkaline oxygen electrocatalysis: a case study on La0.6Sr0.4CoO3-δ/Vulcan carbon composite electrocatalyst, Int. J. Hydrogen Energy 44 (2019) 2760–2769.

[49] J.M. Linge, V. Briega-Martos, A. Hutzler, B. Fritsch, H. Erikson, K. Tammeveski, S. Cherevko, Stability of carbon supported silver electrocatalysts for alkaline oxygen reduction and evolution reactions, ACS Appl. Energy Mater. 6 (2023) 11497–11509.

[50] D. Coertzen, R.J. Kriek, P.B.J. Levecque, A. Falch, Vulcan carbon as support for sputtered oxygen evolution electrocatalysts, Electrocatalysis 10 (2019) 604–612.

[51] S.M. Senthil Kumar, J. Soler Herrero, S. Irusta, K. Scott, The effect of pretreatment of Vulcan XC-72R carbon on morphology and electrochemical oxygen reduction kinetics of supported Pd nano-particle in acidic electrolyte, J. Electroanal. Chem. 647 (2010) 211–221.

[52] X. Li, F. Feng, K. Zhang, S. Ye, D.Y. Kwok, V. Birss, Wettability of nafion and nafion/vulcan carbon composite films, Langmuir 28 (2012) 6698–6705.

[53] T. Zheng, K. Jiang, N. Ta, Y. Hu, J. Zeng, J. Liu, H. Wang, Large-scale and highly selective CO_2 electrocatalytic reduction on nickel single-atom catalyst, Joule 3 (2019) 265–278.

[54] B. Gupta, N. Kumar, K. Panda, V. Kanan, S. Joshi, I. Visoly-Fisher, Role of oxygen functional groups in reduced graphene oxide for lubrication, Sci. Rep. 7 (2017) 45030.

[55] D. Sánchez-Campos, V. Rodríguez-Lugo, F.C. Sánchez-Vargas, D. Mendoza-Anaya, E.S. Rodríguez, L.E. Alarcón, M.I. Reyes-Valderrama, Simple process and uncomplicated reduction of graphene oxide, Mater. Chem. Phys. 242 (2020) 122325.

[56] F. Tuinstra, J.L. Koenig, Raman spectrum of graphite, J. Chem. Phys. 53 (1970) 1126–1130.

[57] M.C. Biesinger, B.P. Payne, A.P. Grosvenor, L.W.M. Lau, A.R. Gerson, R.S.C. Smart, Resolving surface chemical states in XPS analysis of first row transition metals, oxides and hydroxides: Cr, Mn, Fe, Co and Ni, Appl. Surf. Sci. 257 (2011) 2717–2730.

[58] M. Cheng, H. Fan, Y. Song, Y. Cui, R. Wang, Interconnected hierarchical NiCo2O4 microspheres as high-performance electrode materials for supercapacitors, Dalton Trans. 46 (2017) 9201–9209.

[59] P. Salunkhe, M.A. AV, D. Kekuda, Investigation on tailoring physical properties of nickel oxide thin films grown by dc magnetron sputtering, Mater. Res. Express 7 (2020) 016427.

[60] S. Geiger, O. Kasian, A.M. Mingers, S.S. Nicley, K. Haenen, K.J.J. Mayrhofer, S. Cherevko, Catalyst stability benchmarking for the oxygen evolution reaction: the importance of backing electrode material and dissolution in accelerated aging studies, ChemSusChem 10 (2017) 4140–4143.

[61] H.A. El-Sayed, A. Weiß, L.F. Olbrich, G.P. Putro, H.A. Gasteiger, OER catalyst stability investigation using RDE technique: a stability measure or an artifact? J. Electrochem. Soc. 166 (2019) F458.

[62] S. Jung, C.C.L. McCrory, I.M. Ferrer, J.C. Peters, T.F. Jaramillo, Benchmarking nanoparticulate metal oxide electrocatalysts for the alkaline water oxidation reaction, J. Mater. Chem. A 4 (2016) 3068–3076.

[63] M. Görlin, P. Chernev, J. Ferreira de Araújo, T. Reier, S. Dresp, B. Paul, R. Krähnert, H. Dau, P. Strasser, Oxygen evolution reaction dynamics, faradaic charge efficiency, and the active metal redox states of Ni–Fe oxide water splitting electrocatalysts, J. Am. Chem. Soc. 138 (2016) 5603–5614.

[64] M. Görlin, J. Ferreira de Araújo, H. Schmies, D. Bernsmeier, S. Dresp, M. Gliech, Z. Jusys, P. Chernev, R. Kraehnert, H. Dau, P. Strasser, Tracking catalyst redox states and reaction dynamics in Ni–Fe oxyhydroxide oxygen evolution reaction electrocatalysts: the role of catalyst support and electrolyte pH, J. Am. Chem. Soc. 139 (2017) 2070–2082.

[65] Y. Du, D. Liu, T. Li, Y. Yan, Y. Liang, S. Yan, Z. Zou, A phase transformation-free redox couple mediated electrocatalytic oxygen evolution reaction, Appl. Catal. B: Environ. 306 (2022) 121146.

Publication 3

Heterogenized Copper(II) Phenanthroline Catalysts for Electroreduction of CO_2 to C_2 Compounds: Substitution on the Ligand Causes Structural Changes to the Molecular Framework and Stability Enhancement

Na Liu, Trang Minh Pham, Yanan Han, Olga S. Bokareva, Stephan Bartling, Armin Springer, Anke Spannenberg, Christoph Kubis, Jana Weiss, Dmitry E. Doronkin, Wen Ju*, Robert Francke*

DOI: 10.1002/adma.202513702

Abstract: Molecular Cu catalysts have shown promise for electrochemical CO_2 reduction (eCO2RR) to multi-carbon products. Unlike metallic Cu facets, molecular candidates offer precise control over the active site's electronic and steric configuration. However, prior studies identified critical challenges related to irreversible potential-induced formation of Cu particles, which participate in the eCO2RR and obscure the role of molecular motifs. Based on a binuclear Cu(II) phenanthroline catalyst previously reported by us, we developed a structurally modified second-generation system with enhanced stability. By introducing methoxy groups to the phenanthroline ligand, the molecular framework is changed from a binuclear complex to an oligonuclear step-like structure consisting of Cu(II) ions linked by μ_2- and μ_3-OH groups. When immobilized on a gas diffusion electrode, stable operation with a Faradaic efficiency of over 70% for C_2 products was achieved at elevated current densities in an MEA electrolyzer. *In situ* XAS spectroscopy shows only negligible changes in the Cu coordination environment up to 50 mA cm^{-2}. When approaching 250 mA cm^{-2}, partial and reversible phase evolution occurs under Cu^{2+} valence state reduction, followed by phase recovery upon bias removal. The presented system combines structural robustness with adaptive redox behavior, thereby demonstrating a possible route for implementing molecular electrocatalysts in eCO_2RR processes at industrially relevant current densities.

Author contribution: For this manuscript, I performed the electrochemical impedance spectroscopy (EIS) measurements and particular control experiments for the manuscript. Additionally, I supported in the XAS experiments at BESSY II synchrotron (Helmholtz-Center Berlin, Germany) at Beamline KMC-3. My contribution approximately amounts to 10%.

Signature of the student

(Trang Minh Pham)

Signature of the supervisor

(Prof. Dr. Robert Francke)

ADVANCED MATERIALS
www.advmat.de

Heterogenized Copper(II) Phenanthroline Catalysts for Electroreduction of CO_2 to C_2 Compounds: Substitution on the Ligand Causes Structural Changes to the Molecular Framework and Stability Enhancement

Na Liu, Trang Minh Pham, Yanan Han, Linfeng Yang, Olga S. Bokareva, Stephan Bartling, Armin Springer, Anke Spannenberg, Christoph Kubis, Jana Weiss, Dmitry E. Doronkin, Wen Ju, and Robert Francke**

Molecular Cu catalysts have shown promise for electrochemical CO_2 reduction (eCO_2RR) to multi-carbon products. Unlike metallic Cu facets, they offer precise control over the active site's electronic and steric configuration. However, prior studies identified critical challenges related to irreversible potential-induced formation of Cu particles, which participate in the eCO_2RR and obscure the role of molecular motifs. Based on a previously reported binuclear Cu(II) phenanthroline catalyst, a structurally modified second-generation system with enhanced stability is developed. By introducing methoxy groups to the phenanthroline ligand, the molecular framework changes from a binuclear complex to an oligonuclear step-like structure consisting of Cu(II) ions linked by μ_2- and μ_3-OH groups. When immobilized on a gas diffusion electrode, stable operation with a Faradaic efficiency of >70% for C_2 products is achieved at elevated current densities. In situ XAS spectroscopy shows only negligible changes of the Cu coordination environment up to 50 mA cm^{-2}. When approaching 250 mA cm^{-2}, partial and reversible phase evolution occurs under Cu^{2+} valence state reduction, followed by phase recovery upon bias removal. This system combines structural robustness with adaptive redox behavior, demonstrating a route for implementing molecular electrocatalysts in eCO_2RR processes at industrial current densities.

1. Introduction

The capture and conversion of CO_2 emissions into value-added chemicals holds immense potential for closing the carbon cycle.[1] Among various available approaches, the electrochemical CO_2 reduction reaction (eCO_2RR) has attracted significant attention due to its ability to directly utilize surplus renewable electricity for the valorization of CO_2. Depending on the employed catalyst and reaction conditions, this approach generates valuable products such as carbon monoxide (CO), formate ($HCOO^-$), ethylene (C_2H_4), and various multi-carbon oxygenates.[2] Recent advances in electrolyzer design have enabled two-electron reduction processes (i.e., CO and formate generation) to be operated under industrially relevant conditions, which could facilitate commercialization in the near future.[2a,c] In contrast, the electrochemical synthesis of multi-carbon products (e.g., C_2H_4 and C_2H_5OH) faces persistent fundamental and

N. Liu, T. M. Pham, Y. Han, L. Yang, O. S. Bokareva, S. Bartling, A. Spannenberg, C. Kubis, J. Weiss, W. Ju, R. Francke
Leibniz Institute for Catalysis
18059 Rostock, Germany
E-mail: wen.ju@catalysis.de; robert.francke@catalysis.de

The ORCID identification number(s) for the author(s) of this article can be found under https://doi.org/10.1002/adma.202513702

DOI: 10.1002/adma.202513702

O. S. Bokareva
Institute of Chemistry and Department of Life Light and Matter
University of Rostock
18059 Rostock, Germany

A. Springer
Electron Microscopy Center
University Medicine Rostock
Strempelstr. 14, 18057 Rostock, Germany

D. E. Doronkin
Institute for Chemical Technology and Polymer Chemistry and Institute of Catalysis Research and Technology
Karlsruhe Institute of Technology
76131 Karlsruhe, Germany

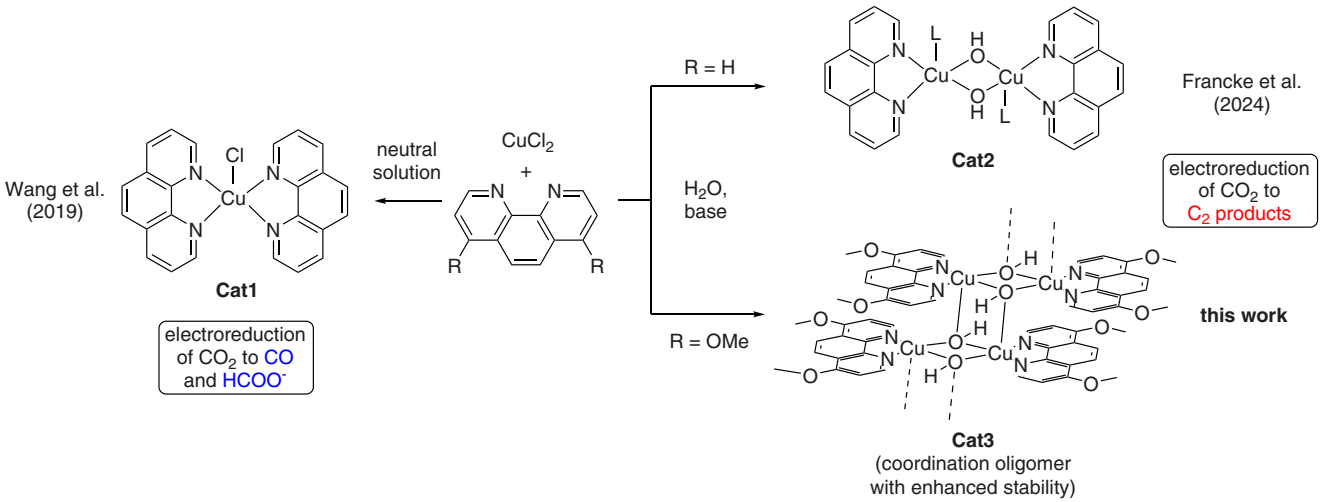

Scheme 1. Mono, bi- and oligonuclear Cu-phen compounds as molecular catalysts for eCO_2RR.[9a,16]

technical challenges. These hurdles arise from i) complicated reaction networks involving multiple electron transfers, protonation steps, C—O bond cleavage, and C—C coupling,[3] ii) the complex interplay between microkinetics, mass transfer, and durability on the device level at industrially relevant current densities,[4] and iii) structural and chemical instability of state of the art catalysts under operating conditions.[5]

Cu-based catalysts remain the benchmark for eCO_2RR to C_{2+} products owing to their unique capability to stabilize $^*CO$ intermediates and facilitate C—C bond formation.[6] However, the situation is complicated by various Cu sites (terraces, steps, defects) with different selectivity,[7] while dynamic phase evolution under operating conditions often leads to a variation of the product distribution over time.[8] Overall, these aspects lead to performance instability, hinder the mechanistic understanding, and complicate the targeted optimization strategies.

To address the challenges along the way to efficient C_{2+} production, the development of well-defined catalyst structures is a prominent strategy. In principle, such structures should enable precise elucidation of structure-performance relationships–particularly for the desired C—C coupling step–while providing opportunities for performance and durability optimization. In this regard, molecular electrocatalysts with well-defined active sites provide interesting opportunities. While many reported molecular systems have achieved high Faradaic Efficiency (*FE*) to CO[9] and HCOOH[10] by using earth-abundant metals such as Fe, Mn, and Co, relatively few works have demonstrated the possibility for generating C_{2+} products using molecular Cu catalysts.[11]

The work to date highlights two critical aspects for the development of new molecular Cu catalysts for the formation of C_{2+} products. First, it appears advantageous when the molecular framework provides two or more vicinal Cu centers enabling C—C coupling between CO_2 reduction intermediates. Consequently, bi- or multinuclear Cu complexes with suitable Cu···Cu distance have shown particularly high selectivity toward C_{2+} products.[12] Second, a robust and cost-effective ligand with suitable steric and electronic properties must be selected. The bidentate 1,10-phenanthroline ligand (phen) was identified as an excellent choice for stabilizing bi- or multinuclear Cu ensembles due to strong and entropically favored binding to metal sites,[13] an excellent π acceptor capability that stabilizes lower metal oxidation states,[14] and a particularly high affinity to Cu ions.[15] Both the influence of polynuclear structural motifs and the stabilizing effect of the phen ligand are well-documented by previous studies on the Cu phen system (**Scheme 1**). While Wang et al. have introduced **Cat1** as a robust catalyst for the generation of C_1 products (CO and $HCOO^-$ in up to 90% combined *FE*),[9a] the binuclear **Cat2** recently reported by us shows a strong tendency to form C_2 products.[16] When immobilized on a carbon electrode, our easy-to-synthesize phen-based **Cat2** shows 62% FE_{C2+} during electrolysis in an H-type divided batch cell. Structural characterization (pre- and post- electrolysis) revealed a hydroxo-bridged binuclear framework with a Cu···Cu distance of 2.93 Å. A remaining challenge in the use of **Cat2** for eCO_2RR is slow leaching into the electrolyte solution, which is why stable long-term operation in a membrane-electrode assembly (MEA) electrolyzer under continuous flow conditions could not be achieved. Consequently, we aimed to develop a more stable system by modifying the phen ligand, which we achieved by introducing methoxy substituents in positions 4 and 7 (**Cat3**, see Scheme 1).

Herein, we present a study on the oligonuclear Cu phen compound **Cat3**, a distinct Cu^{2+} complex synthesized from 4,7-dimethoxy-1,10-phenanthroline and $CuCl_2$ using a straightforward and scalable protocol. **Cat3** features hydroxo-bridged Cu centers that form a cascade-like framework. Compared to **Cat2**, water insolubility is achieved, accompanied by enhanced robustness under electrocatalytic conditions. Taken together, this allows for integrating **Cat3** into an MEA electrolyzer for studies under technically relevant conditions. Remarkably, **Cat3** achieves above 70% FE_{C2+} at current densities up to 200 mA cm^{-2} in the MEA electrolyzer. Stable operation was realized for 10 h with no obvious degradation in performance. To fundamentally address uncertainties about the state of our proposed molecular active Cu sites, in situ XAFS and HERFD-XANES analyses were carried out using both an H-type and an MEA-type spectroelectrochemical cell to explore different current density regions. As a result, merely negligible changes in the Cu coordination environment

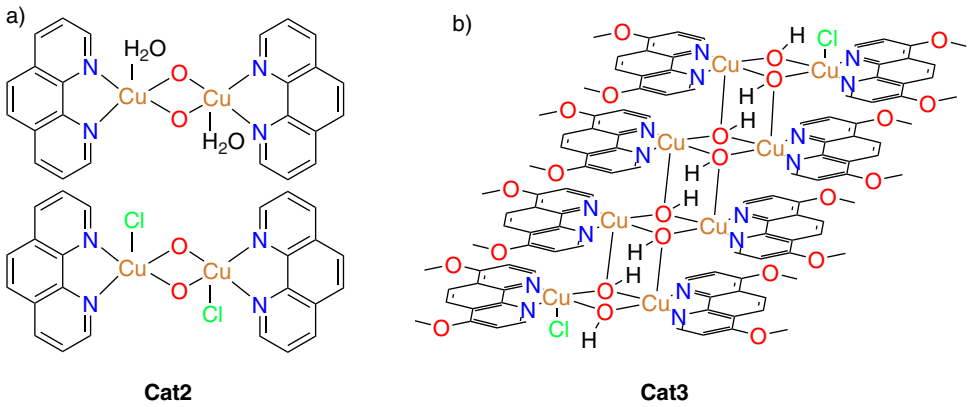

Figure 1. a) The structure of our previously reported **Cat2** and b) the core structure (coordination octamer) obtained after crystallization of **Cat3**.

were observed up to 50 mA cm^{-2}, while partial and reversible phase evolution under Cu^{2+} valence state reduction occurs when approaching 250 mA cm^{-2}. Interestingly, the initial phase recovers upon bias removal, indicating reversible adaptive redox dynamics under reaction conditions. This work not only establishes a robust molecular catalyst for the selective production of C_2 compounds, but also advances operando XAS methodologies for investigating molecular electrocatalysts under industrially relevant current densities.

2. Results and Discussion

2.1. Synthesis and Structural Characterization

Based on our previously reported protocol for the synthesis of **Cat2** (**Figure 1a**),[16] three Cu catalysts with differently substituted phen ligands were prepared from $CuCl_2$ in alkaline solution (for details, see the Supporting Information) and screened with respect to their eCO_2RR activity. Among the derivatives evaluated, 4,7-dimethoxy-substituted phen emerged as optimal, which is why all further efforts were focused on the resulting material (**Cat3**, see Scheme 1).

The molecular structure of **Cat3** was investigated using single-crystal X-ray diffraction (SC-XRD). However, different approaches to growing single crystals unfortunately resulted in samples of limited quality, likely due to the formation of coordination oligomers of varying chain lengths. One of these oligomers could still be selectively crystallized and used for deducing the structure of the molecular core unit from the SC-XRD results. In the analyzed solid state, the Cu compound adopts an octameric architecture (Figure 1b; Figure S1, Supporting Information), in which eight Cu^{2+} ions form a cascade-like framework stabilized by μ-oxo bridges, with peripheral methoxy-substituted phenanthroline ligands and two terminal chloro ligands completing the coordination sphere. Nonetheless, due to the limited SC-XRD data quality, distinguishing between oxo (Cu—O—Cu) and hydroxo (Cu—OH—Cu) bridges, as well as precisely determining the counterions and solvent molecules, was not possible. Therefore, complementary spectroscopic and theoretical approaches were used to resolve these structural ambiguities. In this context, X-ray photoelectron spectroscopic (XPS) analysis shows the exclusive presence of oxygen within μ-hydroxo bridges and methoxy groups (Figure S4, Supporting Information). Protonation of the bridging oxygen atoms was also probed using DFT calculations. For this purpose, the optimized structures of both the protonated and the non-protonated forms of the model dimer, tetramer, and octamer were compared to each other. The results indicate that protonation occurs preferentially on the bridging oxygen atoms, leading to a chemically reasonable model with eight protons per octamer and suggesting that protonation drives overall electronic stabilization of the coordination compound (Figure S5, Table S1, Supporting Information). X-ray absorption spectroscopy (XAS) of the as-prepared material confirms the existence of Cu in the indicated coordination environment and excludes inorganic or metallic phases (Figures S2 and S3, Supporting Information).

For the preparation of electrodes for H-cell and MEA measurements, inks consisting of **Cat3** and an ionomer in a water-*i*PrOH mixture were applied to carbon by drop casting or spray coating. To confirm the identity of the catalyst in the different states, powder and catalyst films were subjected to XPS, XAS, Raman spectroscopy, and powder XRD (P-XRD). A comparison to the results obtained from **Cat3** crystals suggests that the catalyst exists in the same structural states in all three forms (Figures S3 and S6–S10, Supporting Information).

To analyze the morphology of the crystals and the catalyst-coated electrode as well as the elemental distribution across the surface on the µm level, scanning electron microscope (SEM) measurements coupled with energy-dispersive X-ray (EDX) spectroscopy were conducted. SEM images of the studied samples display needle-like crystals, with C, N, O, and Cu species exhibiting a homogeneous distribution in the probed domains (Figures S11 and S12, Supporting Information). The nanostructure was confirmed by scanning transmission electron microscopy (STEM) at lower magnifications while a regular, yet amorphous structure was observed at higher magnifications (Figure S13, Supporting Information).

2.2. Studies in an H-type Divided Cell

The eCO_2RR activity of a **Cat3**-modified carbon paper electrode was studied in a gas-tight H-type divided cell using an aqueous 0.1 M $CsHCO_3$ electrolyte (**Figure 2**; Figures S14–S19, Supporting Information). Linear sweep voltammetry (LSV) curves

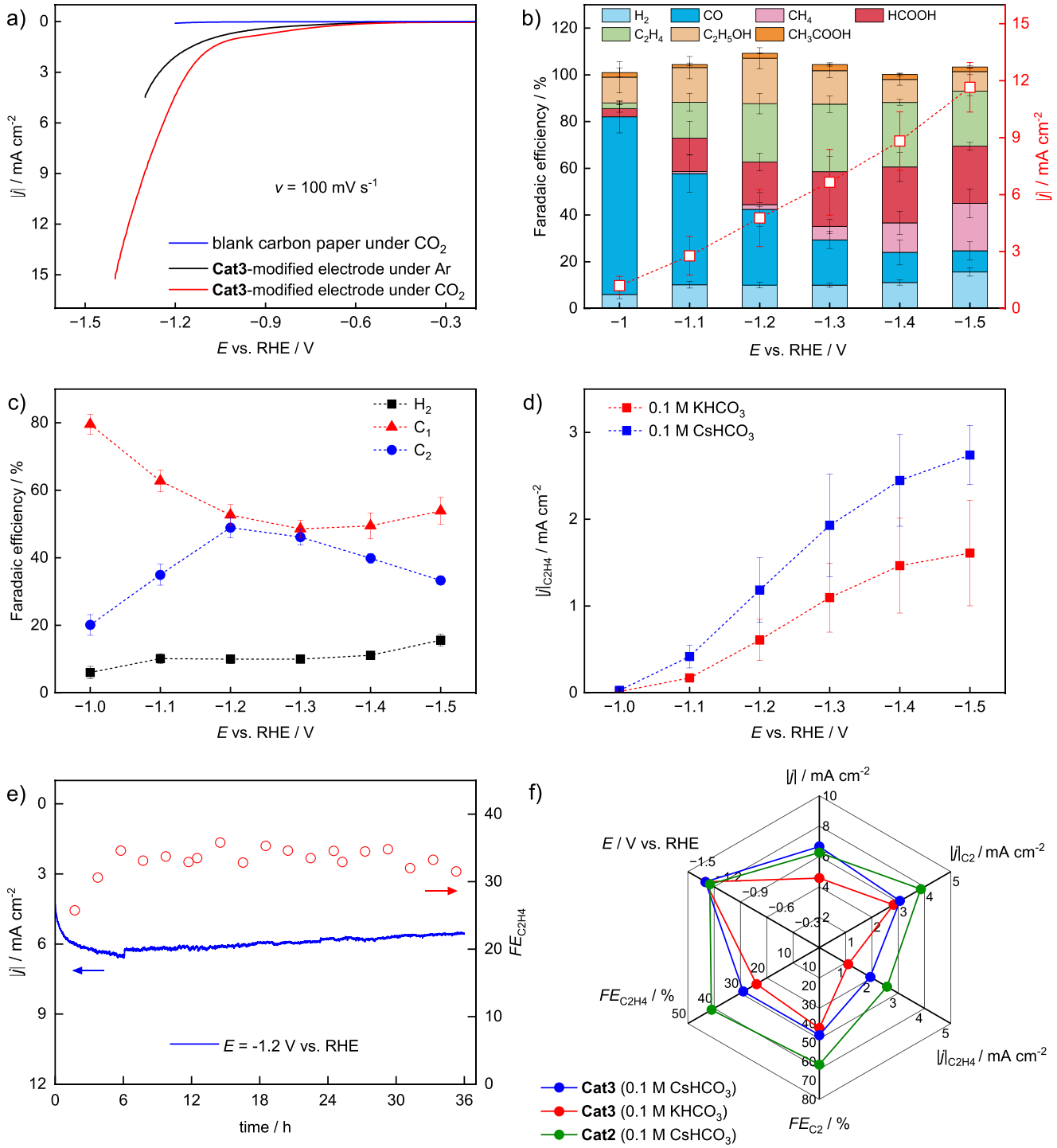

Figure 2. Electrochemical characterization of **Cat3**-modified carbon paper electrodes (aq. 0.1 M $CsHCO_3$ electrolyte, H-type-divided cell). a) LSVs of a **Cat3**-modified electrode under Ar (black, pH 8.9) and CO_2 (red, pH 6.8), respectively. b) Product distributions obtained upon electrolysis at different working electrode potentials using a **Cat3**-modified electrode. c) Comparison of the *FE* values for the generation of C_1 and C_2 products as well as H_2. d) Comparison of the partial current densities for C_2H_4 obtained from CPE in 0.1 M $CsHCO_3$ and 0.1 M $KHCO_3$ using a **Cat3**-modified electrode. e) Long-term stability test of **Cat3** at −1.2 V versus RHE. f) Comparison between eCO_2RR key performance indicators showing the influence of catalyst structure (**Cat2** vs. **Cat3**) and supporting electrolyte ($CsHCO_3$ vs $KHCO_3$). All measurements were carried out in H-cells at the indicated working electrode potential under otherwise identical conditions.

were recorded under both CO_2 and Ar atmosphere, respectively (Figure 2a). Under CO_2, **Cat3** exhibits a more positive onset potential and enhanced current density compared to the response under Ar, demonstrating promising catalytic activity.

To analyze the relationship between product distribution and working electrode potential, controlled potential electrolysis (CPE) was conducted at different potentials between −1.0 and −1.5 V versus RHE in CO_2-saturated solution (Figure 2b). While the gaseous products (mainly C_2H_4, CH_4, CO, and H_2) were detected online using a gas chromatograph (GC) after holding the potential for 14 min, the liquid-phase products (formate, ethanol, and acetate) were analyzed using ^{1}H NMR spectroscopy (for details, see the Supporting Information). At less negative potentials, CO generation is pronounced, but ceases in favor of formate and CH_4 as the driving force increases. C_2H_4 generation begins at −1.0 V and gains significance with increasing potential. At −1.3 V and more negative potentials, C_2H_4 becomes the predominant product, with up to 2.7 mA cm^{-2} partial current density and 30% *FE*. Interestingly, ethanol formation is also relatively strong with *FE* values up to 20%. It should be noted that FE_{H2} remains ≈10% across the studied potential region, highlighting the preference toward eCO_2RR over HER (which is consistent with our previously reported **Cat2**).[16] Analysis of the *FE* for H_2, C_1 and C_2 products at different potentials (Figure 2c) shows that the charge consumption for generating C_1 and C_2 products is almost equal in the range between −1.2 and −1.3 V (below and above this regime, formation of C_1 products is dominant). Control experiments with a blank carbon paper electrode as well as with $CuCl_2$ and Cu nanoparticle loadings show clearly different product distributions (see Figure S18, Supporting Information).

A comparison between the partial current density for C_2H_4 achieved in 0.1 M $CsHCO_3$ and 0.1 M $KHCO_3$ (2.7 and 1.6 mA cm^{-2}, both at −1.5 V) highlights the advantageous effect of Cs^+ ions (Figure 2d), similar to our previous study on **Cat2**.[16] The promoting effect of Cs^+ ions on eCO_2RR has been reported for various electrocatalysts elsewhere. It has been ascribed to i), the weaker hydration shell compared to smaller cations, decreasing the interfacial pH and increasing local CO_2 concentration, ii), improved surface charge-dependent reaction energetics associated with the smaller hydrated ion radius, and iii), the stabilization of key eCO_2RR intermediates.[17] The effect of Cs^+ on the behavior of **Cat3** was studied using impedance spectroscopy and is treated in detail in the SI (see Figure S20, Supporting Information; with corresponding discussion).

Noteworthy, **Cat3** demonstrates exceptional electrocatalytic stability, maintaining stable FE_{C2H4} and nearly constant current density at −1.2 V for over 36 h of continuous operation (Figure 2e; Figures S21–S23, Supporting Information). In Figure 2f, we compare the eCO_2RR performance with the maximum FE_{C2H4} of **Cat3** with our previous **Cat2** in $CsHCO_3$. While **Cat2** seems to outperform **Cat3** in the H-cell configuration, the incorporation of the methoxy substituents significantly enhances the robustness under continuous flow conditions, enabling stable operation in an MEA electrolyzer at high current densities (vide infra). It should also be noted that in the H-cell, **Cat3** exhibits significantly reduced leaching. While ICP-OES analysis of the post-electrolysis electrolyte solution revealed a Cu ion concentration of 2.5 mg mL^{-1} in the case of **Cat2**,[16] only 0.03 mg mL^{-1} was found under the same conditions in the case of **Cat3**.

2.3. Post-Electrolysis Characterization of the Electrocatalyst

After CPE at −1.2 V in CO_2-saturated 0.1 M $CsHCO_3$ solution, the working electrode was analyzed using P-XRD, SEM-EDX, XPS, and XAS (**Figure 3**; Figures S24–S31, Supporting Information). Interestingly, P-XRD analysis of the electrode after electrolysis revealed the same reflection peaks as those of the as-prepared **Cat3** electrode, indicating the preservation of crystalline domains during electrolysis. This finding is consistent with SEM results (Figures S25–S28, Supporting Information), which show microcrystalline objects on the surface (in contrast, the binuclear complex **Cat2** previously investigated by us transitioned completely to the amorphous state during electrolysis).[16] EDX mapping indicates even distributions of Cu, N, O, C, and Cl across the electrode surface. Notably, the Cl content decreased significantly after electrolysis compared with freshly prepared electrodes, indicating reductive dehalogenation of **Cat3** at negative potentials (as observed for **Cat2** in our previous study).

As shown in Figure 3b, XPS analysis of the pre- and the post-electrolysis materials shows two main peaks at 934.2 and 954.2 eV, accompanied by pronounced satellite features in the Cu 2p region, which can be assigned to Cu $2p_{3/2}$ and Cu $2p_{1/2}$ in the Cu^{2+} state.[18] The peaks at lower binding energies (932.2 and 952.1 eV) are associated with Cu^+/Cu^0 and result from reduction through X-ray radiation under high-vacuum conditions during the measurement.[16] This interpretation is confirmed by repeating the XPS measurement of the Cu 2p region after 1 h irradiation, whereby the Cu^+/Cu^0 peaks are significantly enhanced (Figure 3c). The XPS element quantification results are shown in Table S4 (Supporting Information), including the N/Cu ratio, which remains constant for the fresh and used **Cat3**-modified electrode, thus underlining the enhanced stability of the catalyst. In agreement with the EDX mapping results, the signal of the chloride ligand in the post-electrolysis Cl 2p scan is missing (Figure 3d), indicating reductive cleavage of Cu—Cl bonds under eCO_2RR conditions.

The oxidation state and coordination environment of the Cu species within **Cat3** were examined using ex situ X-ray absorption spectroscopy (XAS, for experimental details, see the Supporting Information). Figure 3e shows the normalized Cu K-edge X-ray absorption near-edge structure (XANES) spectra of **Cat3**, Cu_2O, CuO, $CuCl_2$, and Cu nanoparticles. A comparison shows that the reference materials display clear distinctions compared to our synthesized **Cat3**, showing an absorption edge ≈8975 eV. Toward the higher energy region, the K-edge spectrum of **Cat3**, both before and after electrolysis, partially aligns with those of CuO and $CuCl_2$ but lacks the characteristic feature at 8986 eV. The smooth rising edge without a shoulder at 8986 eV is typical for Cu^{2+} coordinated by 5 N/O atoms confirming the SC-XRD results.[19] This suggests that Cu in **Cat3** exists predominantly in the +2 oxidation state and is coordinated by phen ligands, consistent with our previous studies.[16] EXAFS analysis (Figure 3f) further elucidates the local structural environment around Cu atoms in **Cat3**. Fitting of the Fourier-transformed (FT-)EXAFS data (Figure S42, Table S5, Supporting Information) for the as-prepared powder reveals scattering contributions at distances of 1.94 ± 0.01 Å and 2.89 ± 0.02 Å with coordination numbers of 4.2 ± 0.5 for N/O and 2.2 ± 0.8 for Cu—O—Cu, respectively, in

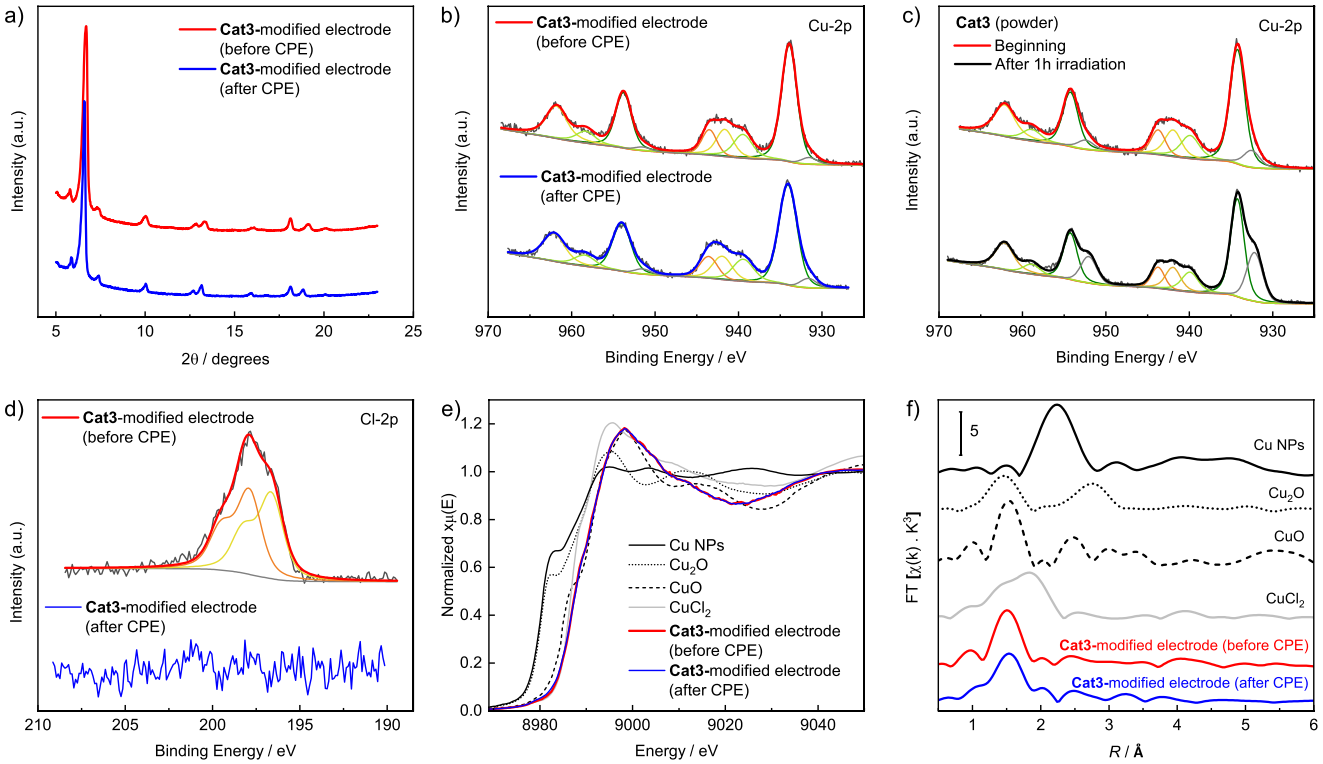

Figure 3. a) P-XRD patterns of **Cat3** after electrolysis. b–d) XPS analysis. Scans in the Cu 2p region using **Cat3**-modified carbon paper electrode before and after electrolysis, monitoring of the progression of the Cu 2p spectrum of as-prepared **Cat3** powder during X-ray irradiation, and scans in the Cl 2p region. e,f) XAS analysis of **Cat3**-modified carbon paper electrode (before and after electrolysis) and of reference materials. Normalized Cu K-edge XANES spectra and Fourier transform EXAFS spectra.

agreement with our single-crystal diffraction data and DFT calculations (Figure S1 and Table S2, Supporting Information).

2.4. X-Ray Absorption Spectroelectrochemistry

Despite the high FE_{C2}, the stable performance over 36 h in the H-cell configuration, and the good match between pre- and post-electrolysis XANES/EXAFS spectra, the progression of the molecular framework of the organometallic Cu species during electrolysis yet remains uncertain. As known from the literature, reductive demetallation of Cu complexes with a negative bias can lead to the formation of CuO_x particles.[20] In some cases, particle formation can even be reversible, i.e., the CuO_x particles transform back into the Cu coordination compounds when the bias is removed or when the potential returns to a more positive value.[21] This in situ phase evolution warrants special attention, particularly in determining active sites. Consequently, XAS spectroelectrochemistry (SEC) was performed under eCO_2RR conditions in a custom-made divided cell in the three-electrode configuration (**Figure 4**; Figure S32–S43, Supporting Information).

XAS analysis was conducted in the dry state (catalyst-sprayed carbon paper mounted in our in situ cell), in CO_2-saturated 0.1 M $CsHCO_3$ solution at open-circuit potential (OCP), and at potentials ranging from −0.9 to −1.4 V versus RHE. In situ XANES spectra showing the full energy range (8850 to 9500 eV) and the enlarged pre-edge region (8970 to 8990 eV) are presented in Figure 4a. The results indicate that across the screened potential range, the Cu oxidation state and the d orbital structure remain nearly constant. Stability of the Cu coordination environment is corroborated by the EXAFS spectra (9030 to 9600 eV) and corresponding Fourier Transformed (FT-EXAFS) profiles (Figure S33a, Supporting Information). A similar trend could be observed in control experiments (0.1 M $KHCO_3$ under CO_2 and 0.1 M $CsHCO_3$ under Ar, displayed in Figures S35 and S36, Supporting Information). The dominant scattering path observed at near 1.9 Å corresponds to Cu interactions with light atoms, such as N/O, in the first coordination shell, whereas minimal Cu—Cu scattering paths appear at ≈2–4 Å, consistent with the oscillations observed in the k-space profiles (Figure S33, Supporting Information). For a more detailed comparison, wavelet-transformed EXAFS (WT-EXAFS) analyses, based on both R-space and k-space profiles, were conducted for selected samples (Figure S34, Supporting Information), confirming the absence of inorganic Cu species and preservation of the local Cu coordination environment in as-prepared **Cat3**.

For the **Cat3**-modified electrode, the primary intensity maximum appears at ≈1.9 Å in R-space and spans k-values from 3 to 10 $Å^{-1}$, corresponding to the first coordination shell while excluding the presence of reference materials such as CuO, $CuCl_2$, and Cu_2O. The intensity maximum in the WT-EXAFS maps was maintained under negative bias, indicating the

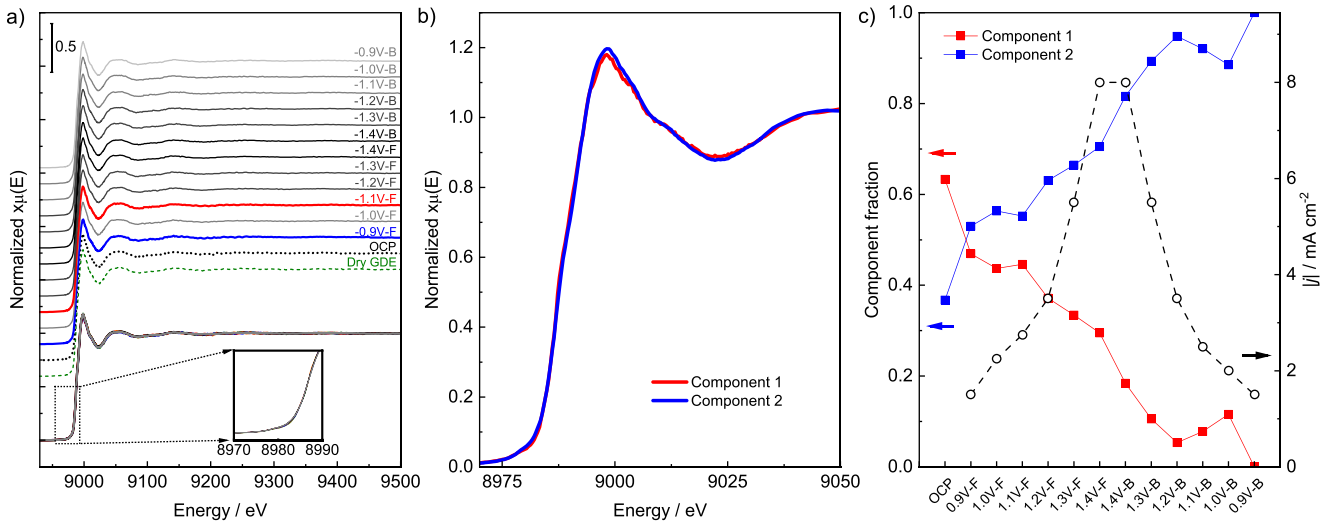

Figure 4. In situ XAS analysis of a **Cat3**-modified electrode performed in a divided SEC batch cell. a) Cu K edge XANES spectra of the electrode in dry form and in aq. CO_2-saturated $CsHCO_3$ electrolyte at OCP and various potentials between −0.9 and −1.4 V versus RHE. b) The two most distinct XANES spectra within the dataset from Figure 4a obtained via multivariate curve resolution-alternating least squares (MCR-ALS). c) Component fractions corresponding to the most distinct spectra (Figure 4b) obtained via MCR-ALS, along with the corresponding current densities measured during in situ XAS analysis.

preservation of the local coordination environment around the Cu centers throughout the applied electrochemical potentials. Based on these findings, we conclude that the molecular scaffold exhibits structural stability up to −1.4 V versus RHE, which is maintained during the reverse potential scan to −0.9 V versus RHE.

To further elucidate the chemical behavior of Cu in **Cat3** under eCO_2RR conditions, multivariate curve resolution–alternating least squares (MCR-ALS) analysis was performed (Figure 4b,c). This analysis enables the deconvolution of overlapping spectral features to track subtle changes in the closer Cu coordination environment. For this purpose, the two spectra with the strongest variation, components 1 and 2, serve as internal references (Figure 4b). Notably, both profiles nearly overlap with each other, highlighting a negligible reaction-induced shift in the Cu oxidation state and coordination environment under e-CO_2RR conditions. A transition to a smoother rising edge with a broader featureless white line is attributed to a very slight increase of the coordination number (Table S5, Supporting Information).[19,22] This effect is possibly be due to reductive cleavage of the Cu—Cl bonds at the terminal Cu centers (vide supra) as well as to coordination of water and/or CO_2RR intermediates. The potential-dependent fractions of the individual components in the spectra are shown in Figure 4c along with the corresponding current densities. Starting from the OCP, the relative fraction of component 2 steadily increases at the cost of component 1, however, since the spectral components are nearly identical, the absolute change in the Cu state is minimal. Despite this gradual change, the Cu centers in **Cat3** consistently remain in the Cu^{2+} state and exhibit nearly unchanged coordination environment at low current densities. This behavior highlights the stability of the molecular framework of **Cat3**, in contrast to the dynamic restructuring observed with Cu nanoparticles under identical conditions (Figure S37, Supporting Information).

2.5. MEA Electrolyzer Studies

For testing the performance at high current density, **Cat3** was spray-coated onto carbon paper gas diffusion electrodes (GDEs) and employed in a membrane electrode assembly (MEA) electrolyzer (Figures S44–S55, Supporting Information). While the cathode was fed with a stream of water-saturated CO_2, aq. 0.1 M $CsHCO_3$ was pumped through the anodic half-cell, with the applied current density ranging from 10 to 200 mA cm^{-2} (**Figure 5a**). The cell voltage (without *IR* drop correction) increases from initially 2.5 to 4 V, which is somewhat higher than reported for metallic Cu catalysts within similar cell configurations.[5,23] At each step, the current was held constant for 15 min., followed by collection of the anolyte for liquid phase analysis by ^1H NMR spectroscopy (for details of product analysis and calculations, see the SI). The major gas-phase products are CO and C_2H_4, while the *FE* for H_2 remains well below 20% across the entire current density range (Figures S46–S48, Supporting Information). Interestingly, the fraction of ethylene increases strongly with rising current density at the cost of CO formation, while the amount of CH_4 formed remains negligible. C_2H_5OH and CH_3COOH were the dominant liquid products, while the fractions of HCOOH and *n*-PrOH each remain below 10%. As a result, the *FE* for all C_2 products shows a steady increase with rising current density, with a maximum of 71% at 200 mA cm^{-2} (Figure S48, Supporting Information). This behavior differs from the results obtained in the H cell, where the fraction of C_2 compounds ceases in favor of CH_4 at elevated current densities (cf. Figure 2c). Furthermore, a control experiment using a GDE loaded with Cu nanoparticles shows a clearly different product distribution (see Figure S52, Supporting Information), once again highlighting the unique behavior of **Cat3**.

Analogous to the previous H-cell studies, the choice of the cation significantly impacted the C—C coupling capability of **Cat3** under MEA conditions (Figure 5b). While a maximum FE_{C2} of

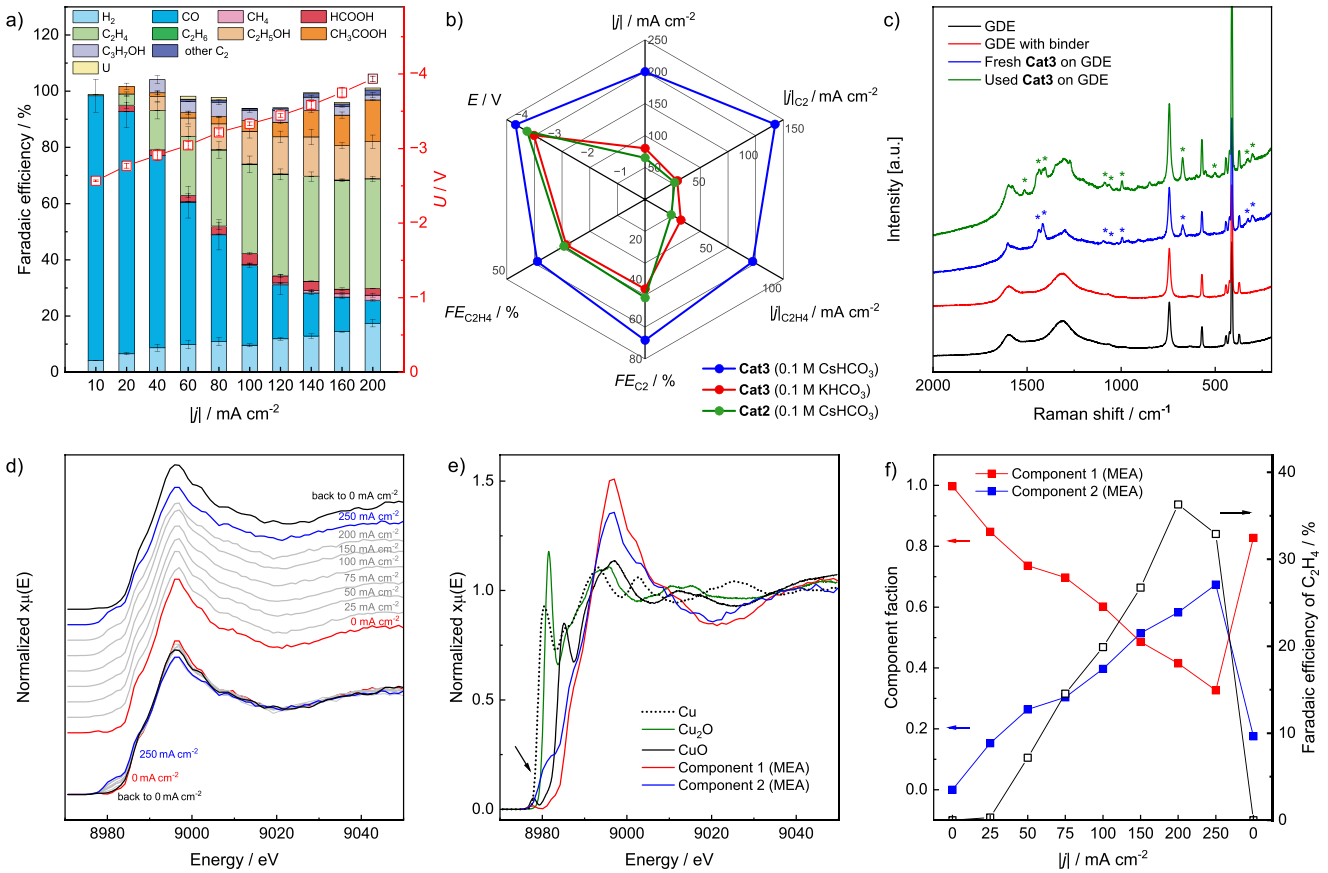

Figure 5. Electrochemical studies in an MEA electrolyzer using a **Cat3**-modified GDE (0.1 M $CsHCO_3$ as the anolyte). a) Relationship between current density, product distribution, and cell voltage. b) Comparison between the performance characteristics of **Cat3** and **Cat2**. c) Pre- and post-electrolysis Raman spectra of **Cat3**-modified electrode (excitation wavelength: 785 nm). Signals assigned to **Cat3** are marked with stars. d) Results of in situ Cu K-edge high-energy-resolution fluorescence-detected (HERFD) XANES analysis of a **Cat3**-modified GDE under eCO_2RR conditions at various current densities (aligning with the measurements in Figure 5a). e) Most distinct Cu K edge HERFD-XANES spectra along with spectra of reference compounds. f) Component fractions corresponding to the most distinct Cu K edge HERFD-XANES spectra (Figure 5e) obtained via MCR-ALS analysis. *FE* values for C_2H_4 are inserted for comparison.

45% is already achieved at 80 mA cm^{-2} when using 0.1 M $KHCO_3$ as the anolyte, a steady increase to 71% is observed at current densities up to 200 mA cm^{-2} when using 0.1 M $CsHCO_3$ (for details, see Figures S46 and S47, Supporting Information). At 80 mA cm^{-2}, FE_{C2H4} remained close to 35% for over 10 h, demonstrating robust and stable performance at continuous operation (Figures S53 and S54, Supporting Information).

Noteworthy, the binuclear Cu complex **Cat2** is significantly less stable in the MEA electrolyzer under the same conditions. Due to slow catalyst leaching, this system cannot be used effectively for a longer period, which is why insoluble **Cat3** offers a clear advantage in the MEA environment. In view of C_2H_4 production rate, **Cat3** exhibits a steadily increasing turnover frequency (*TOF*) with rising current density, reaching 178 h^{-1} at 200 mA cm^{-2}. In contrast, *TOF*(C_2H_4) decreases for **Cat2** when the current density rises above 50 mA cm^{-2} (for details, see Figure S55, Supporting Information).

After disassembling the post-electrolysis MEA, the catalyst layer was examined and subjected to SEM, Raman spectroscopy, and TEM (Figures S56–S63, Supporting Information). Identical to the as-sprayed GDE, the coating retained its greenish color (Figure S56, Supporting Information). SEM-EDX revealed a layer morphology similar to that of freshly prepared electrodes, whereby Cu remains evenly distributed across the surface (Figures S57–S61, Supporting Information). The Raman spectra of the fresh and the used **Cat3**-modified electrode exhibit the same characteristic bands at 302, 327, 674, 910, 995, 1096, 1304, 1418, 1438, and 1602 cm^{-1} (Figure 5c). Additional bands at 374, 410, 441, 570, and 743 cm^{-1} stem from the used sapphire probe and those at 1314 and 1599 cm^{-1} from the carbon paper. The broad bands around ≈530 and 620 cm^{-1}, typical for Cu/CuO_x nanoparticles, (Figure S64, Supporting Information) are neither contained in the spectrum of the fresh nor the used electrode.

To study the structure of **Cat3** under operational conditions, in situ HERFD-XANES was carried out using a custom-made MEA-type spectroelectrochemical cell (Figure S65, Supporting Information). The HERFD-XANES technique with its exceptionally high energy resolution[24] allows to highlight even small spectral changes related to the **Cat3** framework. The applied current density was stepwise increased from 0 mA cm^{-2} (OCV) to 250 mA cm^{-2}. Despite nearly constant spectral features from 8990 to 9500 eV across all current densities (Figure S66, Supporting

Information), a slight but gradual increase in the pre-edge intensity at 8980 eV was observed (Figure 5d; Figure S67, Supporting Information). This growing pre-edge feature, associated with the formally forbidden 1s to 3d transition, could be tentatively attributed to structural distortion (via 3d–4p orbital mixing), weakening of metal–ligand bonds,[25] or formation of inorganic species.[26]

To further disentangle the hybrid/mixed phases present during the reaction, MCR-ALS analysis was applied to the MEA-derived XAS dataset and extracted two distinct spectral components, as shown in Figure 5e. Component 1 closely resembles the initial state of the catalyst, whereas component 2 represents the mixture with the highest concentration of the second phase emerging under electrochemical conditions. In component 2, Cu remains coordinated to two N/O ligands, and a Cu—Cu distance of ≈2.5 Å with a coordination number of 2 is observed. Approximately 35% of the Cu is estimated to be in a reduced state (Figure S68, Table S6, Supporting Information). However, the absence of a significant K-edge shift to lower energies, along with a low average Cu—Cu coordination number, and in combination with higher white line intensity comparable to standard references of Cu, Cu_2O, and CuO (Figure 5e), suggests minimal formation of inorganic Cu-based particles.

At a current density of 200 mA cm^{-2}, the sample exhibits nearly 60% component 2 (Figure 5f), comprising 35% reduced Cu moieties. This outcome corresponds to about a 20% overall reduction, and 80% of the Cu remains in the Cu^{2+} state. These observations are consistent with our linear combination analysis (LCA), where Cu^0 is used to represent the reduced state (Figure S69, Table S7, Supporting Information). Moving to 250 mA cm^{-2}, the contribution of component 2 progressively increased, reaching ≈70% (24.5% reduced Cu), however, causing a degradation of C_2H_4 production (Figure 5f). Interestingly, upon removal of the applied bias, a partial recovery of the Cu electronic state can be observed, both in the pre-edge region and the extended fine structure, indicating a degree of reversibility in the initial local environment of the Cu centers. Notably, K-edge profiles recorded at 200 mA cm^{-2} (Figure S70, Supporting Information), averaged over 4-min intervals (corresponding to the maximum FE_{C2H4} yield, see Figure 5b), suggest that this structural change is potential/current-dependent, but time-independent.

3. Conclusion

Our study provides new insights into the catalysis of electrochemical CO_2 reduction with molecular Cu phenanthroline compounds. Screening of a series of differently substituted phenanthrolines revealed 4,7-dimethoxy-1,10-phenathroline to be the most effective ligand. The resulting water-insoluble **Cat3** is a cascade-like coordination oligomer that features μ_2- and μ_3-hydroxo-bridged Cu centers with relatively short Cu···Cu distances. The material is readily synthesized using inexpensive building blocks and a straightforward protocol. Compared to the previously reported binuclear Cu phenanthroline compound **Cat2**, the stability of **Cat3** under electrocatalytic conditions is significantly enhanced, allowing for operation in an MEA electrolyzer at high current densities. When spray-coated onto a carbon gas diffusion electrode, **Cat3** achieves more than 70% FE_{C2+} at 200 mA cm^{-2}, while stable performance is observed for 10 h with no obvious performance degradation. Pre- and post-electrolysis analysis by SEM and Raman spectroscopy reveal that the electrode is coated with a stable composite matrix containing homogeneously dispersed copper and no obvious formation of inorganic Cu species.

In many previous works, the decomposition of molecular Cu catalysts during eCO_2RR is reported, resulting in the formation of Cu/CuO_x particles that serve as the true active species. Conclusions regarding the type of active site should therefore be drawn with great caution and must be supported by in situ spectroscopic data. To monitor the structural evolution of **Cat3** under reaction conditions, in situ XAS was carried out under potential control in the kinetic regime using a liquid flow cell, and under galvanostatic conditions at high current densities in an MEA-type cell. While in the kinetic regime, no significant changes of the spectral features were observed, the results obtained with the MEA-SEC cell suggest gradual structural changes when increasing the current density from 50 to 250 mA cm^{-2}, i.e., reduction of the Cu oxidation state, decrease of the Cu···Cu distance, and a lowering of the Cu—N/O coordination number. However, in view of the still low Cu—Cu coordination number, absence of K-edge shift to lower energies, and high white line intensities compared to inorganic Cu reference species, no or only minimal formation of Cu/CuO_x particles is assumed. Strikingly, the original phase is largely restored upon bias removal, highlighting both the structural robustness and adaptive redox behavior of **Cat3** under harsh electrolysis conditions. While future studies will address the potential-dependent structural modifications as well as the eCO_2RR mechanism in detail, the present work highlights a possible pathway toward implementing molecular electrocatalysts in CO_2 electrolyzers for the synthesis of C_{2+} products.

4. Experimental Section

Chemicals: Copper chloride ($CuCl_2$, 99%), cesium bicarbonate ($CsHCO_3$, 99.99%), methanol (99.8%), ethanol (99.8%), and isopropanol (99.8%) were purchased from Fisher Scientific. 4,7-Dimethoxy-1,10-phenanthroline (97%) was purchased from BLD Pharmatech Ltd. (China). Triethylamine (99.5%), potassium bicarbonate (99.99%), dimethyl sulfoxide (DMSO, 99.9%), copper nanoparticles (Cu NPs, 40–60 nm, 99.5%), and Nafion 1100W solution were purchased from Sigma-Aldrich (Germany). Anode electrode (commercial IrO_x-coated gas diffusion electrode (GDE)) and Sustainion XA-9 alkaline ionomer powder, both for use in the MEA electrolyzer, were purchased from Dioxide Materials (US). Toray Carbon Paper 060 (wet-proofed), carbon gas diffusion layers (GDL, Freudenberg H23C8), and PiperION anion exchange membranes (20 microns) were obtained from The Fuel Cell Store (US). Deuterium oxide (D_2O, 99.9%) for NMR measurements was purchased from Deutero GmbH (Germany). CO_2 (99.9999%) and Ar (99.9999%) were obtained from Linde AG (Germany).

*Synthesis of **Cat3***: The catalyst was synthesized according to the reported method in the previous work.[16] A solution of 134.45 mg (1 mmol) $CuCl_2$ in 1 mL ultrapure water was combined with a solution of 240.60 mg (1 mmol) 4,7-dimethoxy-1,10-phenanthroline in 4 mL of ethanol under stirring at room temperature, resulting in the formation of a light green precipitate. After stirring for 10 min, 10 mL triethylamine was added to the suspension, leading to an immediate change of the precipitate color to dark green. The mixture was stirred for an additional 10 min. The precipitate was then filtered off, washed with ultrapure water, and dried overnight under vacuum at 60 °C, yielding a crystalline dark green product (yield: 300 mg). Elemental analysis: Cu 18.10, C 46.02, H 3.55, N 7.39, Cl 7.84.

Attempts to prepare high-quality single crystals of **Cat3** for SC-XRD analysis using the previously described crystallization procedure[16] remained unsuccessful. Instead, an alternative procedure was applied, wherein **Cat3** powder (60 mg) was partially dissolved in MeOH, followed by heating to 85 °C for 12h in an autoclave. Afterward, the mixture was allowed to cool to room temperature. Crystallization proceeded within four days. The obtained crystals were subjected to SC-XRD (see Figure S1, Supporting Information).

To confirm the identity of **Cat3** crystals, HERFD XAS (Figure S3, Supporting Information), P-XRD (Figure S8, Supporting Information), and Raman spectroscopy (Figure S9, Supporting Information) were performed. In each case, a good agreement was observed between the results of **Cat3** powder and crystalline **Cat3**.

Materials Characterization: X-ray diffraction (XRD) data were obtained using a Panalytical X'Pert Pro diffractometer with Cu-Kα radiation, while single-crystal XRD (SC-XRD) was carried out on a Kappa APEX II Duo diffractometer from Bruker AXS. The copper content of **Cat3** was analyzed using inductively coupled plasma optical emission spectrometry (ICP-OES) with an Agilent 715-ES spectrometer. Carbon, hydrogen, and nitrogen contents were determined via combustion analysis using a TruSpec Micro elemental analyzer (LECO Instrumente GmbH, Germany). The morphology of the electrode surface, both before and after electrolysis, was examined using scanning electron microscopy (SEM) with a MERLIN VP Compact (Zeiss, Germany) equipped with EDX. ^{1}H nuclear magnetic resonance (NMR) spectroscopy was performed with a Bruker AVANCE 500 NEO spectrometer.

For scanning electron microscopy (SEM, field emission), the samples were mounted on a heavy metal-free Al-SEM-carrier (co. PLANO, Wetzlar, Germany) with adhesive conductive carbon tape (Spectro Tabs, TED PELLA INC, Redding, USA) and coated with carbon (5.0 nm thickness) under vacuum (CCU 010 HV-Coating Unit, Co. Safematic GmbH, Zizers, Switzerland). Analysis was carried out using a field emission scanning electron microscope (SEM, MERLIN VP Compact, Co. Zeiss, Oberkochen, Germany) equipped with an energy-dispersive X-ray (EDX) detector (XFlash 6/30, Co. Bruker, Berlin, Germany). Representative areas of the samples were analyzed and mapped for elemental distribution based on the EDX-spectra data by QUANTAX ESPRIT Microanalysis software (version 2.0). SEM-images were taken from the selected regions.

Scanning Transmission Electron Microscopy (STEM) was performed on a probe aberration-corrected JEM-ARM200F (JEOL, corrector: CEOS) at an acceleration voltage of 200 kV. A High-Angle Annular Dark Field (HAADF) and an Annular Bright Field (ABF) detector were used for imaging. The solid samples were prepared as described in the Supporting Information and deposited without any pre-treatment onto a carbon-supported Ni grid (mesh 300) and finally transferred to the microscope.

XPS (X-ray Photoelectron Spectroscopy) measurements were performed on an ESCALAB 220iXL (Thermo Fisher Scientific) with monochromated Al Kα radiation (E = 1486.6 eV). Samples are prepared on a stainless-steel holder with conductive double-sided adhesive carbon tape. The measurements are performed with charge compensation using a flood electron system that combines low-energy electrons and Ar^+ ions (p_{Ar} = 1×10^{-7} mbar). The electron binding energies are referenced to the C 1s core level of carbon at 284.8 eV (C—C and C—H bonds). For quantitative analysis, the peaks were deconvoluted with Gaussian–Lorentzian curves using the software Unifit 2023. The peak areas were normalized by the transmission function of the spectrometer and the element-specific sensitivity factor of Scofield.

Raman spectra of **Cat3**-modified electrodes (before/after electrolysis) were measured using a Renishaw inVia Raman microscope equipped with a 633 nm air-cooled He-Ne laser. For the measurement, the electrode or a spatula tip of the powdered sample was placed on a microscope slide, and the laser beam was focused on the sample using a ×20 objective. The Laser power was maintained at a relatively low level, ranging from 0.085 to 0.17 mW, to avoid damaging effects that may otherwise occur. The exposure time of a spectrum was 30 s with 3 accumulations. To obtain a broader cross-section of the sample, a selection of samples was analyzed using a Horiba iHR 550 Raman spectrometer equipped with a 785 nm laser source (Oxxius, maximum laser power: 864 mW) connected to a fiber optical ball probe with a sapphire lens (MarqMetrix, 3/8″ Process BallProbe). The samples were measured in the direct contact mode. The measurement parameters varied depending on the sample: exposure time 10–30 s, 3 accumulations.

Electrode Preparation: For measurements in an H-cell, the electrode was prepared according to the previous work.[16] The catalyst (6 mg) was suspended in a mixture containing 450 µL of ultrapure water, 90 µL of isopropanol, and 60 µL of Nafion solution, then ultrasonicated for 15 min to produce a homogeneous ink. Next, 50 µL of the ink was applied to a strip of carbon paper (1 cm wide) by drop-casting, covering an area of 1 cm^2 on both sides (resulting in 2 cm^2 active area in total). The electrode was then allowed to dry in air. The catalyst loading (**Cat3**) for each working electrode was 0.5 mg cm^{-2}.

For measurements in a membrane electrode assembly (MEA) electrolyzer, 40 mg of catalyst was suspended in a mixture of 3 mL ultrapure water, 600 µL isopropanol, and 400 µL Sustainion XA-9 alkaline ionomer solution (5 wt.% ionomer in EtOH, Dioxide Materials). The mixture was ultrasonicated to generate a homogeneous ink. Then, the ink was distributed homogeneously on the micro-porous layer of the carbon paper (Freudenberg C8H23 GDL, 25 cm^2 geometrical surface area) by spray coating at 60 °C, followed by air-drying for 10 min. The GDL was weighed before and after the spray-coating, and the mass difference was kept near 35 mg (on 25 cm^2 electrode), resulting in a catalyst loading of 1 mg cm^{-2} and ≈30 wt.% ionomer content in the dry as-prepared catalyst layer. From the coated GDL, pieces of 5 cm^2 were cut out and used as cathode for MEA measurements.

Electrochemical Experiments: Linear sweep voltammetry (LSV), controlled potential electrolysis (CPE), and controlled current electrolysis (CCE) were performed using a VIONIC potentiostat from Metrohm (Germany). CPE was carried out in an H-cell (separator: glass frit with pore size G4). A platinum plate and a Ag/AgCl electrode (3 M KCl solution) served as a counter and a reference electrode, respectively. A 0.1 M $CsHCO_3$ solution (pH 6.8 under CO_2, pH 8.9 under Ar) served as the electrolyte. Prior to each CPE experiment, CO_2 was bubbled at a flow rate of 40 mL min^{-1} for 30 min. Current densities were calculated based on the total immersed electrode surface area of 2 cm^2. Potentials measured vs. Ag/AgCl were converted to the reversible hydrogen electrode (RHE) using the following relationship.[27]

$$E\ (\text{vs. RHE}) = E\ (\text{vs. Ag/AgCl}) + 0.197\ V + 0.0591 \cdot pH \quad (1)$$

The MEA measurements were performed at room temperature. The spray-coated GDE was used as working electrode for eCO_2RR, and a commercial IrO_x-based electrode (from Dioxide Materials) served as the counter electrode. The cathode and anode chambers were separated using a PiperION anion exchange membrane (thickness: 20 µm). Humidified CO_2 was purged through the cathode chamber at a flow rate of 50 sccm (room temperature), while a N_2 bleeding line (flow rate: 20 sccm) was injected after the electrolyzer, serving as the flow rate internal standard. 0.1 M $CsHCO_3$ solution was circulated through the anode chamber as anolyte with a flow rate of 30 sccm, using a Simdos 10 diaphragm pump.

Product Quantification: Gaseous products from CPE (H-cell) and CCE (MEA set-up) were analyzed using gas chromatography (GC, Agilent 6890) with argon as the carrier gas, calibrated using certified gas mixtures from Air Liquide as standards. A thermal conductivity detector (TCD) was used to analyze H_2 and CO, while a flame ionization detector (FID) was employed to quantify CH_4, C_2H_4, and C_2H_6. For CPE and CCE, cells were connected to the GC for online analysis by using a steady flow of CO_2 gas of 20 mL min^{-1} (H-cell) and 50 mL min^{-1} (MEA set-up), respectively. In the meantime, N_2 bleeding with a flow rate of 22 mL min^{-1} served both as an internal standard and to compensate for the CO_2 that was consumed during the reaction (for details, see Figure S44, Supporting Information). The Faradaic efficiencies (*FE*) for specific gaseous products *x* (e.g., *x* = C_2H_4) were calculated using the following equation,[28]

$$FE_x\,[\%] = \frac{p\,\dot{V}\,\phi_x z F}{RTi} \cdot 100 \quad (2)$$

where $\dot{V}$ refers to the flow rate of the gas delivered to the gas chromatograph at a specified sampling time with N_2 compensation, ϕ_x to the volume fraction of the gaseous product (e.g., C_2H_4) in the gas flow that was delivered to the detector, p to the pressure (1.01×10^5 Pa), R to the gas constant, T to the temperature (296 K), z to the number of electrons transferred for CO_2-to-x (i.e., $z = 12$ for C_2H_4), F to the Faraday constant, and i to the current recorded by the potentiostat.

The liquid products were quantified by ^{1}H NMR spectroscopy using a water pre-saturation method and DMSO as an internal standard. For sample preparation, a 500 µL aliquot of the post-electrolysis electrolyte solution was mixed with 100 µL D_2O and 35 µL DMSO. FE_x was calculated using the following relationship,

$$FE_x\,[\%] = \frac{c_x V z F}{Q} \cdot 100 \tag{3}$$

wherein c_x denotes the concentration of the product (e.g. formate) in the liquid phase, V represents the catholyte volume (17 mL), and Q is the total amount of passed electric charge at the specified sampling time.

Ex Situ and In Situ X-Ray Absorption Spectroscopy (XAS) Measurements: All ex situ measurements for powder and electrode were performed in fluorescence mode. All in situ XAS measurements were carried out using either a divided spectroelectrochemical (SEC) liquid flow cell (three-electrode arrangement) or a SEC MEA cell (galvanostatic conditions) in the fluorescence mode.

For measurements in the SEC flow cell, electrode preparation follows the same procedure as in the H-cell studies (catalyst loading: 1 mg cm^{-2} with 15 wt.% Nafion ionomer, deposited on Freudenberg C2 carbon paper). The anodic and cathodic half-cells were separated by a Nafion 117 membrane. An Ag/AgCl reference electrode was placed in the cathode chamber for control of the working electrode potential. All in situ XAS measurements were carried out at the near (XANES) and extended (EXAFS) Cu K-edge at the XPP KMC-3 beamline (BESSY II). The employed flow cell is shown in Figure S32 (Supporting Information). The X-ray beam was focused to a spot size of 500 × 500 µm at a fixed sample position. The beam energy was scanned from 8900 to 9600 eV (scan rate: 1.6 eV s^{-1}). An aqueous 0.1 M $CsHCO_3$ solution was used as both catholyte and anolyte and pumped through the half-cells at a flow rate of 20 mL min^{-1}. The catholyte was purged with CO_2 for 30 min prior to each measurement and feeding to the catholyte was continued to ensure CO_2 saturation. For every measurement at a defined potential, two in situ XAS spectra were collected. Data reduction and processing of the XANES spectra, including background subtraction, energy correction, normalization, and linear combination fitting were performed using the standard Athena software from the Demeter 0.9.26 program package.

Measurements in the SEC MEA cell (Figure S65, Supporting Information) were performed in the High-Energy-Resolution Fluorescence-Detected XAS (HERFD-XAS) mode at the ID26 beamline of the European Synchrotron Radiation Facility (ESRF, Grenoble, France). The higher harmonics were suppressed by Si-coated mirrors which operate in total reflection mode. The desired energy was selected by a Si(111) double crystal monochromator. The fluorescence X-rays were collected by an X-ray spectrometer using the (800) reflection of two spherically bent Ge crystals, and the photons were counted by a PILATUS3 100K-M detector. The monochromator energy calibration was performed by measuring Cu foil. For the HERFD-XANES measurements the monochromator energy was scanned while the spectrometer was kept fixed at the maximum of the Kβ1,3 emission line (8903.6 eV). The assembly of the MEA SEC was carried out analogously to MEA performance characterization described above (catalyst loading: 1 mg cm^{-2} with 15 wt.% Sustanion XA-9 ionomer, sprayed on Freudenberg C2 carbon paper). The beam energy was scanned from 8900 to 9600 eV (scan rate: 11.6 eV s^{-1}). Characterization of the SEC MEA cell including analysis of the product mixture was carried out separately using the GC quantification protocol detailed above, whereby good agreement with the standard MEA electrolyzer was found. Data reduction and modelling of the EXAFS spectra were conducted using the standard Athena and Artemis software from the Demeter 0.9.26 program package. EXAFS data were analyzed in the R-space using fixed k and R ranges (2.0–11.0 Å^{-1}, R: 1.0–3.0 Å). Wavelet transformations of EXAFS (WT-EXAFS) spectra were calculated using the Hama Fortran program.[29] The Morlet wavelet was used for the analysis. The raw k3 weighted data were added to the Hama_Fortran program for analysis. For the Multivariate Curve Resolution–Alternating Least Squares (MCR-ALS) the spectral datasets corresponding to each measurement were imported and normalized using the FASTOSH v. 1.0.8 software.[30] To derive the pure spectra and the respective relative concentrations, the MCR-ALS Matlab toolbox[31] integrated into FASTOSH was used.

Statistical Analysis: All statistical analyses in this work were performed using the Origin 2023 software. Before data analysis, irrelevant data detection and elimination were performed on the data sets. Experimental errors for FE and average $|j|$ values were calculated as the standard error of the mean using a sample size of $n = 3$. Experimental data in bar diagrams were presented as mean values ± standard deviation.

Supporting Information

Supporting Information is available from the Wiley Online Library or from the author.

Acknowledgements

The authors are grateful for financial support through the DFG Research Training Group 2943 "SPECTRE" (project number 507189291), the DFG Heisenberg Program (FR 3848/4-1, to R. F.), the Chinese Scholarship Council (PhD stipend, to N. L.), and the Leibniz Association (Leibniz Competition, to O. S. B.). The authors acknowledge the European Synchrotron Radiation Facility (ESRF) for provision of synchrotron radiation facilities (proposal number CH-7291) and thank Dr. Sami Juhani Vasala, Dr. Olga Filimonova, and Dr. Pieter Glatzel for their assistance and support in using beamline ID26. The authors also acknowledge BESSY II (Helmholtz-Zentrum Berlin für Materialien und Energie) for the allocation of synchrotron radiation beamtime on beamline KMC-3 (proposal number ST-242-12650), Dr. Götz Schuck for assistance during XAS measurements, and PD Dr. Michael Haumann (FU Berlin) for valuable guidance and support. Furthermore, the author thanks Dr. Nils Rockstroh (LIKAT Rostock) for TEM analysis of the samples.

Open access funding enabled and organized by Projekt DEAL.

Conflict of Interest

The authors declare no conflict of interest.

Data Availability Statement

The data that support the findings of this study are available in the supplementary material of this article.

Keywords

copper, phenanthroline, electrocatalysis, molecular catalyst, CO_2 reduction

Received: July 16, 2025
Revised: September 16, 2025
Published online:

[1] a) I. Sullivan, A. Goryachev, I. A. Digdaya, X. Li, H. A. Atwater, D. A. Vermaas, C. Xiang, *Nat. Catal.* **2021**, *4*, 952; b) M. G. Kibria, J. P.

Edwards, C. M. Gabardo, C. T. Dinh, A. Seifitokaldani, D. Sinton, E. H. Sargent, *Adv. Mater.* **2019**, *31*, 1807166; c) D. Gao, R. M. Arán-Ais, H. S. Jeon, B. R Cuenya, *Nat. Catal.* **2019**, *2*, 198.

[2] a) K. Fernández-Caso, G. Díaz-Sainz, M. Alvarez-Guerra, A. Irabien, *ACS Energy Lett.* **2023**, *8*, 1992; b) T. Yan, X. Chen, L. Kumari, J. Lin, M. Li, Q. Fan, H. Chi, T. J. Meyer, S. Zhang, X. Ma, *Chem. Rev.* **2023**, *123*, 10530; c) S. Jin, Z. Hao, K. Zhang, Z. Yan, J. Chen, *Angew. Chem., Int. Ed.* **2021**, *60*, 20627; d) W. Ju, A. Bagger, G.-P. Hao, A. S. Varela, I. Sinev, V. Bon, B. Roldan Cuenya, S. Kaskel, J. Rossmeisl, P. Strasser, *Nat. Commun.* **2017**, *8*, 944; e) D. Bagchi, M. Riyaz, J. Raj, S. Roy, A. K. Singh, A. Cherevotan, C. P. Vinod, S. C. Peter, *Chem. Mater.* **2024**, *36*, 3464.

[3] B. Chang, H. Pang, F. Raziq, S. Wang, K.-W. Huang, J. Ye, H. Zhang, *Energy Environ. Sci.* **2023**, *16*, 4714.

[4] S. Nitopi, E. Bertheussen, S. B. Scott, X. Liu, A. K. Engstfeld, S. Horch, B. Seger, I. E. L. Stephens, K. Chan, C. Hahn, J. K. Norskov, T. F. Jaramillo, I. Chorkendorff, *Chem. Rev.* **2019**, *119*, 7610.

[5] C. P. O'Brien, R. K. Miao, A. Shayesteh Zeraati, G. Lee, E. H. Sargent, D. Sinton, *Chem. Rev.* **2024**, *124*, 3648.

[6] J. Yu, J. Wang, Y. Ma, J. Zhou, Y. Wang, P. Lu, J. Yin, R. Ye, Z. Zhu, Z. Fan, *Adv. Funct. Mater.* **2021**, 31.

[7] Z. Zhang, L. Bian, H. Tian, Y. Liu, Y. Bando, Y. Yamauchi, Z. L. Wang, *Small* **2022**, *18*, 2107450.

[8] W. Quan, Y. Lin, Y. Luo, Y. Huang, *Adv. Sci.* **2021**, *8*, 2101597.

[9] a) J. Wang, L. Gan, Q. Zhang, V. Reddu, Y. Peng, Z. Liu, X. Xia, C. Wang, X. Wang, *Adv. Energy Mater.* **2018**, *9*, 1803151; b) A. Rosas-Hernández, H. Junge, M. Beller, M. Roemelt, R. Francke, *Catal. Sci. Technol.* **2017**, *7*, 459; c) X. M. Hu, M. H. Ronne, S. U. Pedersen, T. Skrydstrup, K. Daasbjerg, *Angew. Chem., Int. Ed.* **2017**, *56*, 6468; d) S. D. Cyrille Costentin, M. Robert, J.-M. Savéant, *Science* **2012**, *338*, 90; e) E. Oberem, A. F. Roesel, A. Rosas-Hernández, T. Kull, S. Fischer, A. Spannenberg, H. Junge, M. Beller, R. Ludwig, M. Roemelt, R. Francke, *Organometallics* **2018**, *38*, 1236; f) C. Steinlechner, A. F. Roesel, E. Oberem, A. Päpcke, N. Rockstroh, F. Gloaguen, S. Lochbrunner, R. Ludwig, A. Spannenberg, H. Junge, R. Francke, M. Beller, *ACS Catal.* **2019**, *9*, 2091; g) R. Francke, B. Schille, M. Roemelt, *Chem. Rev.* **2018**, *118*, 4631.

[10] a) A. Taheri, L. A. Berben, *Chem. Commun.* **2016**, *52*, 1768; b) A. Taheri, E. J. Thompson, J. C. Fettinger, L. A. Berben, *ACS Catal.* **2015**, *5*, 7140; c) S. Roy, B. Sharma, J. Pecaut, P. Simon, M. Fontecave, P. D. Tran, E. Derat, V. Artero, *J. Am. Chem. Soc.* **2017**, *139*, 3685.

[11] a) L.-J. Zhu, D.-H. Si, F.-X. Ma, M.-J. Sun, T. Zhang, R. Cao, *ACS Catal.* **2023**, *13*, 5114; b) L. L. Zhuo, P. Chen, K. Zheng, X. W. Zhang, J. X. Wu, D. Y. Lin, S. Y. Liu, Z. S. Wang, J. Y. Liu, D. D. Zhou, J. P. Zhang, *Angew. Chem., Int. Ed.* **2022**, *61*, 202204967; c) P. Wang, T. Li, Q. Wu, R. Du, Q. Zhang, W. H. Huang, C. L. Chen, Y. Fan, H. Chen, Y. Jia, S. Dai, Y. Qiu, K. Yan, Y. Meng, G. I. N. Waterhouse, L. Gu, Y. Zhao, W. W. Zhao, G. Chen, *ACS Nano* **2022**, *16*, 17021; d) H. Q. Liang, T. Beweries, R. Francke, M. Beller, *Angew. Chem., Int. Ed.* **2022**, *134*, 202200723.

[12] a) D. H. Nam, P. De Luna, A. Rosas-Hernandez, A. Thevenon, F. Li, T. Agapie, J. C. Peters, O. Shekhah, M. Eddaoudi, E. H. Sargent, *Nat. Mater.* **2020**, *19*, 266; b) D. Grammatico, A. J. Bagnall, L. Riccardi, M. Fontecave, B. L. Su, L. Billon, *Angew. Chem., Int. Ed.* **2022**, *61*, 202206399; c) N. Liu, W. Ju, R. Francke, *Curr. Opin. Electrochem.* **2025**, *49*, 101598.

[13] P. G. Sammes, G. Yahioglu, *Chem. Soc. Rev.* **1994**, *23*, 327.

[14] A. Bencini, V. Lippolis, *Coord. Chem. Rev.* **2010**, *254*, 2096.

[15] a) G. Anderegg, *Helv. Chim. Acta* **1963**, *46*, 2397; b) G. Anderegg, *Helv. Chim. Acta* **1963**, *46*, 2813.

[16] N. Liu, S. Bartling, A. Springer, C. Kubis, O. S. Bokareva, E. Salaya, J. Sun, Z. Zhang, S. Wohlrab, A. M. Abdel-Mageed, H. Q. Liang, R. Francke, *Adv. Mater.* **2024**, *36*, 2309526.

[17] a) M. R. Singh, Y. Kwon, Y. Lum, J. W. Ager III, A. T. Bell, *J. Am. Chem. Soc.* **2016**, *138*, 13006; b) J. Resasco, L. D. Chen, E. Clark, C. Tsai, C. Hahn, T. F. Jaramillo, K. Chan, A. T. Bell, *J. Am. Chem. Soc.* **2017**, *139*, 11277; c) M. C. O. Monteiro, F. Dattila, B. Hagedoorn, R. García-Muelas, N. López, M. T. M. Koper, *Nature Catal.* **2021**, *4*, 654.

[18] M. C. Biesinger, *Surf. Interface Anal.* **2017**, *49*, 1325.

[19] E. Borfecchia, K. A. Lomachenko, F. Giordanino, H. Falsig, P. Beato, A. V. Soldatov, S. Bordiga, C. Lamberti, *Chem. Sci.* **2015**, *6*, 548.

[20] a) J. Du, B. Cheng, L. Jiang, Z. Han, *Chem. Commun.* **2023**, *59*, 4778; b) C. F. Wen, M. Zhou, P. F. Liu, Y. Liu, X. Wu, F. Mao, S. Dai, B. Xu, X. L. Wang, Z. Jiang, P. Hu, S. Yang, H. F. Wang, H. G. Yang, *Angew. Chem., Int. Ed.* **2022**, *61*, 202111700; c) X. Xie, X. Zhang, M. Xie, L. Xiong, H. Sun, Y. Lu, Q. Mu, M. H. Rummeli, J. Xu, S. Li, J. Zhong, Z. Deng, B. Ma, T. Cheng, W. A. Goddard III, Y. Peng, *Nat. Commun.* **2022**, *13*, 63.

[21] a) D. Karapinar, N. T. Huan, N. Ranjbar Sahraie, J. Li, D. Wakerley, N. Touati, S. Zanna, D. Taverna, L. H. Galvao Tizei, A. Zitolo, F. Jaouen, V. Mougel, M. Fontecave, *Angew Chem Int Ed Engl* **2019**, *58*, 15098; b) Z. Weng, Y. Wu, M. Wang, J. Jiang, K. Yang, S. Huo, X. F. Wang, Q. Ma, G. W. Brudvig, V. S. Batista, Y. Liang, Z. Feng, H. Wang, *Nat. Commun.* **2018**, *9*, 415.

[22] T. Gunter, H. W. Carvalho, D. E. Doronkin, T. Sheppard, P. Glatzel, A. J. Atkins, J. Rudolph, C. R. Jacob, M. Casapu, J. D. Grunwaldt, *Chem. Commun.* **2015**, *51*, 9227.

[23] Z. Zhang, X. Huang, Z. Chen, J. Zhu, B. Endrodi, C. Janaky, D. Deng, *Angew. Chem., Int. Ed.* **2023**, *62*, 202302789.

[24] a) J. Wang, C. S. Hsu, T. S. Wu, T. S. Chan, N. T. Suen, J. F. Lee, H. M. Chen, *Nat. Commun.* **2023**, *14*, 6576; b) Y. N. Xu, B. Mei, Q. Xu, H. Q. Fu, X. Y. Zhang, P. F. Liu, Z. Jiang, H. G. Yang, *Angew. Chem., Int. Ed.* **2024**, *63*, 202404213.

[25] a) J. Halldin Stenlid, M. Gorlin, O. Diaz-Morales, B. Davies, V. Grigorev, D. Degerman, A. Kalinko, M. Borner, M. Shipilin, M. Bauer, A. Gallo, F. Abild-Pedersen, M. Bajdich, A. Nilsson, S. Koroidov, *J. Am. Chem. Soc.* **2025**, *147*, 4120; b) B. B. Sarma, F. Maurer, D. E. Doronkin, J. D. Grunwaldt, *Chem. Rev.* **2023**, *123*, 379; c) G. E. Cutsail Iii, S. DeBeer, *ACS Catal.* **2022**, *12*, 5864.

[26] B. Boro, P. Kalita, A. Vijayaprabhakaran, D. Q. Dao, S. Nandy, K. H. Chae, Y. Nailwal, M. Kathiresan, J. Mondal, *ACS Appl. Nano Mater.* **2023**, *6*, 11788.

[27] C.-T. Dinh, T. Burdyny, M. G. Kibria, A. Seifitokaldani, C. M. Gabardo, F. P. García de Arquer, A. Kiani, J. P. Edwards, P. De Luna, O. S. Bushuyev, C. Zou, R. Quintero-Bermudez, Y. Pang, D. Sinton, E. H. Sargent, *Science* **2018**, *360*, 783.

[28] X.-M. Hu, H. H. Hval, E. T. Bjerglund, K. J. Dalgaard, M. R. Madsen, M.-M. Pohl, E. Welter, P. Lamagni, K. B. Buhl, M. Bremholm, M. Beller, S. U. Pedersen, T. Skrydstrup, K. Daasbjerg, *ACS Catal.* **2018**, *8*, 6255.

[29] https://www.esrf.fr/UsersAndScience/Experiments/CRG/BM20/Software/Wavelets/HAMA.

[30] G. Landrot, E. Fonda, *J. Synchrotron Radiat.* **2025**, *32*, 1085.

[31] J. Jaumot, R. Gargallo, A. de Juan, R. Tauler, *Chem. Int. Lab. Sys.* **2005**, *76*, 101.

Appendix 2. Curriculum Vitae

TRANG MINH PHAM

Personal Information

Date of Birth	27.09.1995 in Hai Phong, Vietnam
Nationality	Vietnamese
Address	Südring Nr. 72H, 18059 Rostock, Germany
E-Mail	trang.pham@catalysis.de
ORCID	0009-0007-3538-9326
Languages	Vietnamese (native), English (fluent), German (intermediate)

Academic Education

2021 - 2025	**Doctoral Researcher** in Electrochemistry & Catalysis at Leibniz Institute for Catalysis (LIKAT), Rostock, Germany Supervisors: Prof. Dr. Robert Francke and Dr. Annette-Enrica Surkus Thesis: Development of Heterogeneous Electrocatalysts for Conversion of Small Molecules Toward Sustainable Energy Transition Funding: Fellowship of RoHan Catalysis SDG Graduate School (09/2021 – 08/2024) and IREKA Project (German industrial H2Giga project) (09/2024 – 09/2025)
2019 - 2021	**Master of Science** in Chemical Engineering at Hanoi University of Science and Technology (HUST), Vietnam and Leibniz Institute for Catalysis (LIKAT), Rostock, Germany funded by RoHan Catalysis SDG Graduate School Supervisors: Assoc. Prof. Dr. Thuy Thi Bich Hoang and Dr. Annette-Enrica Surkus Thesis: Synthesis of MOFs catalyst materials for electrochemical reduction of CO_2 Funding: Fellowship of RoHan Catalysis SDG Graduate School (03/2020 – 08/2020)
2013 - 2018	**Engineer** in Chemical Engineering at Hanoi University of Science and Technology (HUST), Vietnam Supervisor: Dr. Dung Trung Dang

Publications

Doctoral Thesis	
1	T.M. Pham, M. Plevova, S. Bartling, N. Rockstroh, A. Springer, A. Slabon, J. Hnat, A.-E. Surkus, R. Francke, Oxygen-deficient annealing boosts performance of CoNiFe oxide electrocatalyst in oxygen evolution reaction, J. Catal., 438 (2024) 115675
2	T.M. Pham, N. Liu, S. Bartling, N. Rockstroh, R. Eckelt, W. Ju, A.-E. Surkus, R. Francke, Pre-treated carbon additive enables reduction of metal loading in CoNiFe oxide-based OER electrocatalysts while maintaining performance, J. Catal., 450 (2025) 116299
3	N. Liu, T.M. Pham, Y. Han, O.S. Bokareva, S. Bartling, A. Springer, A. Spannenberg, C. Kubis, J. Weiss, D.E. Doronkin, W. Ju, R. Francke, Heterogenized Copper(II) Phenanthroline Catalysts for Electroreduction of CO_2 to C_2 Compounds: Substitution on the Ligand Causes Structural Changes to the Molecular Framework and Stability Enhancement, Adv. Mater., n/a (2025) e13702

Others

4 Y. Peng, N. Rockstroh, J. Rabeah, S. Bartling, X. Dai, X. Qin, T.M. Pham, A.-E. Surkus, R. Thomas, H. Seitz, H. Junge, M. Beller, Photocatalytic synthesis of ethylene glycol and hydrogen from methyl tert-butyl ether, Nat. Commun., 16 (2025) 3959

5 P.M. Trang, A.-E. Surkus, L.T.T. Hang, H.T.B. Thuy, Studying in catalytic properties of Ni@ZIF-8 for electrochemical reduction of CO2, Proceedings of the 6th National Scientific Conference: Corrosion and protection of metals for sustainable development, (2021)

6 M.T. Tung, V.D. Luong, P.M. Trang, L.V. Tuyen, H.T.B. Thuy, N.-L. Wu, Activated carbon with hierarchical porosity derived from biomass for lithium sulfur batteries, Vietnam J. Chem., 57 (2019) 182-188

7 M.T. Tung, V.D. Luong, P.M. Trang, L. Van Tuyen, H.T. Bich Thuy, N.-L. Wu, The synthesis and characterization of high purity mixed microporous/mesoporous activated carbon from rice husk, Vietnam J. Chem., 56 (2018) 684-688

Project participation

During doctoral study

1 National Hydrogen Strategy, Flagship Project H2Giga, QT1.3 IREKA (2021 – 2025)
Project title: Iridium-reduzierte Anodenkatalysatoren für die PEM-Wasserelektrolyse
(Link: Wasserstoff-Leitprojekte: H2Giga-Projekte)
Project manager: Dr. Annette-Enrica Surkus (LIKAT, 18059 Rostock)
My contribution: develop low-Ir content materials, perform experimental works: material synthesis, optimization for synthesis procedures as well as the electrochemical measurements, progress electrochemical analysis in RDE conditions, evaluate analytical data, report and discuss project results.

2 National Hydrogen Strategy, Flagship Project H2Giga, SEGIWA (2021 – 2025)
Project title: Serienproduktion von Elektrolyseuren im Gigawatt-Bereich - Large scale production of PEM electrolyzers in GW range
(Link: Wasserstoff-Leitprojekte: H2Giga-Projekte)
Project manager in the topic of Alternative catalysts: Dr. Annette-Enrica Surkus (LIKAT, 18059 Rostock)
My contribution: synthesis and optimize the low-Ir content materials

3 For the Volkswagen's project (2025)
Project title: Elektrochemische CO_2-Reduktion zu Monoethylenglykol (MEG)
My contribution: perform experiments of converting ethylene to ethylenglycol by electrochemical oxidation reaction

4 For SLV Mecklenburg-Vorpommern GmbH (2024)
My contribution: test the performance of Ni-plates for hydrogen evolution reaction in alkaline medium

In the past

5	Vietnam-Taiwan Protocol Collaboration Research Project Nr. NDT.19.TW/16 (2016-2019) Project title: Novel mesoporous materials $CSiO_x$ for advanced power sources from Rice Husks Project manager: Prof. Dr. Mai Thanh Tung (HUST, 10000 Hanoi, Vietnam) My contribution: perform laboratory experiment in Vietnam, evaluate data
6	World Bank Project Nr 15/FIRST1a/HUST (2017-2019) Project title: Technological transfer of Lithium-ion Batteries to Vietnam Project manager: Prof. Dr. Mai Thanh Tung (HUST, 10000 Hanoi, Vietnam) My contribution: perform laboratory experiment in Vietnam, evaluate data

Poster & Oral Contributions

Oral	
1	T.M. Pham, J. Hnat, A.-E. Surkus, R. Francke, The Electrochemical Society (ECS2024), San-Francisco, USA, May 2024 Oral title: Oxygen-Deficient Thermal Treatment Boosts Performance of Co-Ni-Fe Oxide Electrocatalyst in Oxygen Evolution Reaction (DOI 10.1149/MA2024-01341832mtgabs)
2	T.M. Pham, A.-E. Surkus, RoHan - Summerschool 2023 "Catalysis for a Sustainable and Innovative Future", Rostock, Germany, June 2023 Oral title: Development of oxygen evolution catalysts with reduced noble metal content for water electrolysis
3	T.M. Pham (contributor), A.-E. Surkus, REGWA Energie-Symposium 2024, Stralsund, Germany, November 2024 Oral title: Einfluss des Pyrolysegases in der Synthese von CoNiFe-Oxiden auf deren katalytische Leistung hinsichtlich der alkalischen Wasseroxidation (OER)
Poster	
1	T.M. Pham, A.-E. Surkus, R. Francke, 2024 GDCH Electrochemistry, Braunschweig, September 2024 Poster title: Effects of Annealing Conditions on OER Performance of Co-Ni-Fe Oxides
2	T.M. Pham, A.-E. Surkus, RoHan - Summerschool 2023 "Catalysis for a Sustainable and Innovative Future", Rostock, Germany, June 2023 Poster title: Low Ir-Content Materials as Electrocatalysts for Oxygen Evolution Reaction (OER) under Acidic Conditions
3	T.M. Pham, T.T.B. Hoang, R. Francke, H. Junge, A.-E. Surkus, ComBioCat Symposium, Rostock, June 2022 Poster title: Ni@ZIF-8 derived materials for electrochemical reduction of CO_2 to CO
4	T.M. Pham (contributor), A.-E. Surkus, The Electrochemical Society (ECS2024), San-Francisco, USA, May 2024 Poster title: Low Ir-Containing Materials As Anode Catalysts for PEM Water Electrolysis (DOI 10.1149/MA2024-01341760mtgabs)
5	N. Rockstroh, T.M. Pham, C. Kreyenschulte, A.-E. Surkus, R. Francke, The 17th European Microscopy Congress (EMC 2024), August 2024 Poster title: Effect of preparation and oxygen evolution catalysis on CoNiFe oxide electrocatalysts revealed by STEM-EELS (DOI 10.1051/bioconf/202412925036)

6	A.-E. Surkus, T.M. Pham, R. Francke, 76th Annual ISE Meeting, Mainz, Germany, September 2025 Poster title: Reduction of Metal Loading in CoNiFe Oxide-Based OER Electrocatalysts by Admixture of Pre-Treated Carbon
7	A.P. Philip, T.M. Pham, W. Ju, A.-E. Surkus, R. Francke, 76th Annual ISE Meeting, Mainz, Germany, September 2025 Poster title: Efficient Electrocatalytic Oxidation of Glucose using CoNiFe Oxide
8	T.M. Pham (contributor), C. Schare, C. Klose, A.-E. Surkus, 5th International Conference on Electrolysis, Freiburg, Germany, August 2025 Poster title: Low Iridium-Content Materials as Anode Catalysts for PEM Water Electrolysis
9	T.M. Pham (contributor), R. Francke, A.-E. Surkus, GET Duisburg (4th Conference of the GDCh Division of Chemistry and Energy), April 2025 Poster title: Effects of Annealing Conditions on OER Performance of Co-Ni-Fe Oxides
10	T.M. Pham (contributor), A.-E. Surkus, 2024 GDCH Electrochemistry, Braunschweig, September 2024 Poster title: Low Ir-Content Materials as Anode Catalysts for PEM Water Electrolysis
11	T.M. Pham, G. Xue, E. Salaya, A.M. AbdelMageed, S. Wohlrab, H. Junge, C.B. dos Santos, S. Kölle, A.-E. Surkus, H2Giga Status Conference, Frankfurt am Main, September 2025 Poster title: Low Ir-Containing Materials as Electrocatalysts for Oxygen Evolution Reaction (OER) under Acidic Conditions - IREKA
12	T.M. Pham, G. Xue, E. Salaya, A.M. AbdelMageed, S. Wohlrab, H. Junge, C.B. dos Santos, S. Kölle, A.-E. Surkus, H2Giga Status Conference, Berlin, September 2024 Poster title: Low Ir-Containing Materials as Electrocatalysts for Oxygen Evolution Reaction (OER) under Acidic Conditions - IREKA
13	T.M. Pham, G. Xue, E. Salaya, A.M. AbdelMageed, S. Wohlrab, H. Junge, A.-E. Surkus, H2Giga Status Conference, Berlin, September 2023 Poster title: Oxygen Evolution Reaction (OER) in Acidic Media over TiN/IrO_2 Promoted by Second Metal
14	G. Xue, T.M. Pham, E. Salaya, A.M. AbdelMageed, A.-E. Surkus, S. Wohlrab, H. Junge, M. Beller, H2Giga Status Conference, Frankfurt am Main, September 2022 Poster title: Oxygen Evolution Reaction (OER) Performance of TiN/IrO_2 Electrocatalyst Promoted by Second Metal in Acidic Media

Volunteering

2025	Volunteer for Open Night of Science (LNDW) Rostock
2024	Volunteer for Open Night of Science (LNDW) Rostock
2013 - 2016	Member of volunteer group at Hanoi University of Science and Technology, Hanoi

Appendix 3. Selbstständigkeiserklärung